Chair of Subsurface Engineering

Master's Thesis

Geological and geotechnical characterization and correlation of samples from El Misti (Peru)

Ruben Nicolas Winstel, B.Sc.

October 2024

MONTANUNIVERSITÄT LEOBEN
www.unileoben.ac.at

EIDESSTATTLICHE ERKLÄRUNG

Ich erkläre an Eides statt, dass ich diese Arbeit selbstständig verfasst, andere als die angegebenen Quellen und Hilfsmittel nicht benutzt, den Einsatz von generativen Methoden und Modellen der künstlichen Intelligenz vollständig und wahrheitsgetreu ausgewiesen habe, und mich auch sonst keiner unerlaubten Hilfsmittel bedient habe.

Ich erkläre, dass ich den Satzungsteil „Gute wissenschaftliche Praxis“ der Montanuniversität Leoben gelesen, verstanden und befolgt habe.

Weiters erkläre ich, dass die elektronische und gedruckte Version der eingereichten wissenschaftlichen Abschlussarbeit formal und inhaltlich identisch sind.

Datum 12.10.2024

Unterschrift Verfasser/in
Ruben Nicolas Winstel

Acknowledgments/Danksagung

Das Schreiben dieser Arbeit wäre ohne die Hilfe von Vielen nicht möglich gewesen, an dieser Stelle möchte ich mich bei allen bedanken, die diese Arbeit ermöglicht haben.

An erster Stelle gebührt mein Dank Frau Assoz. Prof. Dr. Marlene Villenueve, die meine Arbeit betreut hat und mich stets mit fachlichem Rat und Anregungen unterstützt hat.

Des Weiteren möchte ich Herrn Univ.-Prof. Mag. rer. nat. Dr. mont. Frank Melcher für die geologische und mineralogische Begleitung und Betreuung der Masterarbeit ganz besonders danken.

Außerdem bedanke ich mich bei den Mitarbeitern des Lehrstuhles für Subsurface Engineering und Lehrstuhles für Geologie und Lagerstättenlehre. Hervorheben möchte ich Prof. Mag. et Dr. rer. nat. Rantitsch für die Unterstützung und Messung der RFA-Daten, Bak. Ivaylo Martinov für die Probenpräparation, sowie Ing. Jörg Krainz und Miguel Marek für die Unterstützung, Präparation und Messung der geotechnischen Parameter. Außerdem möchte ich mich bei Joel Bensing für die Hilfe mit den BIB-SEM Aufnahmen bedanken.

Des Weiteren möchte ich mich bei Guido Edgard Salas Álvarez und Carlos Alberto Luza Huillca für die Probennahme und Probenbeschreibung im Feld bedanken.

Mein Dank gilt auch meinen Studienkollegen aus Bachelor- und Masterstudium, die mich stets unterstützt und motiviert haben.

Besonderer Dank gilt meiner Familie, besonders meinen Eltern für die allzeitige Unterstützung und das Ermöglichen meines Studiums. Meiner Freundin Lena möchte ich auch an dieser Stelle besonders danken für die Unterstützung und Motivation während meines Studiums und der Abschlussarbeit.

Kurzfassung

In den letzten Jahren wurde vermehrt die Interaktion und Beeinflussung von geotechnischen Parametern auf Gesteinseigenschaften untersucht. Im speziellen wurden der Einfluss der Porosität und der Anteil der Phänokristalle auf die Gesteinsfestigkeit in Vulkaniten analysiert.

Im Rahmen der UNSA II Kooperation wurden Vulkanite des Stratovulkans El Misti in Peru beprobt und auf ihre Lithologie, die geologische Vergleichbarkeit, sowie zur geologischen und geotechnischen Charakterisierung untersucht. Des Weiteren wurde betrachtet, ob sich Parameter untereinander beeinflussen oder korrelieren.

Hierzu wurden die Proben geotechnisch auf uniaxiale und triaxiale Druckfestigkeit, Zugfestigkeit, P-Wellengeschwindigkeit, sowie Porosität und Dichte untersucht. Zur geologischen Charakterisierung wurde Polarisationsmikroskopie, Rasterelektronenmikroskopie und Gesteinsgesamtanalyse mit Hilfe der Röntgenfluoreszenzanalyse durchgeführt.

In den meisten geologischen Eigenschaften unterscheiden sich die Proben, bestehend aus Ignimbriten, Rhyoliten und Andesiten kaum zu den aus der Literatur beschriebenen Gesteinen von El Misti, außerdem ähneln sie vergleichbaren geotechnischen Untersuchungen an anderen Stratovulkanen. Es sind mineralogisch keine großen Unterschiede zwischen den Ignimbriten und Rhyoliten festzustellen. Auch geochemisch unterscheiden sich die Proben kaum. Deutliche Unterschiede konnten nur im Phänokristallanteil, der Porosität und der davon beeinflussten Parameter, wie der Gesteinsfestigkeit, bestehend aus Zugfestigkeit, uniaxialer und triaxialer Druckfestigkeit festgestellt werden. In den Andesiten sind Unterschiede in Zusammensetzung und Geochemie besonders zwischen den Proben des Rio Chili und der Probe des Rio Andamayo feststellbar. Letztere zeigt einen erhöhten K_2O Gehalt und ist trachyandesitisch in ihrer Zusammensetzung.

Bei der Korrelation der geotechnischen und geologischen Daten zeigt sich der starke Einfluss der Porosität auf die Stabilität und geotechnischen Eigenschaften aller Proben. Wenn jedoch die Proben in die Pyroklastika und Effusiva unterteilt werden, zeigt sich, dass in den Pyroklastika die Phänokristalle im Gegensatz zu der Porosität, eine deutliche positive Korrelation zu den meisten Festigkeitsparametern aufweisen. Ein kausaler Zusammenhang konnte nicht nachgewiesen werden. Dahingegen ist in den Effusiva die Matrixzusammensetzung neben der Porosität entscheidend für die Gesteinsfestigkeit. Außerdem führt ein höherer Anteil an Phänokristallen zu einer Verringerung der Zugfestigkeit in den Effusiva.

Abstract

Recently, the interaction and influence of geological characteristics on geotechnical parameters has been increasingly investigated. In particular, the influence of porosity and the proportion of phenocrysts on the rock strength in volcanic rocks is of interest.

As part of the UNSA II cooperation, volcanites from the El Misti stratovolcano in Peru were sampled and examined regarding the lithology, geological comparability and geological and geotechnical characterization. Furthermore, it was tested whether parameters influence or correlate with each other or not.

For this purpose, the samples were analysed for uniaxial and triaxial compressive strength, tensile strength, P-wave velocity, porosity and density. Polarisation microscopy, scanning electron microscopy and total rock analysis using X-ray fluorescence analysis were carried out for geological characterization.

In most parameters and properties, the samples, consisting of ignimbrites, rhyolites and andesites hardly differed from the Misti rocks described in the literature, and they are also similar to comparable geotechnical investigations on other stratovolcanoes. Mineralogically, no major differences are found between the ignimbrites and rhyolites. The samples also hardly differ geochemically. The main differences are only found in the phenocryst content, the porosity and the parameters influenced by this, such as the rock strength, consisting of tensile strength, uniaxial and triaxial compressive strength. Differences in composition and geochemistry are described in the andesites, particularly, between the andesites of Rio Chili and Rio Andamayo. The latter shows an increased K_2O content and is trachyandesitic in composition.

The correlation of the geotechnical and geological data prove the strong influence of porosity particularly on the stability and geotechnical properties of all samples. However, by subdividing the samples in pyroclastics and effusives, the pyroclastics show a clear positive correlation of the phenocryst content to most strength parameters, which contradicts to the negative correlation of porosity. A causal relationship has not been proven. Whereas in the effusives the matrix composition is decisive to rock strength in addition to the porosity. An increase in phenocryst content in the effusives leads to a reduction in tensile strength.

Contents

1 Introduction and research issues

El Misti volcano (Peru) is one of the potentially active volcanoes of the central Andean volcanic zone. The increasing number of inhabitants in the city of Arequipa and the surrounding basin, reaching nearly a million living only up to 9 km distance from the crater of Misti (Sandri et al. 2014), make a better understanding of the volcano necessary.

Sandri et al. (2014) identified multiple hazards for the city of Arequipa, consisting of pyroclastic flows, lahars and tephra falls. As the most likely hazard, lahars with 10 %/year were identified. Beside those hazards, slope failure, as already visible on the today's volcano cone northwest flank (Thouret et al. 2001), reveal the necessity of rock strength investigations of the volcanites of El Misti.

Although the rocks of Misti have been already investigated by Thouret et al. (2001) and Rivera et al. (2016) in terms of mineralogy, geochemistry and magma evolution, a geotechnical characterization has not been conducted so far. The rock strength of volcanic rocks and its influences have been investigated as numerical modelling or on other volcanos in Heap et al. (2014), Heap et al. (2016), Zorn et al. (2018), Heap and Violay (2021), Heap et al. (2021), Villeneuve and Heap (2021). As major rock strength controlling factors porosity, crystal content and pore shape have been identified. Therefore, as part of the UNSAII cooperation, including the university of St. Augustin in Arequipa (Peru), the Colorado school of mining (USA) and the Montanuniverstät Leoben (Austria), samples from Rio Chili and Rio Andamayo canyon have been investigated. These macroscopically similar samples are part of this thesis.

The samples were examined for their lithology, petrography, geochemistry and geotechnical parameters. This is achieved by the determination of uniaxial compressive strength, Youngs modulus, tensile strength, cohesion and friction angle beside a mineralogical and geochemical characterization. Additionally, correlations between the data shall be found, the influence factors identified and compared to the current state of research.

2 Theoretical background

2.1 Failure Criteria

2.1.1 Mohr-Coulomb and Hoek-Brown criterion

Theoretical background - failure criteria

For the determination of rock strength properties of joint rock masses, the interlocking and the separating surface condition, the Mohr Coulomb and Hoek-Brown criterion are used. While the Mohr Coulomb Criterion is widely used for intact rock (Jaeger et al. 2007), the Hoek-Brown criterion is suitable for joint rock as well and provides determination of the Mohr Coulomb parameters, taking in account further rock characterizing parameters (Hoek E. 2007).

Mohr Coulomb Criterion

According to Prinz and Strauß (2018) the shear strength τ is often taken as the rock strength, because if exceeded, movement at one or more surfaces, without further stress increase is possible. After Coulomb the shear strength τ consists of the cohesion c [GPa] or S_0 and the friction angle φ [°]and can be described as a function of the normal stress σ, which is defined by the maximal stress σ_1 and the minimal stress σ_3 in a triaxial setting, as follows:

$$\tau = c + \sigma * \tan(\varphi)$$

In the Mohr Coulomb criterion different shear tests can be used for the determination of the cohesion and the friction angle (Prinz and Strauß 2018) (figure 1A), even if this was not applied in this work. Cohesion represents the internal cohesive force holding the rock components together, whereas the friction angle defines the increase of shear strength τ taking into account the normal stress σ[MPa]. In general, failure will occur if the stress condition at any point on the envelope (figure 1A) is reached (Jaeger et al. 2007). After failure τ_f the shear resistance will decrease to a residual shear resistance τ_r [MPa] (Prinz and Strauß 2018).

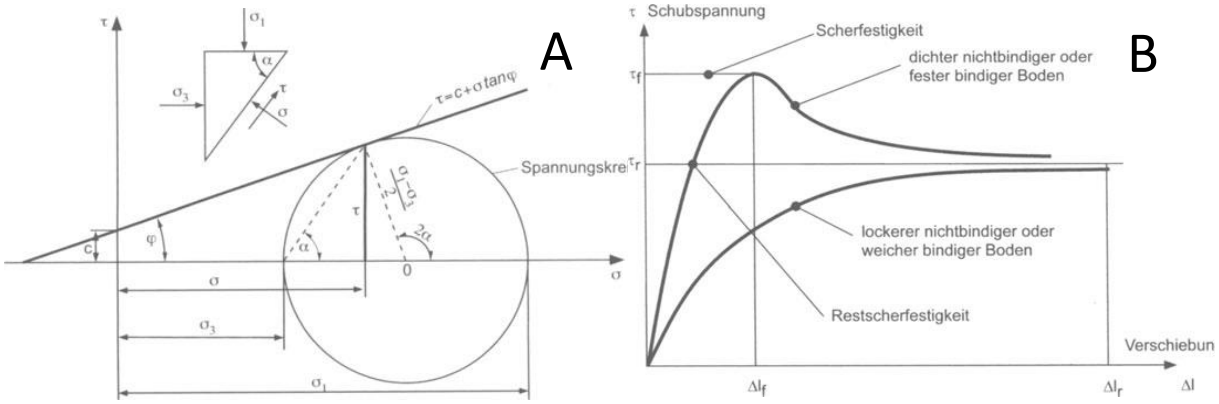

Figure 1: Graphs of the Mohr envelope [A] and shear stress-strain curves of brittle and ductile deformation [B] according to Prinz and Strauß (2018)

The Mohr Coulomb equation expresses a straight line and can also be described as:

$$\sigma_1 = 2c\frac{cos\varphi}{1-sin\varphi} + \sigma_3\frac{1+sin\varphi}{1-sin\varphi}$$ after Jaeger et al. (2007)

Hoek-Brown criterion

While the Mohr-Coulomb criterion shows a linear correlation of τ and σ, experiments have shown that the increase of σ_1 with respect to σ_3 is not linear. Therefore, a nonlinear relation is needed, generally described as:

$$\sigma_1' = \sigma_3' + \sigma_{ci}'(m_0 * \frac{\sigma_3'}{\sigma_{ci}'} + s)^a$$ after Hoek (2007)

The σ_1 and σ_3 represent the maximum and minimum effective stress, while σ_{ci} is the uniaxial compressive strength. The m_0 is the Hoek Brown constant, ranging between 5 and 30, depending on the rock type (Hoek 2007). The constants s and a depend on the rock mass characteristics, therefore the formula for intact rock is:

$$\sigma_1' = \sigma_3' + \sigma_{ci}'(m_0 * \frac{\sigma_3'}{\sigma_{ci}'} + 1)^{0,5}$$ after Hoek (2007)

2.2 Regional geology

2.2.1 Geology of the Andes

The formation of the Andean orogen is highly complex and still controversially discussed concerning its detailed mechanisms (Boschman 2021) (figure 2 A & B). The strong diachronology between north, south and the central orogen further complicates a generally valid formation history.

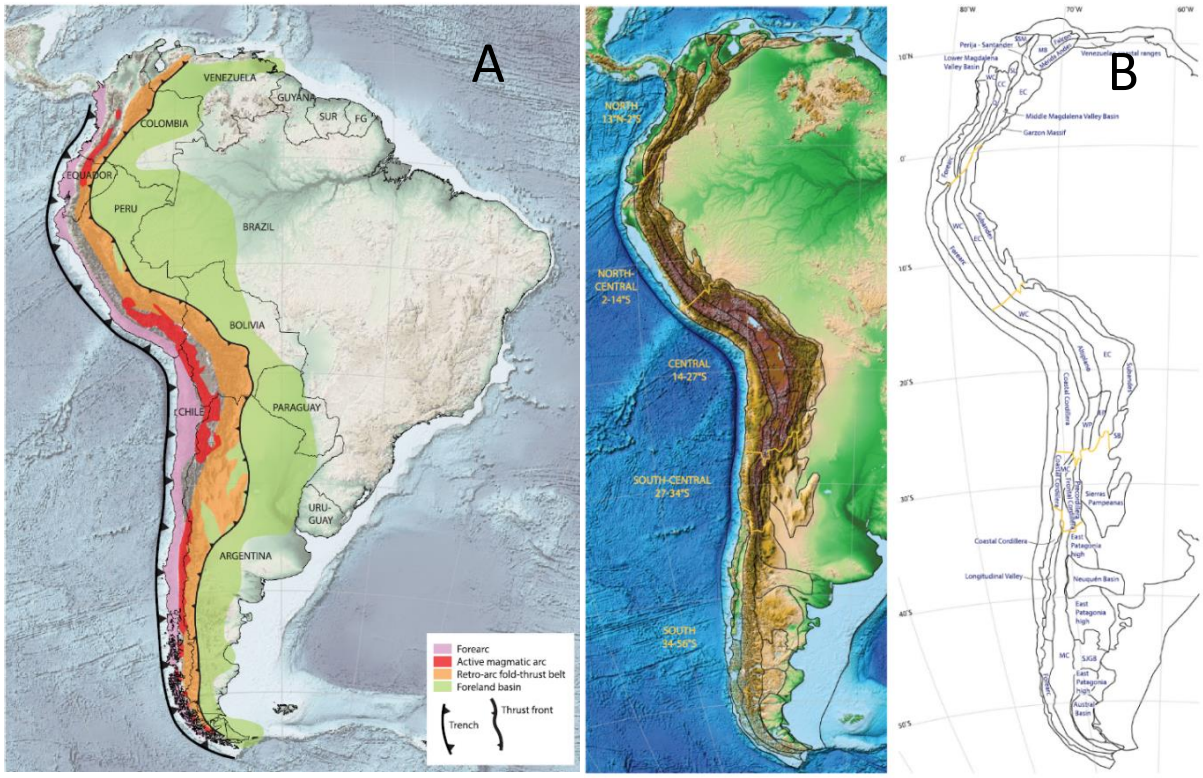

Figure 2: East-West zonation of the Andes [A] and the subdivision of the different cordilleras and areas [B] according to Boschman (2021).

According to Lomize (2008) the formation of the basement in the early to middle Paleozoic is taken as a starting point for the description of the orogeny. Terrain accretion along the Gondwana margin occurred during the growth of Pangea. Since the late Paleozoic an unconformable overlapping of the first subduction related volcanism occurred (Lomize 2008). These volcanic rocks are attributed to the early Triassic (Boschman 2021) .

During the early Jurassic this subduction zone was reactivated and an island arc system formed. Along this zone, andesites to basaltic andesites were produced. A 100 km wide volcanic belt formed (Lomize 2008) (Figure 3), emerging above the sea level in the area of today's coastal cordillera, pointing out to 200-300 km subduction erosion until today (Boschman 2021). In the early Cretaceous the magmatic arc moved 20-30 km inland causing synclinal structures and intrusion of diorites and granodiorites. In combination with the high

Mesozoic sea level, extension along the western cordillera caused, lakes and costal plane areas in back arc and intra arc basins (Boschman 2021). Collision of the South American plate with the Caribbean marked the start of mountain building in the northern Andes at around 80 Ma. The extensional regime and the formation of a back arc caused intra arc and intracontinental rifting that led to crustal thinning of up to 30-35 km (Lomize 2008). This phase is called the initial subsidence stage (Lomize 2008).

In the mid Cretaceous, a change in the stress state at the continental margin led to the Peruvian tectonic phase. Again, the volcanic belt moved 50-60 km further east to the area of the later formed Precodillera (Lomize 2008). The high thickness of the sediments transported into those basins at 70-60 Ma shows that there was as a change from extension to compression caused by the opening of the Atlantic Ocean and closing of back arc basins (Boschman 2021). The compression along the Andean margin caused a crustal thickening and horizontal shortening of up to 40 km (Lomize 2008). This phase is called Preorogenic stage in Lomize (2008).

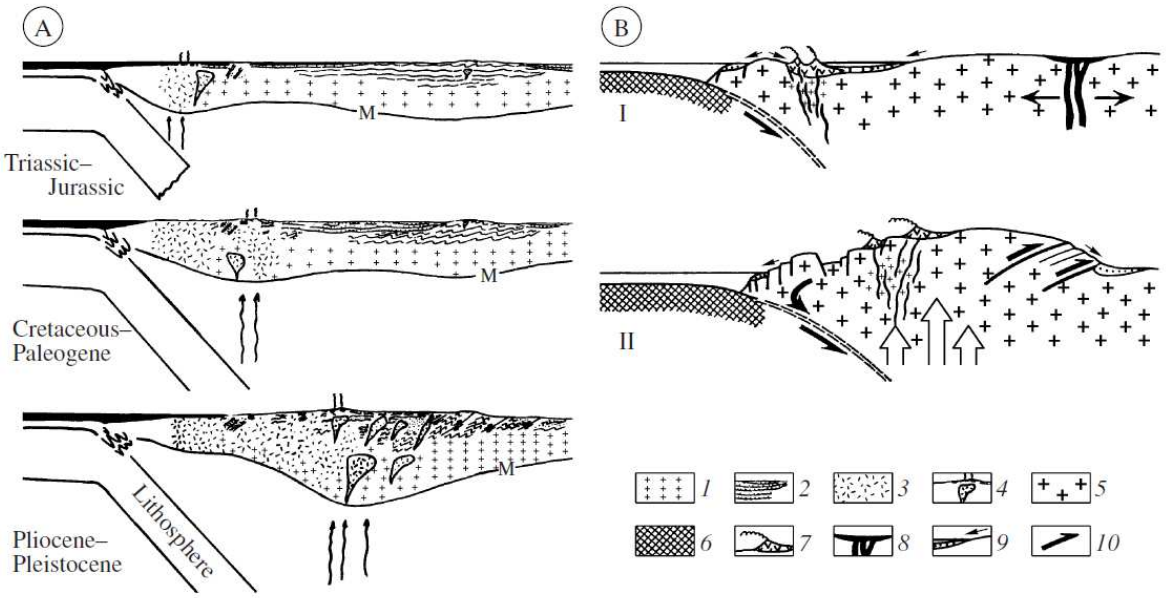

Figure 3: Evolution models of the Andes active continental margin according to James et al. (1971) in Lomize (2008) [A] and by Lomize (2008) sowing the early (I) and orogenic stage (II)[B]

In the orogenic stage, starting in the early Eocene, the currently visible orogen was formed. The ongoing compression led to a horizontal shortening of 250 km. In the early stage (early to middle Eocene) of the orogeny the shortening was limited to weakened zones, like the active volcanic belt in the west or in rift systems. Therefore, the uplift rate was rather small (Lomize 2008). According to Boschman (2021), at 55 Ma another west-directed shift of the magmatic

arc occurred. In the Oligocene the shortening of the central Andean Altiplano with the precordillera and eastern cordillera took place, although still being around 550 km wide. Previous reverse and thrust fault systems expanded and shortened the area by 65-85 km at rates of 1 mm to 8 mm a year (Lomize 2008). The uplift remained relatively small with the Altiplano at <2000 masl in the middle Eocene (Lomize 2008). The inhomogeneities of the deformation of the brittle crust led to a mechanical separation to the lower viscous deeper crust according to Lomize (2008). The heating of the crust caused by the thickening led to partial melting and therefore ignimbritic, rhyolitic and dacitic volcanism. During the transition from Eocene to Oligocene, the Andean volcanic belt was reactivated and shifted 90 km westward into the western volcanic cordillera where it is still active today. In the Miocene (20 Ma) the uplift of the eastern, southern and central domains occurred, while in the northern Andes the uplift migrated northward (Boschman 2021). In the last 10 Ma the uplift of the central Andes up to their current height took place (figure 4). Especially in the late Miocene, a change of the tectonic setting caused a rapid rise of the Altiplano and an eastward migration of the deformation front (Boschman 2021). The exact mechanism is still discussed very controversially (Boschman 2021). Lomize (2008) interprets the rapid uplift by the viscous crust shortening between the craton and frontal zone.

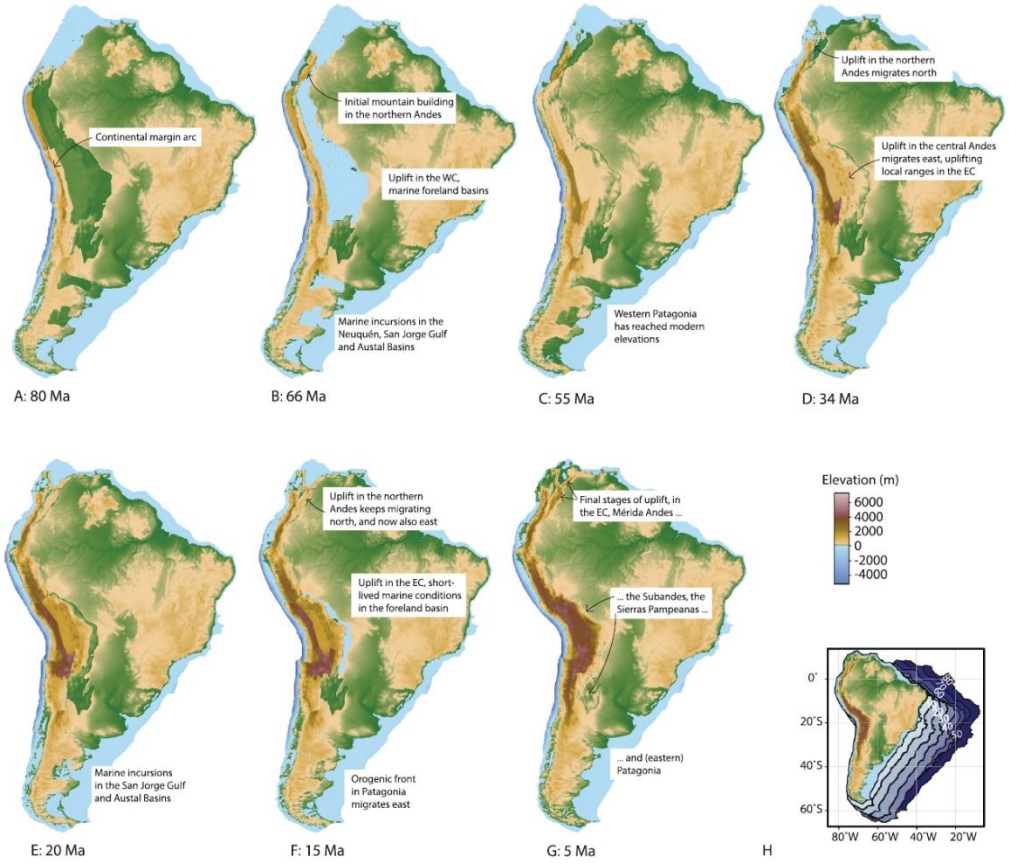

Figure 4: Evolution of the Andes during the last 80 Ma after a paleoelevation reconstruction by Boschman (2021)

2.2.2 Subduction related volcanism

Subduction related volcanoes (SSV) can be found all around the Pacific, namely in the Circum-Pacific "Fire Belt". Depending on the development status different magmatic processes appear (Gill 2010). During the subduction in a continental-oceanic setting, the oceanic basaltic crust (6-7 km thick), consisting of variably hydrothermally altered sediments and basalts (slab), is subducted under the less dense continental crust (up to 70 km thick). Depending on the dipping angle of the oceanic plate, volcanism occurs. In South America the steeply dipping Nazca plate (30-50°) causes the formation of the central Andean volcanic zone (CVZ), as well as the northern (NVZ) and southern Andean volcanic zone (SVZ) (Chen et al. 2001; Gill 2010). These zones are separated by areas of flat subduction zones, where no volcanism occurs.

During the subduction of the oceanic crust, temperature and pressure increase. The chemical signature of the magma and seismic tomography argue against melting of the slab, and rather support that the hydrated, altered rocks of the slab are metamorphosed under amphibolite to eclogite facies conditions. The crystal water is driven out by this process and rises into the overlying mantle wedge, consisting of peridotite, lowering the solidus and leading to partial melting of the mantle wedge (Grove et al. 2012; Gill 2010). The melts then rise upwards. Depending on the thickness of the overlying crust, different melts differentiate. It is suggested that this is caused by a density filter, causing less evolved magmas to stagnate and fractionate, while less dense evolved magmas rise further upwards (Devine 1995; Gill 2010). A change in composition is also supported by the assimilation of the surrounding continental crustal rocks. Especially in the Andes the thickness of the crust leads to high temperatures at its base, melt formation and assimilation. The calc-alkaline melts form mature arc lithologies, such as porphyritic, high-K rhyolites, dacites and andesites, which tend to be enriched in incompatible elements (Gill 2010). At microscopic scale, the fractionation and assimilation cause oscillatory zoning, as well as resorption and overgrowth textures. Depending on the volatile content and preeruption degassing, different eruption types occur, from lava effusion to explosive volcanism. The different eruption styles lead to the formation of stratovolcanoes such as Misti. Here, sequential layers formed by outflowing magma, whereas pyroclastic and mass flow deposits build up cone-shaped volcanoes (Zepp 2011).

2.2.3 Geology of El Misti

El Misti volcano is a composite volcano of the Central Andean Volcanic Zone (CVZ). Geographically, El Misti is situated in southern Peru near the city of Arequipa. Its peak at 5820 masl has a prominence of more than 3000 m over the Arequipa basin at around 2300 masl. The city center is at a 17 km linear distance from the crater. Two major river valleys border the volcano to the southeast and the northwest, Rio Andamayo and Rio Chili, respectively,

leading to the Arequipa basin. The city of Arequipa itself had 900,000 inhabitants in 2014 and is the second largest city in Peru after Lima (Sandri et al. 2014). As illustrated in Figure 5 the urban areas have spread rapidly in the last 50 years, already reaching the slopes of El Misti volcano. The volcano straddles the southern slope of the Cordillera Occidental (Western Cordillera) and the northern edge of the Arequipa depression (Thouret et al. 2001). El Misti is the most recently active Pleistocene volcano in the region, and is located next to the dormant Chachani volcano, 15 km to the northwest, and the extinct Pichu Pichu volcano, 20 km to the southeast (Thouret et al. 2001).

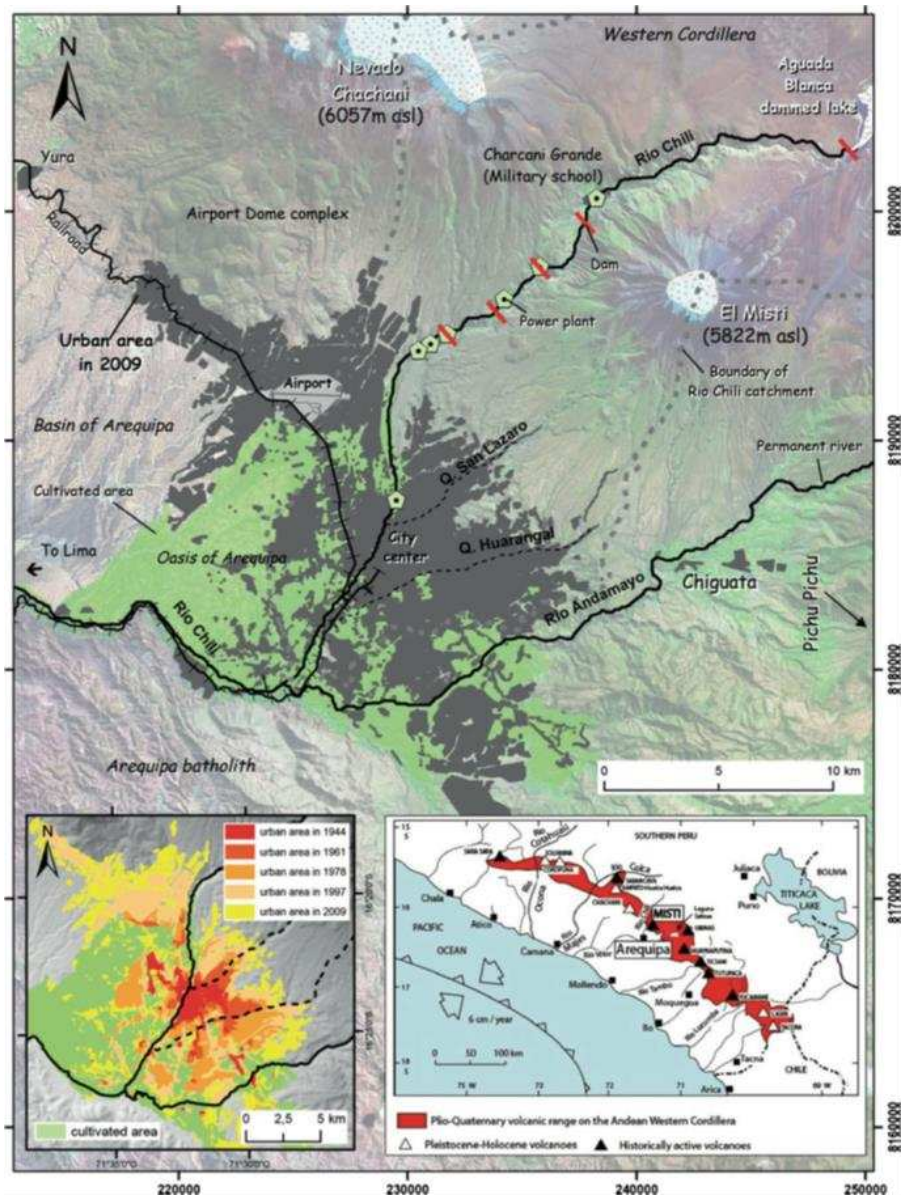

Figure 5: Development of land use of the city of Arequipa (Sandri et al. 2014)

The volcanism of Misti is explained by the offshore convergence and subduction of the 44 Ma old Nazca plate (Rivera et al. 2017). The CVZ reaches from northern Chile into southern Peru, containing seven potentially active volcanoes (Thouret et al. 2001). Like most volcanoes in this

zone, Misti is mostly composed of andesitic to dacitic lava flows with interposed pyroclastic sequences. Misti itself can be subdivided into at least four phases, named Misti 1-4 (Rivera et al. 2017) (Figure 6). In Thouret et al. (2001) some lithologies at the base of Misti 1 are described as Pre-Misti up to 13.8 Ma in age. In Rivera et al. (2016) some of those ignimbrites are assigned to Chachani volcano, while others are not assigned to a specific eruption center.

Misti 1 is assigned by Rivera et al. (2016) and Thouret et al. (2001) as part of Misti volcano. The rocks were dated as older than 112 ka and represent the first known Misti stratocone of approximately 500 m in height. The formation of Misti 1 was dated between 833 ± 6 ka and 112 ± 6 ka (Rivera et al. 2016), consisting of andesitic to dacitic blocky lava flows (20-60 m thick) and andesitic scoria flow deposits (4-12 m). Thouret et al. (2001) describe those rocks as andesitic lava flows within pyroclastic sediments and unwelded ignimbrites. As visualized in figure 7 A and B the rocks of Misti 1 are still exposed along the Rio Chili canyon with up to 400 m in thickness. The sequences are covered by the avalanche deposits of the Misti 1 collapse at around 122 ka (Rivera et al. 2016).

Misti 2 formed on top of the Misti 1 lithologies and represents another composite stratocone that reaches from the base at 3000-3800 up to 4400 masl. The younger Misti 2 was dated between 112 to 40 ka. Misti 2 is composed of three lithologic sequences (M 2-1/M 2-2/M 2-3). Especially along the two river valleys, block ash and pumice flow deposits occur. In addition, andesitic breccias (10-20 m) from the south flank collapse can be found (70-50 ka). On the southeast base 12-25 m thick andesitic to dacitic pumice flows are also present (50-40 ka). According to Thouret et al. (2001) these lithologies indicate collapse of volumetric domes, caldera formation or cluster of large craters.

In Misti 3 four different lithological groups reaching from 4400-5600 masl can be found. The eruptions that built up Misti 3 occurred from 50 and 14 ka (Thouret et al. 2001), leading to an overlap with Misti 2 in the first and Misti 4 in the second sequence. The yellowish volcanic lithologies are mostly present along the southern flank of Misti volcano. The first and oldest sequence of Misti 3 is composed of dacitic ash flow deposits and rhyolitic tephra fall deposits (Rivera et al. 2016; Thouret et al. 2001). The base of those deposits was dated to 34-33 ka B.P. Large ignimbrite deposits indicate an enlargement of the assumed Misti 2 caldera. The following Misti 3-2 group contains dacitic block and ash flows and pyroclastics, as well as pyroxene and amphibole bearing andesite successions (Thouret et al. 2001), marking a growth of Misti 3 from 30-25 ka B.P. The andesitic succession of Misti 3-3 is composed of five block and ash flow deposits, including pumice fall deposits, dating between 25-20 ka B.P. (Thouret et al. 2001). The tephra deposits were most likely reworked by meltwater from the second large glacial maximum (24-12 ka B.P.). The truncated Misti 3-4 sequence represents the caldera formation of Misti 3-4 at 14-11 ka B.P. The formation is defined by welded scoria flow

deposit cliffs, pyroclastic flow deposits and an elliptical structural boundary at 5400 masl (Thouret et al. 2001).

According to Rivera et al. (2016) and Thouret et al. (2001), Misti 4 consists of different lapilli and ash flow and fall deposits named Misti 4-1 (<11 ka B.P.) and recent deposits of tephra in the last 2 ka. Most noticeable are the VEI-5 eruption that created the 900 m diameter crater and the VEI-2 eruption that formed the still present lava plug (Rivera et al. 2016). Recent historical volcanic activity is limited to phreatic and fumarolic events.

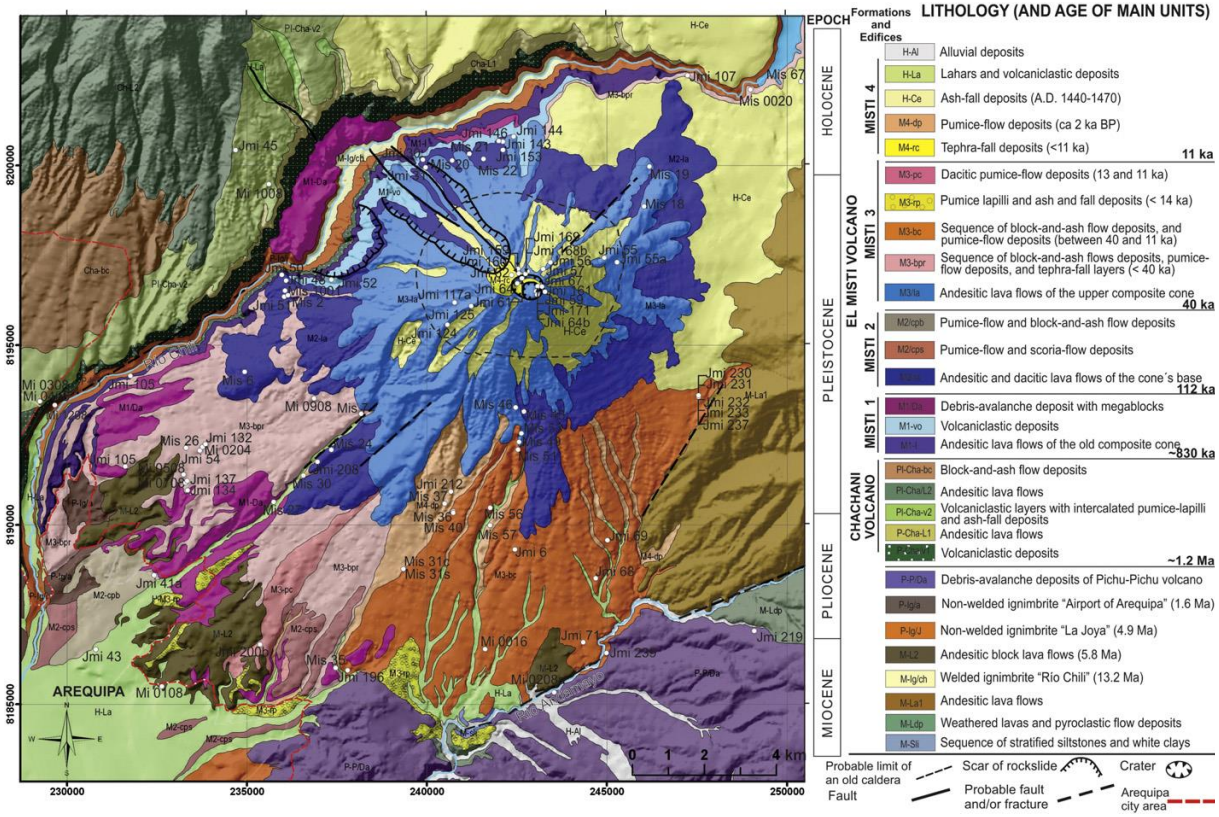

Figure 6: Geological map of Misti (Rivera et al. 2016)

Rio Chilli and Rio Andamayo- sampling area

The area of sampling is located in both river valleys of Rio Chili and Rio Andamaya, bordering the Misti in the northwest and southeast (figure 7 C). The majority of the sample points are located in the Rio Chili canyon. The present rocks consist of deposits reaching from Premisti (>833 ka), Chachani (1.2 Ma -830 ka) to Misti 2 (>40 ka) base. Even if Thouret et al. (2001) are differing in detail from Rivera et al. (2016) in the description of the lithologies and occasionally in age, it can be said that different sequences of andesitic lava flows, ignimbrites of different welding degree as well as pumice, scoria and ash flows and debris-avalanche deposits can be found (figure 7A). Thouret et al. (2001) also mention a rhyolitic protrusion in Misti 1. In the canyon entrance, lahar and volcanoclastic deposits of Misti 4 occur. In contrast the Rio Andamayo valley lithologies mainly consist of non-welded ignimbrites of Misti 2 (40-50 ka),

lacustrine sediments of Misti 3 and andesitic lava flows of Misti 3 (Thouret et al. 2001). in contrast Rivera et al. (2016) describe Misti 3 sequences of block and ash flow deposits and pumice flow deposits (10-40 ka) on the southern flank of Misti, lahars and volcanoclastic deposits like in Rio Chili, the debris-avalanche deposits of Pichu-Pichu (>1.2 Ma) and Premisti andesitic block lava flows (5.8 Ma) (figure 7).

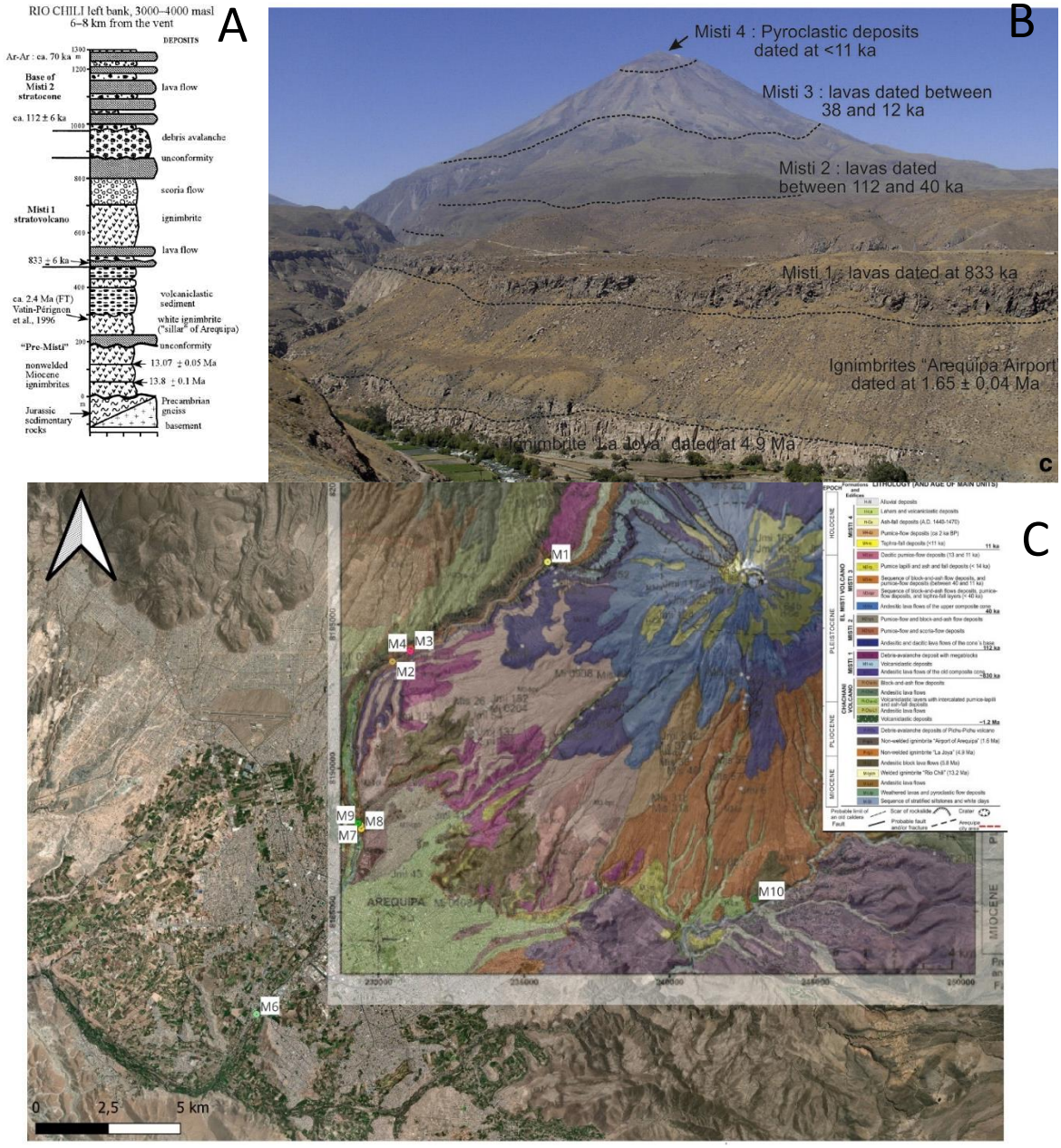

Figure 7: Lithologies of the Rio Chili left bank according to Thouret et al. (2001) [A] and a picture of Misti with the different stages of Misti 1-4 from SW perspective (Rivera et al. 2016) *[B] and a map of the sample area with the geological map after Rivera et al. (2016)* and Bing Areal map in the background.

3 Methods

3.1 Methods geology and mineralogy

3.1.1 Polarized light microscopy

In addition to the characteristics described below in the transmitted and reflected light microscopy, the habitus of the minerals as well as the presence of cleavage, twinning and zoning is documented and facilitates the mineral identification.

Transmitted light microscopy

Transmitted light microscopy is a method for the discrimination of mineral phases at a microscopic scale. Polarized light from a tungsten filament lamp, sometimes in combination with a blue filter, is used (Gribble and Hall 1985, 1992). A polarizer is used to polarize the light, transferring it from vibrating in different directions into a single plane vibration; this is also called plane polarized light, short PPL. This light is transmitted through a, in this case 30 µm thick, thin section of the sample material, reaching it in E-W vibration. The thickness must be known and should remain constant for the whole section. The light is further led through an objective to an eyepiece (Gribble and Hall 1985, 1992) (figure 8A)

The optical properties of minerals can change the wavelength composition of the light reaching the eye. With parallel polarizers the natural colors of minerals are visible. Minerals like quartz or most feldspars appear colorless, while others like biotite are mostly of brown color, due to selective absorption of wavelengths. If there is a complete absorption, the mineral appears black and is referred to as an opaque phase. These, mostly metallic ore minerals, have to be determined with reflected light microscopy. Some minerals also show a change of color, depending on their orientation in comparison to the vibration direction of the light. This is called pleochroism, which is caused by an unequal absorption of light in different orientations (Gribble and Hall 1985, 1992).

These features can be used with the habitus, cleavage, color and relief, which depends on the refraction difference, to identify the mineral.

For further determination different additional lenses can be added. The analyzer, which is basically another polarizer, can be inserted between the objective and eyepiece. This filter is only transmitting N-S vibration light, holding back light uninfluenced in vibration direction by the sample. Therefore, this analysis is called crossed polarizer (cP or xP) (Gribble and Hall 1985, 1992).

With crossed polarizers isotropic minerals appear dark, whereas in anisotropic minerals differing colors occur. These colors, are called interference colors and appear four times in a

360° rotation of the mineral, intermitted by four times black. This can be used to determine the mineral-specific bireflectance by plotting it on the Michelle Levi color plate. According to this plate the interference colors are subdivided into colors of different orders, bordered by red (I, II, III etc.). In rare cases the interference colors can be abnormal (Pichler and Schmitt-Riegraf 1997).

An additional way of differentiation for anisotropic minerals is the interference figure, which can be uni- or biaxial positive or negative. For that, an isotropic “cutting position” is needed, which can be challenging, especially in minerals that are fine, fractured or orientated. If found, a magnification of at least 40x is necessary. The Bertrand lens is inserted and the aperture diaphragm is opened. Then, in the ideal normal position a black cross is visible, dividing the visible cycle into 4 sections. With rotation of the stage at a uniaxial mineral the cross stays unchanged, while with a biaxial mineral the cross splits in two half cycles. In a normal position a first order red accessory plate is added. Depending on which quadrants (I and III or II and IV) an addition or a subtraction appears, a positive or negative character can be determined.

Reflected light microscopy

In reflected light microscopy polarized light is used as well (figure 8B). In contrast to transmitted light microscopy, the source of light is located above the sample and only reflected light is detected. It is used for the determination of opaque phases.

As a light source, tungsten halogen quartz lamps are used, similar to the transmitted light microscopy (Gribble and Hall 1985, 1992). To prevent a change of color by the yellow tint of the light, a blue correction filter is used. The light reaching the sample is filtered in E-W vibration plane by a polarizer.

In reflected light microscopy fewer additional lenses can be applied so that fewer characteristics can be determined. Furthermore, an analyzer, as in transmitted light microscopy, is used for the reflected light microscopy, too.

The relative hardness can be determined either by direct comparison of the penetration depth of scratches on the section from polishing, or by the Kalb light line, which is caused by the differing material removing during polishing, due to the ore hardness (Gribble and Hall 1985, 1992). Also, an important characteristic is pleochroism, as in transmitted light microscopy, describing the change of color with parallel polarizers. In combination with the color, certain minerals can be determined.

The reflectance is given in percent and describes the brightness with which the minerals reflect the light. High percentages can be found in galena or gold, while iron oxides and -

hydroxides tend to have lower reflectance values. When the reflectance is changing with rotation of the stage, this is called bireflectance, caused by anisotropies.

The anisotropy can be detected if the analyzer is inserted. Similar to transmitted light microscopy, minerals show different colors depending on its position. For some minerals internal reflexes appear. These strong colored spots in the mineral occur in semi opaque phases, by the penetration of light into the mineral and reflection inside the mineral (Gribble and Hall 1985, 1992).

For the images in transmitted and reflected light Keyence digital microscope was used.

Mineral composition point counting with JMicro-vision

For point counting the program JMicro-vision was used. A panorama image of the thin section in transmitted light, parallel polarizers and crossed polarizers were used, and different classes of phenocryst, matrix and pores were established. Then a fitting area was chosen and at least 600 points were determined. If no changes in the evolution plot were visible, the measurement was terminated. The program calculated the proportions of the different classes and displays the results. Considering the difficulties of mineral identification from an image, mostly the matrix proportions were quantified. At repeated point counting locations, differences of ±3% have been observed.

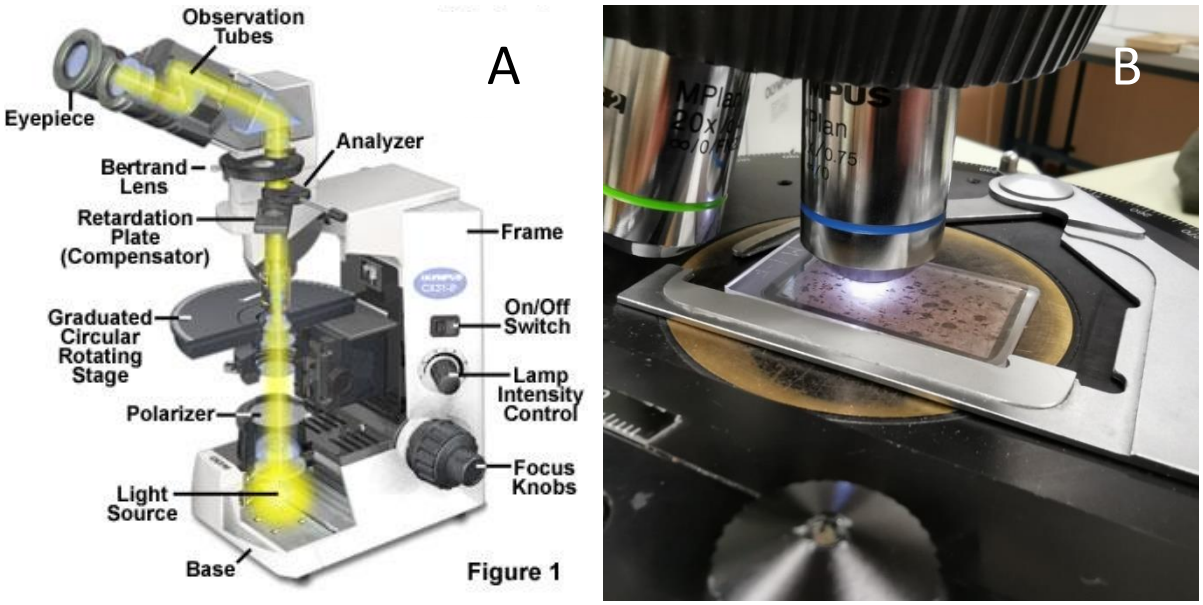

Figure 8: Systematic picture of a polarization microscope for transmitted light according to Dimitruk and Davidson (A) and a picture of a thin section under the microscope by R.Winstel (B)

3.1.2 Scanning electron microscope and Broad ion beam scanning microscope ((BIB)-SEM)

Scanning electron microscopy (SEM) is used in mineral and material science as a valuable instrument for the determination of microstructures and composition of materials (Ali et al. 2023;Temiz 2022). To achieve these goals a high voltage electron beam (<30 kV) is focused in a scanning motion on the sample. During this procedure the interaction of the beam with the sample leads to different detected signals which can be used. For a better quality of the images and to prevent charging effects (Ali et al. 2023) a conducting coating, in this case graphite, is applied.

The electron beam can be generated by the electron gun, which can use different electron sources. In this case a tungsten emitter, heated with 15 kV, was used, which produces electrons in vacuum, continuously and uniformly (Temiz 2022). The electron beam is demagnified by up to three condenser lenses (Ali et al. 2023) into a fine probe, which scans across the sample surface. Here, a tear drop shaped interaction (figure 9) with the sample occurs, which depends on the sample composition and electron beam energy (Ali et al. 2023).

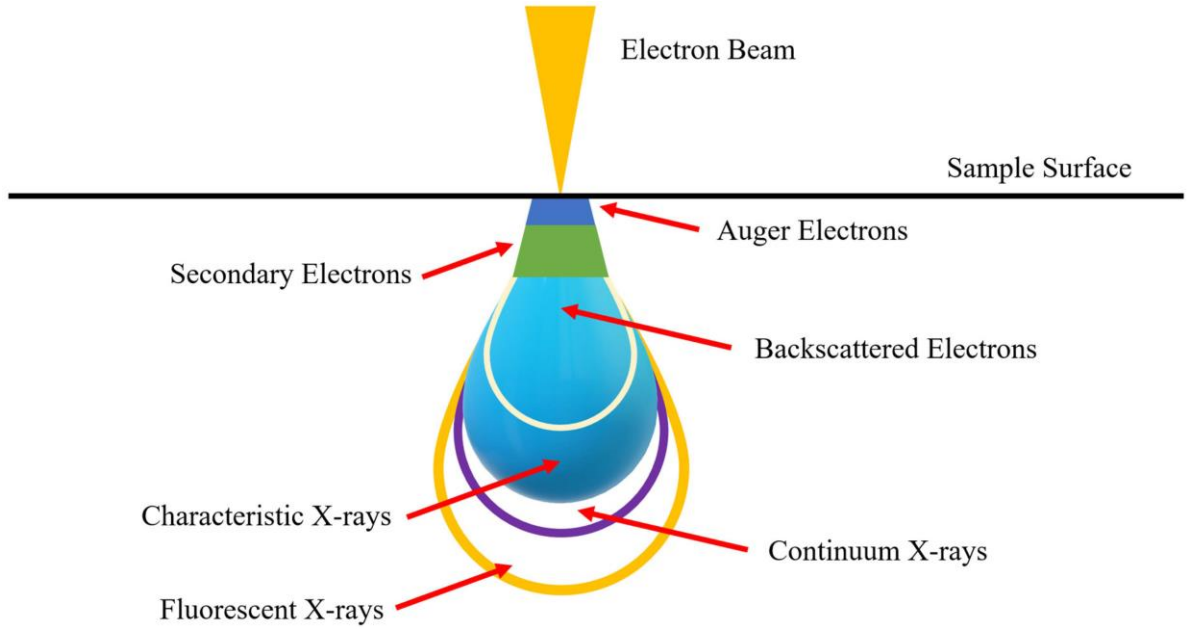

Figure 9:Tear drop shaped area of interaction (Ali et al. 2023)

For this work backscattered electrons and energy-dispersive X-ray signals have been detected. Therefore, these will be described in detail. By elastic interaction of high energy electrons (50 eV – 30 keV), some get reflected and detected as backscattered electrons (BSE) (Ali et al. 2023). In contrast to secondary electrons, which are generated by inelastic collision of the samples' upper 10 nm, due to their low energy level (90% <10 eV), used for a detailed topographical imaging of the sample (Temiz 2022; Ali et al. 2023), the backscatter electrons

are used for a high-resolution imaging of the element composition of the specimen. The difference in atomic number of the present elements leads to a contrast image; elements with higher atomic numbers leading to brighter areas (Ali et al. 2023), for example causing a Ba containing feldspar to appear brighter than an Na containing feldspar. This distinction of compositional variations is used for the determination of mineral phases present in the sample area (Ali et al. 2023).

The BSE analysis in this work was coupled with an energy dispersive X-ray spectroscopy (short EDS or EDX). The penetration of the sample by the electron beam, generates characteristic X-rays by the energy level change of an electron taking a place from a higher valence shell to a lower valence shell (Ali et al. 2023). The emitted characteristic X-ray intensity (amplitude) and spectrum is used for quali- and quantification. Also, compositional mappings are possible (Ali et al. 2023).

For this thesis the scanning electron microscope Evo MA 10 (ZEISS) and EDX Detector (BRUKER XFlash), with the fitting Quantax software were used. Calculation of mineral formulas out of the energy dispersive X-ray spectroscopy results:

Even if there is software for direct calculation of mineral phases out of the EDS results, this was not applied here. The oxide weight % of the different elements were exported into a csv data file and further normalized to the oxygen in the general mineral formula according to (Deer et al. 2013). Hence, the relative composition as well as the results of the polarized light microscopy were used for the differentiation of compositionally similar mineral phases like amphiboles and pyroxenes. For minerals like magnetite a correction of Fe^{2+} and Fe^{3+} was needed, caused by the fact that the detector cannot differentiate between the different iron oxidation states. The correction was done according to Droop (1987). The compositional results are plotted in Origin 24b software.

Broad ion beam scanning electron microscope-(BIB-SEM)

The BIB Sem is a powerful tool for the determination of pore structures, characteristics and microfracture investigation.

Therefore, for each sample an area has been selected to extract a specimen (ca. 0.8 ×0.8 ×0.5 cm) to fit in the BIB-SEM holder (Shi et al. 2023). The specimen is pre-polished with silicon carbide sandpaper. For the main polishing a Hitachi ArBlade 5000 broad argon ion beam is used, creating a 2 mm^2 planar surface. Gold serves as coating of the sample surface. For high resolution pictures TESCAN Clara field emission SEM with Everhart-Thornley (E-T) detector and a backscattered electron detector for detecting secondary electrons (SE) and backscattered electrons (BSE) is used. With the TESCAN Essence Image Snapper software it is possible to scan the area of interest with BSE and SE for a better analysis of properties(Shi et

al. 2023). For the pictures an acceleration voltage of 10 kV and a sample current of 1 nA were used, therefore magnifications up to 20 000x are possible. For this thesis 1 large mapping (4000x), as well as 3 smaller mappings (20 000x) per sample have been done.

3.1.3 X-ray fluorescence (XRF)

In general, X-ray fluorescence spectroscopy (XRF) is a widely used and established, powerful tool for the major element determination of geological samples (Oyedotun 2018). Especially for the determination of parent rock or climatic environment interactions, XRF is used for a high-resolution elemental composition assessment (Oyedotun 2018).

The XRF can be subdivided into two main branches (Marguí et al. 2022): wavelength dispersive X-ray fluorescence (WDXRF), which was used in this thesis, and energy dispersive X-ray fluorescence (EDXF).

The wavelength-dispersive principle is based on the emitted relative abundance of X-ray photon of energy or wavelength feature of individual atoms (Oyedotun 2018). The main difference between EDXF and WDXRF is the way they discriminate the radiation signal from the sample (Marguí et al. 2022). Similar to EDX spectroscopy of the SEM, an electron of an inner orbital is knocked out, resulting in an excitation of the atom and the emission of characteristic wavelength high energy radiation, which is detected, integrated, transformed into intensities and further into concentrations. By this measurement and comparison to a fitting known standard qualitative and quantitative results can be provided, reaching concentrations down to ppm range.

Depending on the sample, different preparations are possible. In this case the samples were ground into a fine powder, taking into account that the sample must have been representative for the whole rock and can get contaminated by the mill material. In this case an agate vibration mill was used (figure 10 A), with volatiles driven out by a heating step for 12h. The powder is weighed to 1 g, precision of 0.0005 g, and mixed with 8 g of the flux. Lithium tetraborate was used, in the ratio of 1:8. Precise work is crucial in this step, to assure reliable results. Then, the sample was inserted into a platinum crucible, heated up to 1200° and poured into a platinum mold (figure 10 B). The cooled down fused bead can be used for measurement, under the condition that the melting and mixing of the sample was complete and no fractures or scratches are visible. For the measurements, a PANALYTICAL Axios max advanced was used. The results and correlations are plotted in Origin 24b and Microsoft excel software.

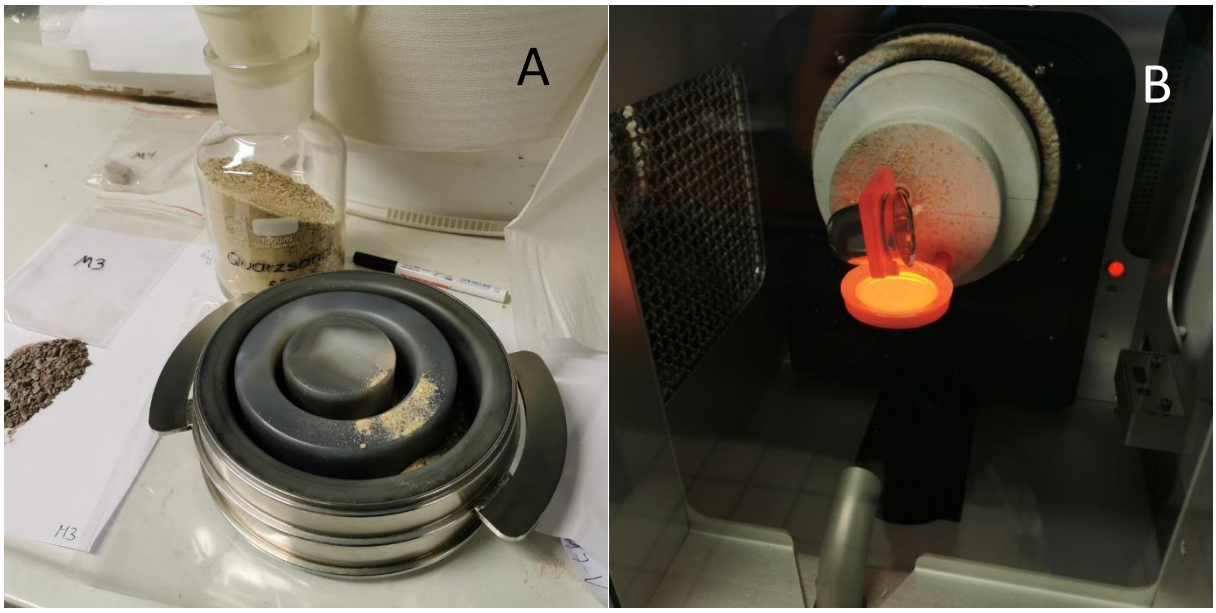

Figure 10: Agate vibration mill used for milling down the samples (A) and pouring of a bread (B), both pictures by R. Winstel

3.2 Geotechnical methods

All samples have been drilled with a diamond drill to achieve a drill core with the diameter of 50 ±5 mm. These cores have been cut into 100 ± 5mm cylinders with a diameter to length ratio of 1:2 according to the standards ÖNORM B 3124-9, ÖNORM EN 1926 and ASTM D4543-19. For testing, both ends were grinded until parallel. Cut off pieces of the cylinders were used for Brazil testing and density measurements. The cylinder sides need to have a maximal deviation 0.3 mm and therefore been grinded down by hand. The results and correlations are plotted in Origin 24b software.

3.2.1 Density and porosity measurements

Mechanical properties and the porosity are often highly correlated. Therefore, the determination of the porosity is important. For the determination of porosity, the standards of ISRM (1979): "Suggested methods for determining water content, porosity, density absorption and related properties" are applied.

In this work the porosity is determined through the saturation method. The sample has to meet the following requirements: water resistant and non-friable. Swelling of the sample through interaction with water needs to be excluded. If the requirements are met the following steps must be carried out:

First the free water in the sample has to be driven out for the dry mass M_s determination. Therefore, the cylindrical samples are dried at 105 °C for at least 24 h to achieve a constant mass. The sample is weighed three times, and the average value is taken for further calculation. The volume V_c (Caliper method) of the sample is calculated by the cylindrical shape, by using the average of three diameter and length measurements. Thereby, the calculation of the dry density ρ_d is possible (ISRM 1979).

Afterwards in a desiccator, the sample will be saturated with distilled water in vacuum with a maximum pressure of 800 Pa for at least 1 h. A good indicator for the saturation development are rising air bubbles from the sample. Using the Archimedes principle the saturated sample is transferred into an immersion bath and weighed with and accuracy of 0.1g to determine the submerged mass M_{sub} of the sample. The saturated mass M_{sat} is determined by taking the sample and removing the surface water with a moist cloth and weighing of the sample three times, using the average sample for calculation of following parameters (ISRM 1979). For this calculation it is also necessary to point out, that only the connected porosity can be measured. Consequently, self-contained pores are not measured. Especially for volcanic rock samples this must be noted.

Dry density $\rho_d \left[\frac{g}{cm^3}\right] = \frac{M_s}{V_{(c)}}$

Bulk volume $V[cm^3] = \frac{M_{sat} - M_{sub}}{\rho_w}$

Pore volume $V_p[cm^3] = \frac{M_{sat} - M_{sub}}{\rho_w}$

Porosity $n[\%] = \frac{100 \times V_p}{V}$

3.2.2 Tensile strength testing -Brazil test

Another important parameter for the determination of the overall rock strength is the tensile strength. Because the direct tensile strength determination is complicated and expensive to execute, the indirect tensile strength (Brazilian Test) is widely used (Basu et al. 2013). The testing for this thesis has been done according to the ISRM (1978) “Suggested methods for determining tensile strength of rock materials”.

The sample is positioned in a flat jaw holder into a compression testing machine (figure 11). For the indirect tensile strength measurement, a compression-induced extensional fracturing is induced. By applying a compressive diametral force along a cylindrical sample with the diameter-thickness ratio of 2:1, a formation of extension fractures is induced until failure of

the sample. The loading direction in relation to rock anisotropies has to be recorded. The loading rate has to be chosen in a way, that a continuous load is applied, leading to a failure within 1-10 minutes. The maximum load is measured and with the dimensions of the cylinder a calculation of the tensile strength is possible:

Tensile strength $$\sigma_T[MPa] = \frac{P}{\pi R t}$$

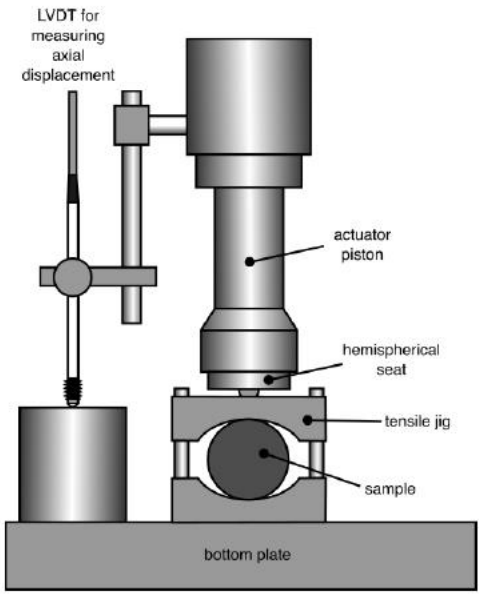

Figure 11: Setup of the Brazil test according to Heap et al. (2021)

3.2.3 Uniaxial compressive strength test (UCS)

The uniaxial compressive strength is an important parameter for the determination of the overall mechanic strength of a rock sample. For this thesis the samples have been tested following the ÖNORM B 3124-9 (1986) in an oven dry condition.

For the uniaxial strength tests, the same cylindrical samples as for the porosity and density tests are used and prepared similarly by drying at 105°C until constant mass is reached. The compression testing machine is built of two rigid plates, of which the upper plate is seated on a spherical joint to ensure plane parallelism, which can be impaired by uneven sample surface. In addition to the pressure, the axial and diametral deformation are measured. Different types of sensors are used, in this case a chain has been used for the diametral measurement and two extensometers for the axial measurement. It must be ensured that the measuring sensors are directly applied to the sample and are not able to move.

The testing can be divided in two measuring phases. After applying the first 100 - 500 N of primary pressure to assure contact between the machine and the sample, the elastic

parameters of the samples are measured by applying a loop of compression and decompression. As range for the maximum and minimum pressure during the loops, the ÖNORM B 3124-9 (1986) recommends 50% of the expected uniaxial compressive strength (UCS) in a range of ±10%. If necessary, a range between 20-80% of the UCS is possible. The loading rate has to be constant with 0.5-1 ‰ per minute or 0.5-1N/mm^2 per second (here 3*10^{-6} -10*10^{-5} (mm/mm)/s). This procedure of compression and decompression is repeated once. Afterward the load is increased with a radial deformation rate of 3*10^{-6} (mm/mm)/s until the sample fails. After the sample fails, a continuing compression is conducted to capture the residual strength.

After measuring the maximal compressive force at the point of failure F_{max}, the uniaxial compressive strength can be derived by dividing F_{max} by the sample surface area A.

Uniaxial compressive strength $$\sigma_{UCS}[MPa] = \frac{F_{max}}{A}$$

Out of the measured change of length and diameter during the loop measurement, the calculation of the Young's modulus as well as the calculation of the Poisson's ratio is possible.

Axial strain $$\varepsilon_a[-] = \frac{\Delta l}{l_0}$$

Diametral strain $$\varepsilon_d[-] = \frac{\Delta d}{d_0}$$

Young's modulus $$E[GPa] = \frac{\Delta\sigma}{\varepsilon_{a(unloading)}}$$

Poisson's ratio $$\nu[-] = \frac{\varepsilon_d}{\varepsilon_a}$$

3.2.4 Triaxial compressive strength test (TCS)

For the triaxial strength testing two different methods are applied. For some samples a Hoek cell was used and for others an MTS 815 with triaxial cell was used. A cylindrical sample with same requirements as for the UCS is used. For triaxial testing an axial force is applied by the compression testing machine, similarly to the UCS testing. However, in contrast to UCS testing a confining pressure, σ_3, which is maximal 50 % of the UCS, is applied. The axial force is increased at a constant confining pressure until the sample fails, and as for UCS testing, measurement after failure until residual behavior is possible.

In both the Hoek cell (figure 12 B) and MTS cell (figure 12 A) an oil pressure is used for the confining pressure. The internal diameter of Hoek testing cell (HTC) is 50 mm with platens with spherical seats for a centered sample position. In the Hoek cell the confining pressure can be adjusted manually by pumping oil into the steel cylinder with an oil chamber. A permanently

installed impermeable rubber sealing sleeve prevents the direct contact of the sample and the oil. This is important, because the oil can chemically attack the sample and therefore weaken it. Additionally, a penetration of oil would lead to an increase of the pore pressure and therefore would change the effective pressure conditions of the test. In the Hoek cell an axial loading rate of 0.00022 (kN/mm²)/s is applied until failure (Hoek 2007).

Figure 12: Setup of the TCS testing with a triaxial testing setup of MTS (R. Winstel) (A) and Hoek Cell, photo taken by Marlene Villeneuve (B)

For the triaxial test with the MTS 815 and attached pressure vessel, the oil pressure is controlled automatically. Because the sample is positioned inside the pressure vessel, it must be protected by a plastic sleeve. In contrast to the Hoek cell, this sleeve has to be attached to each sample manually. The sample is placed under pressure between two steel caps with an upper and a lower O-ring (figure 13). Depending on the sample size a fitting sleeve is pulled over. In the next step, the sleeve is contracted by heating. Hence the sample is sealed airtight without any air is captured inside. The O-ring is then incorporated with 1 cm distance to the end of the sleeve. If the sample is uneven or porous, gypsum is used to even it out and prevent the sleeve from getting damaged.

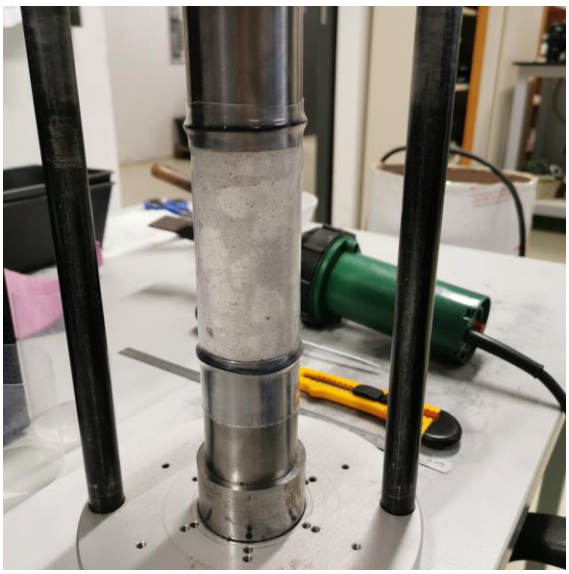

Figure 13: Rubber sleeve application on a sample, with white gypsum to fill the pores.

A benefit of this cell is, if the sample is in position in the vessel, extensometers are applied, allowing the measurement of the change in length and diameter during the measurement (figure A &B). The samples were tested with a deformation rate of $5*10^{-6}$ (mm/mm)/s before failure and after failure with $1.5*10^{-5}$ (mm/mm)/s. (Hoek 1968;MTS Systems Corporation 2023; Hoek 2007).

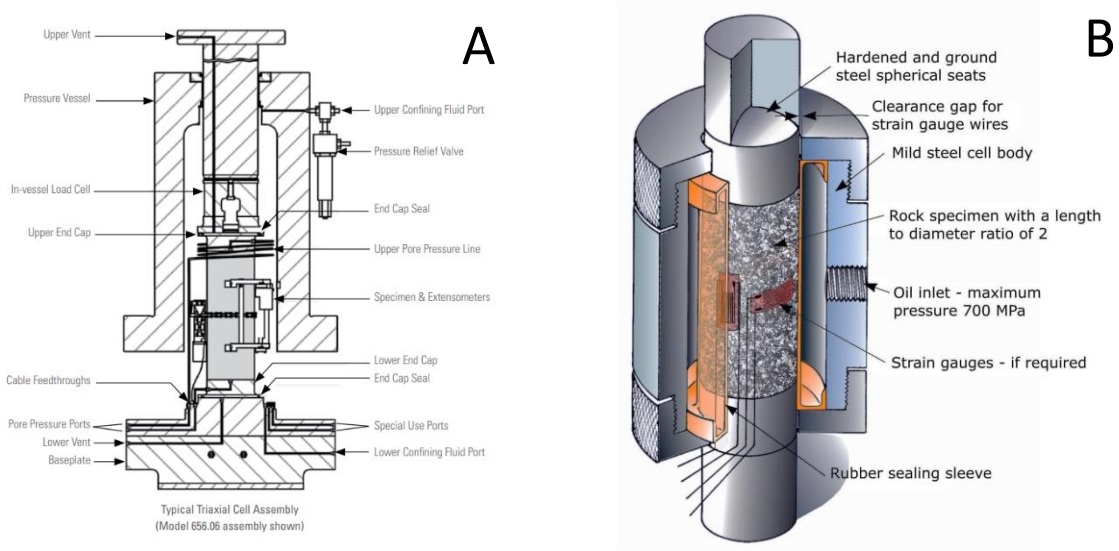

Figure 14: Function of the setup for the triaxial testing machine after MTS Systems Corporation (2023) *and the Hoek cell after* Hoek (2007)

For each lithology at least two samples were tested for the triaxial strength according to (ISRM 1983). The same lithology is tested in different confining pressures at least one time each to be able to use it for Mohr-Coulomb and the Hoek-Brown Failure Criterion (Hoek 2007).

The Mohr-envelope is derived by taking the maximal pressure (σ_1) at the failure point and the corresponding confining pressure (σ_3) and draw a Mohr cycle with the radius of ((σ_1+σ_3)/2) (Prinz and Strauß 2011), are centered on the axis (Barsanescu et al. 2018) and intersect with the x-axis of normal stress at σ_1 and σ_3 (Ghimire et al. 2022). If necessary, the UCS (σ_3=0 MPa) and the tensile strength (σ_3=-DTS; σ_1=0 MPa) can be used as well. After inserting the cycles, a tangent is drawn along those cycles, forming the Mohr envelope. The intersection value with the y-axis (shear stress τ in MPa) at σ=0, is the cohesion c, the slope angle is the internal friction angle ϕ (Barsanescu et al. 2018; Ghimire et al. 2022).

3.2.5 P-wave velocity measurements

The compressive wave, p-wave, velocity measurement is another method for sample characterization. This parameter is highly powerful in terms of rock characteristics, especially when considered/interpreted together with porosity and overall rock structure. Therefore, the samples are measured three times; dry and saturated before triaxial compressive testing and dry after the testing. The triaxial sample is held together by the plastic sealing sleeve and can be measured even after testing.

For this testing only p-waves are measured. As a p-wave source a Geotron Elekronik ultrasonic generator USG 40 (figure 15) is used with a cleverscope oscilloscope CS320A to conduct ultrasonic measurements.

The signal is triggered continuously. As resonance frequency 250 kHz is used. The measurement starts with the measurement of a standard aluminum cube. If the values are realistic, the rock cylinders can be measured. The sample is positioned between two housed transducers, acting as signal transmitter and receiver. For a better signal transmission, the contact surface is coated with an ultrasonic gel. Then a pressure of 2.5 bar is applied to fix the sample. The travel time T_P is measured, and with the known sample length L_P the p-wave velocity V_P can be determined.

$$V_P \left[\frac{m}{s}\right] = \frac{L_P}{T_P}$$

For testing the ASTM D2845-00 Standard Test Method for Laboratory Determination of Pulse Velocities and Ultrasonic Elastic Constants of Rock was used.

Figure 15: Geotron Elekronik ultrasonic generator USG 40 used for the measurements (R. Winstel)

4 Results

4.1 Mineralogical and geological results

4.1.1 Polarized light microscopy

M1

M1 which was macroscopically described as welded ignimbrite, is characterized by a porphyritic texture with a hypocrystalline matrix and phenocrysts of plagioclase, quartz, biotite, alkali feldspar, less common magnetite and accessory amphibole. According to the point counting the matrix makes up to 85% of the section, with the most dominant phenocryst being plagioclase with about 8%.

The main mineral phase in the thin section is plagioclase. The up to 1800 µm long phenocrysts are often present with polysynthetic twinning and a zonation. One grain yielded a biaxial negative character, which fits to low albite. Most plagioclase crystals are hypidiomorphic, many are broken or rounded. In case of wide or missing lamellae the differentiation to alkali feldspar or quartz becomes difficult. A statistical differentiation is therefore problematic

based on optical microscopy. Alkali feldspar is present as large phenocrysts with rounded edges, often recognizable by curved cracks (figure 16 A) and rare Karlsbad twinning. The quartz is xenomorphic with rounded edges and embayment filled with matrix material.

Biotite is a minor mineral in the section and reaches sizes up to 800-1500 µm. The shape is hypidiomorphic to xenomorphic; a strong reaction rim to matrix is visible, and the edges are frayed along the longitudinal cleavage. The strong pleochroism results in a light to dark brown color, becoming darker towards the edges (figure 16 B).

Amphibole is an accessory, also showing rounded edges and in some intersections its typical 56° cleavage. Low interference colors up to green II and a dominant brown color characterize the amphibole. Often dark rims are present.

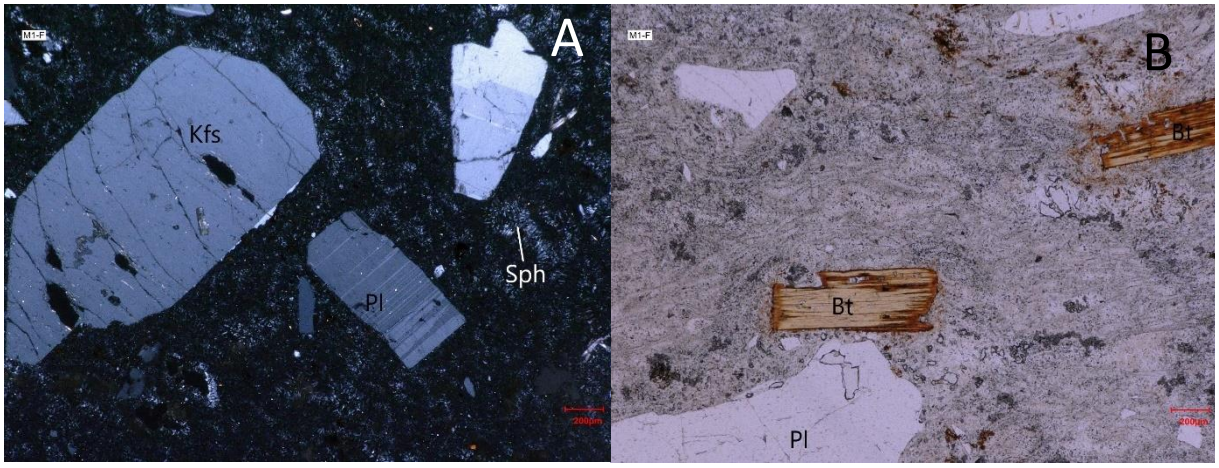

Figure 16: Alkali feldspar and plagioclase with polysynthetic twinning in M1 (crossed polarizers) [A]; Biotite and plagioclase phenocrysts in the fine matrix of M1 (parallel polarizers) [B]. Mineral abbreviations are defined in the appendix 10.1.

Magnetite with ilmenite lamellae is the only opaque phase recognizable in thin section. Magnetite is present as phenocryst and as small crystals in the matrix as well. Often the typical unmixing lamellae of ilmenite are visible, indicating the presence of titanomagnetite. The crystals are xeno- to hypidiomorphic and are mostly rounded, sometimes intergrown with other phases or present as inclusions in larger phenocrysts like plagioclase.

In thin section a separation of different matrix areas is possible. Besides the matrix, elongated brighter areas are visible, which could be interpreted as elongated juvenile volcanic fragments or alteration products, also called (pseudo-)fiamme. Especially with crossed polarizers, the separation into a coarser grained area and a darker fine-grained area with phenocrysts is prominent. The coarser grained area is characterized by larger fibrous minerals which appear spherical to fan shaped. In contrast, the grains in the finer grained areas are more axolithic shaped, also fewer crystals are apparent, with a dominant presence of isotropic phase. Different types of devitrification occur in the section. Additionally, areas of mosaic quartz are

present, with could point to alteration by an escaping vapor phase. Minerals close to those areas show stronger signs of alteration. These are typical for the high-temperature devitrification of natural glass. The darker appearance is rooted in a higher glass content (figure 17). For information about composition and exact mineral phases, SEM investigations were carried out. But due to the colors and the low bireflectance, a quartz or feldspar composition is likely.

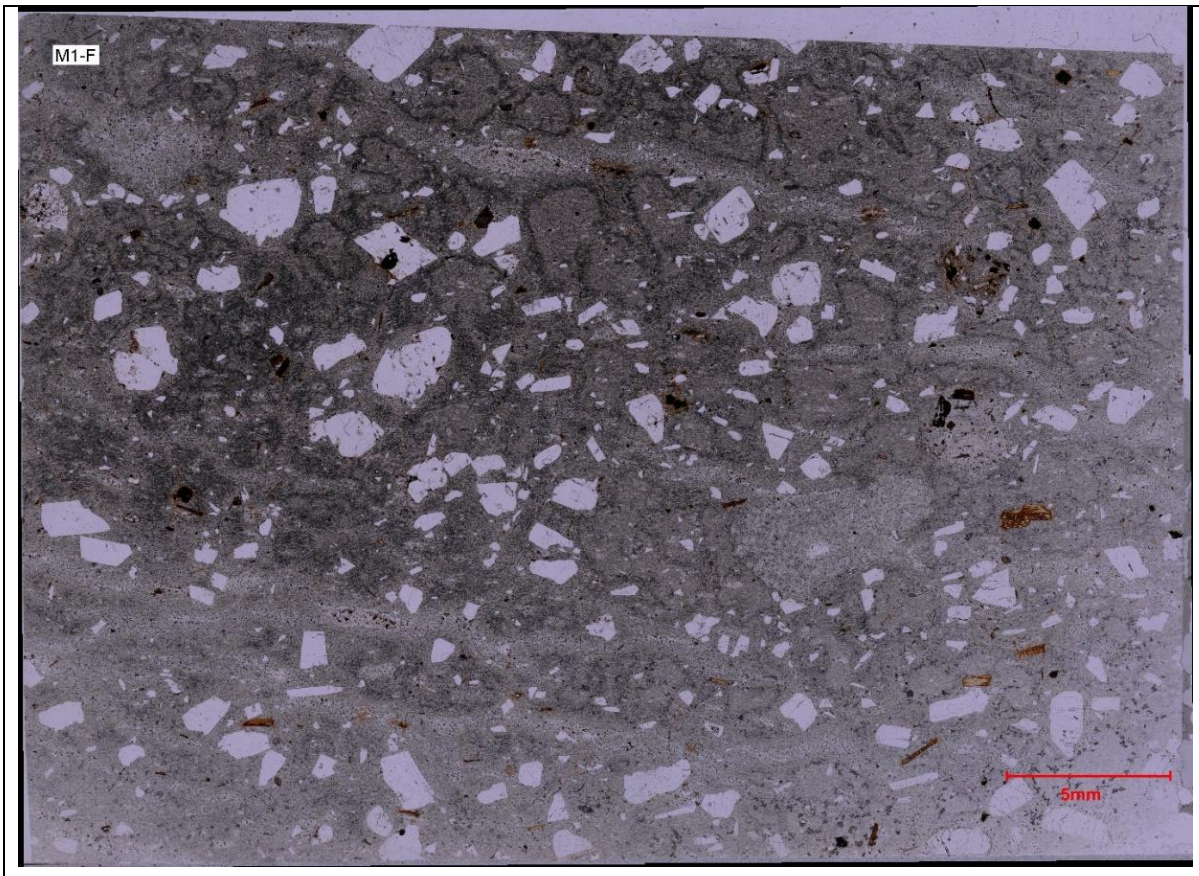

Figure 17: Panorama image of M1 with parallel polarizers, notably visible dark rims and broken phenocrysts

M2

M2 is characterized by a porphyritic texture, a typical hiatal crystal size distribution, containing large 2000 µm alkalifeldspar and plagioclase phenocrysts, with smaller biotite (500 µm) and accessory quartz (800 µm). According to the point counting the matrix makes up 86.2% of the section, with the most dominant phenocryst being plagioclase with about 9.8%.

Feldspar dominates the phenocrysts. The differentiation of the non-colored phenocryst is difficult, since especially K-feldspar and quartz do not show typical morphologies.

The plagioclase is idiomorphic to hypidiomorphic. Some crystals are in excellent condition. Others are more broken; fragments are sometime separated by just 100 µm. Disregarding uneven breaking edges, the crystal edges are straight, and most corners are sharp.

Polysynthetic and crossed hatched twinning can be found (figure 18 A & B). In larger phenocrysts larger brown melt inclusions beside biotite can be found. Oscillatory normal zonation can be found.

The hypidiomorphic alkali-feldspar tends to show rounded edges and curvy cracks. Less common Karlsbad twinning occurs, and crystals are often broken. The quartz is xenomorphic, with rounded edges and embayment, filled with matrix material.

Biotite and amphiboles occur rarely (figure 18 A). The biotite is xenomorphic and shows a dark reaction rim, partly coloring the surrounding matrix. The amphiboles are smaller and rounded, but cleavage and interference colors are diagnostic.

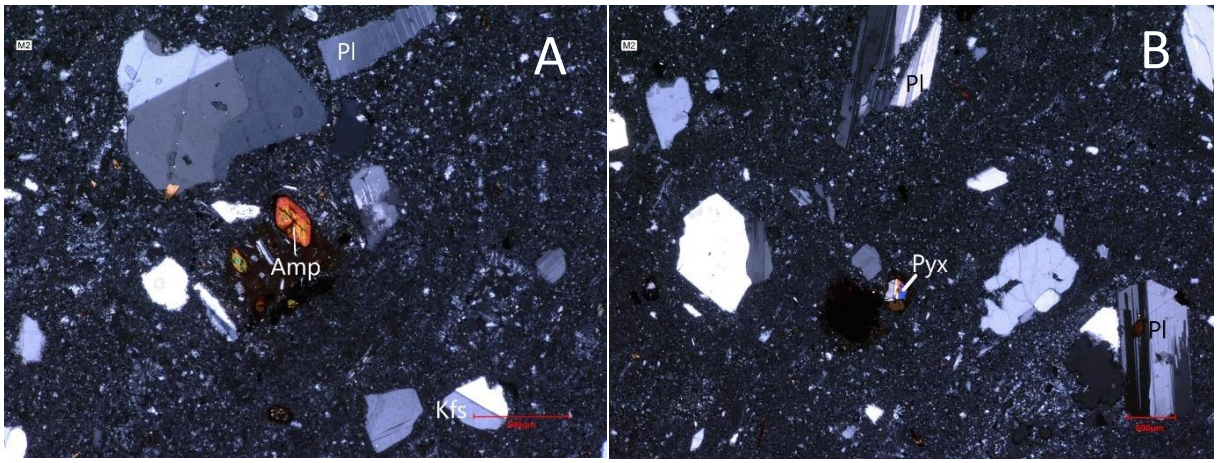

Figure 18: Alkali feldspar, amphibole and plagioclase with polysynthetic twinning in M2 (crossed polarizers) [A]; Pyroxene and plagioclase phenocrysts in the fine matrix with minor devitrification of M2(crossed polarizers) [B]

The homogeneous matrix is of light grey color, with a hint of green, mostly containing a fine, probably quartz- feldspar, mosaic to spherulitic devitrification. Thereby, the matrix can be described as hypo crystalline.

Besides the grey matrix, which makes up the largest part of the thin section, there are areas which differ in color. The brighter matrix appears mostly in elongated areas, which could be interpreted as elongated vesicles or tube-pumice, which shows first signs of welding. Also visible are areas that can be interpreted as vapor phase crystallization, changing the entire texture.

Besides those pumices, there are areas of dark brown to brown-red color; at a closer look larger crystals of amphibole are present in this area (figure 19). The composition of the matrix was not possible to determine, due to its fineness. The original color of the area has been covered by red-brown alteration products of the amphiboles. In the other areas the amphiboles are missing.

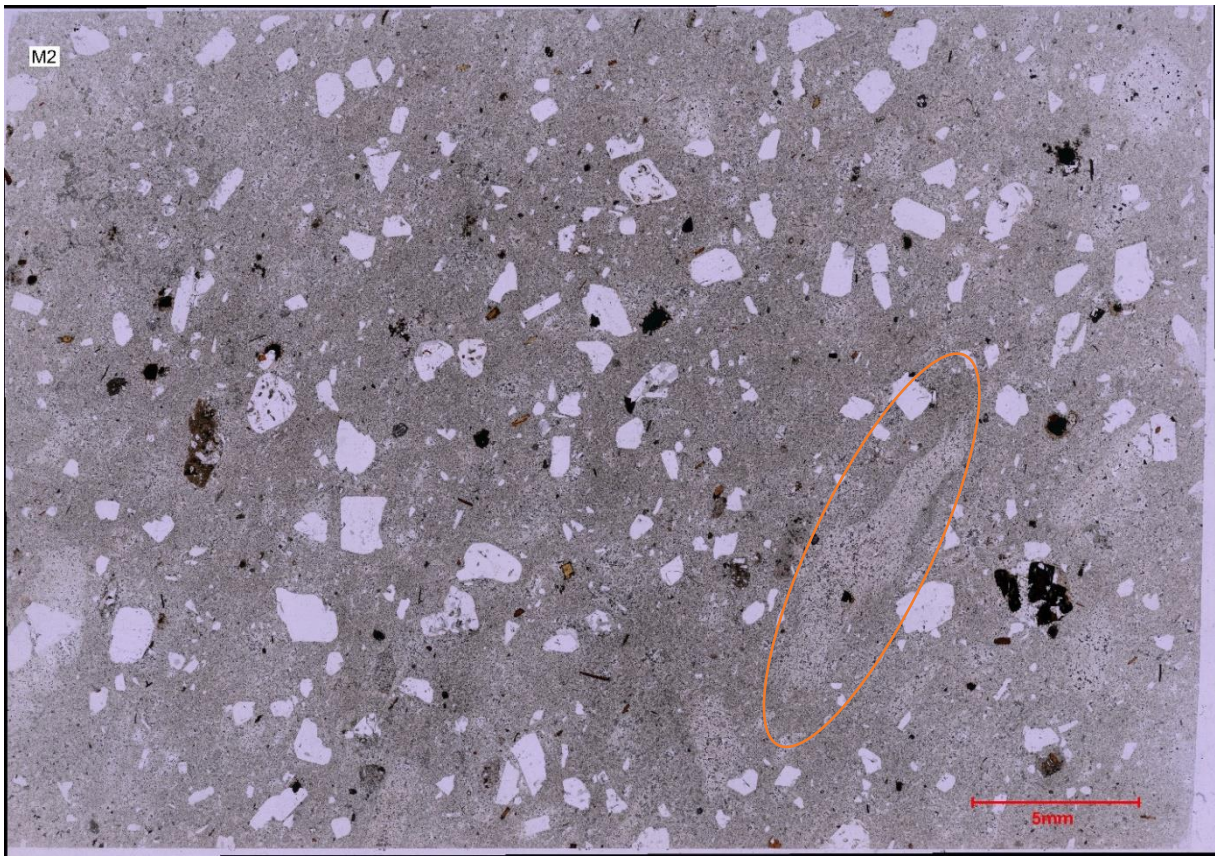

Figure 19: Panorama picture of M2 with parallel polarizers, with bright pumice and tube-pumice (orange circle)

M3

M3 was macroscopically described as rhyolite. Disregarding the porphyry texture, M3 differs from samples M1 and M2. According to the point counting the matrix makes up 85.2% of the section, with the most dominant phenocryst being plagioclase with about 8.3%.

Phenocrysts are, as in the M1 and M2 samples, dominantly feldspar and quartz, less common biotite. Plagioclase (3300 µm) shows polysynthetic and crossed hatched twinning, also continuous normal zonation can be found, rarer oscillatory normal zoning (figure 20). The plagioclase shows often straight crystal edges and sharp corners. Often in broken plagioclase the central part is isotropic and is either filled with clear glass or resin. In some phenocrysts a very small centre shows sieve structure with nearly colorless melt inclusions (figure 20).

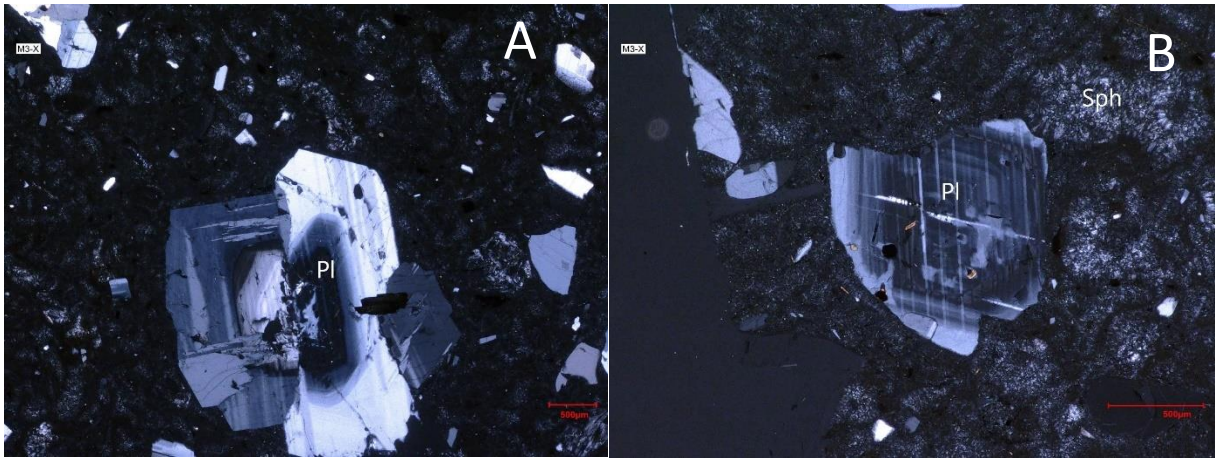

Figure 20: Two zoned crossed hatched twinned plagioclase (left) and a single cross hatched twinned plagioclase in M3 (both with crossed polarizers) [A] and strong devitrification of the matrix (right) [B]

The larger alkali feldspar (2500 µm) tends to be subangular and often appears to have a sieve structure, but here also devitrification of what was likely glassy fragments has occurred. Embayment is widespread. Some show Karlsbad twinning. The quartz is xenomorphic, with rounded edges and embayment filled with groundmass material (figure 21 A).

Other phenocrysts are rare. Biotite (1100 µm) occurs in some areas as hypidiomorphic longitudinal flakes, often with a strong reaction rim. It occurs less commonly as inclusions in the feldspar, and here reaction rims around biotite are missing.

Besides the biotite, xenomorphic amphibole clasts (300 µm) can rarely be found (figure 21 B). In other areas only the shape of secondary opaque phases points to possible amphibole fragments. The opaque phase found in this thin section is magnetite (300 µm). In contrast to M1 and M2, in M3 the magnetites are in a remarkably bad condition of preservation. The xenomorphic mineral shows no lamellae. They often appear with rounded edges and were barely noticeable. The matrix shows a quite unique texture, causing different areas of brightness. Small areas of bright grey color are bordered by irregularly shaped bodies about 200 µm diameter in size (figure 21). The irregular shaped bodies range from longitudinal, star-shaped to nearly round areas. The x and y shaped bodies in M3 may correspond to cuspates due to vesicle junction.

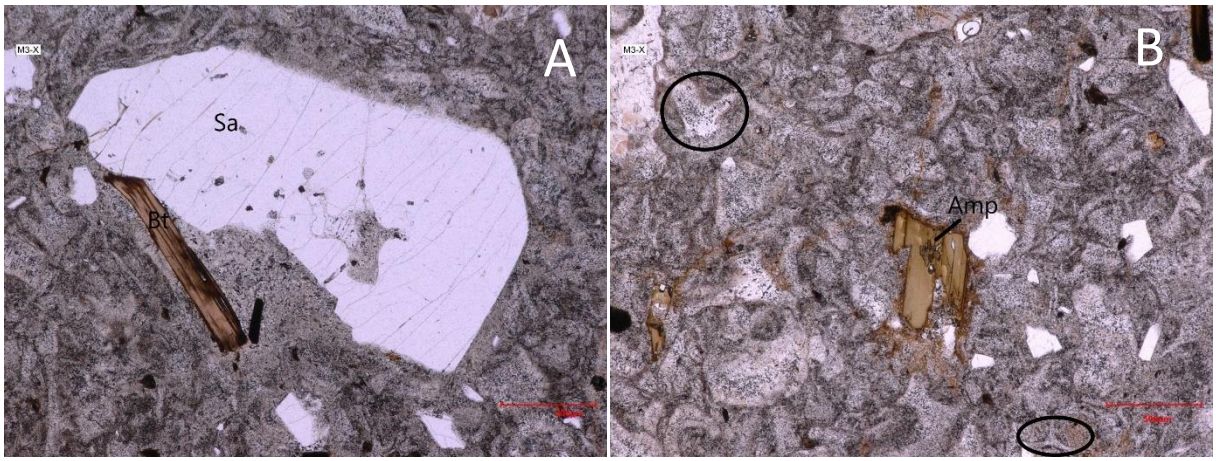

Figure 21: Bended and slightly altered biotite and alkali feldspar with embayment in M3 and a xenomorphic amphibole with reaction rim and brown iron oxide coloring of the surrounding matrix with x- and y- shaped areas in M3 (both with parallel polarizers)

These areas appear to be filled with coarser grained crystals, especially visible with crossed polarisers. The bordering matrix appears to be isotropic and is mainly dark in any position. Less common larger areas of fine crystals form round spherulites, surrounded by a fine quartz mosaic matrix (figure 22). The spherulites are axiolitic towards the matrix and fan shaped in the centre. Axiolitic as described in McPhie et al. (1993) are spherulites radiating from a line. Completely round spherulites are missing. Along some clasts and fractures the grey matrix has a fine red-orange rim.

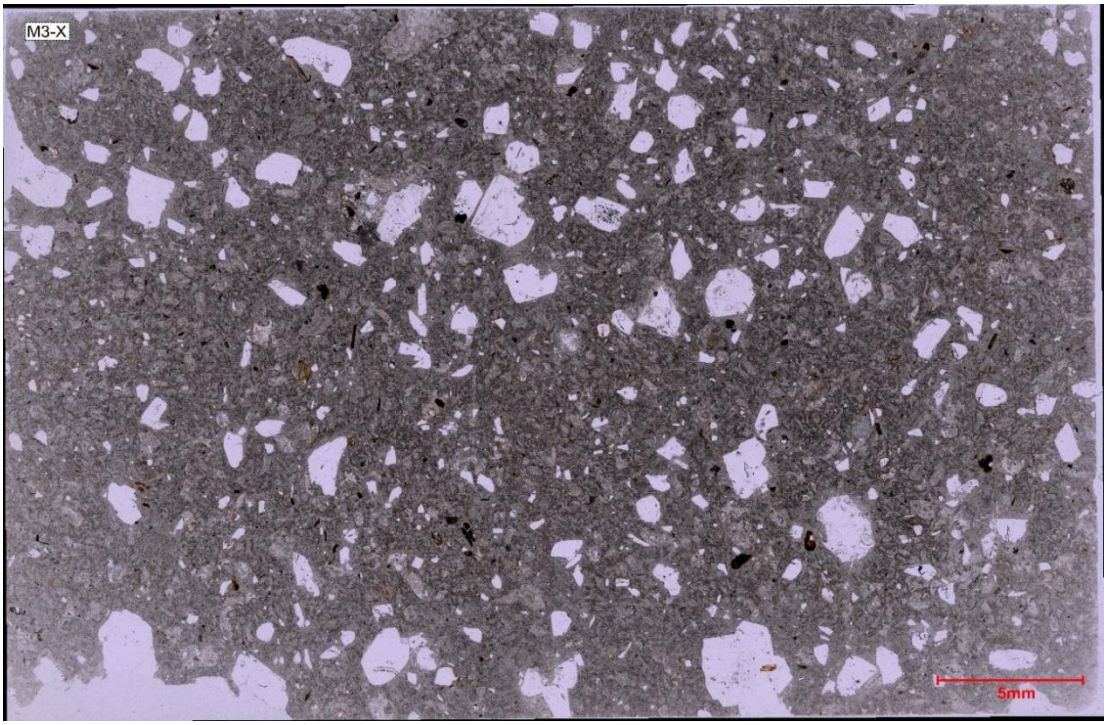

Figure 22: Panorama picture of M3 with parallel polarizers with the small, devitrified shard shaped areas

M4

M4 is also clearly distinct from most other samples, except M3. It has a porphyry texture, with large phenocrysts of plagioclase, alkali feldspar, rarer quartz and biotite. Also, size and morphology of the phenocrysts do not differ much from M3. According to the point counting the matrix makes up 84% of the section, with the most dominant phenocryst being plagioclase with about 10.7%.

Most apparent minerals are plagioclase phenocrysts, which are mostly hypidiomorphic, less common xenomorphic. The hypidiomorphic crystals reaching a size of up to 1400 µm show polysynthetic twinning and zonation in larger phenocrysts. The zonation is also apparent in smaller clasts, rarer in hypidiomorphic phenocrysts. In addition, alkali feldspar is present, often showing a sieve structure. Quartz of about the same size (1050 µm) is present, showing signs of dissolution, especially visible at rounded edges, and devitrified matrix inclusions. Biotite can also be found, mostly as smaller crystals up to 600 µm with a strong reaction and sometimes broken rim, with signs of ductile deformation. Accessory amphibole is present, reaching up to 700 µm in size. The cleavages are clearly visible, as well as the dark reaction rim. As opaque phase only magnetite was identified, showing similar properties like M3: residual lamellae, xenomorphic grains without lamellae, mostly fractured.

The major difference to M3 can be found in the matrix. M4 seems to be of similar color (except for some reddish matrix parts), but the structure differs significantly. While in M3 there was no overall anisotropy or general elongation direction, here it can be found. Most noticeable around phenocrysts, it appears to have a flow direction. This is mostly visible by color differences. The matrix can be described as cryptocrystalline, no grains are visible at 50x magnification. Moreover, no flow direction can be observed in the matrix. An exception can be found around vesicles, here an axiolitic recrystallisation formed (figure 23 A & B), showing no flow orientation, rather orienting along the vesicle borders. Larger areas showing signs of devitrification are present. For instance, two elongated, parallel areas are observed, which show with distance to the matrix short axiolitic devitrification, changing with distance to longer bowtie and completely globe spherulites (figure 23 A). Less common axiolitic spherulites are present in the matrix, always bordered by cryptocrystalline dark matrix. These areas are elongated and appear to be twisted, more rarely forming x and y shapes, like the possible cuspates in M3. Pumice wisps are present as well, reaching a size up to 1000 µm, rarer 2500 µm. These wisps are mostly elongated and are also mostly devitrified. Occasionally wisps show a rotation around a phenocryst. which could be caused by a magmatic flow, fitting to the already mentioned flow direction. Two areas of round shape with diameter of 100-200 µm differ in their devitrification compared to the pumice wisps and vesicles (figure 23 C).

The mosaic quartz indicates stronger alteration, or maybe vapor phase release. This is supported by the occasionally occurring strongly altered biotite.

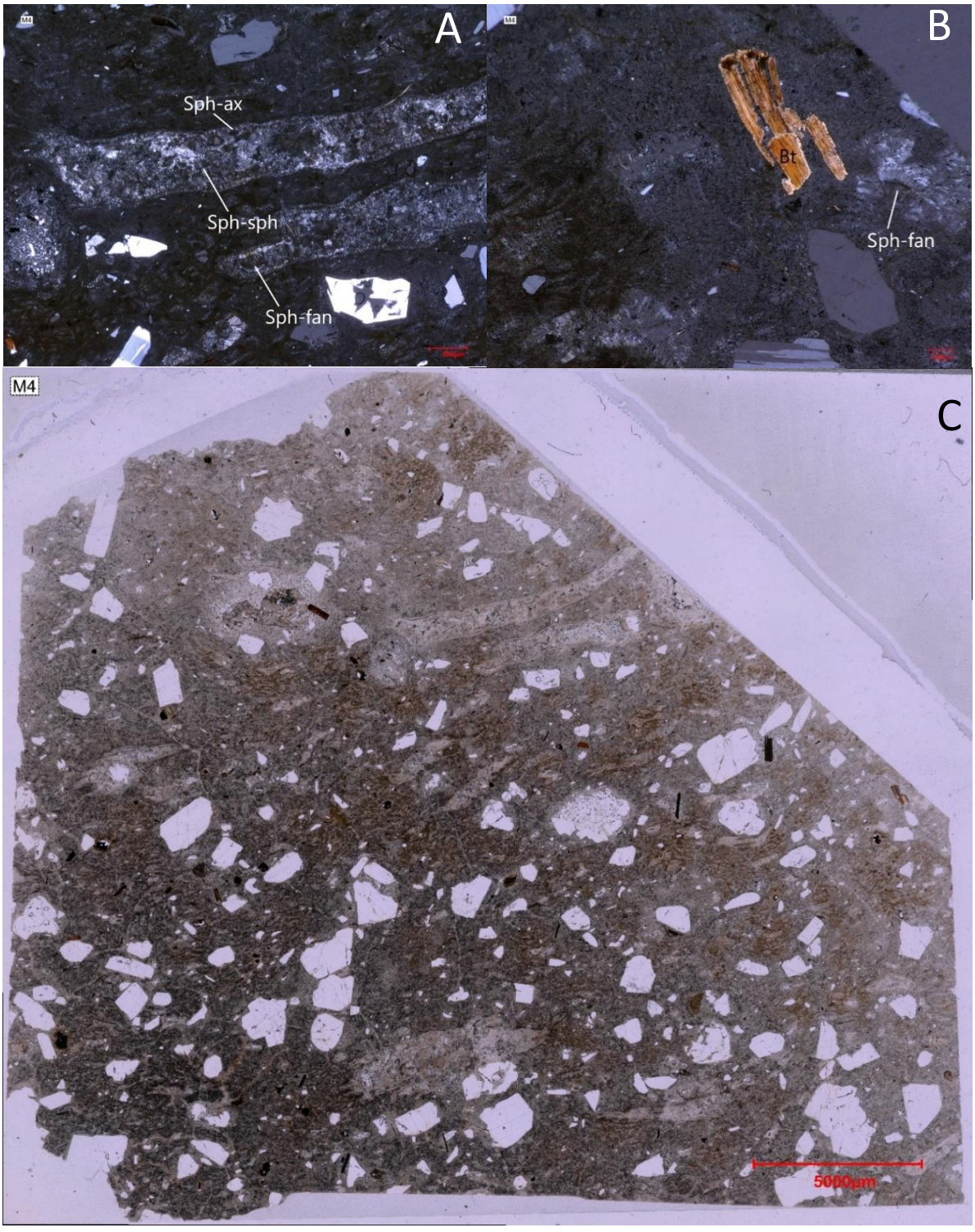

Figure 23: Strongly devitrified area in M4 reaching from axiolitic on the edges to spherical in the center [A], broken and bent biotite beside a fan shaped devitrification (Sph-fan) [B] and collapsed vesicles (both with crossed polarizers), panorama picture of M4 with parallel polarizers [C]

M6

M6 has been described macroscopically as andesits, explaining the strong microscopic difference in comparison to the rhyolitic samples M1-4. Disregarding the phenocrysts, M6 is relatively homogeneous with porphyritic texture. The phenocrysts are composed of plagioclase (1500 µm) and amphibole (700 µm) with minor clinopyroxene (355 µm). According to the point counting the matrix makes up 85% of the section, with the most dominant phenocryst being plagioclase with about 5.6%.

Especially the plagioclase differs from those described from previous samples. It is rounded in shape, rarely broken and shows a sieve structure (figure 24), as well as melt inclusions of dark brown to pale green color, surrounded by a melt-free rim at the outer edge. The broken phenocrysts appear to be less abundant than in the rhyolitic lithologies, but if they appear, than the pieces are just a few mm apart. The clasts do not have a melt free rim along the fractures and fold lines. Besides the sieve structure, polysynthetic twinning is more frequent than crossed hatched twinning.

Furthermore, amphibole phenocrysts are very abundant. Most can be described as hypidio- to idiomorphic, with visible cleavages and straight edges. Dark rims of opaque phases, probably magnetite, are noticeable. These follow the edges at about 50 µm distance (Fig. 24 B).

The smaller pyroxenes, probably augites, are xenomorphic, rounded, sometimes sickle shaped, and are evenly distributed in the thin section. In the bright field they are bright to dark brown colored, rarer pale green.

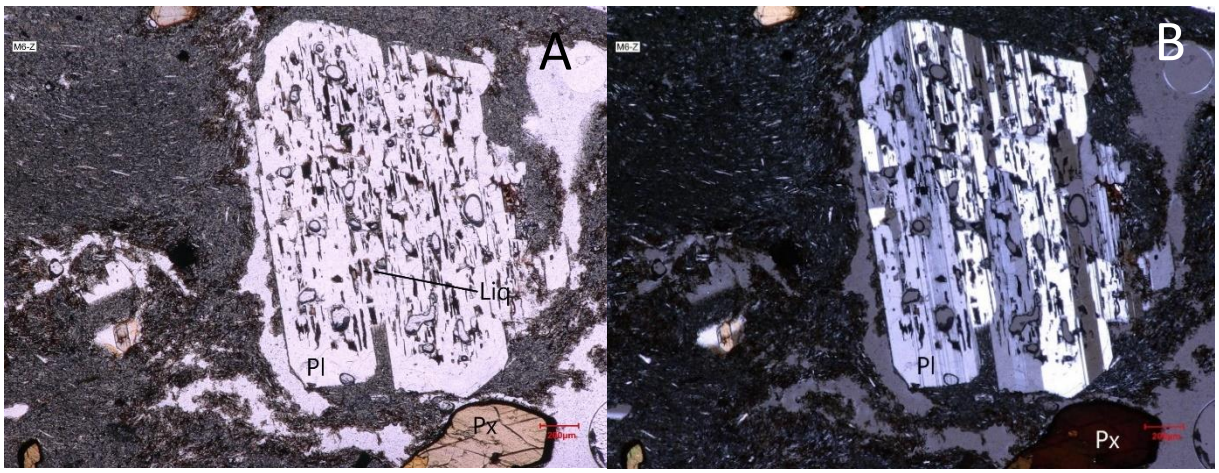

Figure 24: Plagioclase with sieve structure (brown melt inclusions) and twinning in M6 with parallel [A] and crossed polarizers [B] in M6

The only opaque phase found in the section was magnetite (figure 25 A). It is mostly idiomorphic in shape with a darker reaction rim, but still showing the original crystal shape.

Less commonly, the magnetite is rounded, but shows the typical lamellae, however thicker than in the rhyolite samples. They also appear intergrown with amphiboles and pyroxenes (figure 25 B).

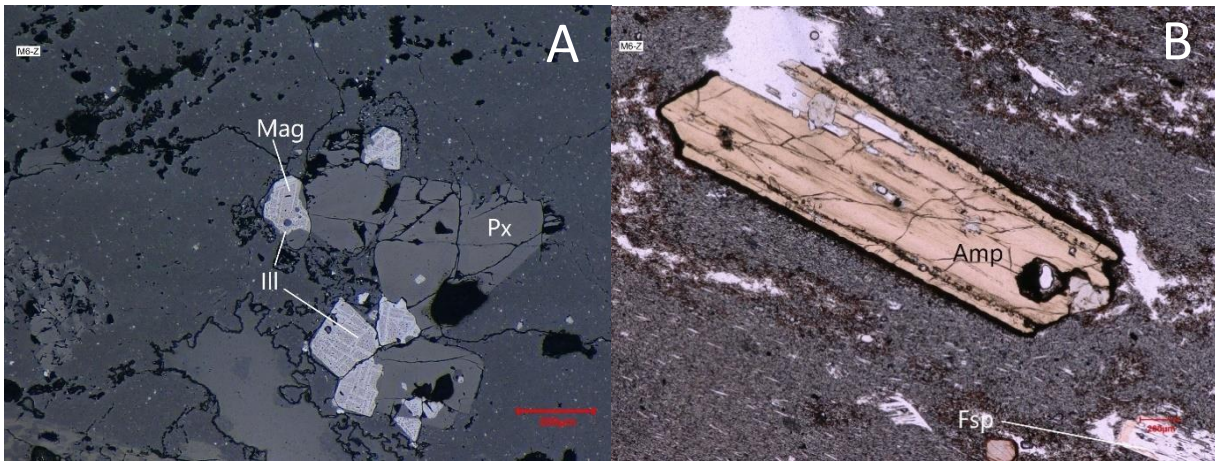

Figure 25: Broken magnetite with ilmenite lamellae and fine disseminated magnetite in the matrix with reflected light[A] and an amphibole phenocryst with flow texture matrix, defined by fine plagioclase and pyroxene with parallel polarizers [B] in M6

The matrix also differs from the rhyolitic samples, mostly by color, which is dark grey. This color is omnipresent except around the irregular shaped pores; here a dark red rim, reaching about 30 µm into the matrix, can be found. In the section larger pores and fractures are also present, which are filled with resin and do not show rims.

The matrix itself is composed of a dark mineral, which could not be determined. Opaque magnetite and larger plagioclase crystals, showing a flow direction, are especially visible around the phenocrysts (figure 26).

Looking at the matrix under reflected light, round fractures in matrix rich areas can be identified in the section. The fractures do not cross phenocrysts and could be seen as pearlitic fracturing. All in all, the sample can be described as porphyritic pyroxene-hornblende plagioclase andesite.

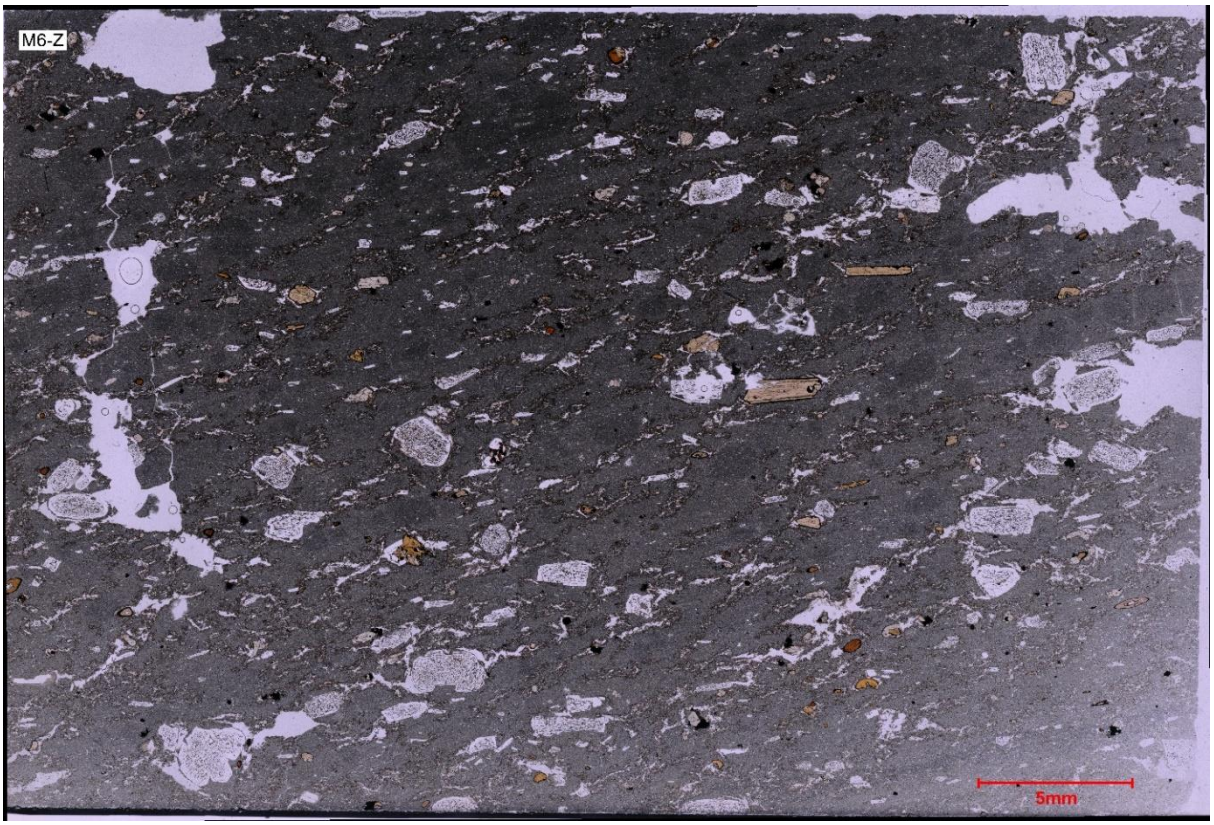

Figure 26: Panorama picture of M6 with parallel polarizers, with visible red rims along fractures and pores

M7

M7 was macroscopically described as ignimbrite. In fact, it has high similarities to sample M2. Especially the matrix shows grey to pale green coloring (figure 27 A & C). The texture can be described as porphyritic with a hypo- to holo-, cryptocrystalline matrix. According to the point counting the matrix makes up 88% of the section, with the most dominant phenocryst being plagioclase with about 5.6%.

Most dominant phenocrysts are plagioclase (1500 µm), rarer alkali feldspar about the same size. Most feldspars are broken and can be described as hypidiomorphic. There are even feldspars, which are completely scattered, exhibiting cavities in between, but still forming the phenocryst shape on a larger scale. In general, the clasts are variable in size. The edges are straight, less often curved, the corners are rounded. The fold line is uneven. In plagioclase polysynthetic twinning, crossed hatched twinning and zonation can be found. The zonation is a combination of continuous and discontinuous normal zonation. In contrast, no zonation can be found in the alkali feldspar, but Karlsbad twinning is common.

Besides the feldspars, quartz is the other dominant phenocryst (1500 µm). It can be described as xenomorphic, nearly skeletal in shape. All quartz crystals show many embayments filled

with groundmass. Biotite is present as a micro phenocryst (<400 µm). The hypidiomorphic laths of biotite are of red-brown color and show a strong reaction rim. Sometimes they are intergrown with opaque phase. Similar in color are xenomorphic amphiboles, reaching sizes up to 200 µm.

Also, glassy fragments outside of phenocrysts can be found. Their color is similar to the mentioned fragments in quartz. These fragments are highly devitrified. Again, the devitrification is axiolitic towards the matrix and becomes spherical toward the center.

The opaque phenocrysts present in thin section are magnetite. The magnetite is strongly altered, sometimes only skeletal in shape and lamellae are present (figure 27 B). The matrix of M7 is quite homogeneous, and rarer areas of devitrification are visible, less common in y and x shape, reminding of pyroclastic cuspate. Hardly distinguishable pumices show a coarser crystalline structure than the groundmass, phenocrysts are rare.

In the dominant groundmass vesicles can be found, most irregularly shaped. The rounder vesicles can be described as miarolitic cavities. Here quartz appears to have crystallized and formed idiomorphic crystals, growing into the cavity. Furthermore, dark melt fragments can be found, containing similar minerals and groundmass as M6 (figure 27 A). Feldspar phenocrysts with similar shape can be found, but finer. The fine dark and bright minerals showing the flow direction in M6 are present, but less orientated. In addition, a magnetite is present in this area, but finer dissimilated.

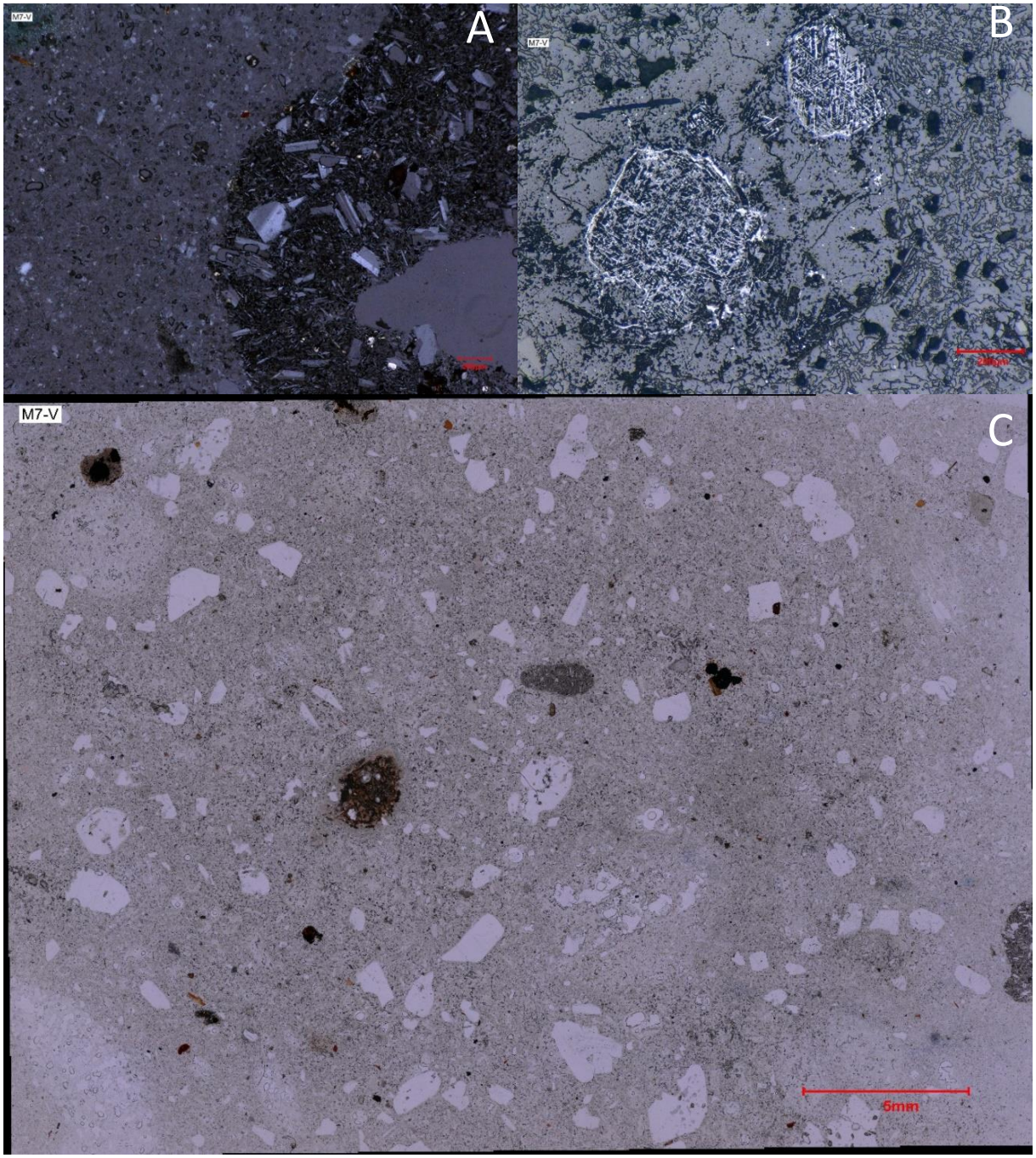

Figure 27: Dark lithic clast with a high phenocryst content in M7 (crossed polarizers) [A] and strongly altered magnetite (reflected light) [B]; panorama picture of M7 with parallel polarizers [C]

M8

M8 was also macroscopically described as ignimbrite. In fact, it has high similarities to M7. The thin section can be described as hypocrystalline, with a cryptocrystalline and partly glassy groundmass or grey to pale green color, with a porphyritic texture. According to the point

counting the matrix makes up 88% of the section, with the most dominant phenocryst being plagioclase with about 8.1%.

The major phenocrysts are plagioclase. Most are broken, therefore showing all crystal sizes from 200-2200 µm and can be described as hypidiomorphic. In contrast to M7, completely shattered phenocrysts are missing. The crystal edges are straight, the corners are slightly rounded, the fold lines are uneven. Polysynthetic twinning is rare, crossed hatched twinning slightly more common. Also, zonation can only be found occasionally. If present, the zonation can be described as normal continuous.

Alkali feldspar is also present, with a size around 500 µm. As in M7 no zonation occurs, but Karlsbad twinning is visible. The edges are curved in contrast to the plagioclase.

Also, quartz phenocrysts are present (figure 28 A), but of a smaller size (700-1000 µm) than in M7. The xenomorphic crystals show a high amount of embayment, filled with groundmass. In some areas dark brown melt incisions have been found as well. Biotite is also present as micro-phenocrysts, reaching sizes up to 600 µm. Most crystals are in worse condition than the biotite in M7 and have lost nearly all characteristics. The dark reaction rim has nearly consumed the entire mineral (figure 28 B). Finally, amphibole is present as phenocrysts in better condition. Even if the outer edges are uneven, the cleavages are clearly visible. The largest crystal reaches a size of 1000 µm and shows an opaque inclusion.

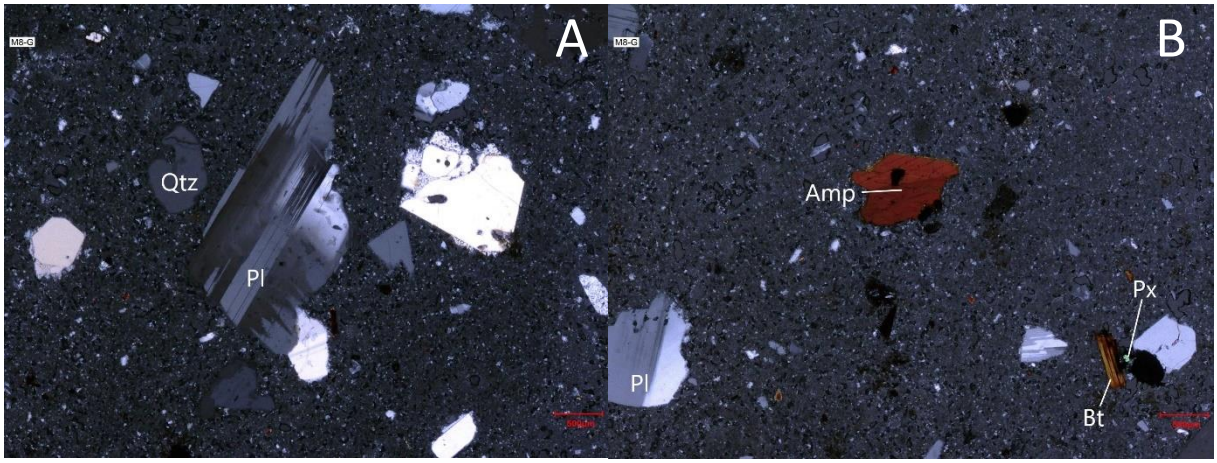

Figure 28: Plagioclase clast with crossed hedged twinning [A] and an amphibole clast with magnetite inclusion in M8 (both crossed polarizers) [B]

The opaque phase in M8 is magnetite, also in better condition than in M7 (figure 29 A). Disregarding the uneven outer edges and missing habitus, the lamellae are still visible. Around some phenocrysts also larger areas of dark brown non devitrified volcanic glass occur.

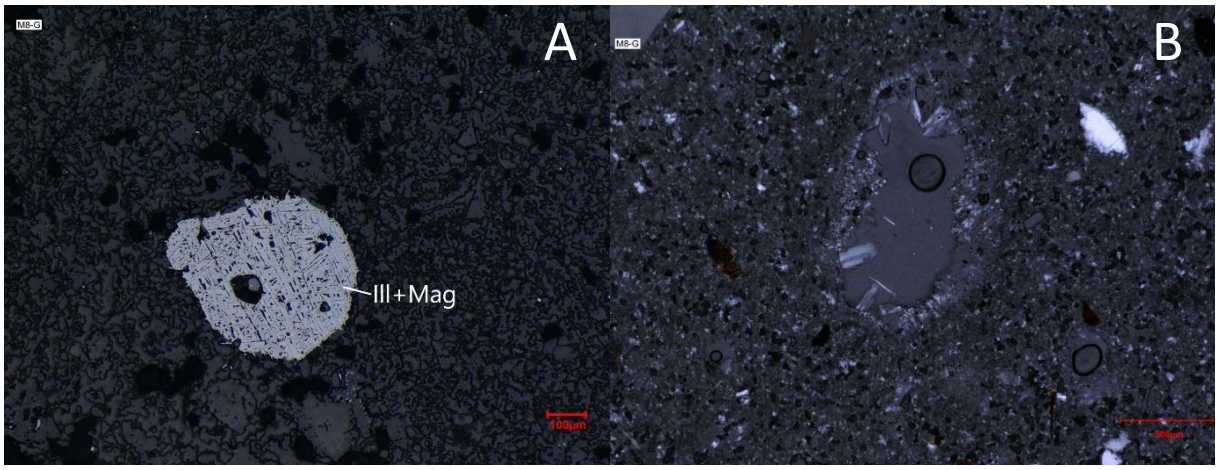

Figure 29: Magnetite- lamellae [A] in reflected light and miarolitic cavities with crossed polarizers [B] in M8

The groundmass of M8 resembles the matrix of M7, characterized by grey-white micro- to cryptocrystalline minerals with fine disseminated melt shards in between. In the homogeneous matrix x- and y- shaped areas can be found, looking like pyroclastic cuspates. Some are even wave shaped like bubble junction shards. Rounded pumice can also be found. The pumice differs from the matrix by higher porosity, coarser crystals and therefore brighter appearance (figure 29 B). Phenocrysts in the pumice are rare, one that might have been an amphibole is completely weathered (figure 30).

Also very common are miarolitic cavities, varying in size from 150-700 µm. Restricted to the round cavities, fine quartz has grown into the cavities, forming idiomorphic crystals. Besides, irregular shaped cavities are present. Cognate lithic clasts are missing.

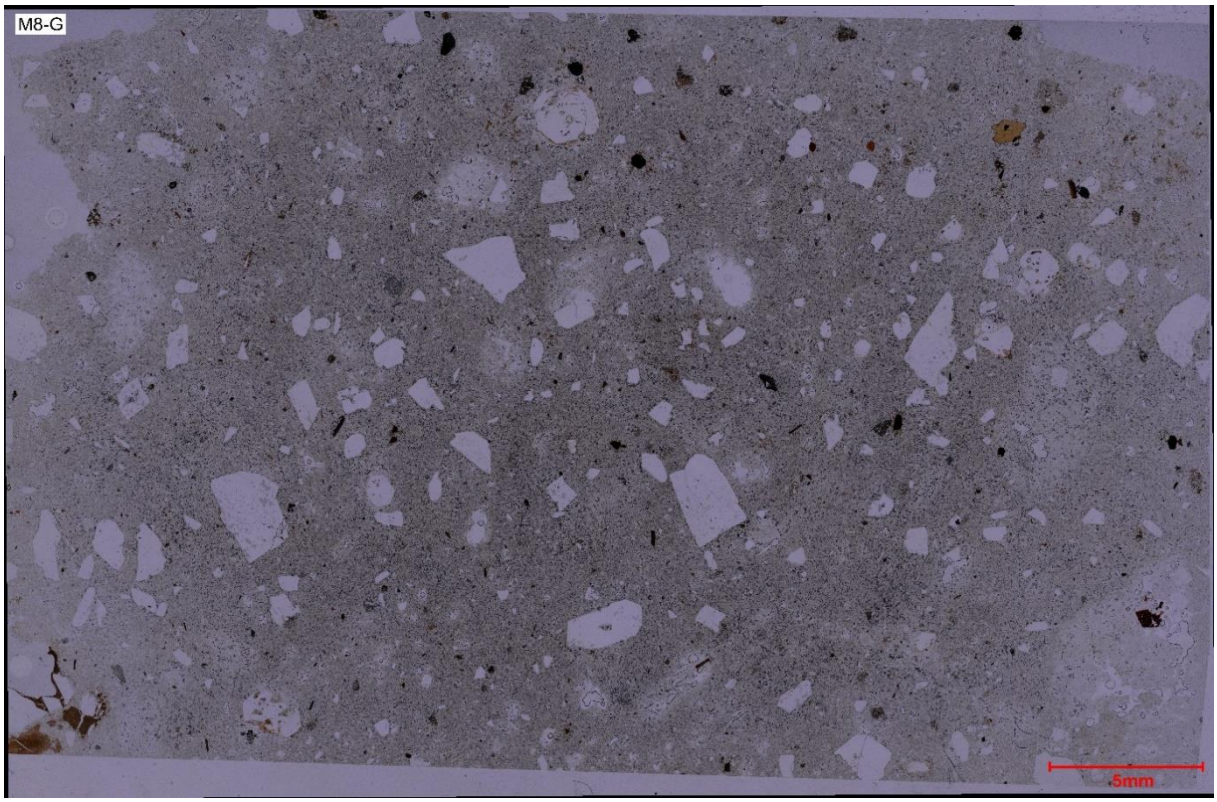

Figure 30: Panorama picture of M8 with parallel polarizers

M9

M9 was described macroscopically as andesite, similar to M6 and M10. The texture can be described as hypocrystalline-porphyritic. It has a remarkably red color, homogeneous through the entire sample. According to the point counting the matrix makes up 84% of the section, with the most dominant phenocryst being plagioclase with about 7.9%.

Main minerals are phenocrysts, most noticeable plagioclase, reaching sizes up to 1400 µm. Again, many phenocrysts are broken, many of the fragments are only a few 100 µm away from each other. Most edges are straight to slightly curved. The corners are rounded. Therefore, the crystals can be described as hypidiomorphic and subangular. In nearly all grains sieve structure with dark brown melt inclusion can be found, along with polysynthetic twinning and crossed hatched twinning. The polysynthetic twin lamellae appear to be thicker than in the other samples. Zonation cannot be found (figure 31).

Due to the bad shape of some grains a complete determination was not possible. A few grains can also be alkali feldspar.

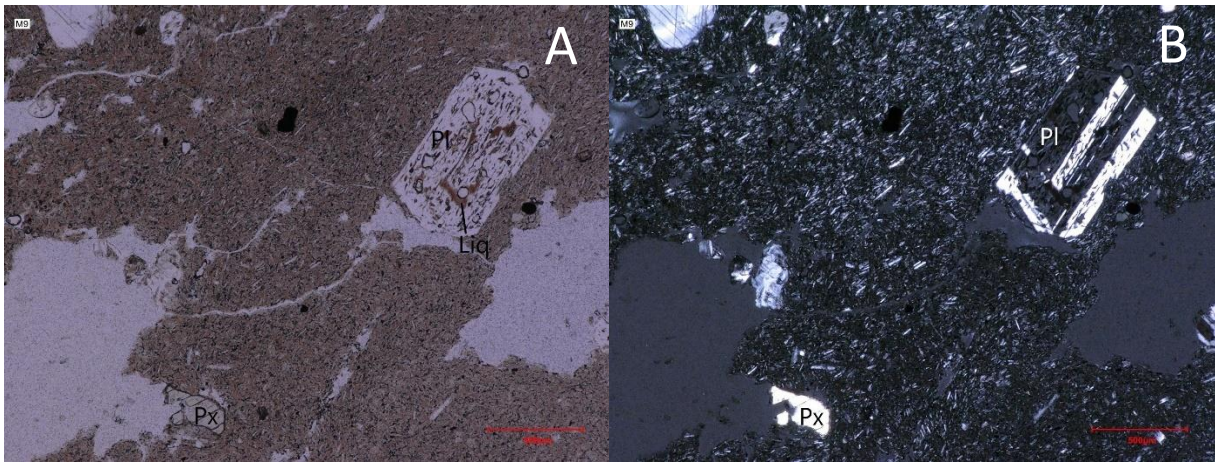

Figure 31: Plagioclase with sieve structure in a matrix with flow texture (crossed [A] and parallel polarizers [B]) of M9

Besides plagioclase, pyroxene (700-1000 µm) is mostly present. The crystals are in poor, xenomorphic condition. The shape is subangular to rounded and shows signs of embayment. For the determination twinning lamellae and the interference colors have been used. Many crystals are broken, forming clusters of smaller rounded clasts of pyroxene (figure 32 A).

Barely recognizable, amphibole (700 µm) is present. In contrast to M6, M9 has more pyroxene than amphibole. The reaction rim around the crystals is remarkably thick, embayment can be found as well, more than 50 µm are common. Some crystals are even completely consumed by the rim. In larger crystals the core is still intact, where cleavage and color can be used for mineral identification (figure 32 B).

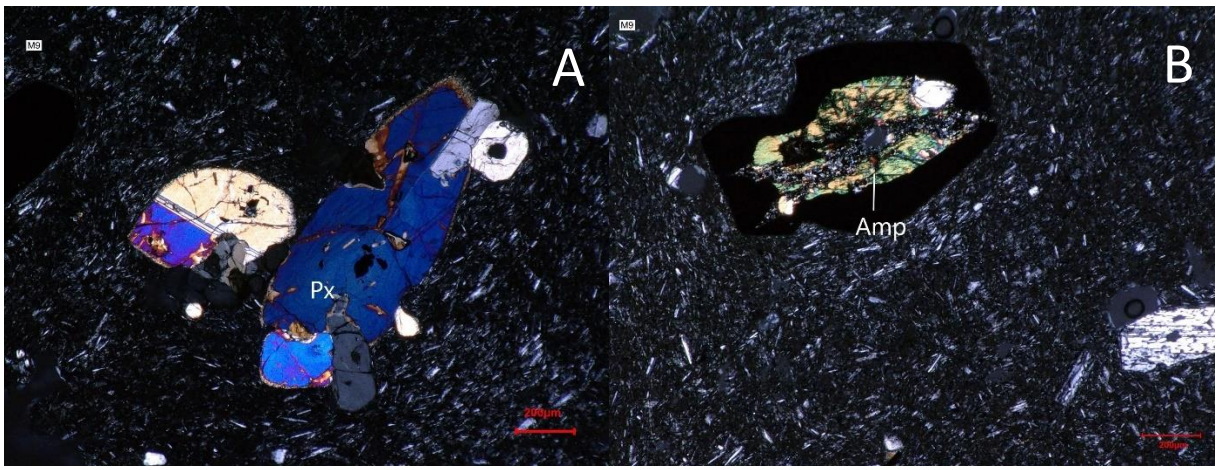

Figure 32: Pyroxene with twinning lamellae [A] and amphibole with strong reaction rim but still with visible cleavage [B] of M9

The opaque phase on the other hand is magnetite (<400 µm), which often occurs in clusters or as inclusions in larger crystals. In contrast to other samples, the magnetite, even if in good condition, does not show any lamellae (figure 33 A & B).

The matrix texture equals the one from M6, small bars of white minerals in an extremely fine red, in this case glassy matrix. The matrix shows a flow texture, but not as dominant as in M6. Fine disseminated magnetite is present as well. Like in M6, irregular cavities are widespread, but with no sign of alteration. Pumice and lithic clasts are missing as well. No signs of devitrification have been found. In reflected light microscopy round, pearlitic fractures can be found, in transmitted light they appear a little darker red (figure 33 C). All in all, the sample can be described as porphyritic pyroxene-hornblende plagioclase andesite.

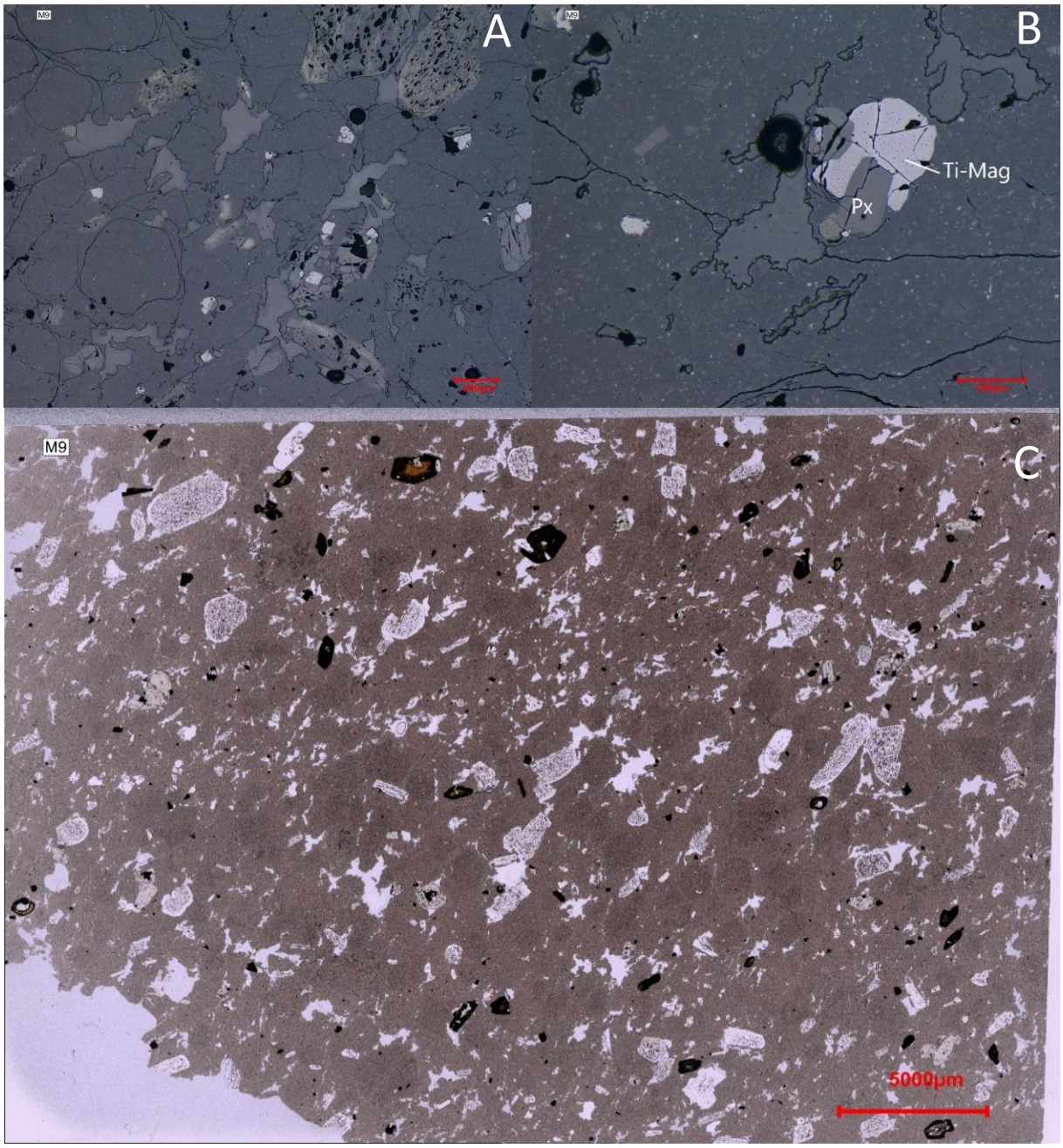

Figure 33: Fe-Ti-oxides in reflected light with different magnifications[A&B]; Panorama picture of M9 with parallel polarizers [C]

M10

As for M6 and M9, M10 was described macroscopically as andesite, showing most similarities to M6, especially in color. The groundmass is of a homogeneous grey. The texture is hypocrystalline porphyritic. According to the point counting the matrix makes up 75% of the section, with the most dominant phenocryst being plagioclase with about 13.3%. The main minerals are phenocrysts of plagioclase, pyroxene and minor amphibole.

The plagioclase (1300 µm) has a wide range of conditions, from subangular hypidiomorphic, xenomorphic clasts to nearly idiomorphic crystals, the latter showing straight edges and sharp corners. All have a sieve structure, with pale green, less common brown melt inclusions occupying the crystal center. Additionally, a melt-free rim of 70-200 µm is widespread. One specific crystal shows a melt free core, a rim of melt inclusions followed by a melt free outer edge. Zonation is present and can be described as oscillatory normal zoning. Twinning is common, polysynthetic twinning being most frequent, followed by crossed hatched twinning. In the hypidiomorphic to xenomorphic plagioclase, embayment can be observed (figure 34 A).

The second common phenocryst is pyroxene (400-2000 µm), which can be described mostly as rounded xenomorphic minerals, with cleavage angle and interference colors used for identification. Most pyroxene crystals do not show straight extinction and are therefore clinopyroxenes. Less common are idiomorphic minerals, where. Embayment occurs regularly. Some crystals are sheared off. Twinning lamellae, a zonation, sometimes even visible with parallel polarizers, can also be found. Most pyroxenes occur in clusters with other pyroxene, amphibole, rarer plagioclase and opaque phases (figure 34 B).

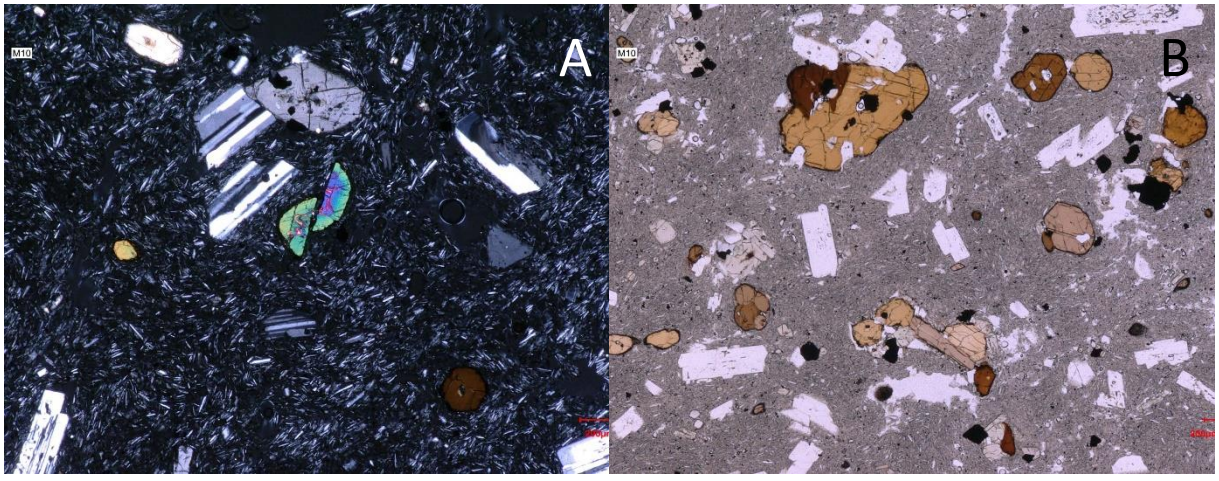

Figure 34: Broken and sheard of feldspar and pyroxene phenocrysts (parallel [A] and crossed polarizers [B]) of M10

The amphiboles (1000 µm) can be identified by their interference colors, elongation and cleavage angle. The minerals show similar properties to the pyroxene, with often rounded edges and embayment (figure 35).

The magnetite (100-400 µm) of M10 looks like the one of M9 in appearance, hypidiomorphic, without lamellae and sometimes with a strong reaction rim of probably ironhydroxides, due to its low reflectance.

The matrix is dark grey and is composed of a dark mineral, which could not be determined without SEM. Opaque magnetite and larger plagioclase laths show a flow direction, especially visible around the phenocrysts. Looking at the matrix under reflected light, round fractures in matrix rich areas can be identified in the section. The fractures do not cross phenocrysts and could be seen as pearlitic fracturing. All in all, the sample can be described as porphyritic pyroxene-hornblende plagioclase andesite.

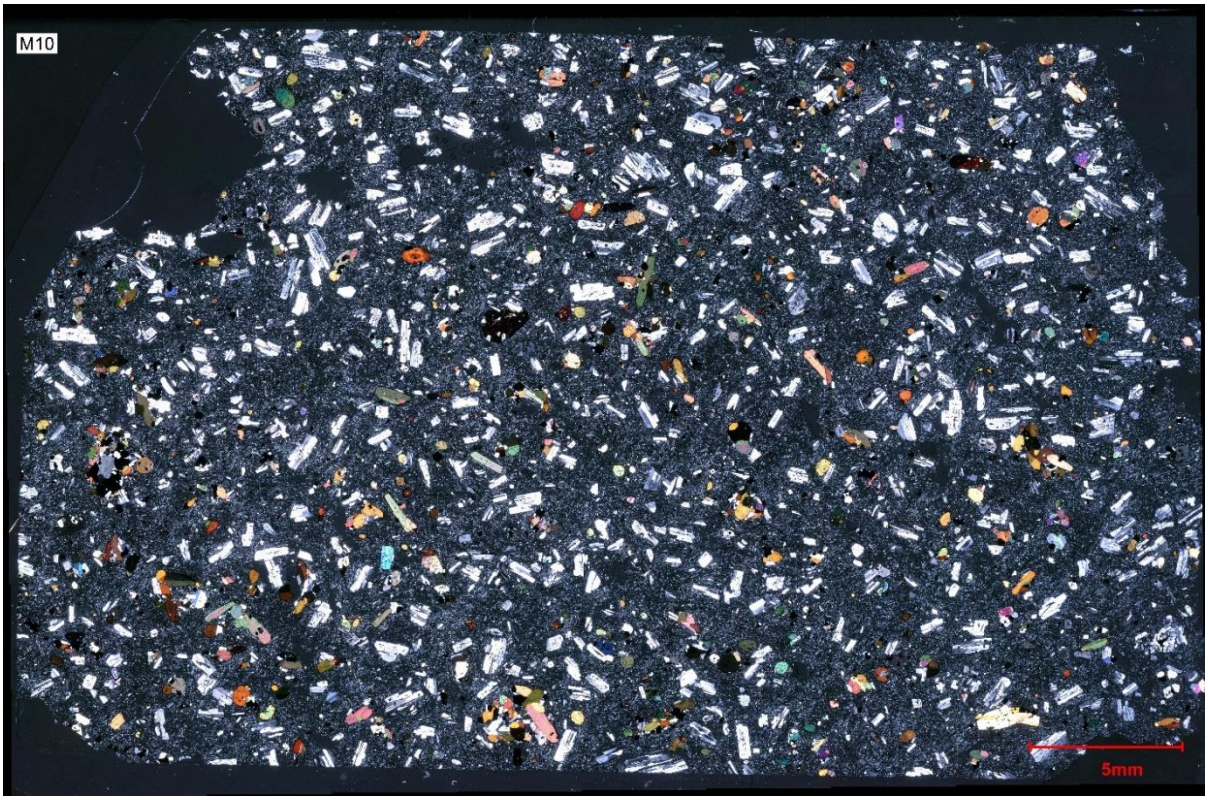

Figure 35: Panorama picture of M10 with crossed polarizers and a noticeably higher phenocryst content

4.1.2 Scanning electron microscopy (SEM)

The main purposes of the SEM work are mineral identification and confirmation on the one hand and on the other the identification of the matrix composition and micro texture. Because

the mineral chemistry is normalized to the oxides of the mineral formula the following compositions will be given in “per formula unit”, short pfu.

Feldspar

The feldspar was identified in all thin sections in the polarized light microscopy. Nevertheless, the determination of the composition was not successful. Therefore, the scanning electron microscope with energy dispersive x-ray spectroscopy is needed (appendix 10.3.1).

In M1 characteristics like zonation are visible. This zonation can also be confirmed in the SEM in some of the plagioclase phenocrysts, while others do not show a zonation (figure 36).

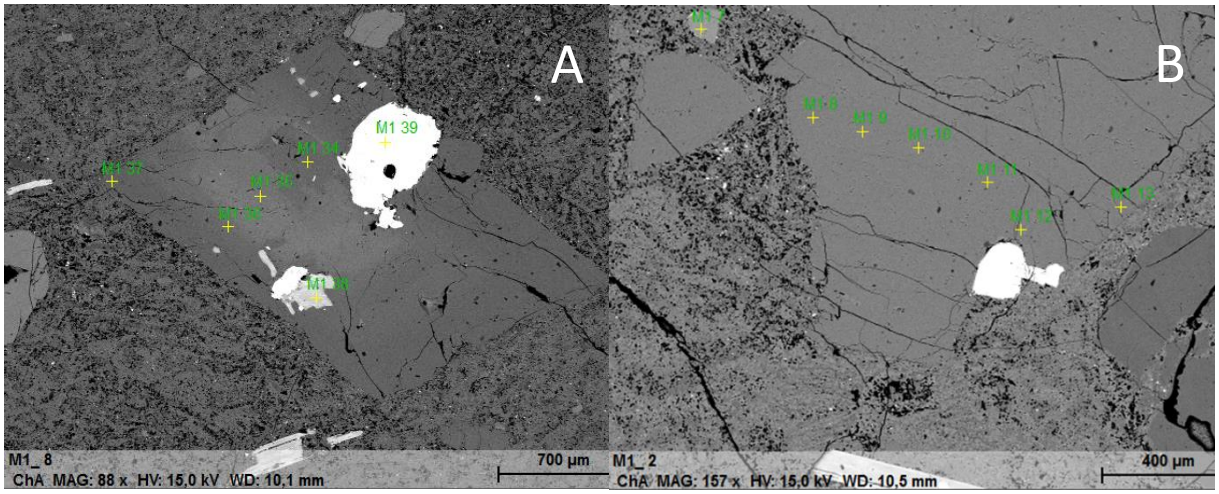

Figure 36: BSE image of plagioclase (all measurements except M1-39 and M1-33) in M1, zoned [A] and without zonation [B]

In one of the phenocrysts the zonation is caused by a change in composition. The brighter center (M1-35) is calcium rich, containing 0.45 Ca and 0.53 Na pfu, while the darker surrounding areas are more sodium rich containing 0.67-0.71 Na pfu and 0.24-0.28 Ca pfu. The potassium content differs as well. The sodium rich areas have more potassium than the calcium rich areas. Still, the potassium content does not reach 0.1 K pfu in either area.

In contrast to the zoned plagioclase, also unzoned plagioclase is present (figure 37). The composition in these phenocrysts varies, larger ones containing 0.76-7.78 Na pfu and 0.16-0.18 Ca pfu. The potassium content in these crystals is less than 0.1 K pfu. In contrast smaller ones contain more Ca than the larger ones with up to 0.36 Ca pfu and 0.6-0.65 Na pfu.

The other feldspar present was alkali feldspar. Here no variations in compositions have been found, containing 0.55-0.59 K, 0.40-0.45 Na and 0-0.015 Ca pfu. Remarkably, all contain a small amount of barium (<0.001 Ba pfu). The feldspar present in the matrix as fine crystals intergrown with chalcedony is mostly alkali feldspar as well, containing 0.59 K pfu and 0.40 Na pfu, 0-0.13 pfu Ca and a small amount of Ba (<0.014 pfu). Only occasionally, plagioclase is

present in the matrix; these are Na dominated (0.58 pfu). In conclusion, M1 contains andesine, oligoclase and Na-sanidine.

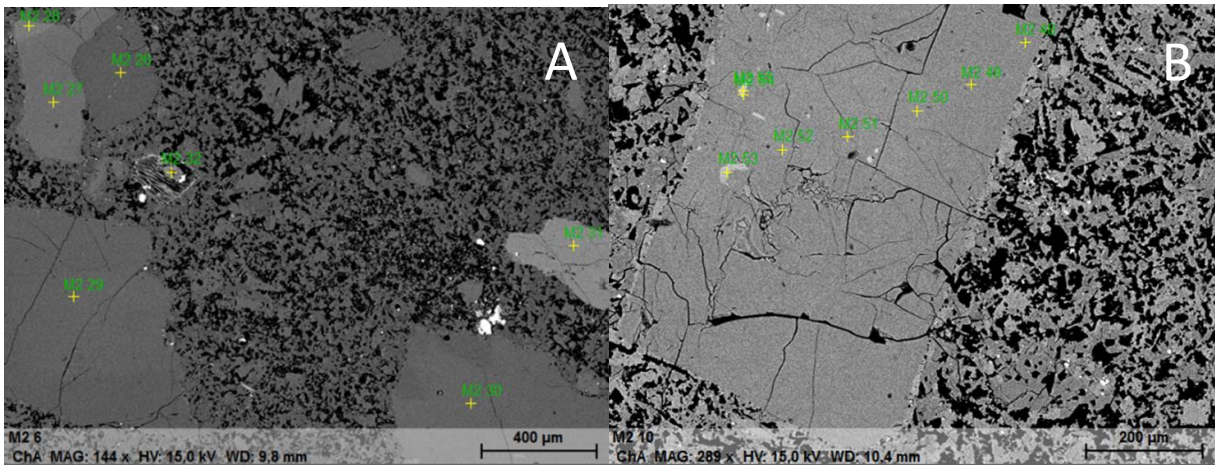

Figure 37: BSE images of missing zonation in the plagioclase clast (M2-26-29) [A] and phenocrysts (all measurements) [B]

The plagioclase of M2 has a noticeable higher Ca content in the measured phenocrysts than M1, varying between 0 to 0.56 pfu Ca. Simultaneously the Na content also has a higher range from 0.33 to 0.79 pfu. Zonation has been found in some phenocrysts but not as strong as in M1. The M2 zonation is characterized by an omnipresent higher Na content, a more calcium rich center with about 0.23 Ca and 0.75 Na pfu and a more sodium rich outer area with 0.16 pfu Ca and 0.69 Na pfu.

Also, alkali feldspar has been measured in M2. In contrast to M1, the alkali feldspar phenocrysts do not contain any Ba, except one inclusion. The phenocrysts contain 0.60 K pfu, 0.39 pfu of Na and no Ca (figure 38).

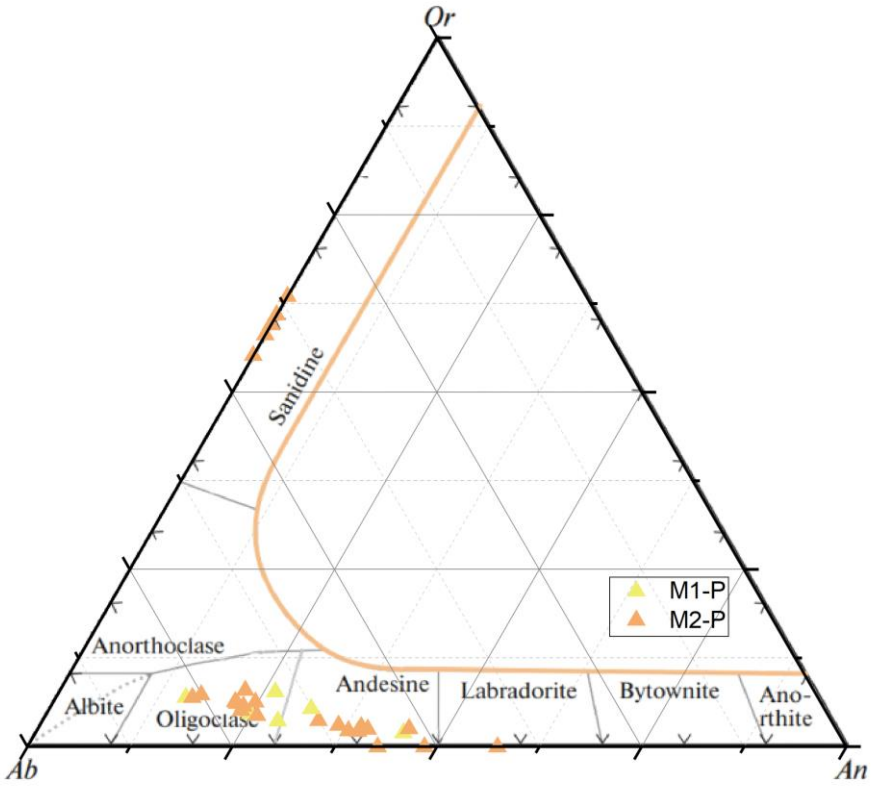

Figure 38: The measured feldspar of M1 and M2 in a modified tertiary feldspar diagram after Demonterova et al. (2023), note that the orange line is temperature dependent

The feldspars of M3 differ from the previous samples (M1 and M2). While the anorthoclase composition was missing, in M3 it is present. The labradorite of M3 contains less calcium. Also, some potassium and calcium containing sodium-feldspars are present. The calcium richer crystals are mostly broken, with irregular edges (figure 39). As seen in figure 41 C measurements regarding the zonation show that M 3-3 and M3-4 are sodium richer than M3-1, M3-2, M3-5 and M3-6. Consequently, changing compositional from andesine (0.40-0.46 Ca pfu) to labradorite (0.52-0.55 Ca pfu), even if this compositional difference is not visible in the SEM.

The compositional change appears also in the opposite direction, from labradorite to andesine, in this section. As seen in the element mappings of figure 40, calcium rich cores with transition to sodium richer edges are present. The potassium feldspar ranges, similar to M1 and M2, in the Na-sanidine composition (0.58-0.65 K pfu), containing nearly no calcium.

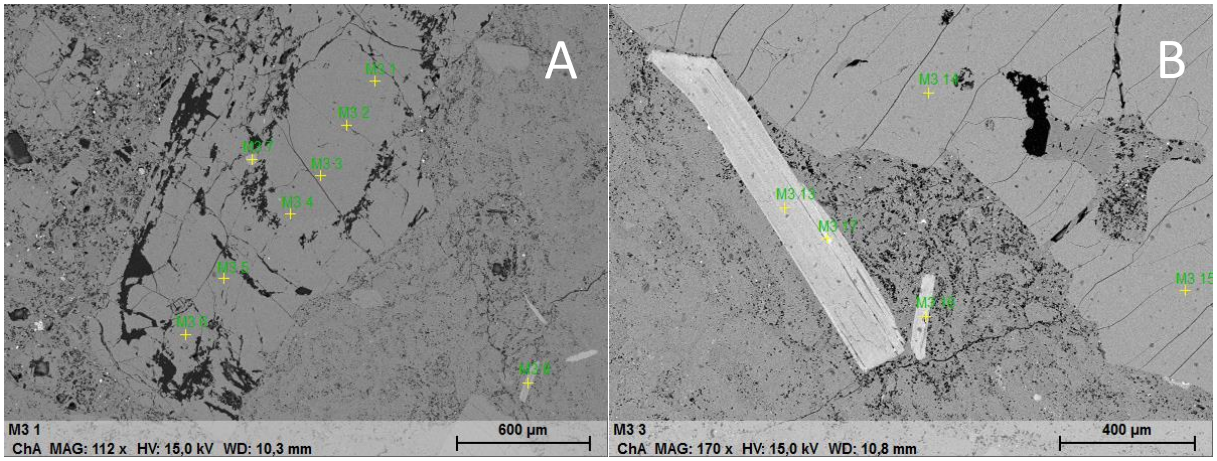

Figure 39: BSE images of feldspar phenocryst of bad condition (all measurements) [A], alkali feldspar with embayment (M3-11& M3-15) [B]

In contrast to the previous samples, labradorite in M4 is not present among the plagioclase solid solution, and only andesine and oligoclase are present, reaching from 0.51-0.79 Na and 0.15-0.49 Ca pfu. Especially in the oligoclase higher potassium values can be found (< 0.1 pfu).

In some crystals a strong zonation is visible (figure 40), while others do not show a strong zonation, but all exhibit a transition from calcium rich to sodium rich towards the edges. The stronger zonation even shows a transition from andesine to oligoclase.

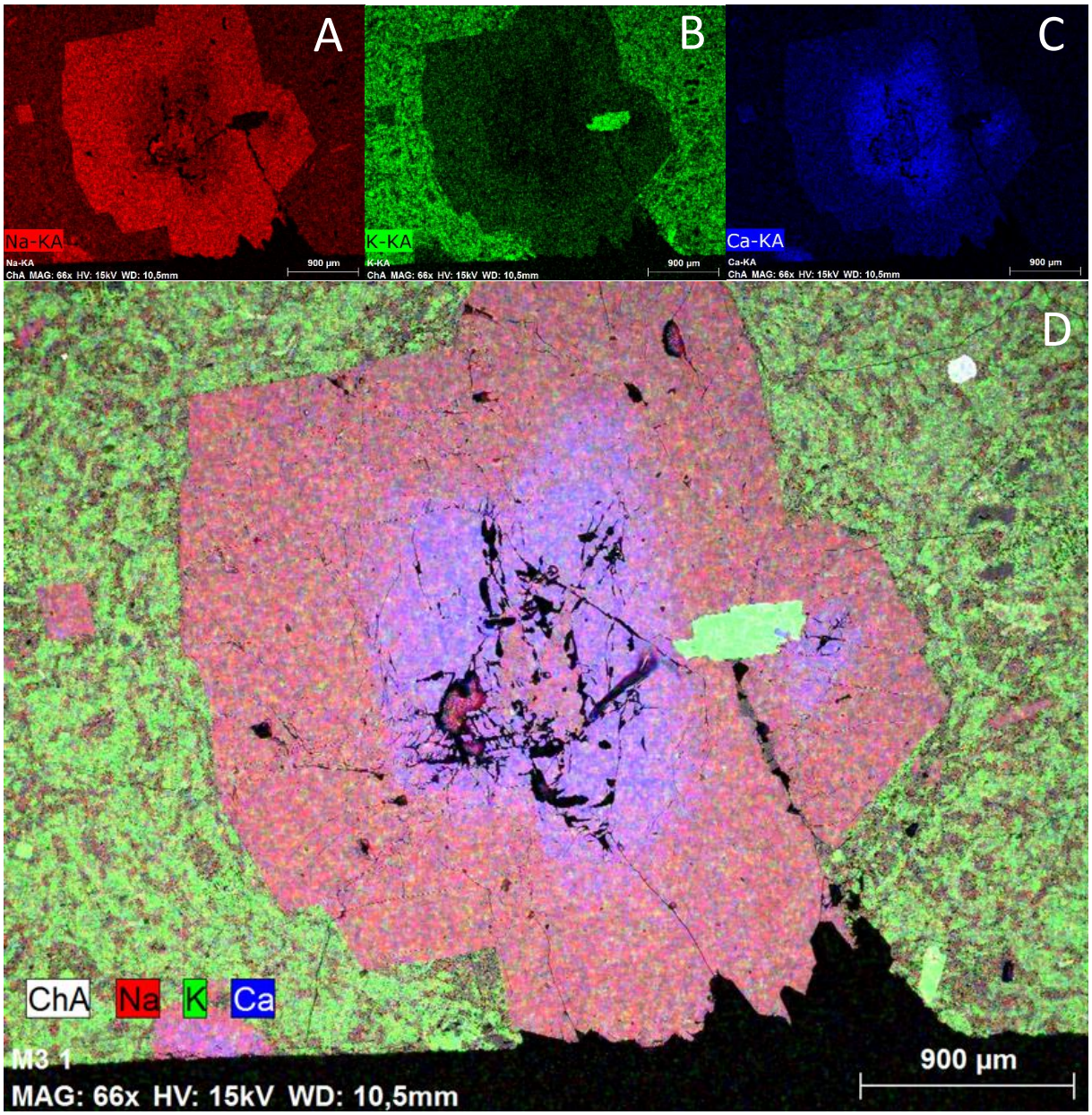

Figure 40: Mapping of different plagioclase phenocrysts in M3 for the element Na [A], K [B], Ca [C] Compositional zonation of a plagioclase with two calcium rich cores with an ingrown biotite in M3 [D]

The alkali feldspar shows no zonation as in the previous samples, showing a Na-sanidine composition. In this sample, higher variations can be found; the potassium content ranges from 0.38-0.62 K pfu (figure 41)

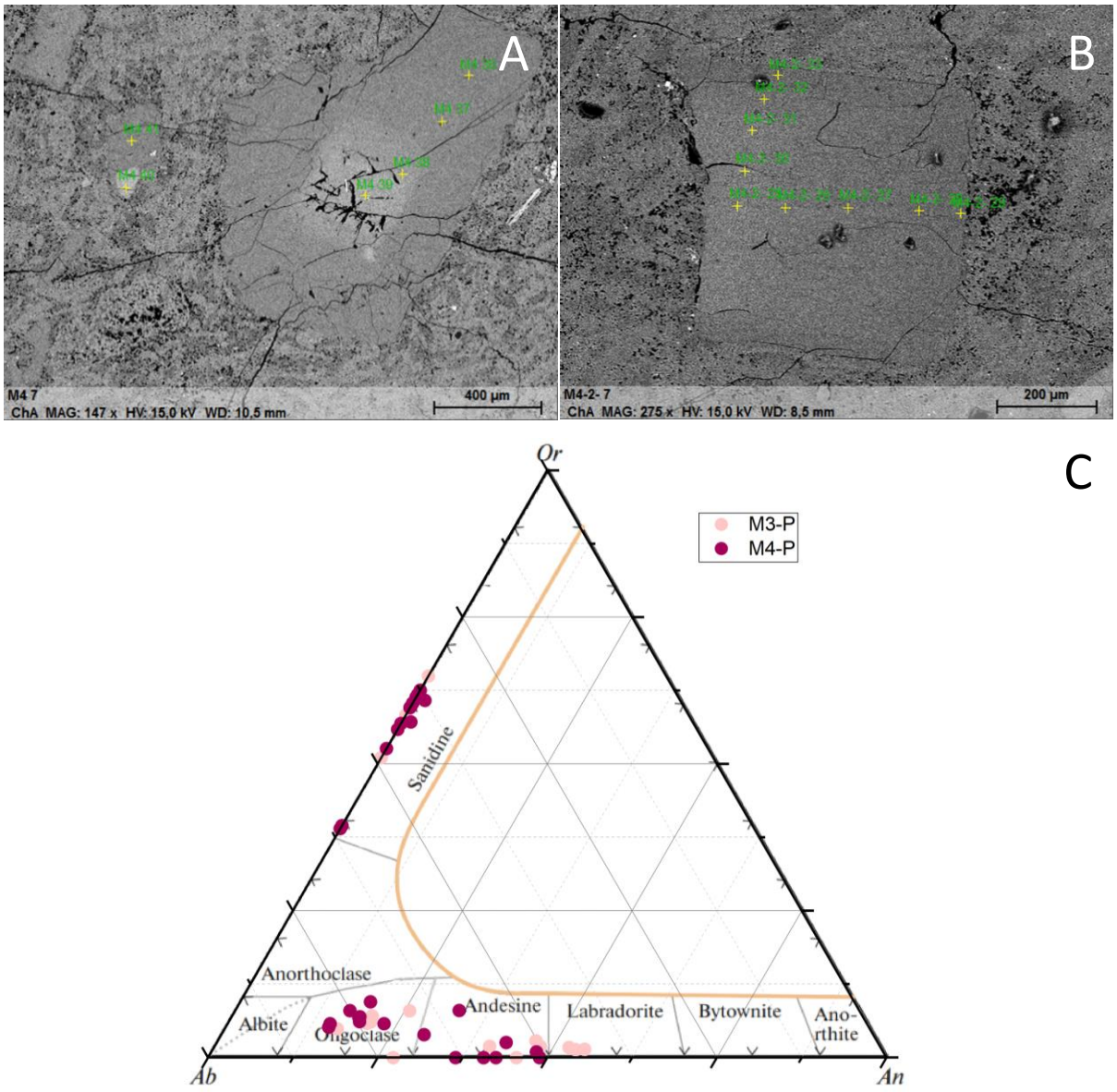

Figure 41: BSE image of strongly zoned (M4-36 to -39) [A] and weakly zoned (all measurements) [B] plagioclase of M4 and the measured feldspar of M3 and M4 in modified tertiary feldspar diagram after Demonterova et al. (2023) [C]; note that the orange line is temperature dependent

In M6, feldspar is less present than in the other samples. Noticeably no alkali felspar can be found in the phenocrysts. The plagioclase is more calcium rich compared to the previous samples (0.5-0.69 Ca pfu) and therefore the sodium values range between 0.33-0.48 pfu, and potassium is also present (<0.02 pfu). Zonation in these labradorites cannot be found in the SEM, but slight differences are detected, revealing calcium richer areas. Also worth mentioning are the fine matrix embayments, which are potassium rich (figure 42 A & B).

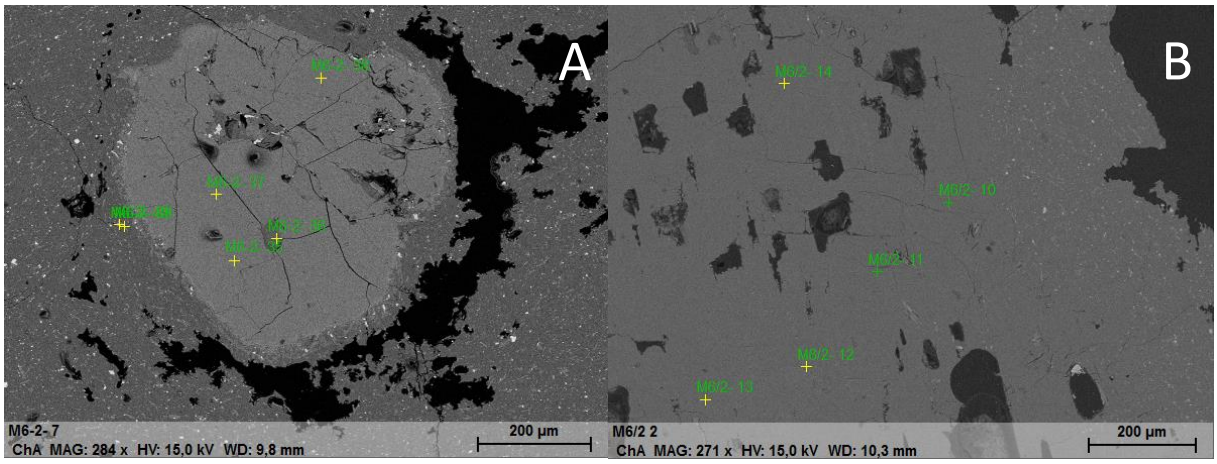

Figure 42: BSE image of felspars with matrix embayment (M6-2-35 to -38) [A] and sieve structure (all measurements) [B] in M6

The feldspar in sample M7 is similar to the samples M1-M4. The plagioclase phenocrysts do not show any embayment and are andesine and oligoclase, rarer labradorite in composition, characterized by 0.18-0.57 Ca, 0.41-0.85 Na and <0.1 K pfu. The chemical zonations are less extreme compared to other samples. The measured alkali feldspar was a sanidine, with 0.81 K pfu (figure 40 A).

Feldspar in M8 has a noticeably low compositional range. The plagioclase is sodium dominated (0.64-0.78 Na; 0.16-0.31Ca pfu), ranking therefore from andesine to oligoclase. The alkali feldspar is again only Na-sanidine (0.43-0.64 K pfu) (figure 43 B & C).

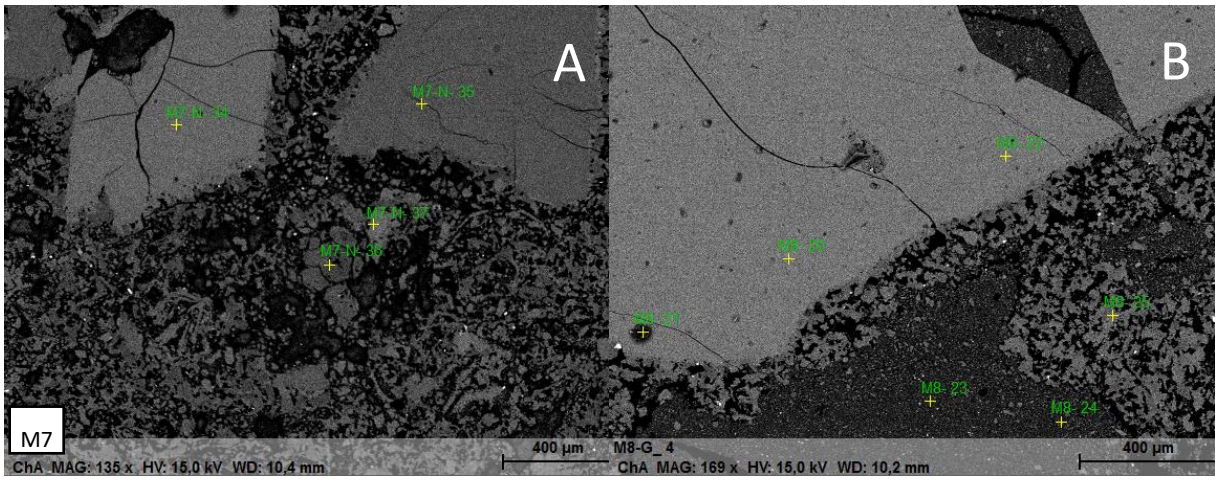

C

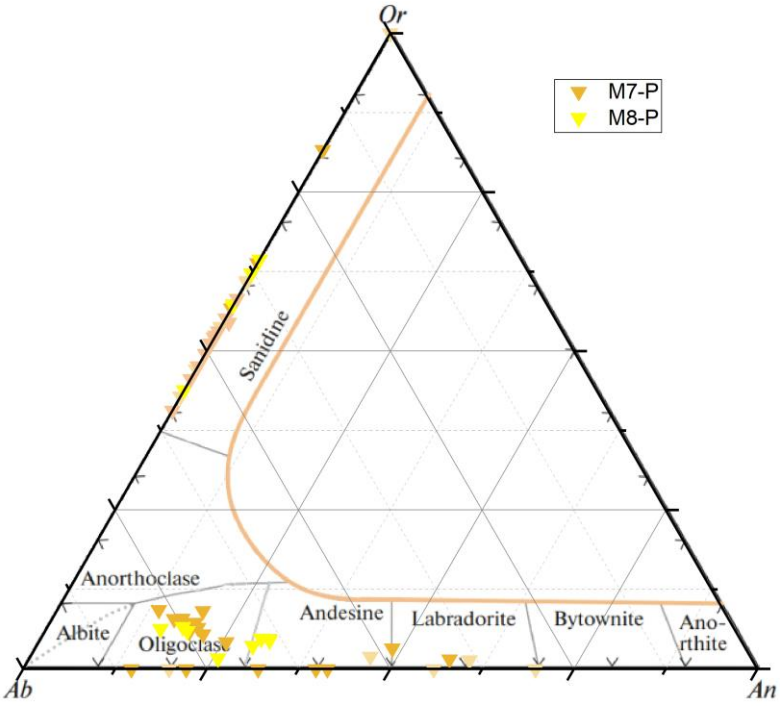

Figure 43: BSE image of feldspar phenocrysts in M7 (M7-34 & -35) [A] and M8 (M8-20 & -22) [B] glass fragment (fine matrix) with phenocryst, modfied tertiary feldspar diagram after Demonterova et al. (2023) of the measured feldspar of M7 and M8 in a; note that the orange line is temperature dependent [C]

In M9 the felspar is similar to the one in M6. As in M6 alkali feldspar is rare and if found, Na-sanidine (0.35K pfu). The plagioclase shows a strong variation in composition, reaching from andesine to bytownite (0.45-0.79 Ca; 0.2-0.54 Na pfu). Zonation has not been observed (figure 44).

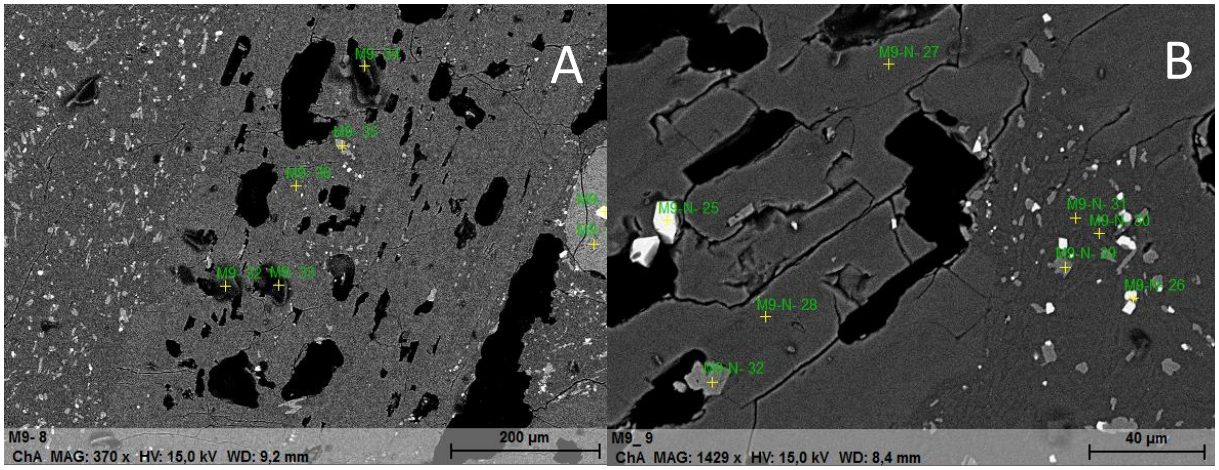

Figure 44: BSE image of feldspars with matrix embayment and sieve structure in M9 [A and B] (M9 -32 to -36 & M9-N -27 &-28)

On contrast, in M10 zonations are clearly visible (figure 45 B-E). The plagioclase shows a calcium rich core with zones of changing sodium content around. Noticeably, some of the crystals' outer composition varies between a calcium rich and a sodium rich edge. The composition reaches from andesine to bytownite. In some crystals potassium and sodium rich embayment can be found. Alkali feldspar does not occur as phenocrysts.

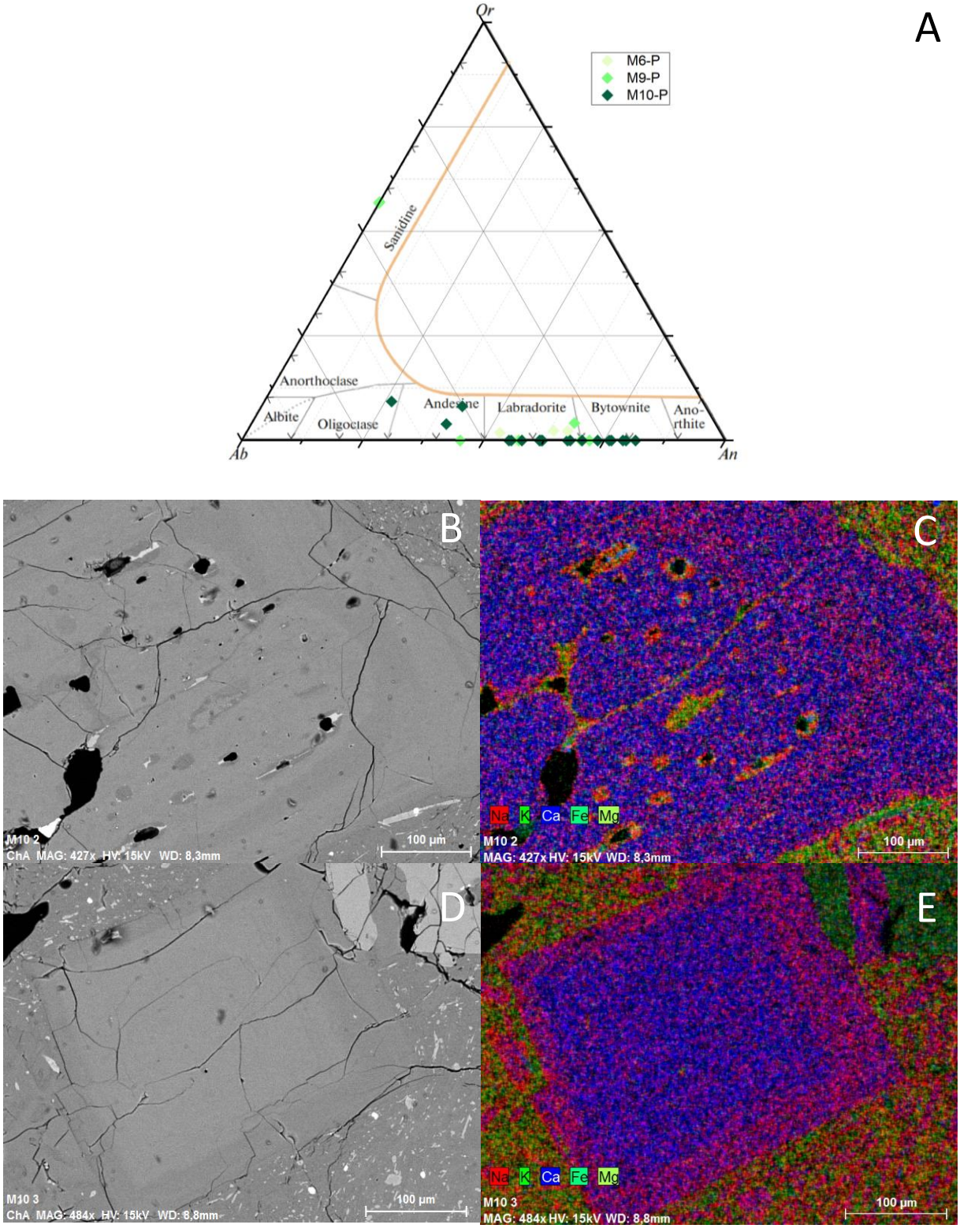

Figure 45: The measured feldspar of M7 and M8 in a modified tertiary feldspar diagram after Demonterova et al. (2023) [A] note that the orange line is temperature dependent; BSE and element mapping images of feldspars with matrix embayment and sieve structure with matrix composed of glass fragments in M10 [B, C, D, E]

Besides the feldspar phenocrysts, also matrix feldspars are present. Compositionally, these felspars often differ from the feldspar phenocrysts. In M1 the matrix feldspars are andesine, oligoclase and Na-sanidine in composition, forming small brighter islands in the denser areas of the porous matrix (figure 46 A). The matrix feldspars of M2 appear similar to M1, however these feldspars even reach the labradorite composition field. The size also differs from M1. The fine intergrowth with quartz does not occur, whereby rather fine crystals of random orientation cause an extremely high porosity.

Even if the microstructure of M3 is similar to M1 and M2, the M3 sample has a lower porosity in the SEM, caused by an almost interlocking intergrowth of fine feldspar and quartz minerals. In contrast to M1, the porosity of M3 is not homogeneously distributed, rather longitudinal areas of denser intergrowth are separated by areas similar to M2. Sample M3 also differs in composition. The matrix feldspars are Na-sanidine, anorthite and oligoclase, causing a homogeneous brightness in the low-magnification BSE-image, while in close up areas of different brightness are visible. In some areas the devitrification of the matrix can be seen in the SEM. Spherulites form spherical areas of feldspar, with sodium core and potassium rim (figure 46 B-D). Silica forms the matrix with larger lamellae of feldspar. M4 in this respect is very similar to M3. The characteristic of feldspar containing spherulites forming denser center and porous outer areas, is even more noticeable. The composition ranges from calcium rich andesine, anorthoclase, albite to Na sanidine. In M6, the dense matrix is different. Here the potassium feldspar forms the groundmass, holding together feldspar and pyroxene . The composition of the feldspars therefore reaches from labradorite and andesine to potassium and calcium rich anorthoclase and Na-sanidine. The pores in this section are not disseminated in the matrix, rather forming large pores and cavities along fractures. M7 is similar to M2 for the most parts. The randomly orientated feldspars and SiO_2 crystals form the porosity. The feldspars are composed of bytownite, labradorite, andesine, sanidine and Na-sanidine. Melt fragments in one area show similarities to M6. Around some pores even idiomorphic SiO_2 minerals can be found (figure 46 E). Additionally to the SiO_2 in the matrix of M8, feldspars of Na- sanidine with different composition occur. The microstructure is similar to M7. M9 feldspar is again similar to M6, compositionally and in terms of microstructure. Feldspars of labradorite, potassium and calcium rich anorthoclase and Na-sanidine with high calcium content together with pyroxene form fine bars in the SiO_2 groundmass with nearly no pores visible. M10 fits into the group of M6 and M9, the only difference is the lower potassium content in the feldspars.

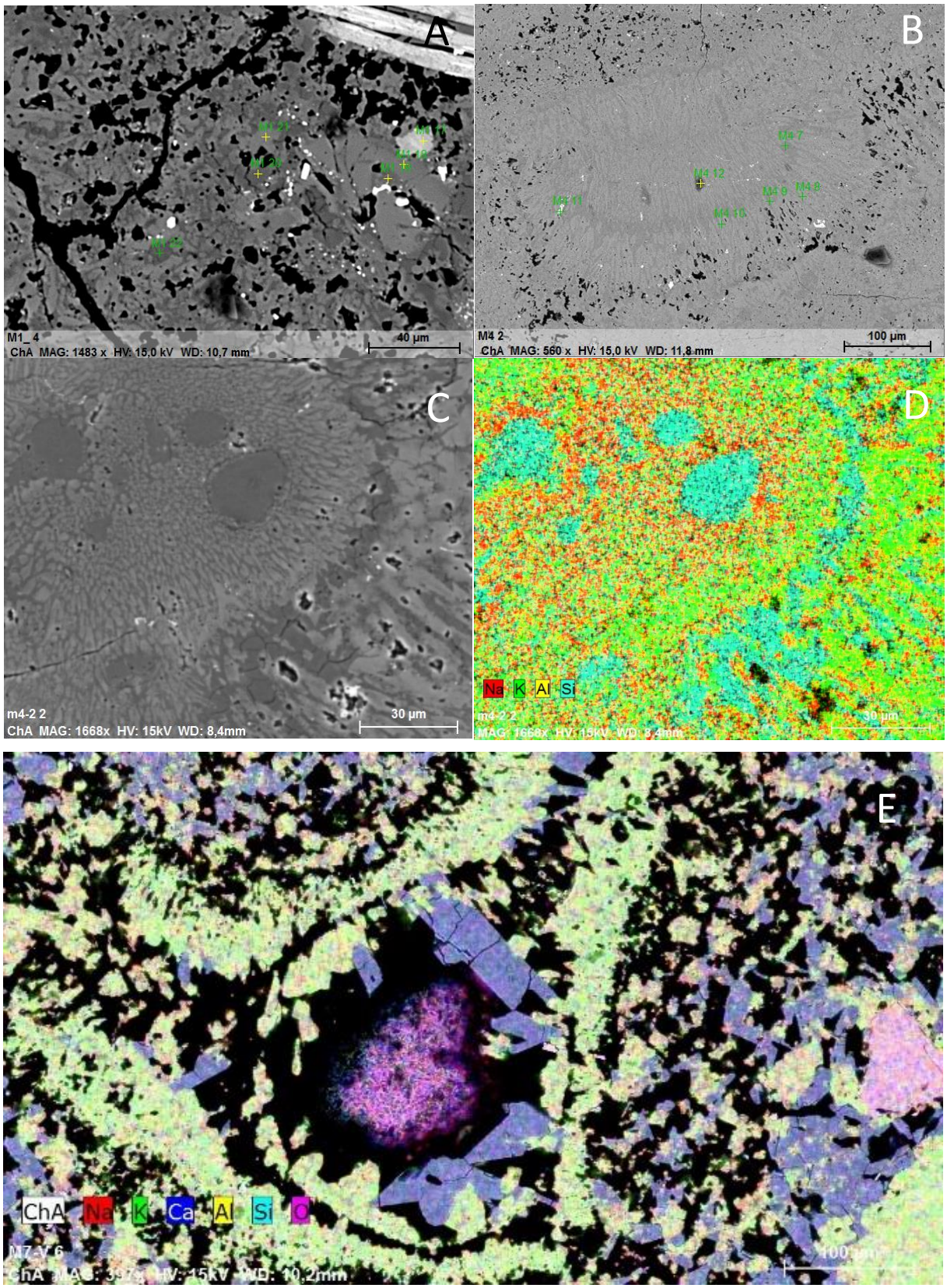

Figure 46: Highly porous matrix in M4 with a collapsed vesicle and spherulitic and fan devitrification (all measurements) in BSE and element mapping [A-D], mineral growth in a pore (red Na-center is a wrong detected element signal due to the pore size) [E]

Biotite

The biotite has been found in samples M 1, 2, 3, 4, 7 and 8. The composition is relatively homogeneous, nevertheless slight compositional differences can be found. Taking the general biotite/mica formula $XY_3(Si,Al)_4O_{10}(OH,Cl,F)_2$ (Markl 2015), the X position is mostly filled with potassium leading to 0.96-0.75 K pfu. The highest potassium values have been measured in the sample M1 with 0.85-0.96 K pfu, while the others show mostly values around 0.75 K pfu, except for three measurements in M 3, M4 and M7, where values of 0.88 K pfu are reached. The missing positions in X are filled by sodium (0.0-0.24 Na pfu). The Y position is filled with iron and magnesium for the most part. Strong variations in the Mg/(Mg+Fe) ratio can be found, the lowest measured in M2 (Mg/(Mg+Fe) =0.47) and the highest in M8 (Mg/(Mg+Fe) =0.70) Additionally, the Y position contains titanium and some manganese. Titanium is present in all biotites and ranges from 0.20-0.39 Ti pfu. Manganese on the other hand is only present in M1 and M2 and ranges from 0.06-0.45 Mn pfu. By applying these values to the biotite classification diagram after Rieder et al. (1998), the minerals are classified as biotites (figure 47).

The position of OH^-, F^-, and Cl^- is mostly filled with OH^-, except in M3, 4 and 8, where significant amounts of F^- can be found (0.34-0.78 F pfu). Cl^- is rarely detected and has lower values, reaching from 0.014-0.024 Cl^- pfu in the samples M1 and M4 (appendix 10.3.4).

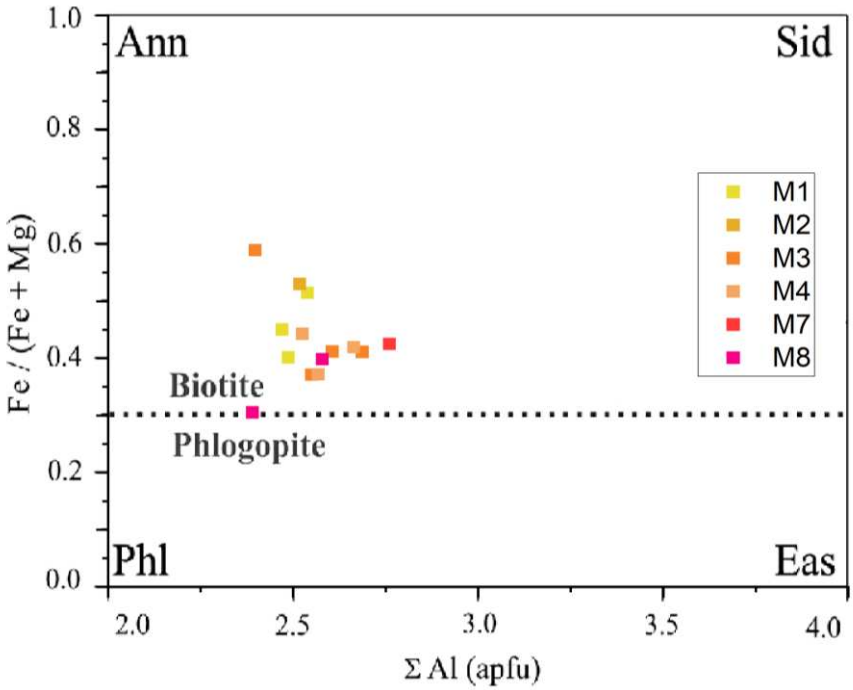

Figure 47: Classification diagram for biotite after Rieder et al. (1998) in Bhattacharya et al. (2014), with the measured biotite compositions.

Amphibole

Amphiboles have been found in all samples except M7 as phenocrysts (figure 48). Using the occupation by elements on various sites in the general amphibole formula $A_{0-1}B_2C_5T_8O_{22}(OH, F)_2$, the mineral name can be determined. Therefore, the positions are filled from T towards A. The T-position is filled with Si and Al, excess Al is used for the C-position, together with Mg, Fe, Mn, Ti. Excess Fe, Mg is also incorporated in the B position and can then be used with Ca and Na for the classification into the amphibole groups. In all samples the necessary requirements for a classification into the calcium amphibole group are met ($\sum$ (Mg, Fe^{2+}, Mn^{2+}, Li) ≤0.50 pfu, ^{B}(Ca, Na) ≥ 1.00 and ^{B}Na <0.50 pfu (Deer et al. 2013). Therefore, different graphs can be used for the determination of the mineral name. According to Deer et al. (2013), the variation of Na and K in the A position with the Si pfu on T can be used. Leake et al. (1997) provide more detailed information on nomenclature.

While determining the mineral names, it becomes clear that the individual samples differ in their amphibole composition. M1 contains only pargasite and is therefore Mg dominated in the C position. In contrast, M2 consists of pargasite, edenite and magnesio-hornblende. In the diagram after Deer et al. (2013) it is visible, that the magnesio-hornblende of M2 is on the border to edenite, and therefore very similar in composition. The pargasite on the other hand is also on the border to edenite, but its composition differs significantly. Noticeably also the texture of the different amphiboles varies. While the edenite and the magnesio-hornblende have straight edges, the pargasite is rounded (figure 48).

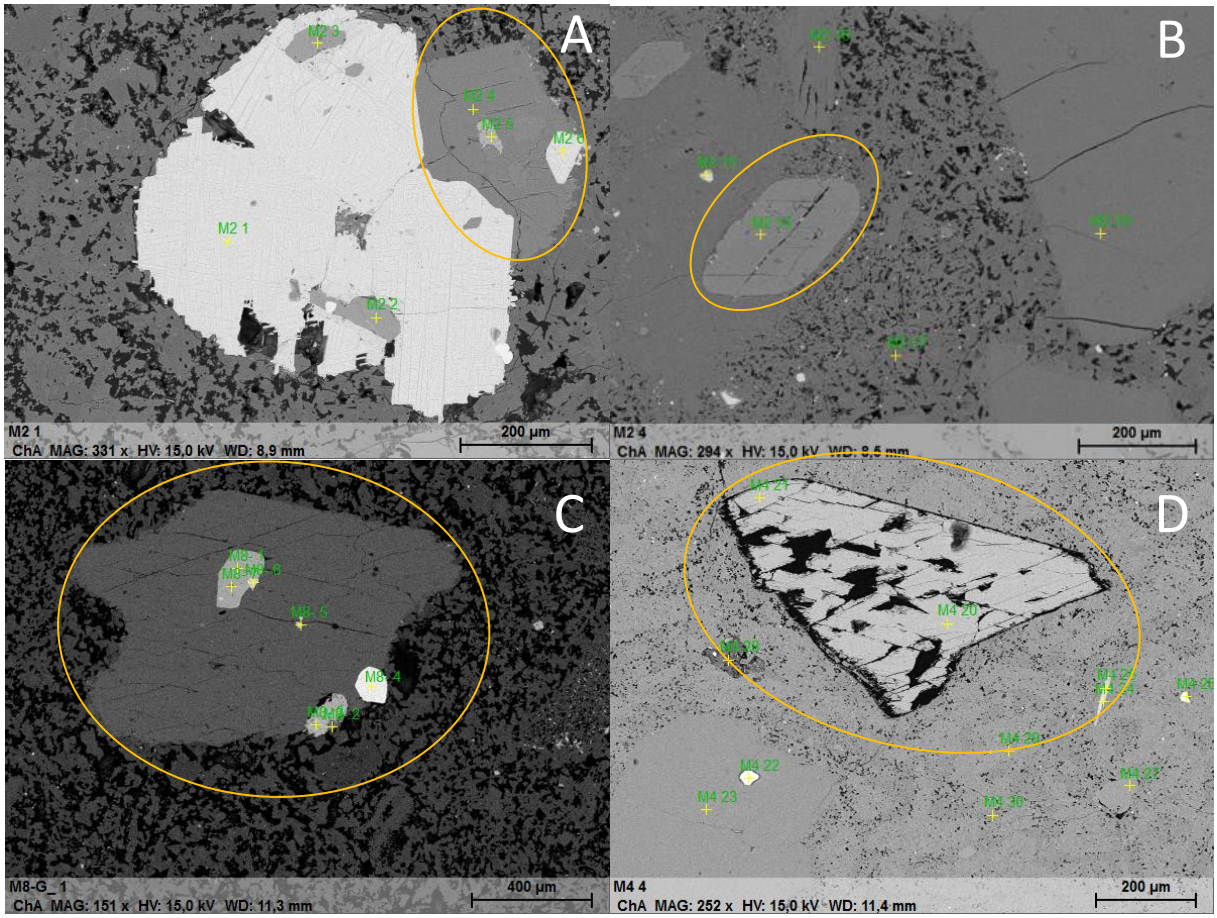

Figure 48: BSE image of different occurrences of amphibole in different samples (M2, M4 and M8), from rounded to broken and intergrown [A-D]

The amphiboles of M3 do not show a variation as strong as the amphiboles of M2. Here only magnesio-hornblende of similar composition is present, showing partly intergrowth with Fe-oxides.

Additional to a similar composed magnesio hornblende like M3, M4 contains edenite. Like in M1, the edenite is similar in composition to the magnesio-hornblende. Both measurements were made in different areas of the same crystal.

Sample M6 contains more amphibole than the samples before. Most of the amphiboles are pargasites, except two measurements that are classified as edenite and tschermakite. Single crystals show chemical variability, e.g. edenitic and pargasitic compositions within a single grain.

Sample M8 only contains magnesio-hornblende, but with a larger compositional range, almost being tremolitic in composition. Besides also magnesio-hornblende bordering the edenite field is present.

The amphiboles of sample M9 show a wide range of composition, comprising nearly all members of the calcic amphibole family from magnesio-hornblende, edenite, tschermakite to pargasite. As seen in figure 49 A the inner center of one crystal is pargasite, while the outer edge is tschermakitic in composition. Tschermakite is also present in other crystals, having a dark reaction rim. The magnesio-hornblende is often in a poor condition, with a high amount of iron oxide inclusions (figure 49). In sample M10 pargasite is the dominant amphibole. Besides, a few edenites and a magnesio-hornblende occurs. Similar to M9, edenite and pargasite are detected in different areas of the same or intergrown amphibole crystals. Noticeably the amphiboles have straight edges and no visible reaction rim in the SEM (appendix 10.3.3).

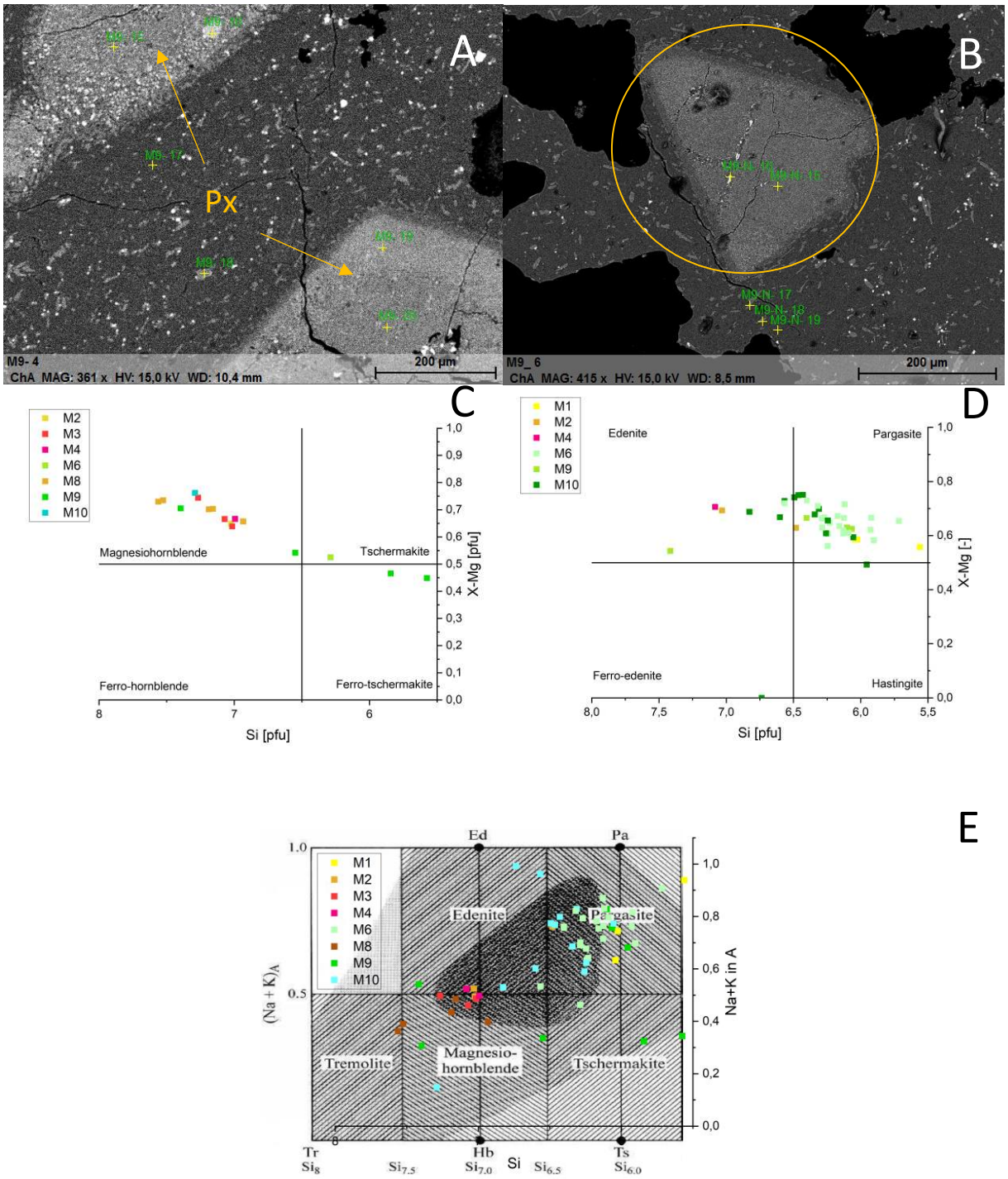

Figure 49: BSE images of occurrences of amphibole as phenocryst (M9-15,-16, -19, -20 &M9-M9-N-15 & -16) and measurements of the matrix (pyroxene and feldspar) [A and B] and the classification for calcic amphiboles after Leake et al. (1997) [C and D] and Deer et al. (2013) [E].

Pyroxene

Pyroxene is less common than amphibole. Except for samples M6, M9 and M10, only two crystals of pyroxene have been found, one in M1 and one in M2 (appendix 10.3.2). Noticeably

both are in bad condition, especially the one in M1. Looking at the analytical data, a compositional difference can also be found. While the pyroxene of M2 is classified as augite, almost diopside, the pyroxene of M1 is enstatite with Mg/(Mg+Fe) =0.69.

In the samples M6, M9 and M10 pyroxenes occur frequently. As in the previous samples the pyroxenes can be divided into groups:

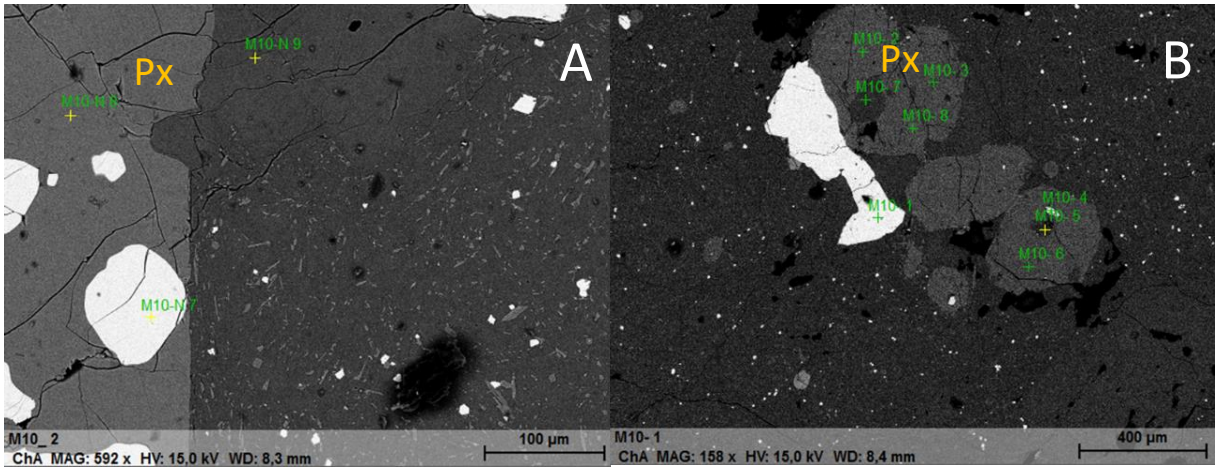

Figure 50: BSE images of the different pyroxenes in M10 [A and B] (pyroxene measurements: M10-N-8 [A]; M10-2 to M10-6 & M10-8 [B]

In M6, three groups of pyroxenes are present: (I) diopside, (II) augite-pigeonite at the field-boundary reaching 0.25 Ca pfu, 0.48 Mg pfu and 0.80 Fe pfu; and (III) enstatite, similar to the one found in M1 (Mg/(Mg+Fe) =0.66). In sample M9, enstatite, pigeonite on the border to enstatite, and diopside are encountered. In contrast in M10 phenocrysts only occur with enstatitic composition (figure 51).

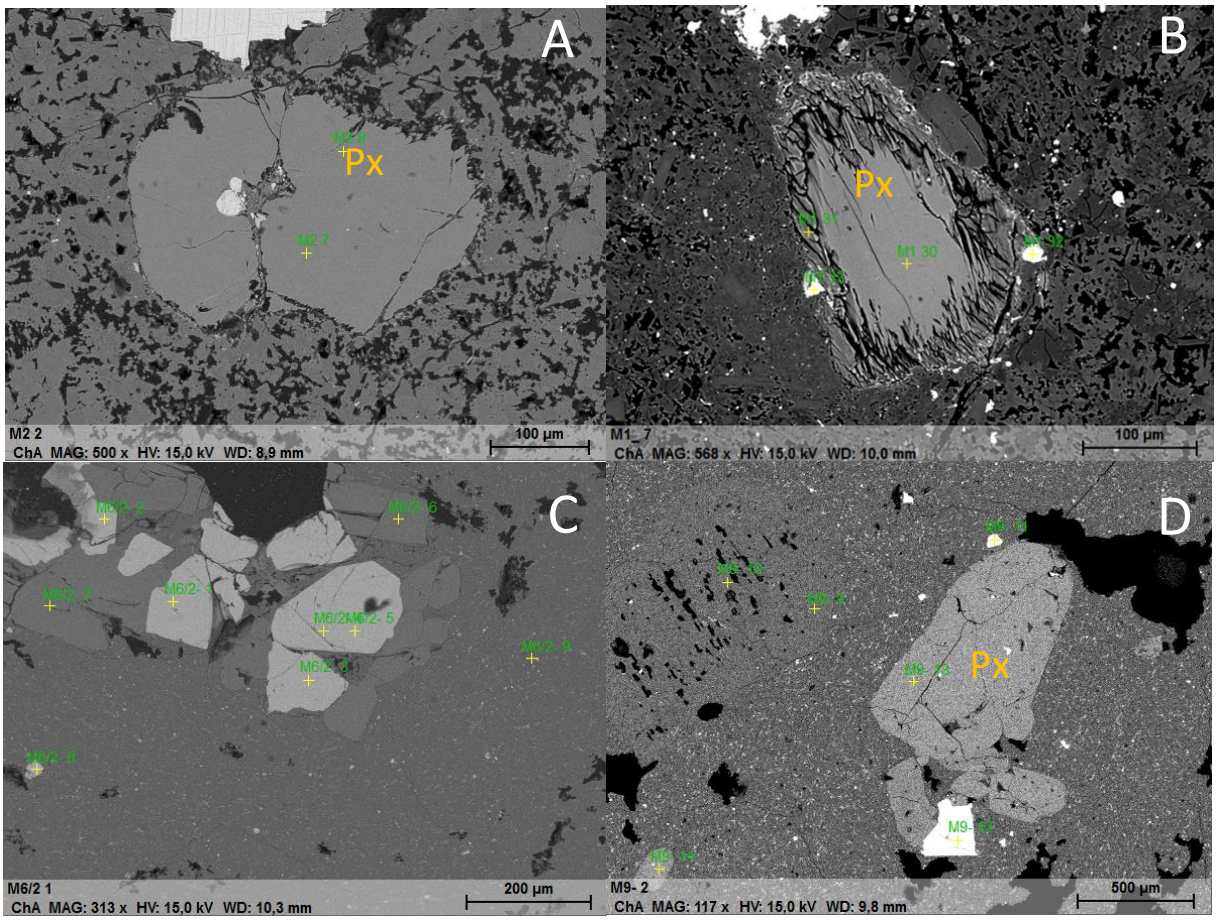

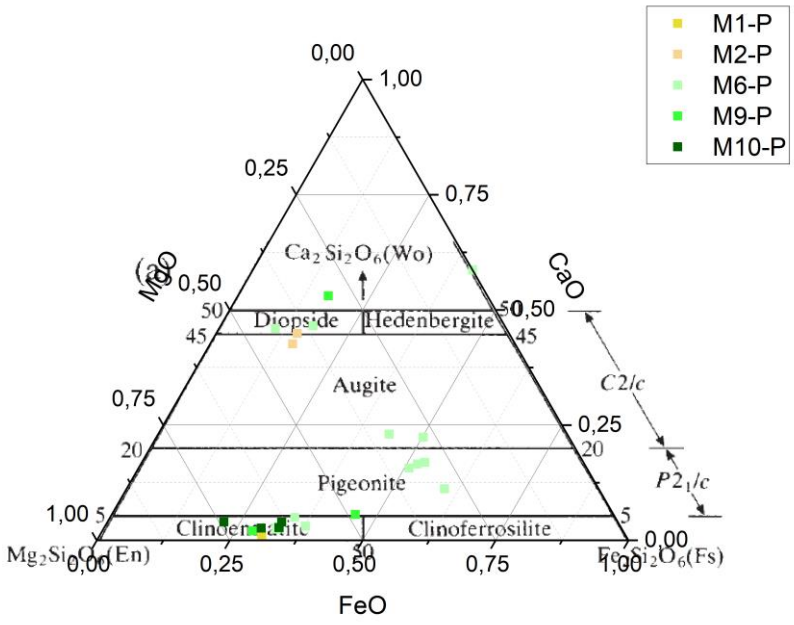

Figure 51: BSE images of different textural types of pyroxene, as phenocryst and in the matrix [A-D] Classification diagram (Morimoto (1988) in Deer et al. (2013)) with compositions of phenocrysts (MX-P) [E];

Pyroxenes are not only present as phenocrysts in M6, 9 and 10, but also in the matrix as fine mineral laths (figure 52 A & B). Here it can be seen that in the matrix of M6 only pigeonite and enstatite are present forming a cluster with calcium rich pigeonite, enstatite and calcium poor, iron enriched pigeonite. In M9 diopside, even reaching into the field above, and augite with only slight compositional variations occur. M10 contains diopside, augite, pigeonite and enstatite. The enstatite and pigeonite form a trend reaching from the central enstatite into the central pigeonite field.

Taking into consideration both, matrix and phenocrysts, two major groups can be determined. The pigeonite-enstatite containing group, following a trend from the central enstatite to the central pigeonite field and the diopside- calcium rich augite containing group (figure C & D).

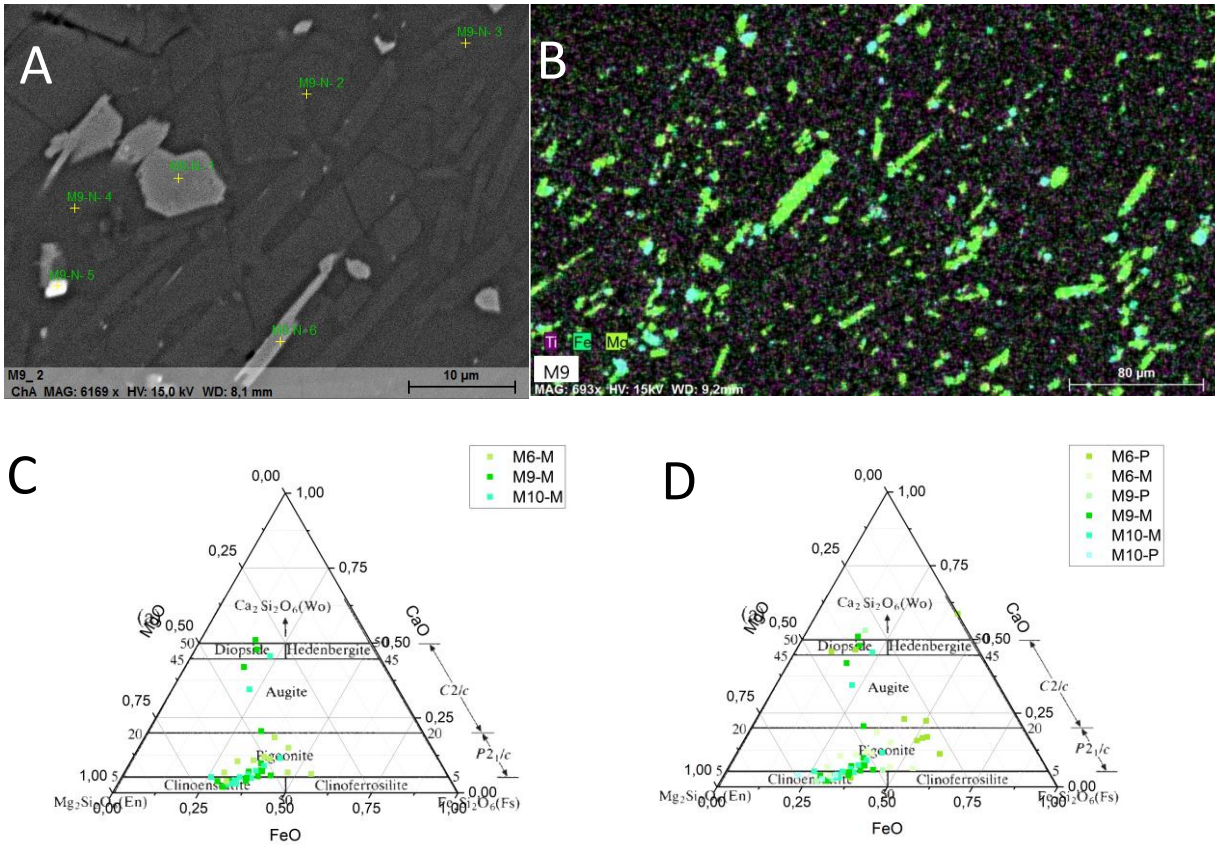

Figure 52: The fine matrix pyroxene in BSE image [A] and on a combined Ti-Fe-Mg element map [B] in sample M9. [C] Classification of the matrix pyroxenes (MX-M) after Morimoto (1988)in Deer et al. (2013) [D] Classification of all pyroxene data (P-phenocryst, M-matrix)

Apatite

In all samples except M4 and M9 apatite has been identified. Apatite is very homogeneous, but contains variable amounts of Cl and F. While F is present in all measured apatites (0.34-1 F pfu), Cl is not present in all. Chlorine was not detected in M1, M6 and M7, but in the other

samples maximum values 0.20 pfu (in M10) are reached. One crystal in M1 also contains small amounts of REE like Ce and Nd. In other samples no REE in apatite has been measured.

Zircon

Zircon has been found in M1, 3 and 8, showing typical compositions ($ZrSiO_4$). In one crystal of M1 also small amounts of Hf, U and Th have been measured.

REE-minerals

By its BSE brightness, REE-minerals are quite easy to locate. Here, one REE mineral has been found. For crystals of that size, one has to keep in mind, that surrounding areas influence the measurement as well (figure 53). Rare earth element minerals are present in M1, M2 and M3. All are similar in composition, except the one of M1 having lower Ce, Nd and Ti values, but therefore higher La values. The minerals are located within a plagioclase or silica rich matrix and are intergrown with zircon, apatite and magnetite. Based on the EDS analysis, it is possible that the mineral is part of the chevkinit-group ($(REE,Ca)_4Fe^{2+}(Fe^{2+},Fe^{3+},Ti)_2Ti_2(Si_2O_7)_2O_8$) (Macdonald et al. 2019). The oxide concentrations of the rare earth elements are Ce_2O_3 13.4 %, 7.9% La_2O_3 and Nd_2O_3 2.2% (M1). Beside the REE, also 1.98% ThO_2 have been measured. In samples M2 and M3, REE-minerals contain 5.65-7.32 % Nd_2O_3 and 20.58-23.54 % Ce_2O_3. No La_2O_3 has been detected. The measurements show stable concentrations of SiO_2 (17.3-18 oxide%) and for most measurements TiO_2 (22.44- 24.70 oxide%).

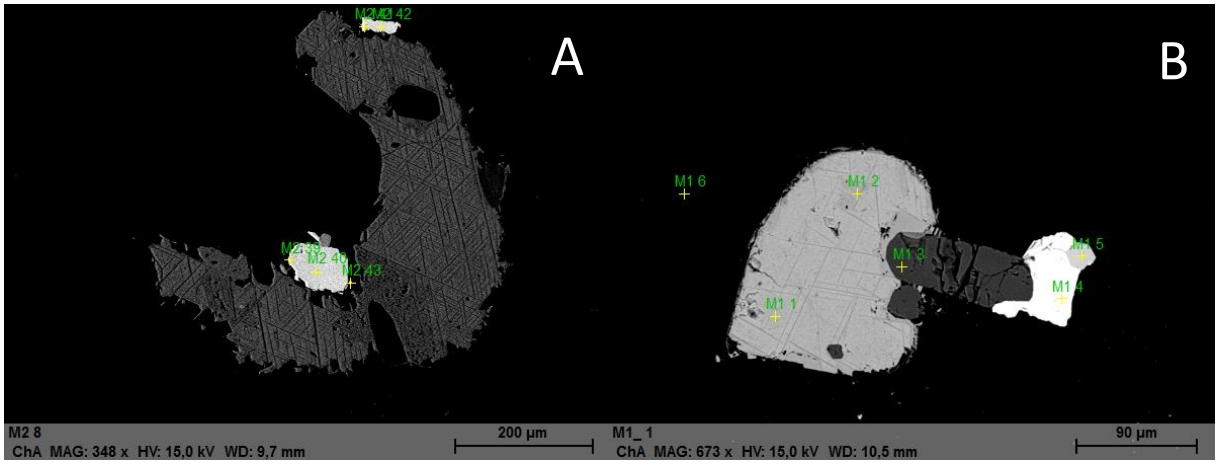

Figure 53: BSE image of the intergrown of REE-minerals, magnetite, apatite and zircon in M2 [A] and M1 [B]

Magnetite

Magnetite is present in all samples with differing substituting elements. Additional to the almost omnipresent Ti, Mn, Mg and Al are also common. In some minerals in samples M1 and M7, vanadium has also been measured. The magnetite has ilmenite lamellae (figure 54), but in the measurements the surrounding magnetite often led to impaired results, especially if

the magnetite was already decomposed. The additional element contents are variable. Magnesium ranges between 0-0.38 pfu in M6, M7, M9 and M10. The Al content is also between 0-0.49 pfu, with the highest values in M6 and M7. The highest manganese values can be found in M2 and M7 reaching 0.14 pfu, while the titanium reaches 1.64 pfu in the ilmenite lamellae (figure 55). The points plotting in between Magnetite and hematite in figure 55, are probably mixed analysis or are caused by the Fe^{3+}-correction.

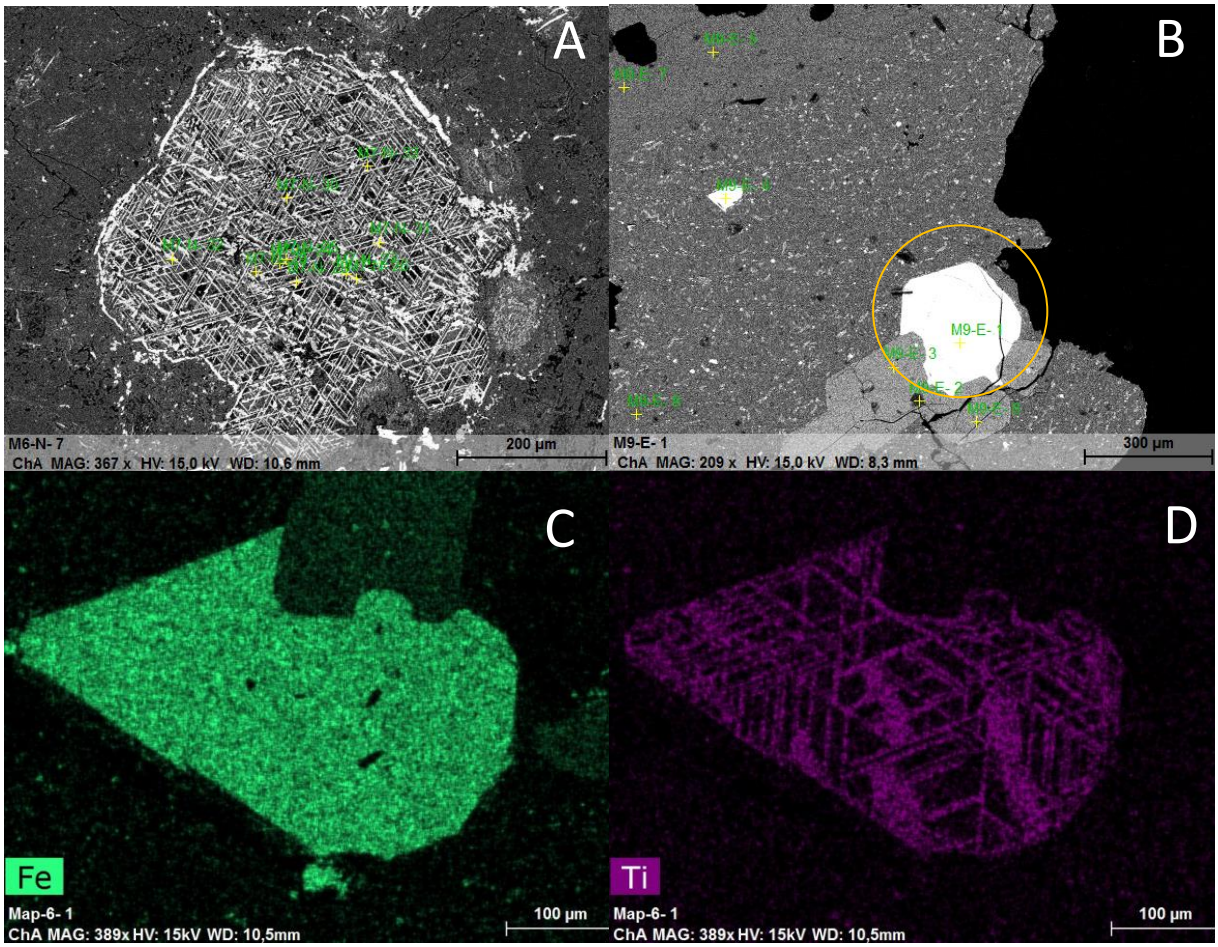

Figure 54: BSE image and mapping of magnetite (Bright areas) in samples M6 and M9, with [A, C and D] and without lamellae [B], oxidized and non-oxidized

One phase is difficult to identify. One reason for that is the bad condition. The measurements show an element combination unknown as a mineral, but based on the surrounding minerals, it is likely that this measurement represents a mixed measurement with vanadium containing magnetite and secondary vanadium-iron phase surrounding it. This phase has only been observed in M7 (table 1).

Table 1: Oxide-% of the secondary phase and vanadium containing magnetite

Spektrum	V_2O_5	Al_2O_3	SiO_2	CaO	TiO_2	FeO	MgO	P_2O_5
	oxide %	oxide %	oxide %	oxide %	oxide %	oxide %	oxide %	oxide %
M7_76	1,491	4,033	8,211	3,757	-	57,166	2,726	1,928
M7_77	0,979	2,831	9,245	2,205	1,372	50,747	1,526	1,350
M7_78	0,763	4,878	17,627	2,146	-	45,041	2,435	-
M7_79	0,277	2,064	-	-	9,943	68,657	-	-

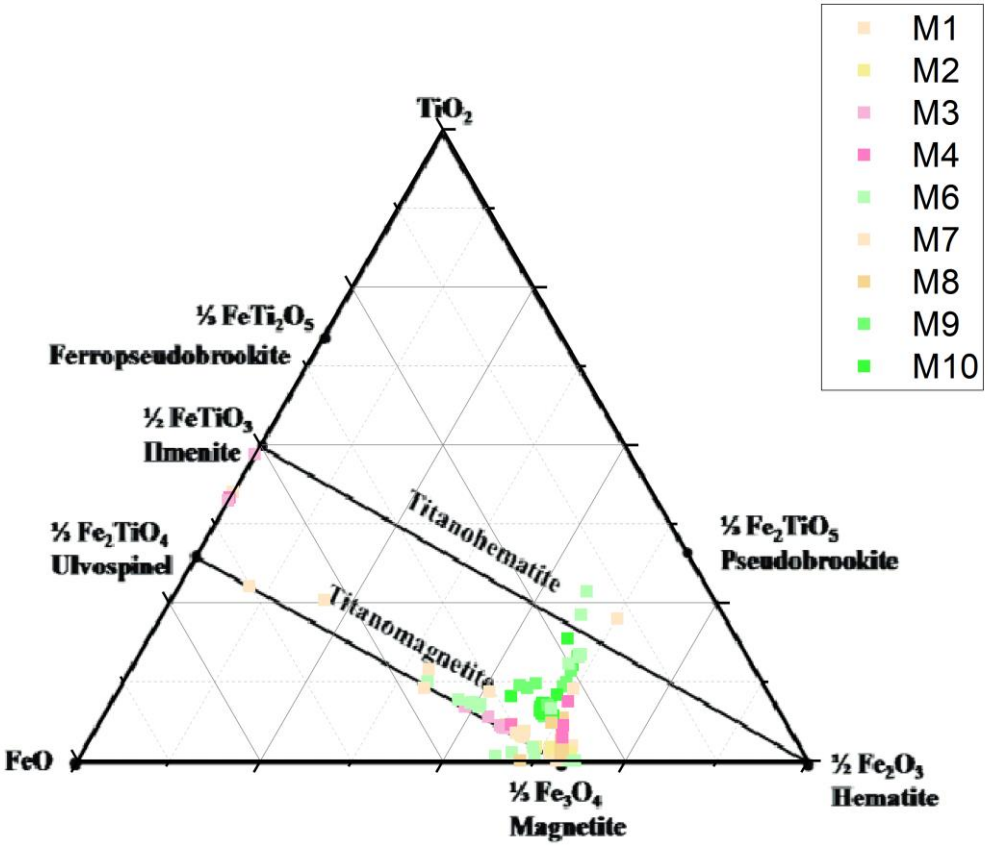

Figure 55: Measured Fe-Ti-oxides after Deer et al. (2013) with the Fe^{3+} correction after Droop (1987), the data between the solid solution lines are probably mixed data or a problem with the Fe^{2+} /Fe^{3+} correction.

4.1.3 Broad ion beam scanning microscope (BIB-SEM)

The main goal of the BIB-SEM investigation was the determination of the fractures, shape and number of pores and the general micro texture. Therefore, for each sample, one area at 4000x magnification and three at 20000 x magnification have been investigated.

M1

In M1 a high number of fine pores can be found (fig. 56 A). The pore size rarely rises above 28 µm. Different kinds of pore shapes are present. Angular pores are defined by fine mineral laths of random orientation forming cavities in between. Secondly, irregular shaped pores exist, which are defined by mineral phases growing into the open pore space. The round shape of these minerals causes a highly irregular branched pore shape. Noticeably areas of coarser matrix tend to form the angular pores, while in the finer matrix area the branched pores dominate. In the BSE image, compositional brightness differences are visible as described in the Scanning electron microscopy (SEM). Of course, there are also pores, which represent a mixture of both types. In some pores the round shapes and mineral phases are growing inside a primary angular shaped pore (figure 56 [A]).

Fractures are rare in M1 and range within a few µm in size (<18 µm) (figure 56 [B]). In most areas the fractures are interconnecting, sometimes with other fractures and something with the pores, independent of their shape. The most fractures occur, seen in the BSE picture as darker areas, which are intergrown with lath shaped minerals and some of the round shaped minerals as well.

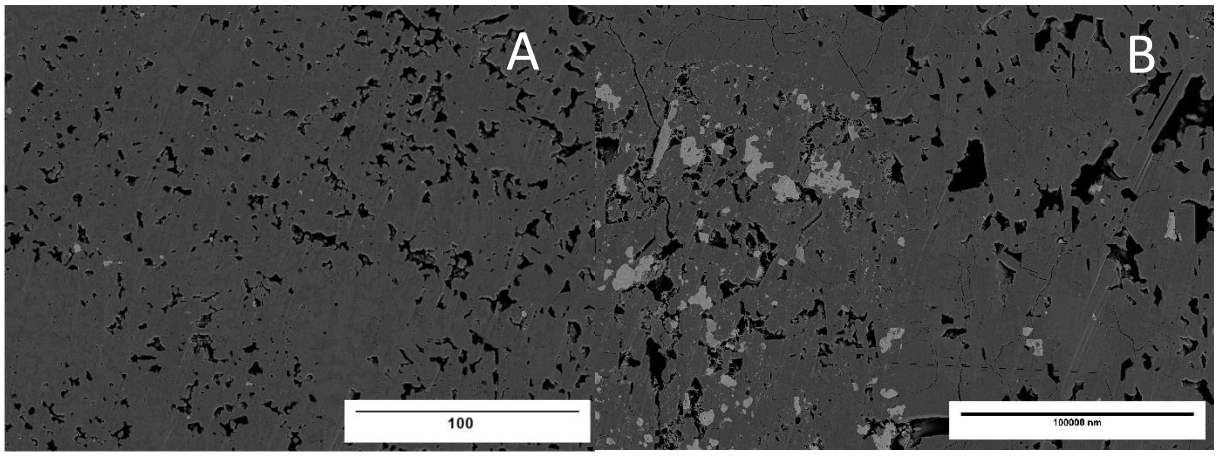

Figure 56: BSE images of M1 with 4000x magnification [A] with denser areas, separated by the pores and 20000x magnification [B] with lath shaped minerals forming the irregular pores

M2 is more porous than M1 (figure 57 A) and the pore shapes are different. The matrix is very similar to M1, the lath shaped minerals are less common and if present, other minerals have

grown on the crystal surface. These crystals are similar to the round minerals (<4 µm) found in M1; additionally, fine flaky to needle-like sometimes even skeletal crystals occur (figure 57 B). These minerals lead to a different shape of the pores, similar to the branched pores of M1. Most of the larger pores (63 µm) are somehow connected, if not directly, then through fine cracks of the same size as in M1. Some micro cracks (13 µm) propagate from pores. Again, most cracks occur mostly in the darker areas in the BSE image. Even some larger cracks are present, from which finer crack propagate. Only the fines pores seem to be isolated.

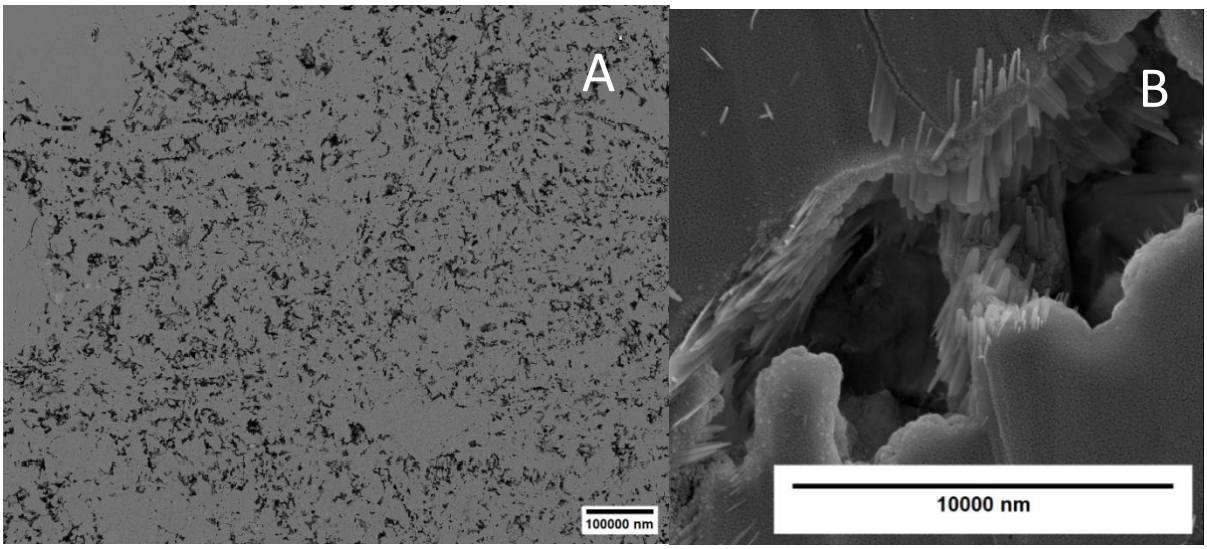

Figure 57: BSE images of M2 with 4000x magnification [A] with denser areas and areas of high porosity with fine minerals in the pore space [B]

M3 differs noticeably from the M1 and 2, as both, the pore size and the number of pores are smaller (<21 µm) (figure 58 A). The pore shape is highly irregular, mostly branched, filled with flaky stacked mineral phases (9 µm) (figure 58 B). Less commonly, round pores have been found. Most of the pores are not interconnected to each other, neither by fractures nor directly. Exceptions can be found, especially in the areas where the rare fractures meet. Here the pores are sometimes even multiply interconnected, forming zones where the rock is barely intact. On a closer look the fractures (400 µm) follow compositional boundaries, visible in the BSE image. As described in the SEM chapter, the matrix is characterized by dark groundmass, spotted with brighter, mostly rounded areas of different composition.

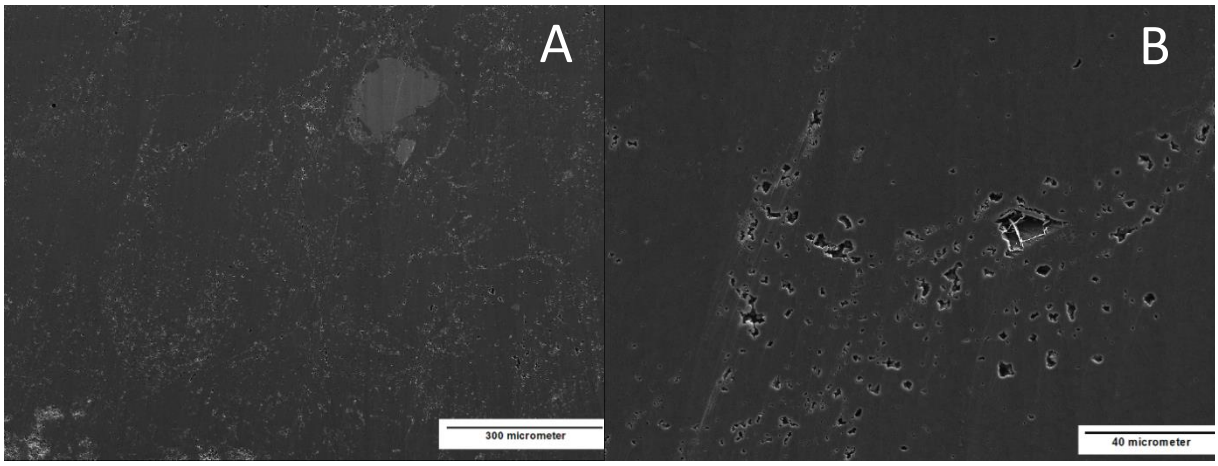

Figure 58: BSE images of sample M3 with 4000x magnification [A] and 20000x magnification [B] of an area of higher porosity with mineral growing in the pore space

In M4, the porosity is higher than in M3, but lower than in M1 and M2. Nevertheless, the pore shape is similar to M3 (<18 µm). The mostly very fine, disseminated pores are irregular branched to spherical in shape, caused by the growth of round mineral phases (3 µm) (figure 59 A). Some pores are overgrown by the round minerals. The pores are mostly not interconnected, except in the area of larger fractures (900 µm). Major fractures are visible, significantly larger than in M3 (figure 59 B). Noticeably also mineral phases precipitated in these fractures but did not close them.

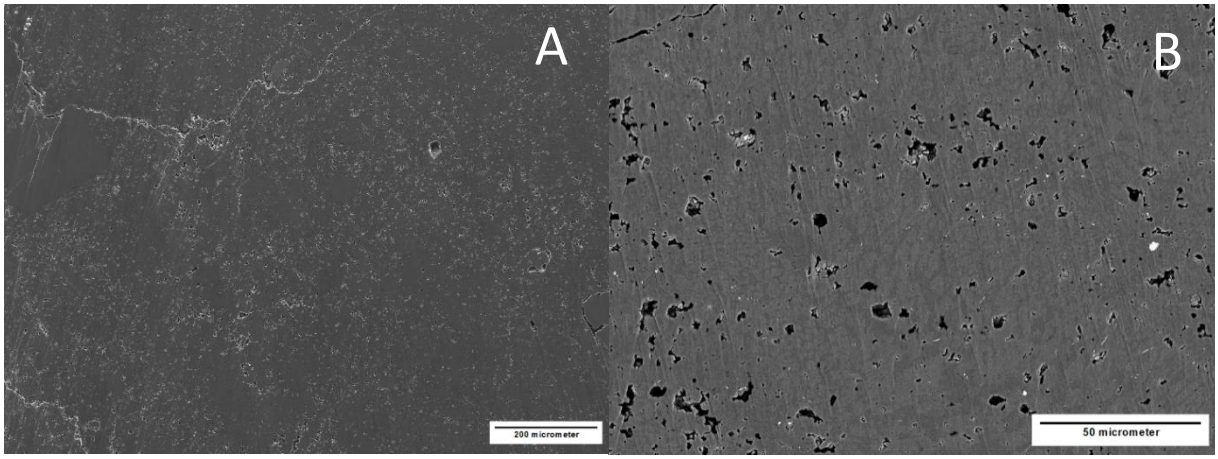

Figure 59: [A] BSE image of sample M4 with matrix of different composition, visible through brighter and darker areas, 4000x magnification; [B] fractures and finer pores at 20000x magnification

Sample M6 has a very low porosity, except in a single capture (4000x), where a higher number of pores can be found. Even if the number is different, the shape of the pores is similar (figure 60 A). The pores are irregular, branched due to mineral growth into the open pore space, forming an even coating of the pore walls (4 µm) (figure 60 B). Some pores are interconnected

through fractures. Larger fractures (280 µm) are rare. Besides, micro fractures occur all over the area in the matrix, mostly following grain boundaries, reaching a length of 37 µm.

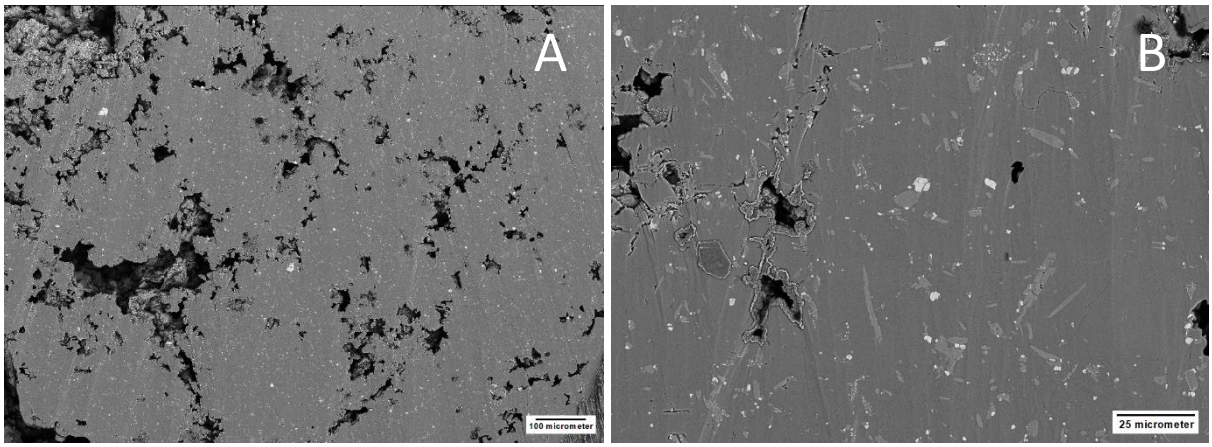

Figure 60: BSE pictures of M6 with 4000x magnification with major, large pores [A] and 20000x magnification [B] of mineral growth in the pores and fine mineral bars in the matrix

M7 is defined by an extremely high porosity. Denser areas of random shape and orientation lead to a high number of irregular pores (100-230 µm) (figure 61 A), highly branched and differing in size. Crystal growth in this pore space is present (4 µm), but less dominant than in M6 or M2. At a closer look, the denser areas have even finer pores, which are not connected to the larger pores. These pores are y shaped, beside many round pores. Fine fractures through the denser areas lead to an interconnection between the larger pores (100 µm) (figure 61 B). Major fracture zones are not visible.

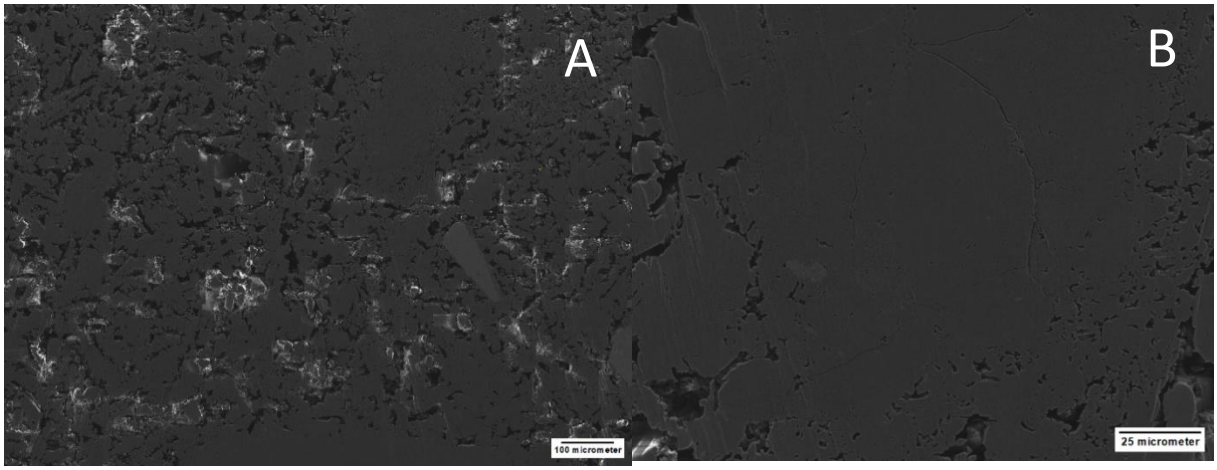

Figure 61: SE images of the highly porous M7 with 4000x magnification [A] and 20000x magnification [B] of a fracture in a denser area of M7

M8 is very similar to M7. Also, here a high porosity can be found (figure 62 A), also irregular shaped. Denser areas form branched pore spaces (<200 µm) with crystal growth inside (8 µm). The pores are also connected by micro fractures (30 µm) (figure 62 B). In contrast to M7, fine

round pores are rare, instead fine disseminated bright spots can be found, often keeping a distance of 5-10 µm to the pore space in the BSE. Again, major fracture zones are missing.

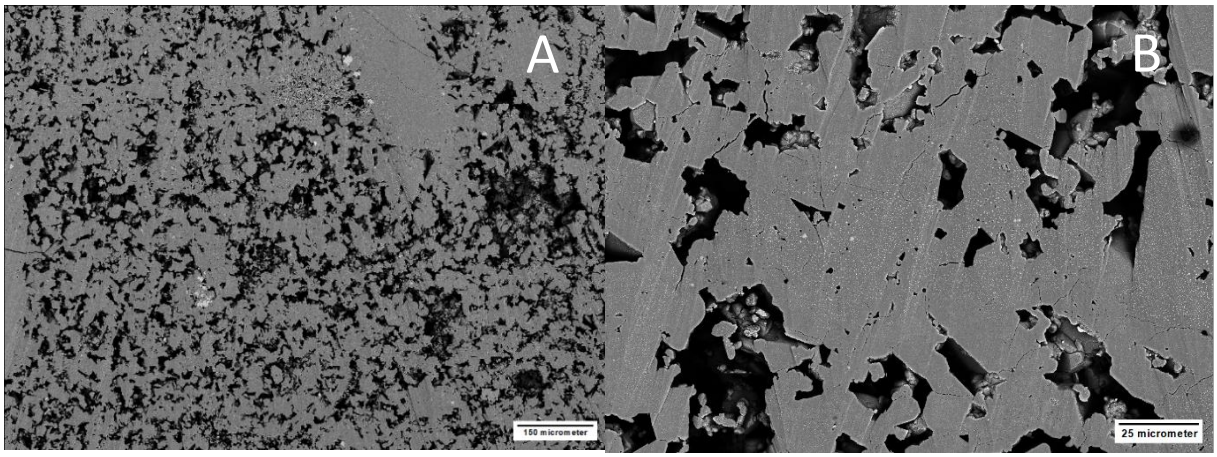

Figure 62: BSE images of M8 with 4000x magnification [A] and 20000x magnification with the highly reflecting, finely dissimilated, bright phase [B]

M9

M9 is very similar to M6. The porosity is limited to a few major pores (<350 µm) (figure 63 A), irregular and branched in shape, caused by an intergrowth of mineral phases (17 µm) into the open space. These larger pores are interconnected by many fractures (>1000 µm), propagating from the pore spaces and meeting in between the pores. Where fractures intersect, sometimes smaller fractures propagate even further. Other microcracks follow compositional boundaries in the matrix. Also, fractures are visible in this matrix, ending in the almost sponge-type structures (figure 63 B), in a highly fractured area. Noticeably only in this area crystals have crystallized in the fracture. Beside those, fine fractures can be found all over the areas, often around 10 µm in length.

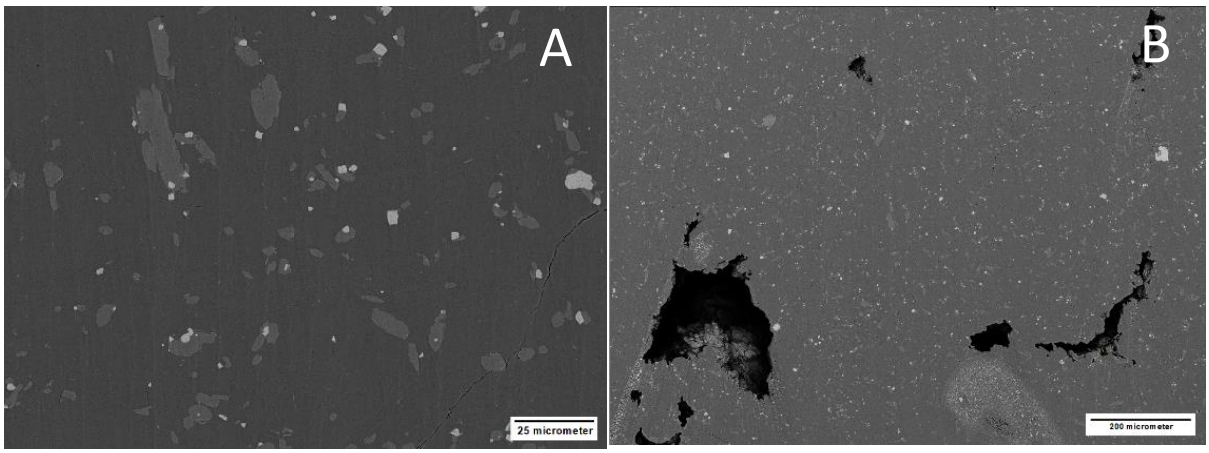

Figure 63: BSE images of M9 with 4000x magnification [A] with major large pores and 20000x magnification [B] of dens matrix with mineral bars and microfractures

M10

M10 is very similar in terms of porosity to M6 and M9. Here also, a small amount of larger irregular pores (200 µm) with intergrowing mineral phases (<16 µm) are interconnected by fractures (500 µm) (figure 64 A), which are, if opened wide enough, filled with a fine round mineral phase. Smaller fine fractures (14 µm) (figure 64 B) are present in the whole area as well. In M10 also a denser area is present that is more fractured than the rest of the area.

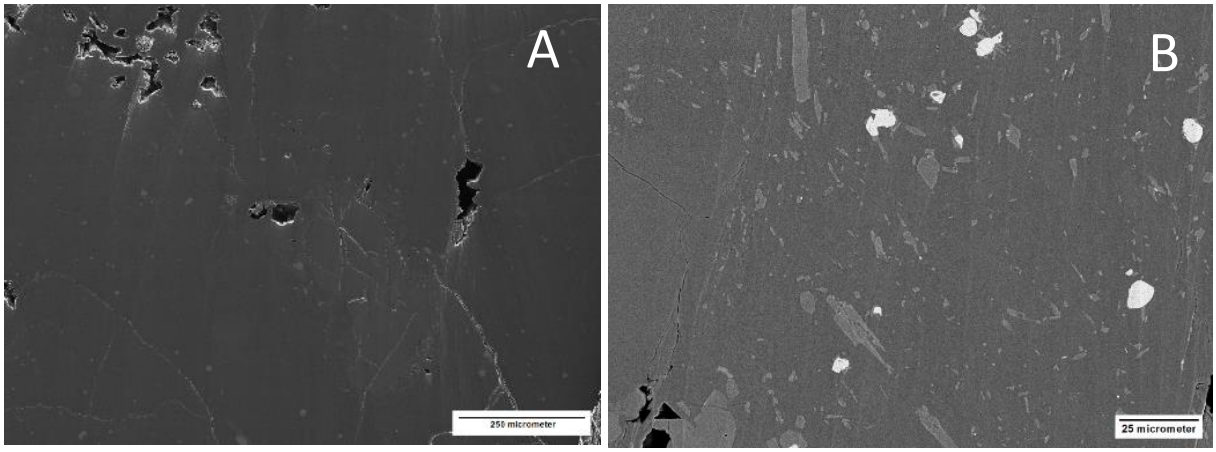

Figure 64: BSE images of M10 with 4000x magnification with a phenocryst with microcracks [A] and 20000x magnification [B]

4.1.4 X-ray fluorescence (XRF)

The chemical bulk rock composition of each sample is determined by XRF analysis. The complete XRF results are displayed in table 1.

General overview

The XRF data show that in terms of composition the samples can be divided into two groups. Group one consists of samples M1, M2, M3, M4, M7 and M8 (G1), while group two contains M6, M9 and M10 (G2).

Looking at the SiO_2 concentrations, the difference is already evident. The samples in group one reach from 74.30–75.50 %, while those in group two reach a maximum concentration of 62.04 %. Similar to the SiO_2 is the K_2O with <4.75 % in group one and <3.24 % in group two.

For the Al_2O_3 content, the relation is reversed, higher values are present in group two with 17.45 % in M9. Group one on the other hand reaches a maximum value of 13.74 % in M7. A similar observation can be made regarding CaO (G1: < 0.99 %; G2: <5.53 %), TiO_2 (G1: < 0.14 %; G2: <5.53 %) and P_2O_5 (G1: < 0.04 %; G2: <0.27 %) contents. An even stronger difference is visible by looking at the Fe_2O_3 and MgO concentrations. While group one reaches 1.49% max. Fe_2O_3, in group two, values of 5.23-6.10 % are common. Regarding the MgO content, the

difference becomes even more noticeable, because in group one all values are below 0.01 %, while reaching 2.33 % in M10 for group two.

No major differences can be seen in the Na_2O and MnO contents. Na_2O is on average slightly lower in group one (3.98%) in comparison to group two (4.02%), as for MnO with 0.06 % in group one and 0.08% in group two.

Regarding the trace elements, it becomes clear that the measured trace elements can be divided into the ones that are increased in group one and the ones increased in group two. The only exception is La, where the values range from <42 to 72 ppm for both groups.

The trace elements of group one with higher contents compared to group two, are Ce, Nb, Pb, Rb, Th and Y.

Contrary, the trace elements with higher contents in group two compared to group one, are Ba, Co, Cr, Cu, Ga, Sr, V, Zn and Zr; most prominent are Ba, Sr, V and Zr.

Table 2: Results of the XRF analysis normalized to the loss on ignition

		M3	M4	M2	M7	M8	M1	M9	M6	M10	
Sum	%	98,043	98,478	98,329	99,945	98,836	98,902	98,114	97,653	98,590	
∑+loss on ignition		98,616	99,211	98,779	100,422	99,285	99,288	99,120	98,802	99,343	
SiO2	%	74,464	74,231	73,954	75,129	74,365	74,854	61,416	61,084	59,788	
TiO2	%	0,124	0,133	0,135	0,141	0,135	0,121	0,664	0,672	0,729	
Al2O3	%	13,031	13,256	13,424	13,678	13,467	13,263	17,185	17,246	17,281	
Fe2O3	%	1,149	1,476	1,240	1,272	1,243	1,109	5,257	5,171	6,051	
MnO	%	0,032	0,024	0,075	0,062	0,077	0,074	0,079	0,078	0,094	
CaO	%	0,666	0,795	0,839	0,985	0,832	0,734	4,664	4,701	5,490	
MgO	%	<0.01	<0.01	<0.01	<0.01	<0.01	<0.01	1,527	1,473	2,316	
Na2O	%	3,857	3,952	4,046	3,918	4,062	4,031	3,889	3,965	4,202	
K2O	%	4,694	4,580	4,583	4,723	4,623	4,692	3,205	3,034	2,368	
P2O5	%	0,026	0,031	0,033	0,037	0,032	0,025	0,229	0,228	0,270	
Ba	ppm	617,079	695,563	686,653	737,756	727,868	703,057	1042,402	994,473	937,645	
Ce	ppm	72,334	100,093	117,438	79,641	90,718	129,385	77,854	84,192	73,019	
Co	ppm	<7	<7	<7	<7	<7	<7	13,041	10,988	15,634	
Cr	ppm	<8	<8	<8	<8	<8	<8	16,158	11,700	28,150	
Cu	ppm	<7	<7	<7	<7	<7	<7	49,786	50,731	71,611	
Ga	ppm	17,711	15,395	17,456	17,776	16,179	15,690	21,239	19,810	23,223	
La	ppm	57,272	55,532	44,596	54,590	<42	54,082	<42	70,692	46,449	
Nb	ppm	12,037	11,278	8,187	9,933	10,500	12,086	6,568	6,548	5,979	
Ni	ppm	<4	<4	<4	<4	<4	<4	<4	3,806	11,125	
Pb	ppm	127,796	24,851	86,305	97,682	103,437	92,790	59,560	22,965	44,346	
Rb	ppm	198,835	190,049	189,549	186,252	191,728	196,670	77,915	79,428	46,453	
Sr	ppm	88,231	112,403	116,805	125,540	114,585	97,909	645,833	653,414	803,561	
Th	ppm	40,276	27,925	40,281	26,176	34,372	39,343	9,102	6,951	<9	
V	ppm	14,284	20,978	20,568	14,684	17,181	19,036	97,008	100,996	117,820	
Y	ppm	34,151	32,195	34,820	32,169	33,154	33,330	10,348	13,766	7,013	
Zn	ppm	29,476	29,134	30,890	27,908	28,430	29,119	73,268	77,347	84,692	
Zr	ppm	101,365	116,656	110,142	110,054	116,074	104,745	216,036	217,145	182,047	
loss on ignition	%	0,573	0,733	0,450	0,476	0,449	0,386	1,006	1,149	0,752	

Comparison of trace elements to mantle and crustal compositions

When compared with the average values of the trace elements of the crust according to Markl (2015) and the mantle according to Anderson (1983), it is clearly visible in figure 65, that the values for M1, M2, M3, M4, M7 and M8 mostly fit the values of crust. Nonetheless, a slight increase in La, Nb and Y and a strong increase in Pb, Rb and Th are visible, while Sr and most

noticeably V, Cr, Ni and Cu are depleted. The group of M6, M9 and M10 fits even better to the crust composition; here only slight enrichment of Ba, Ce, Cu, Ga, La, Pb, Sr and Th besides a decrease of Y, Cr and Nis is visible.

The depletion and enrichment trends are even stronger in comparison to the mantle (figure 65).

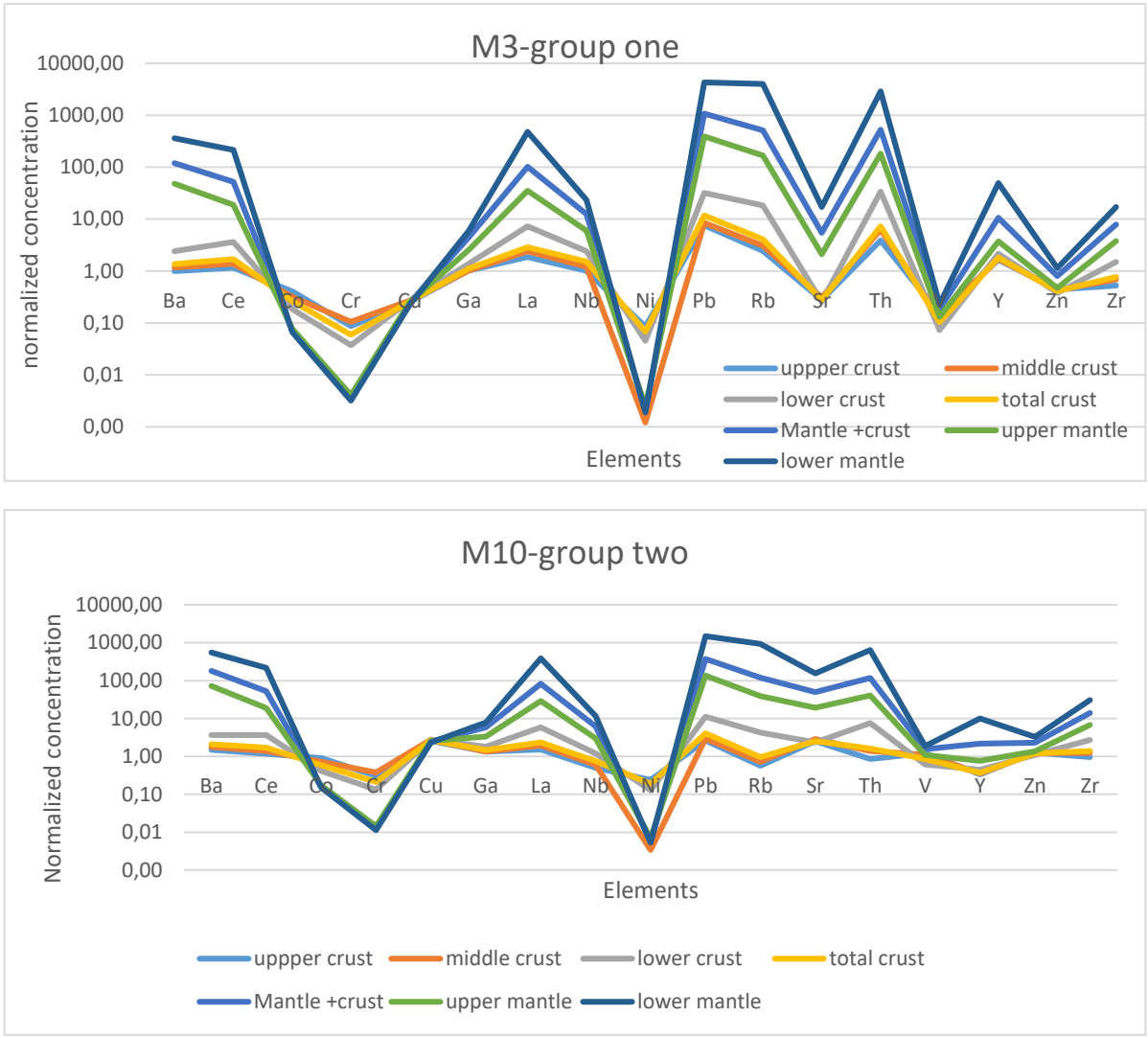

Figure 65: Chemical composition of M3 and M10 normalized to different crust and mantle compositions after (Anderson 1983) and (Markl 2015).

Magma type and tectonic setting discrimination

Total alkali silica diagram

The Na_2O+K_2O value in combination with the SiO_2 content is used in the total alkali silica diagram (TAS) (figure 66) for the determination of the volcanic magma type. Here M1, M2,

M3, M4, M7 and M8 plot in the center of the rhyolite field, while M6, M9 and M10 plot in the trachy-andesite field, close to the border to andesite.

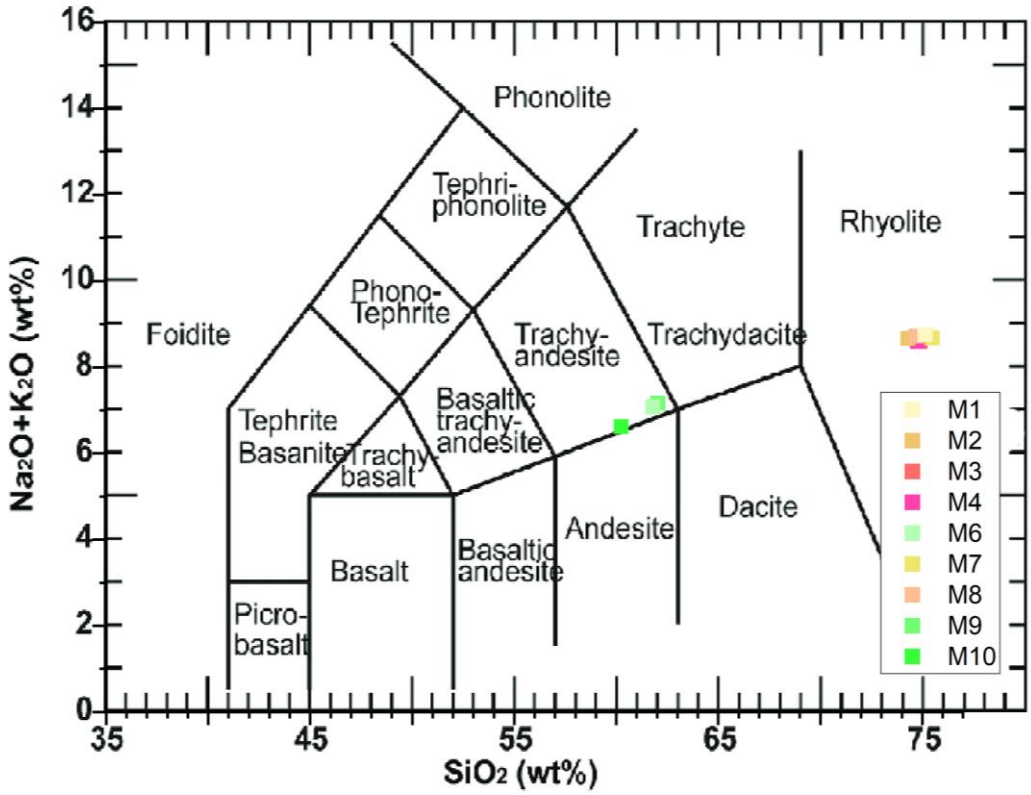

Figure 66: TAS diagram after Vingiani et al. (2014) with analyzed samples

Diagrams after Winchester and Floyd (1976)

Plotting the samples in the SiO_2-Zr/TiO_2 and SiO_2-Nb/Y diagrams, samples M1, M2, M3, M4, M7 and M8 are in the rhyolite field; M6, and M9 plot in the andesite field, bordering the rhyodacite-dacite field in the SiO_2-Nb/Y diagram and the trachyandesites in the SiO_2-Zr/TiO_2 diagram. M10 is different, plotting in the trachyandesite field SiO_2-Nb/Y and in the andesite field in SiO_2-Zr/TiO_2 (figure 67).

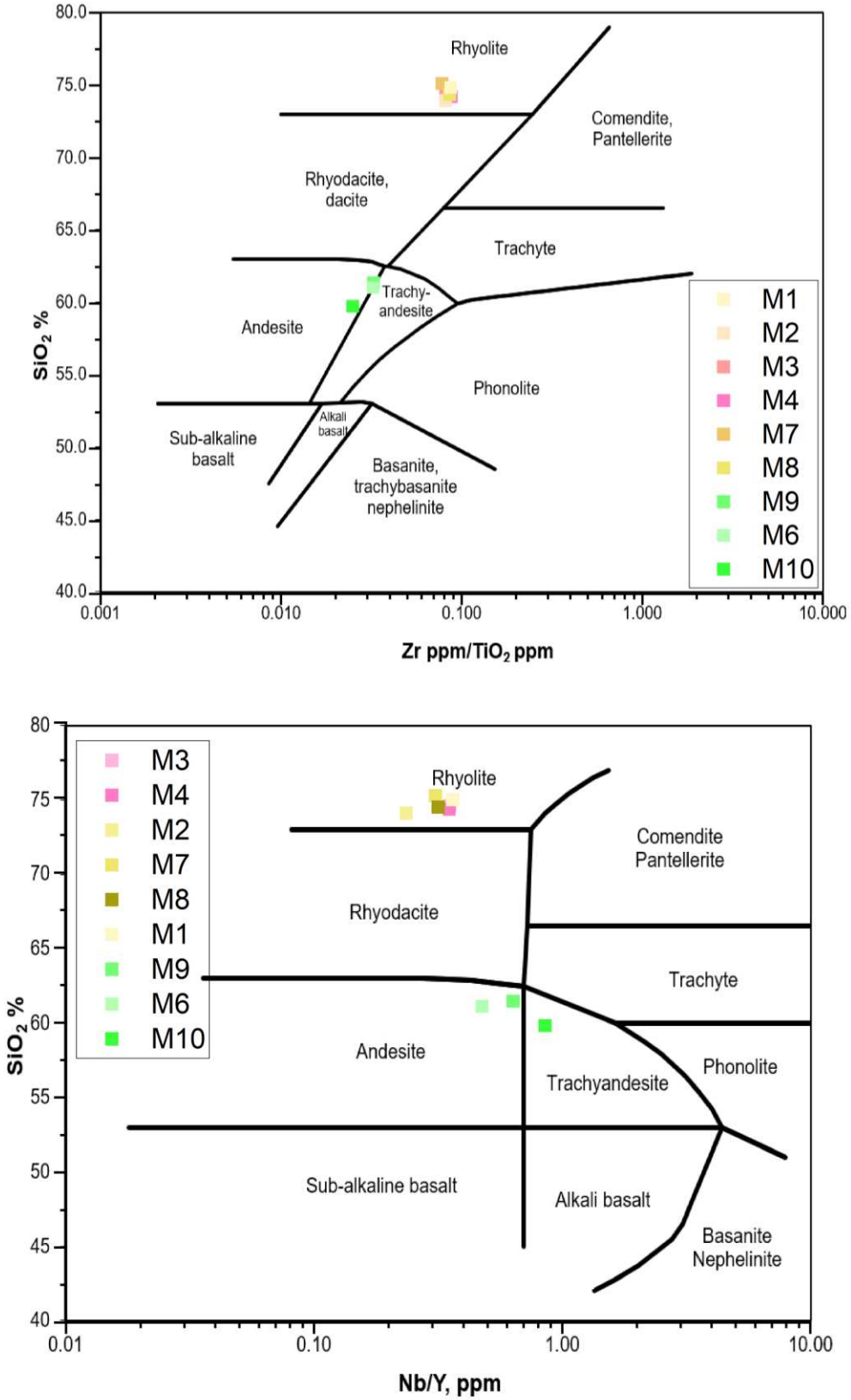

Figure 67: SiO2-Zr/TiO_2 and SiO2-Nb/Y diagrams after Winchester and Floyd (1977) illustrating the sample composition used draft after Kurt Hollocher

When the samples are plotted in the Zr/TiO_2-Nb/Y diagram M1, M2, M3, M4, M7 and M8 are attributed to the rhyodacite-dacite field, with M1, M3 and M4 near the rhyolite field. M6 and M9 also plot in the rhyodacite-dacite and M10 in the trachyandesites. In the Zr/TiO_2-Ga diagram data plot similar to the Zr/TiO_2-Nb/Y diagram with the difference that M1, M4 and M8 plot towards the rhyolite field (figure 68).

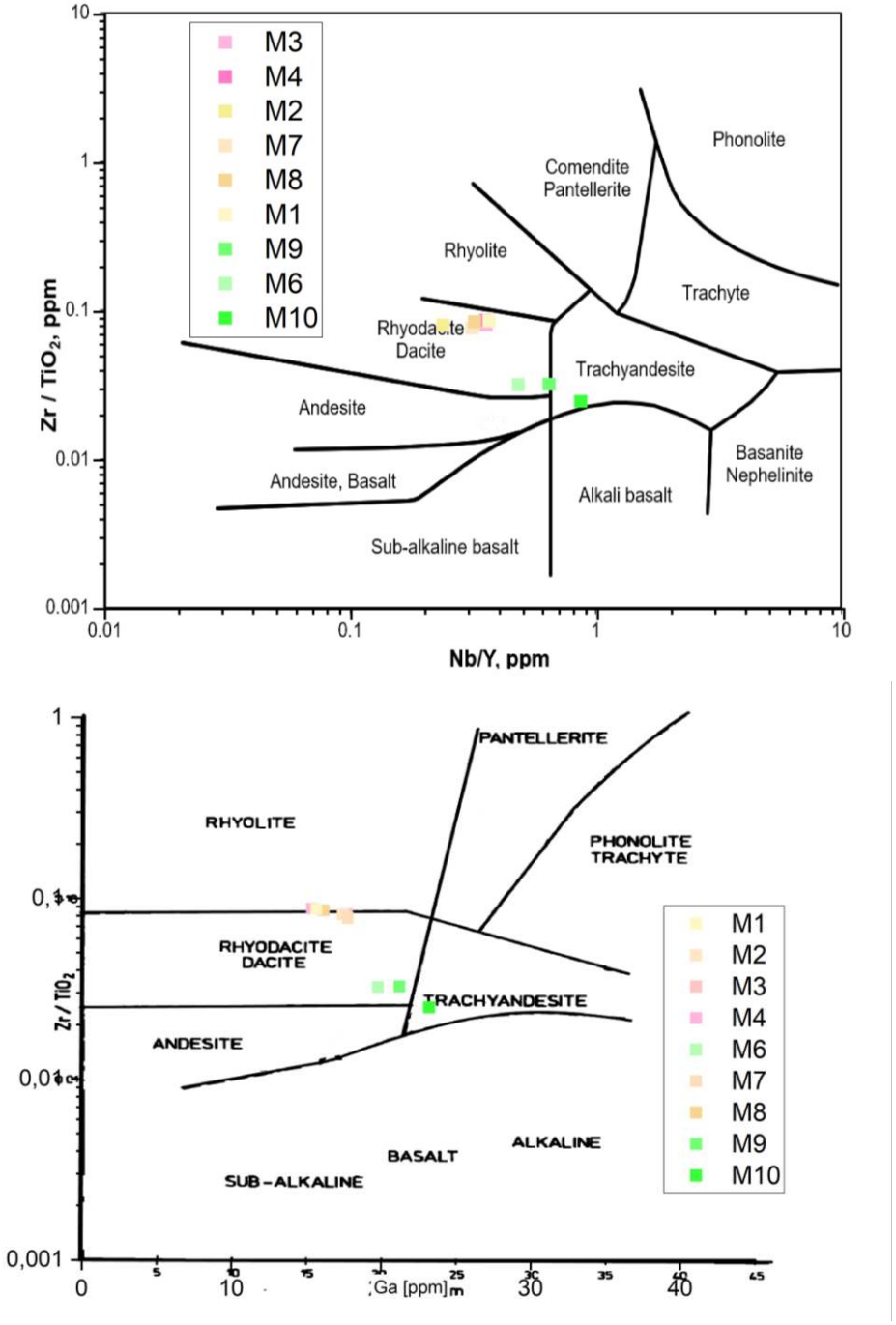

Figure 68: Zr/TiO2-Nb/Y and Zr/TiO2-Ga diagrams after Winchester and Floyd (1977) used draft after Kurt Hollocher

Magmatic trend discrimination

AFM-diagram and K_2O-SiO_2 diagram

The AFM (alkalis-FeO-MgO) diagram is commonly used for determination of the magmatic trend. Here M1, M2, M3, M4, M7 and M8 are on the far-left lower side. M6, M9 and M10 on the other hand plot in the upper center, forming together an iron-rich calc-alkaline trend (figure 69). In the K_2O-SiO_2 diagram after Peccerillo and Taylor (1976), all samples plot in the high-K calc-alkaline series (figure 69).

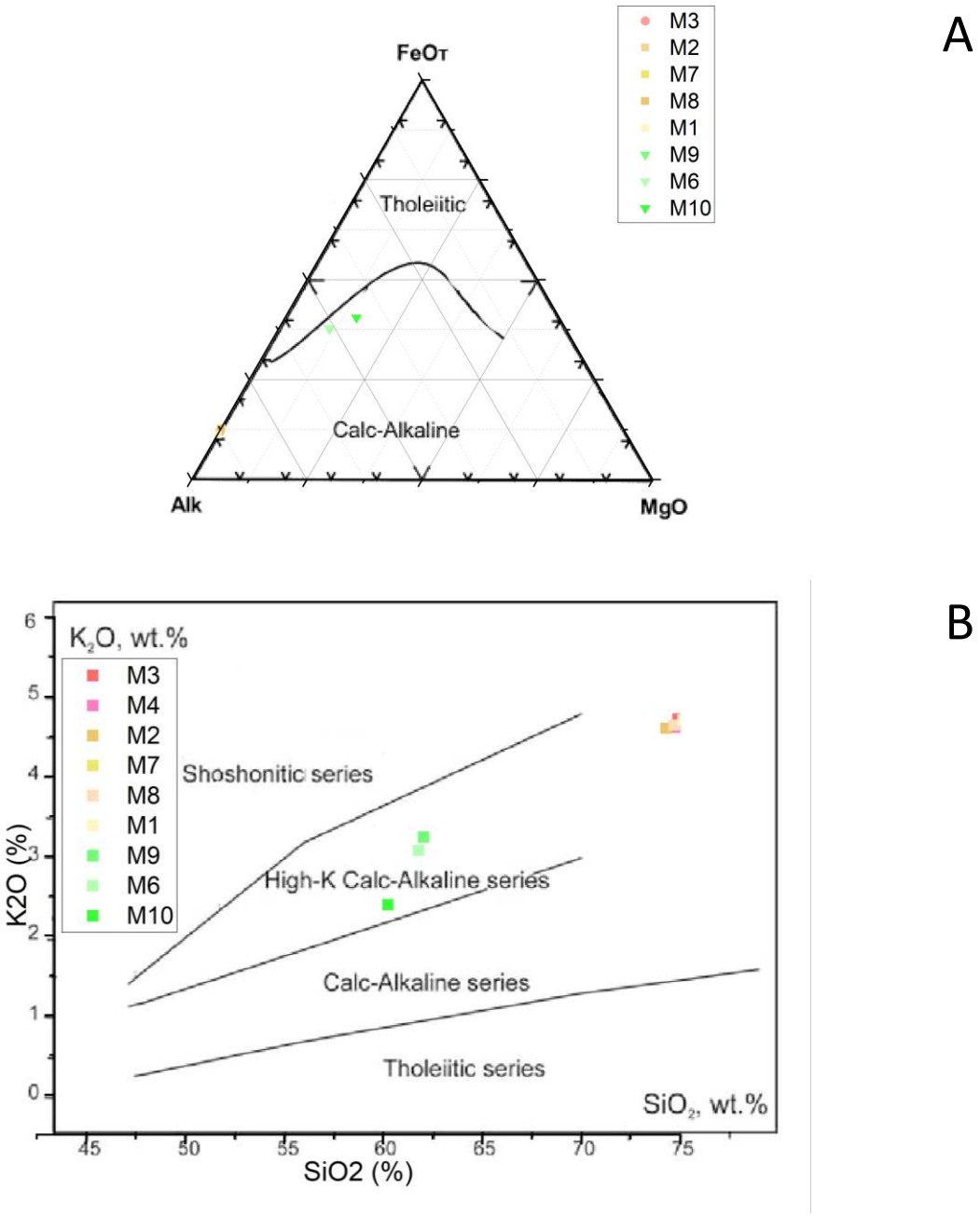

Figure 69: Magmatic series diagrams after Irvine and Baragar (1971) in Nitoi et al. (2000) and Peccerillo and Taylor (1976) in Golovko and Kaminsky (2010)

4.2 Geotechnical measurement results

4.2.1 Density and Porosity

The petrophysical parameters that have been determined are porosity and density (Appendix 10.5.1).

The porosity found in the samples has a wide range, the highest porosity can be found in M7, with 42.12 % in average, followed by M8 with 37.55 %. Still relatively high porosity can be found in M2 (25.66%) and M1 with 13.13%. Noticeably, M3, M4, M6, M9 and M10 have a porosity under 10 %, the lowest occurs in M4 with 8.09 % and M3 with 4.61 %.

Keeping the porosity in mind the bulk density shows a similar reversed ranking for the samples of M1, M2, M7 and M8, where the lowest density measured is 1.41 g/cm³ in M7, followed closely by M8 with 1.52 g/cm³. The highest density is detected in the low porosity rocks, M6 with 2.51 g/cm³, M10 (2.47 g/cm³). M9 (2.33 g/cm³) and M3 (2.33 g/cm³) have very similar values, while M4 (2.28 g/cm³) shows a lower density.

4.2.2 Brazilian Testing

The direct tensile strength (DTS) was determined by multiplication of the Brazilian tensile strength by the factor 0.83 (Perras and Diederichs 2014). Taking the average values of the DTS, the highest value is found in M6 with 4,31 MPa, followed by M9, M3 and M10 with 3.33 MPa, 3.19 ±0.34 MPa and 3.07 ±0.39 MPa respectively. The lowest values are for the samples of M2 (1.32 ±0.47MPa), M7 (0.98 ±0.21 MPa) and M8 (0.81 ±0.06 MPa). The DTS of M1 and M4 ranges in between 2.96 ±0.38 MPa and 2.57 ±0.49 MPa (Appendix 10.5.2).

4.2.3 Triaxial compressive strength testing (TCS)

The triaxial strength testing has been conducted using either a Hoek cell or an MTS 815 triaxial press. In total 51 cores have been tested, 35 with the triaxial press and 16 with the Hoek cell. The results are shown in the Appendix (10.5.3). For additional data, the measured UCS and tensile strength based on the Brazilian test have been used to calculate cohesion and friction angle according to the Mohr-Coulomb failure criterion as well as σ_{ci} and m_i according to the Hoek-Brown failure criterion using the spreadsheet from Villeneuve und Heap (2021). For the calculation at least four measurements of each sample have been selected to achieve the smallest error. Due to different confining pressures of the different samples due to differing UCS strengths, a direct comparison of strength increase is difficult. Therefore, a closer look on the samples is presented individually and the calculated parameters of cohesion and friction angle are compared individually.

Peak strength and behavior of the samples

For M1, four cores have been tested, with a confining pressure of 10, 20, 30 and 40 MPa. Considering a calculated σ_{ci} of 75.6 MPa, an increase of strength by the factor of 3.125 has been measured at a confining pressure of 30 MPa, with a peak strength of 205 MPa. At a σ_3 of 40 MPa the TCS increases slightly to 219.34 MPa. All samples show brittle behavior.

For M2, five cores have been tested at 5 and 10 MPa; two at 15 and 20 MPa confining pressure. An increase compared with the calculated σ_{ci} (31.4 MPa) by the factor 2.69 has been measured at σ_3 = 20 MPa, ductile behavior occurs as well in M2-C (σ_3=20 MPa). The residual TCS is at 86 MPa. In the measurement at σ_3 = 10 MPa a similar TCS is observed (figure 70 A).

The cores of M3 have been tested at confining pressures of 5, 10, 15, 20 and 50 MPa. The highest TCS has been measured at σ_3 = 50 MPa with 450 MPa (no failure), even if the difference to the 20 MPa measurement with 441 MPa is relatively small. Therefore, the peak strength increased in comparison to σ_{ci} (124.1 MPa) by the factor of 3.63. When the sample failed a brittle behavior was noticed (figure 70 B).

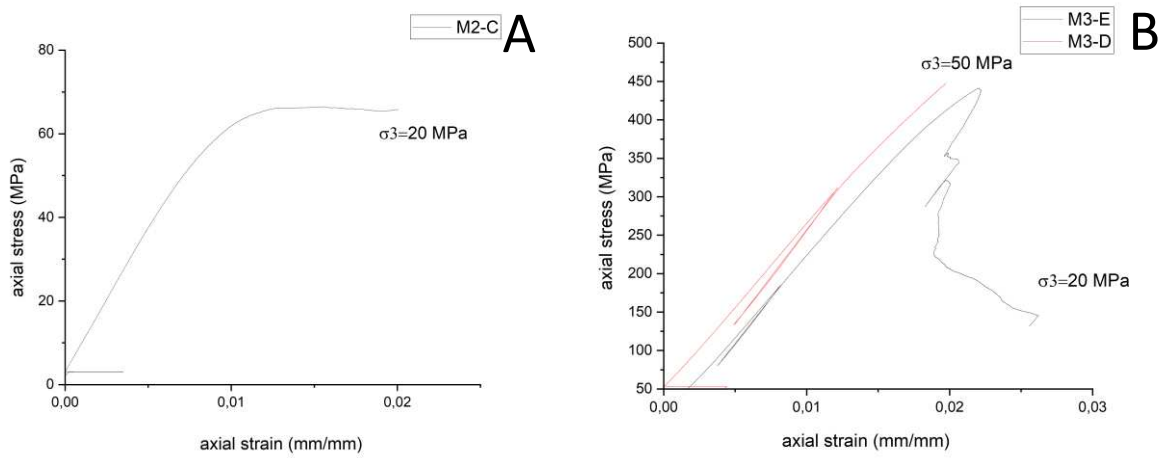

Figure 70: Ductile behavior of M2-C at a confining pressure of 20MPa [A] and the behavior of M3 E with brittle failure and M3-E without failure [B]

For M4, the TCS of ten cores has been measured at σ_3 = 5, 10, 15, 20 MPa, two times at 21 MPa and two times at 30, 40 and 50 MPa. The highest TCS occurs at a confining pressure of 21 MPa with 367.6 MPa, strongly decreasing to 156.79 MPa at 50 MPa. The increase in comparison to σ_{ci} is 3.3. The two measurements at 21 MPa are not differing, while the measurements at σ_3 = 30 MPa differ significantly (Δ 100.25 MPa). In terms of behavior, mostly brittle, but also ductile deformation, M4-U with σ_3=20 MPa, was observed (figure 71).

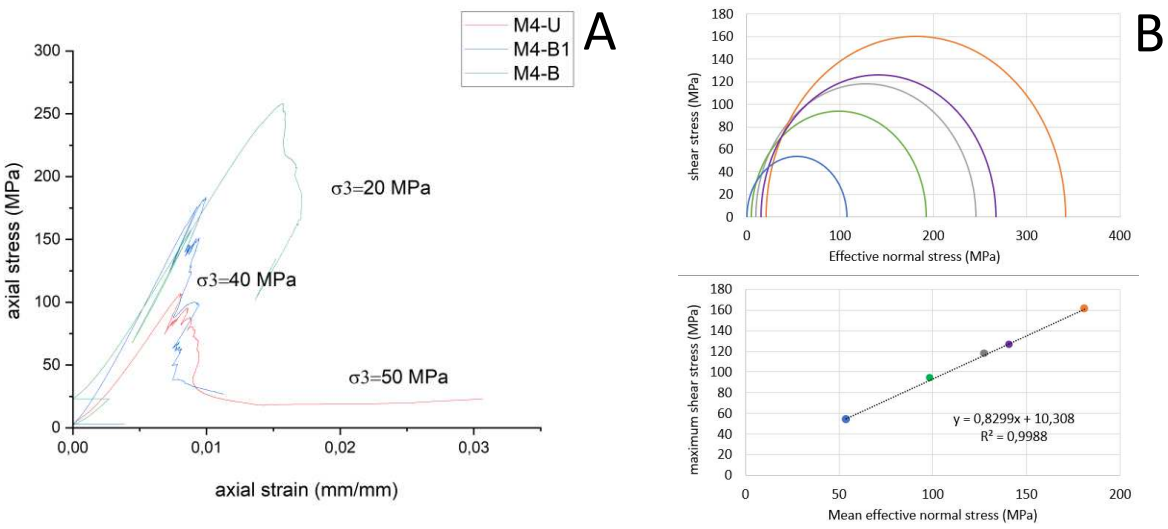

Figure 71: Selected examples of the unused triaxial tests of M4 with different brittle failure [A] and used triaxial data for the calculation of cohesion and friction angle as Mohr circles[B]

For the TCS determination of M6, 7 cores have been analyzed. As for σ_3, three were measured at 5 MPa, 10MPa, 20 MPa and 30 MPa, as well as at 35 MPa. The highest TCS was determined at 30 MPa with 289 MPa and an increasing factor of 5.31. M6 shows both strain hardening, softening and ductile behavior (figure 72)

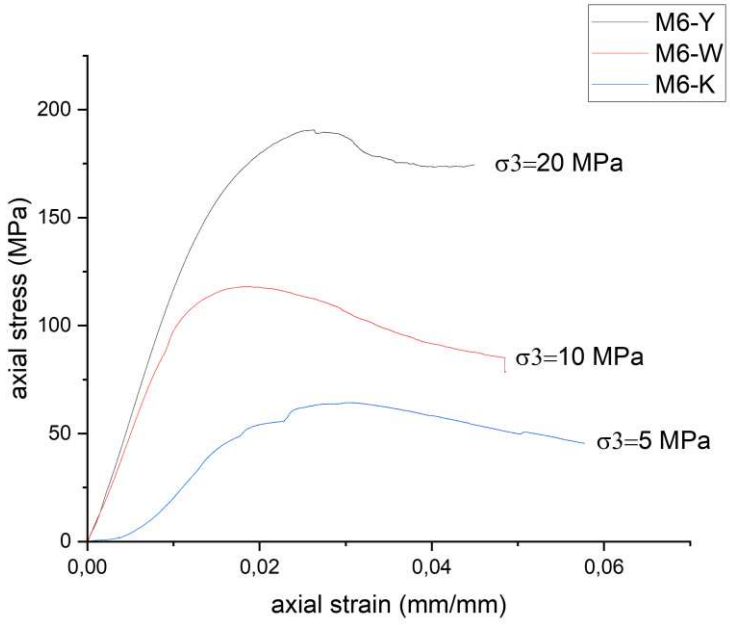

Figure 72: The selected measurements of M6 at different confining pressures and different intensities of strain softening

M7 stands out due to the low confining pressures. In total, five cores have been tested at 0.5, 1, two times 1.5, 2.0 and 2.5 MPa confining pressures. The low σ_{ci} of 5.9 MPa leads to the highest TSC of 13.73 MPa at σ_3=2.5 MPa, already showing ductile behavior. Therefore, the increasing factor is 2.33. The measurements at same confining pressure of 1.5 MPa do differ by 2.59 MPa, both reacted brittle like most other samples.

M8 is very similar to M7. The seven analyzed cores have been tested at 2, two at 2.5, 3, 4 and 5 MPa confining pressure. Their highest determined TCS is at a σ_3 of 5 MPa reaching 22.03 MPa with an increasing factor of 2.72 and ductile behavior. The two measurements of 2.5 MPa σ_3 differ by 2.20 MPa, while one is showing barely ductile behavior (M8-H) and the other strain softening.

For M9, the TCS of three cores has been determined at 10 MPa and two times at 20 MPa, reaching the highest values (260.56 MPa) at 20 MPa confining pressure (increasing factor of 3.92). This value differs significantly from the other σ_3= 20 MPa value by 162.15 MPa. M9-D shows strain softening, while M9-C stain hardening (figure 73)

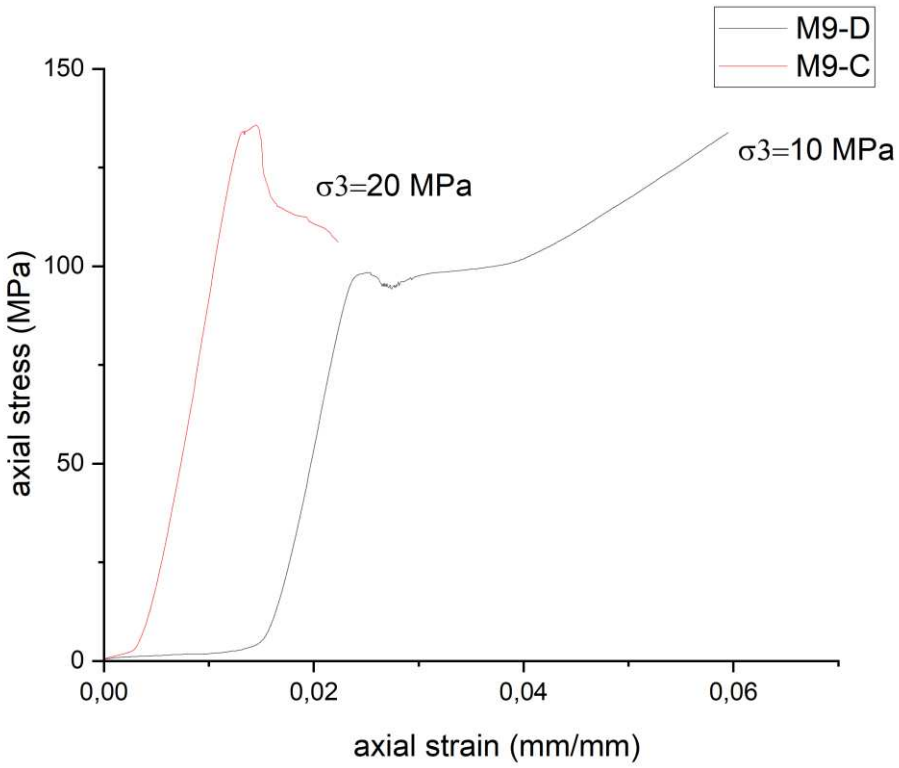

Figure 73: Failure behavior of the used M9-D and M9-C measurement with strain-hardening in M9-D

Finally, five cores of M10 have been used for the TCS determination. The confining pressure ranges from 5 MPa over 10, 20 and 30 to 40 MPa. The highest TCS of 390.58 MPa was observed at a confining pressure of 40 MPa (increasing factor of 5.12). M10-E might have failed caused by a feature. In lower confining pressure brittle behavior occurs, while at higher pressures the behavior transitions to stain softening (figure 74).

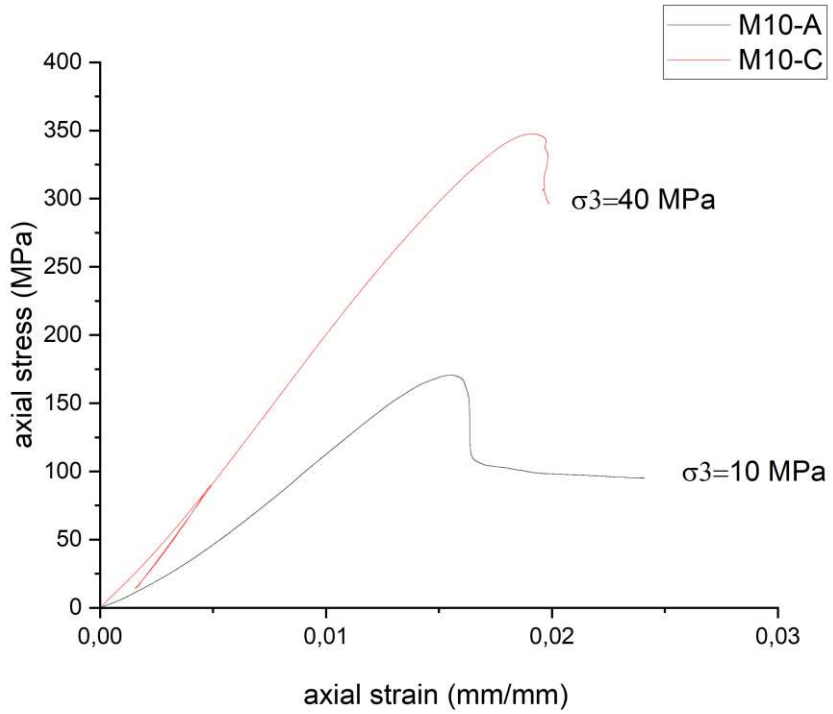

Figure 74: Two brittle behavior measurements of M10

Cohesion and friction angle

Taking the described and selected data into account, it is possible to determine the cohesion, c, and the friction angle, Φ, for all nine sample points (table 3). In terms of cohesion three groups can be differentiated. Group one contains M3 and M4 reaching the highest cohesion values of 18.4-20.1 MPa. Group two includes M1, M6, M 9 and M10 reaching a cohesion between 6.9-10.8 MPa. The lowest cohesion can be found in M7 and M8 between 1 and 1.2. Based on the friction angle, a group with values between 50.5 - 60.4° comprises the samples M1, M2, M3, M4, M6, M9 and M10, which can be distinguished from the samples of M7 and M8, which have noticeably lower values of 41.8° and 43.8°. The standard error for the cohesion is between 0.12 MPa in M7 and 5.04 in M10. For the friction angle the standard errors are 0.70° in M6 and 7.22° in M8.

Table 3: Results of the calculation of cohesion, friction angle, σ_{ci} and m_i after Hoek-Brown criteria

Sample	Cohesion [MPa]	Friction angle [°]	σ_{ci} [MPa]	m_i [-]
M1	7.9	55.1	75.6	26.4
M2	3.7	49.4	31.4	15.7
M3	20.1	60.4	124.1	60.2
M4	18.4	56.5	111.4	38.7
M6	6.9	50.5	54.4	22.1
M7	1.0	43.8	5.9	7.8
M8	1.2	41.8	8.1	6.1
M9	7.5	55.8	66.4	35.3
M10	10.8	52.3	76.3	15.7

σ_{ci} and m_i after Hoek-Brown criteria

The σ_{ci} and m_i are derived from the same data as the cohesion and friction angle and therefore show similar three groups for σ_{ci}. M3 and M4 show the highest values reaching from 111.4 to 124.1 MPa for σ_{ci}. The values of M1, M6, M9 and M10 are lower than in the first group, ranging from 54.4 MPa in M6 to 76.3 MPa in M10.

In m_i a differing grouping can be found. M3 is reaching the highest value with 60.2, while M4 with 38.7 is more similar to M1, M6 and M9 reaching values between 22.1 and 35.3. M2 and M10 show the same values of 15.7. M8 and M9 have the lowest values at 6.1 in M8 and 7.8 in M7.

4.2.4 Uniaxial compressive strength testing

In general, the results for the uniaxial compressive strength of the 32 Misti (table 4) samples have a wide range reaching from very low 2.11 MPa in M8-B to high 175.99 MPa in M3-E. This broad range can be also found in the results of the Young's modulus reaching from 1.38 GPa to 40.63 GPa in M7-B and M3-A, respectively. The highest Poisson's ratio is for sample M8-E with 0.25, while the lowest are detected in M3-G, M4-V, M6-E and M7-H with 0.1 as displayed in table 3.

Table 4: Results of the UCS testing of all measured samples with the calculated Young's modulus and Poisson's ratio

Sample	UCS [MPa]	Young´s modulus [Gpa]	Poisson´s ratio [-]
M1-A	84.89	18.82	0.11
M1-C	74.49	26.52	0.13
M1-D	70.21	21	0.15
M1-E	74.74	19.95	0.14
M1-W	58.39	16.63	0.24
M2-A1	36.93	9.88	0.15
M3-A	140.65	40.63	0.16
M3-B	146.28	38.28	0.13
M3-G	175.99	40.36	0.1
M3-S	78.89	26.87	0.11
M3-U	116.76	39.16	0.11
M4-T	98.13	30.14	0.1
M4-C1	123.69	37.9	0.24
M4-A	107.47	30.64	0.11
M4-V	101.43	33.65	0.1
M4-W	29.97	17.08	0.17
M6-B	59.28	21.51	0.15
M6-E	24.37	9.26	0.1
M6-F	46.3	29.05	0.13
M7-A	6.63	3.49	0.15
M7-B	3.94	1.38	0.23
7M7-D	3.93	2.87	0.19
M7-H	4.17	4.44	0.1
M7-A1	2.61	2.76	0.24
M8-B	2.11	3.26	0.21
M8-E	9.13	3.84	0.25
M8-G	9.81	4.86	0.13
M9-A	85.23	37.14	0.10
M9-B	76.31	36.36	0.13
M10-A	106.31	30.9	0.14
M10-D	84.89	18.13	0.12

Uniaxial compressive strength data can be described before and after failure with stress-strain diagrams (Tutluoglu et al. 2014). Therefore, different phases I-V can be determined, consisting of clack closure, elastic, cracking before failure and post failure microcracking and a residual state. Especially phase IV can be used for the differentiation between brittle, plastic failure, as well as strain hardening and softening. Post failure phases are often obscured by the instability of the sample-machine system (Tutluoglu et al. 2014).

Both, axial stress versus axial strain, show some differences in M1, the phase I is more dominant in M1-C than in M1-A. A weaker increase of the curve is often associated with fissure closure, which can be found here. Both have a long elastic phase with a stronger inclination in M1-A. In phase III cracking occurs, followed by failure. In the post failure state, the stress is building up a few times, reaching especially in M1-A nearly the maximal value. At failure the average axial strain is 0.48% and the diametral strain 0.33%. Especially M1-C shows brittle failure (figure 75 A).

In M2, on the other hand, phase I is not visible, and the inclination of the elastic phase II is significantly lower, phase III is as in M1 not very prominent. After failure a building up of stress is also less noticeable (figure 75 A). The failure axial strain is at 0.51% and diametral strain at 0.19%. M2 shows brittle behavior as well.

M3 and M4 are very similar. Phase I is more dominant in M4, while M3 shows a higher increase in the stress/strain ratio. Phase III is short in both samples. After failure the stress is decreasing rapidly. M3 has an axial strain 0.41 % and diametral strain 0.15 %, while M4 has a slightly lower axial strain (0.40 %) but a higher diametral strain (0.19 %) at point of failure. Both samples show brittle behavior (figure 75 B).

M6, on the other hand, does show a very extensive phase I, a short phase II and after failure a short region of post failure strain softening, followed by plastic behavior. The axial strain and diametral strain at failure are 0.30 % and 0.09 % in average. The sample has shown softening failure in total strain.

In M7 both displayed graphs differ significantly in shape. Before failure both are quite similar, and do not show any difference between phase I and II. The maximal stress (figure 75 C) and strain differ significantly (axial strain M7-A 0.18 % and M7-D 0.12 %). Post failure the stress decreases multiple stepwise in M7-A and in two steps M7-D. Therefore, M7-A is failing brittle, while M7-D shows a strain softening failure.

M8 does not show a difference between phase I and II as well. Phase III is more pronounced than in M7. Post failure a plastic behavior is visible, followed by a strong decreasing stress in two steps (figure 75 C).

The displayed M9 graphs show very similar behavior, M9-A has a steeper inclination in phase I and II, which can be clearly distinguished. Both show a brittle failure at an axial strain of 0.37 % and diametral stain of 0.21 % in average.

M10 can be determined by a particular feature in phase I: A rising stress strain ratio decreasing significantly and rising again to phase II. The failure is brittle and occurs at an axial strain of 0.56 % and diametral stain of 0.27 % (figure 75 D).

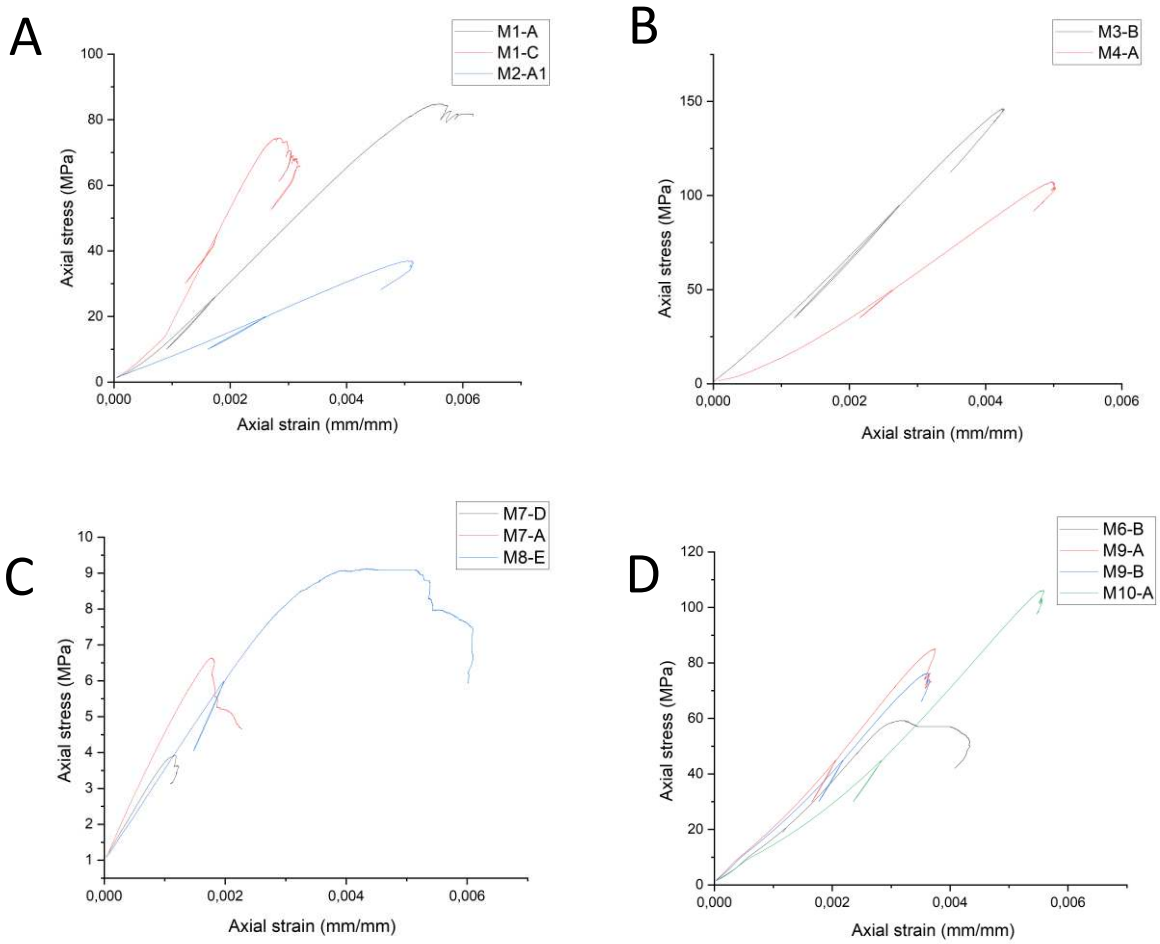

Figure 75: UCS testing axial stress and strain graphs of the measured samples, A: M1 and M2, B: M3 and M4, C: M7 and M8, D: M6, M9 and M10.

4.2.5 P-wave-velocity measurements

The p wave velocity (Vp) has been determined for saturated, dried and after testing (failure) conditions. Based on the last two conditions a p wave velocity reduction after failure is derived (appendix 10.5.4).

The saturated and dried p wave velocity results show that the highest value is found in M9 with Vp_{sat}=4775.38 m/s and Vp_{dry}= 3823.84 m/s followed by M10, M3 and M6 reaching values over 4000 m/s saturated and 2900 m/s dried. The lowest values have M8 (Vp_{sat}=1848.77 m/s, Vp_{dry}= 1901.83 m/s) and M7 (Vp_{sat}=2138.89 m/s, Vp_{dry}= 1839,11 m/s), followed by M2 (Vp_{sat}= 2365.42 m/s, Vp_{dry}= 2101.77m/s). As in the porosity, M4 (Vp_{sat}= 3483.31 m/s, Vp_{dry}= 2283.75 m/s) and M1 (Vp_{sat}=3345.15 m/s, Vp_{dry}= 2448.56 m/s) show values in between those two groups.

The difference between the saturated and the dry p wave velocity is also interesting. While M10, M4, M1, M6 and M9 show a strong relative difference of higher than 20 %, M2, M3 and M7 show a difference between 11 and 17 % while M8 shows nearly no change at all.

Based on the measurement of the dry p wave velocity after destructive testing, Vp reduction values are specified. A high range of values for Vp reduction can be found in the different samples. Values for M1 vary from -14.03 to 34.81%, even higher ranges can be found in most other samples, except M6, M7, M9 and M10, for which all calculated Vp reductions are negative.

Taking average values different groups can be differentiated. The group with increased Vp consists of M1, M2, and M4, ranging between 1.16- 9.79%. A slight decrease can be seen in M3 (-5.39 %) and M8 (-3.25 %). The strongest decrease can be seen in the values of M6, 7, 9 and 10.

5 Discussion

5.1 Acknowledgment of error sources and uncertainties

Before further interpretation and correlation of the data a determination and evaluation of possible errors and uncertainties in sampling, specimen selection, methods and correlation are necessary.

For the samples it has to be pointed out that the main goal was the characterization of specific samples, not the characterization of the whole lithological unit. Therefore, different factors, like compositional differences due to lithic clast and melt fragments, cooling time and therefore degree of devitrification, exposure time to weathering, welding can vary (McPhie et al. 1993) and can influence the appearance and properties of the samples. Besides natural causes, the sampling can cause fractures or a weakening of the rock, as can the transport. These influences are possible in all samples; therefore, the errors have to be considered for all results.

For the geological characterization the error source is depending on the method. For the optical thin section microscopy, the uncertainty is a combination of restricted area (about 12 cm^2), 2D instead of 3D, and experience of the microscoper who might overlook characteristic features. Due to alteration or devitrification, some features are difficult to determine. The random point counting bears an additional uncertainty, since certain areas might get over- or underrated, even if the error in repetitive counting was for most samples below 3%. An additional difficulty of this method is the differentiation of minerals visually.

The uncertainty in this dataset, caused by missing minerals characteristics, and in combination with low crystal content, lead to a restricted use of the data, by only taking the amount of phenocryst [%] into account for correlation of the geological-geotechnical parameters. By using the same thin sections, the scanning electron microscope (SEM) has similar uncertainties. However, the EDX measurement of the mineral composition improved the mineral determination in combination with the optical thin section microscopy. Nevertheless, in terms of composition, the SEM with EDX is less reliable compared to other methods like the microprobe. The error is highly dependent on sample and grain size and condition and the experience of the user. Especially at low concentration, some elements are difficult to detect; overlapping peaks can be overlooked and may lead to an erroneous compositions (Ali et al. 2023). Also, the sample spot caused by the electron beam leads to an influence on the surrounding minerals. Phases only detected in the SEM always bear the risk of misinterpretation, because only compositional data is provided (Ali et al. 2023). The correction, which is applied for the Fe^{2+} and Fe^{3+} differentiation provides an additional error source, because the calculation is just an approximation (Droop 1987). The BIB-SEM uncertainty is limited in this work to the selection of the examined area, representativeness and measuring and scaling mistakes, due to the varying shape of fractures and the effect of perspective. In the XRF, the sample selection can lead to an error, because local variances, as lithic clasts, melt fragments can be over- or underrepresented. Also, by milling down the sample, minor contamination of the mill material is possible. Weighing and contaminated containers are an additional source of error. During the measurement limited sensitivity in ultra trace elements as well as matrix effects are possible. Calibration problems can occur as well, which lead to inaccuracies in measured element concentration, depending on the used standard (Marguí et al. 2022). The number of samples allows in some methods only one general valid value for each sample. A determination of normal distribution of the results is therefore not possible.

For the geotechnical methods multiple errors can occur. For the density and porosity measurement just connected pores are measured. Especially in a volcanic setting, the isolated pores often occur and are therefore not detected in the analysis. Additionally, a minor error while measuring the sample can occur, due to weighing or variations of surface water on the sample. A differing size, especially length diameter ratio is a major error source in UCS and TCS measurements, beside unparallel and uneven surface. Discontinuities like fractures or clasts can also lead to an error in the triaxial, uniaxial and tensile strength measurements. The triaxial tests can also be influenced by membrane rupture and oil leakage, causing increase of pore pressure, and failure at lower compressive stress (Hoek 2007). While calculating the Hoek-Brown criterion, the values leading to the lowest error in the calculation have been

chosen and the results are used for further investigations. The oil contaminated samples show an increase in velocity, probably by filling pores and fractures. Samples which have been contaminated were not used for further interpretation. Finally, sensor or software problems can occur but were not noticed in the measurements for this thesis.

5.2 Geology

5.2.1 Classification and assignment of the samples

Bulk rock geochemical data show that the samples follow a calc-alkaline evolution trend (AFM diagram) and are either rhyolitic (M1, M2, M3, M4, M7 and M8) or andesitic to trachyandesitic in composition (M6, M9 and M10) according to the TAS diagram. The diagrams after Winchester and Floyd (1977) have not been used for further characterization due to decreased reliability caused by the detection limit of the XRF.

For the rhyolitic rocks the mineralogy and geochemistry are very similar, containing plagioclase and alkalifeldspar, biotite and accessory magnetite, apatite, zircon, REE-minerals, minor amphibole and occasionally pyroxene. The textures however allow a differentiation into two groups, ignimbrites (M1, M2, M7 and M8) and rhyolites (M3, M4). Beside the textures described in the thin section and BSE images, the porosity and mechanical characteristics support this differentiation.

The first group (the rhyolitic ignimbrites of M1, M2, M7 and M8) is characterized by lithic clasts, broken phenocrysts and high porosity. Major differences can only be found in porosity and the matrix texture. Devitrification is only present in M1 and M2, which suggests a lower temperature and faster cooling in M7 and M8. Also, welding is only used as a field description by the sample collectors for M1. Therefore, M1 can be called biotite bearing, welded, rhyolitic ignimbrite. M2 can be described as biotite bearing, slightly welded, rhyolitic ignimbrite. M7 and M8 are biotite bearing, rhyolitic ignimbrite. The samples of the second group (rhyolites of M3 and M4) on the other hand are far more dense, and show strong devitrification, ranging from axiolitic to spherulitic. The degree and type of devitrification is temperature dependent, and according to McPhie et al. (1993) allows an estimation of the devitrification temperature. For the rhyolites about 700°C are estimated. The feldspar measurements show a compositional temperature relation of <700 °C for the ignimbrites and a temperature up to 800°C for the rhyolites (figure 76) supporting the differentiation into rhyolites and ignimbrites. The strong devitrification overprinted the primary rock textures, like flow texture of perlitic fractures. Therefore, a pyroclastic origin cannot be fully excluded. Further arguments for a different origin, such as phreatomagmatic shard-rich rock have not been found, but considering the mineralogy, the strength and porosity measurements, as well as the field

description by the samplers, the samples M3 and M4 are therefore described as biotite bearing, devitrified rhyolites.

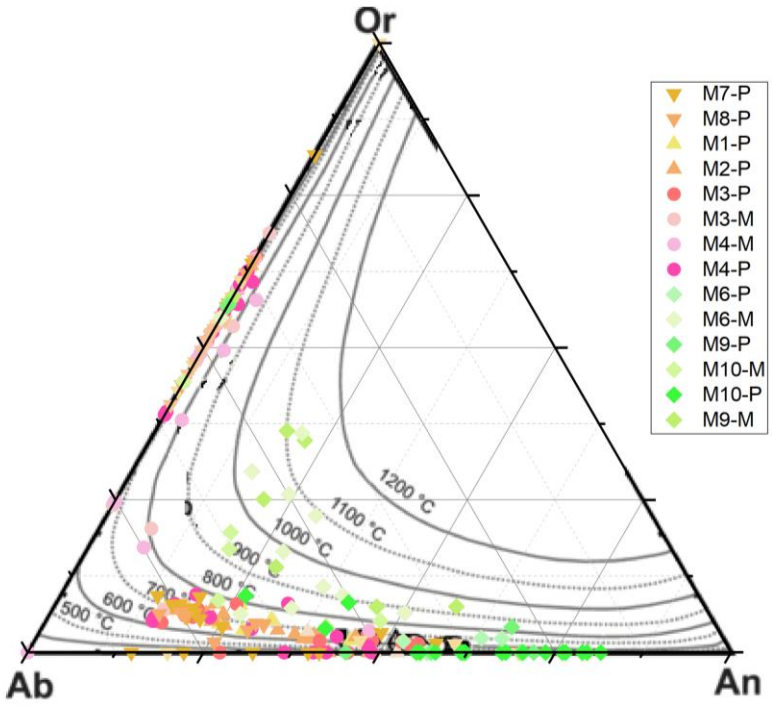

Figure 76: Temperature-dependent feldspar composition at atmospheric pressure for all samples according to Drüppel and Lehmann (2009)

The trachyandesites and andesites (M6, M9 and M10) are difficult to differentiate based on the composition since the mineralogy is very similar. The observed flow texture proves with certainty that these samples are effusive rocks. Further the feldspar composition supports a higher crystallization temperature for the andesites than for the other samples (figure 76). The perlitic fractures low degree of devitrification points towards a rapid cooling rate (McPhie et al. 1993). The observed zoning in the plagioclase and the missing olivine speak for a classification as trachyandesites, whereas the abundance of both clino- and orthopyroxene in the samples points to andesite characteristics (Gill 2010). The typical tectonic setting for trachyandesites differs from andesites. While andesite is typical for subduction related volcanism, trachyandesite is more typical for rifting, including rifting in continental magmatic arcs. Noticeably M10 is more potassium rich than the others and is always plotting in the trachyandesites. Considering the geological map (Rivera et al. 2016), the different andesite units near the M10 sample point differ significantly in age. Whether this points to a change in general melt source and melt composition cannot be clarified in this work. But it can be said that in terms of magmatic trend all samples fit the calc alkaline series, as expected in this subduction related volcanic setting (Markl 2015; Wilson 2000). The number of samples is

insufficient to distinguish the lithologies. Nonetheless, because the units from which the samples are taken from are referred to as andesites by Rivera et al. (2016) and to keep assignment clear, these samples are referred to as andesites in further discussion and can be named as calcic amphibole, clino- and orthopyroxene bearing andesite with accessory apatite and magnetite.

5.2.2 Comparison to the known geology

Whole rock composition comparisons are difficult, due to the lack of certain trace elements. A mineralogical comparison was possible for most samples. Some ignimbrites in the area of Arequipa have been investigated by Lebti et al. (2006). The ignimbrite samples show the major characteristics described, such as the high K calc-alkaline trend and the mineral compositions of plagioclase, biotite, quartz, sanidine and Fe-Ti-oxides. But a further determination or assignment was not possible, due to missing data on trace elements and isotopes. The assignment into the different ignimbrite groups established by Lebti et al. (2006) based on mineral composition of the measured amphibole and biotite was not possible.

The rhyolites on the other hand are not described detailed in literature, due to the comparatively rare occurrence. Some descriptions have been done by Rivera et al. (2016). Here the descriptions of mineral composition and the high K calc-alkaline trend fit mostly to the observation made in this thesis. The feldspar dominance with the biotite supports the measurement, even if the Mg seems to be higher in the measured biotite. Nevertheless, this could be caused by the semi quantitative analysis of the SEM-EDX.

The andesites of El Misti have been mineralogically characterized by Rivera et al. (2016), which fit to the observation in the samples. The feldspar composition and composition of both clino- and orthopyroxene fits as well. Rivera et al. (2016) described enstatite and ferrosiilte, of which the latter was not observed, but additionally diopside, augite and pigeonite was found in the samples. Beside the described tschermakites and paragistes, edenites, hastingites and magnesio-hornblende was observed. The amphiboles and pyroxenes particularly indicate the differentiation trend towards an Fe-poor and SiO_2-rich melt. Also the accessory Ti-oxides and apatite are mentioned in Rivera et al. (2016). For the andesites, the occurrence of both clino- and orthopyroxene along with amphibole, Ti-magnetite and plagioclase with accessory apatite in combination with high K calc-alkaline is equivalent to the literature.

Element signature

By normalizing certain trace elements to the upper mantle some major anomalies in the element signature are visible, even if some elements are missing. The most noticeable negative anomalies can be found in Nb and Ti, the latter anomaly is more present in the rhyolites and ignimbrites than in the andesites (figure 77). These anomalies are often referred to as Nb-Ta and Ti-anomaly and are typical for a subduction related setting (Gertisser and Keller 2003).

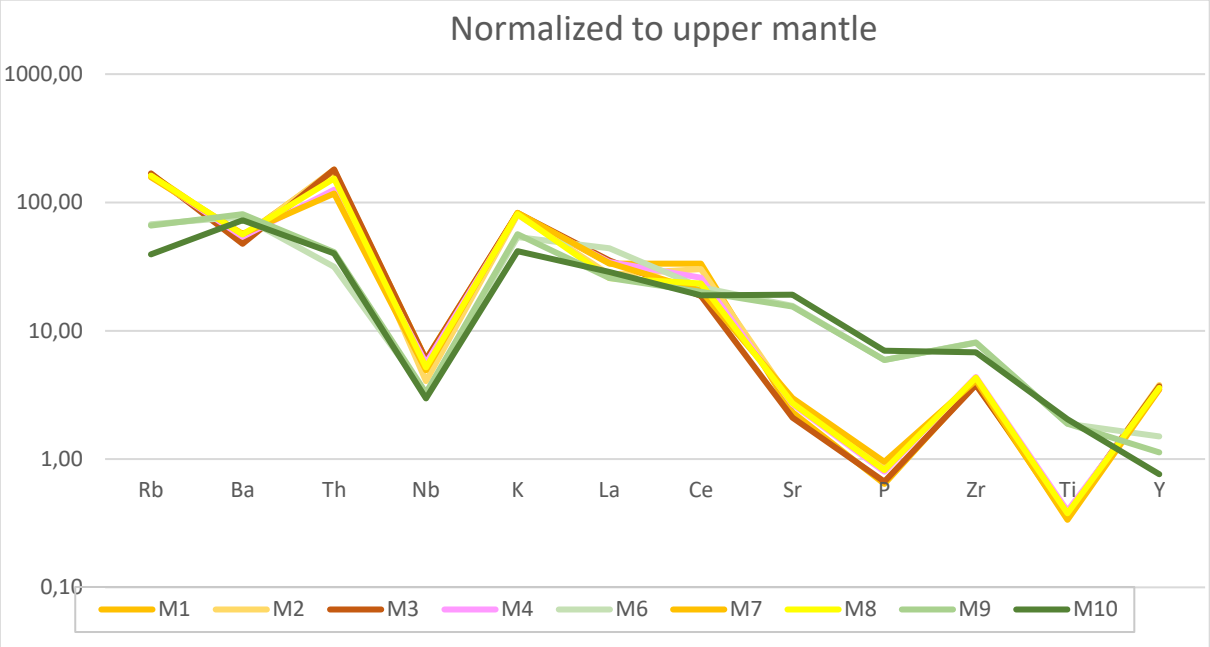

Figure 77: Trace element signature normalized to the upper mantle after Anderson and Don (1983) with the anomalies at Nb and Ti

5.2.3 Correlation of geological parameters

In the correlation of the XRF results, one major observation can be made. The negative correlation of compatible and incompatible elements shows the differentiation of the melt (figure 78), and therefore the enrichment of incompatible elements in residual melts (Markl 2015) leading to the rhyolites and ignimbrites. A positive correlation trend can be seen between SiO_2, K_2O, Nb, Rb, Th and Y while showing a negative trend to TiO_2, Al_2O_3, Fe_2O_3, P_2O_5, Ba, Ga, Sr, Zn and Zr. The MgO, Co, Cr and Cu show also a negative correlation coefficient but do not show significance on a level of $p > 0.05$. The elements MnO, Na_2O, Ce and La do not show a significant or high correlation with either of these groups.

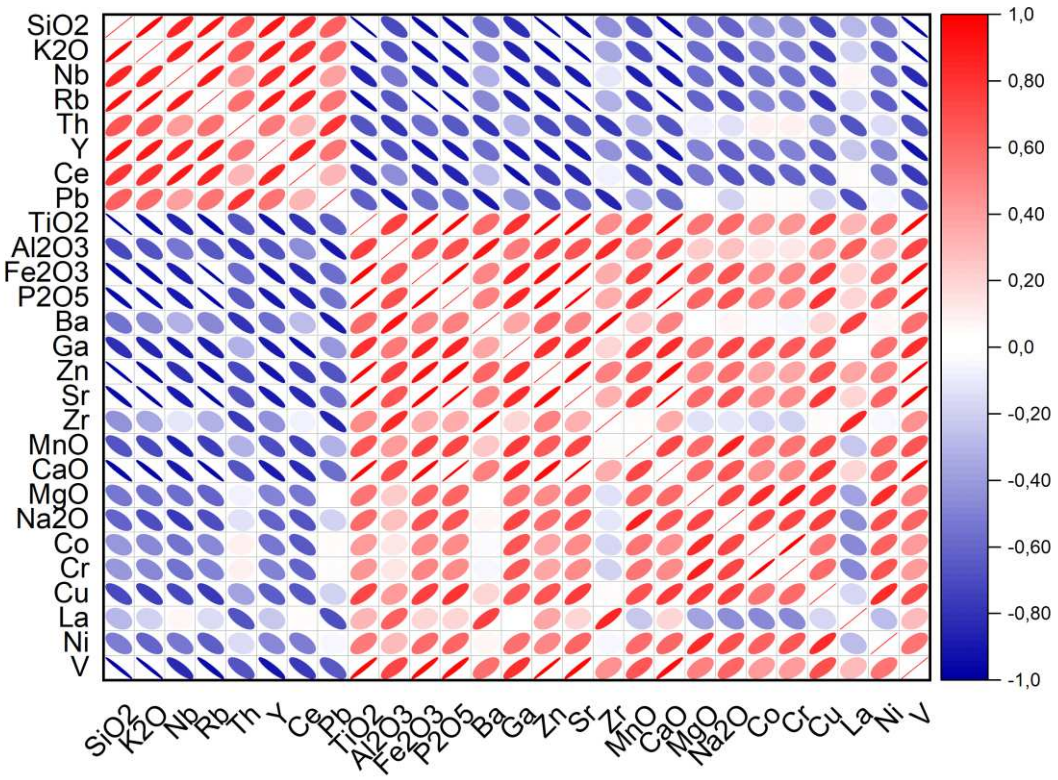

Figure 78: Correlation plot of the measured elements, separating into compatible and incompatible elements

5.3 Geotechnics

5.3.1 Comparison to the known geotechnical properties of volcanic rocks

For a better understanding of the data, a comparison to previously measured volcanic lithologies is necessary. For andesites and ignimbrites, the results of the compressive strength testing is compared to data from Heap and Violay (2021), Mordensky et al. (2018) and Moon (1993). The measured cohesion, m_i and friction angle is compared to Schaefer et al. (2023), Mordensky et al. (2022), Villeneuve and Heap (2021) and for the tensile strength and porosity data from Moon (1993), Mordensky et al. (2022) and Heap et al. (2021) is considered for a comparison. It is important to mention that these publications do not include samples from El Misti, but all use samples of stratovolcanoes, which are mostly part of the pacific ring of fire like Mt. St. Helens, Volcan de Colima, Kumamoto, Ruapehu. One exception is the Chaîne des Puys (France) in Heap and Violay (2021) and some ignimbrites in Valido et al. (2023) from the

Canary Islands. For the rhyolites, Weydt et al. (2021) and Zorn et al. (2018) provided data for the comparison of porosity, tensile and compressive strength.

Porosity

Connected porosity data is available from Heap et al. (2021), Villeneuve and Heap (2021) for andesites and (Moon 1993) for the ignimbrites. The connected porosity of the andesites in Heap et al. (2021) from Volcán de Colima range from 7-23 %, similar to Mordensky et al. (2018) at Ruapehu ranging from 4-28% and Villeneuve and Heap (2021) reaching 11 %. The andesites of in this dataset have a similar connected porosity of up to 11 % in M6. The ignimbrites according to Moon (1993) range between 13.9 – 43 %, as do the ignimbrites of this thesis with 12 – 44 %. The rhyolites of Zorn et al. (2018) have a significantly higher porosity of up to 33 %, those of Weydt et al. (2021) range from 8-21%, while the rhyolites in this sample set barely reach 10%. Overall, the measured porosities of volcanites from Misti do not differ significantly from volcanites of other stratovolcanoes.

Uniaxial compressive strength, Young's modulus and calculated σ_{ci}

In Heap and Violay (2021) mostly andesites have been tested. The UCS data ranges from 20.6 MPa at Volcán de Colima (Mexico) to 83.0 MPa Kumamoto (Japan) (Heap and Violay 2021), whereas in Mordensky et al. (2018) the UCS of andesite from Ruapehu range from 5-162 MPa. The samples of the andesites in this dataset show UCS from 24.37 MPa to 106.31 MPa, with most of the samples, especially in M9 and M10, having UCS higher than 75 MPa. These observations fit to the calculated σ_{ci} as well, even if the σ_{ci} tends to be slightly lower that the UCS. For the ignimbrites a comparison to ignimbrites from New Zealand (Moon 1993) and from the Canary Islands is possible (Valido et al. 2023). Valido et al. (2023) describes values up to 69.82 MPa while Moon (1993) gives a range of 0.23-54 MPa. The ignimbrites of El Misti do slightly differ in UCS. M1 reaches even higher values of up to 84.89 MPa, while the values of M2, M7 and M8 fit to the range described by Moon (1993). For the rhyolites, the results from this testing range from 79 to 176 MPa, which is comparable to the range in Weydt et al. (2021) of 94 to 124 MPa. The Young's modulus of volcanic rocks reach <25 GPa for pyroclastics and dacites and <52 GPa for andesites, according to Heap et al. (2021), and <20 GPa for rhyolites in Weydt et al. (2021). The results of this work draw a similar picture. The andesites stay below 60 GPa, the ignimbrites even under 3 GPa, whereas the stiffness for the rhyolites is higher than in Weydt et al. (2021) reaching up to 40 GPa.

Cohesion and friction angle

For the comparison of cohesion and friction angle results, data from Villeneuve and Heap (2021) and Schaefer et al. (2023) is used for the andesites. The cohesion reaches up to 19.5 MPa in Villeneuve and Heap (2021) and from 7 to 52 MPa in Schaefer et al. (2023) for the

andesites, which is similar to the measured cohesion of the samples in this thesis (<10.8 MPa). The ignimbrites of this sample set also do not show major differences in comparison to Moon (1993) and fit into the given range of 0.74-13 MPa. The values of the friction angle in the andesites reach 35.8-56.1° compared to <56.7° and 37-54° in Villeneuve and Heap (2021) and Schaefer et al. (2023), respectively, while the friction angle of the ignimbrites is significantly higher with 55.1° versus < 35 ° in (Moon 1993).

Hoek-Brown coefficient m_i

The Hoek Hoek-Brown coefficient m_i is compared for the lava flow samples (M3, M4, M6, M9, M10) with Schaefer et al. (2023). A slightly wider but similar range can be found in the Misti samples. While in Schaefer et al. (2023) most values range around 40-50, some reach maximal 55.64 and minimal 39.61. The samples from Misti show both lower (35.3) and higher (60.2) m_i values. For the ignimbrites no fitting values have been found. But if compared to other volcanic rocks, the m_i values fit to by Mordensky et al. (2022) described strongly altered volcanic rocks with a range of 5-31 (Mordensky et al. 2022) and 5.6-29 in the samples from Misti.

Tensile strength

Tensile strength of the ignimbrites does not differ significantly for the samples of M1 and M2, being at the lower end of the given range (1.3 – 7.1 MPa) by Moon (1993) while M7 and M8 are significantly lower with 0.78±0.06 and 0.98±0.21 MPa. The andesites' tensile strength of 3.13-5.2 MPa is slightly lower than in Heap et al. (2021)with indirect tensile strength to 4.2-6.5 MPa and falls within the range of Mordensky et al. (2022) with 1.87-8.55 MPa.

5.3.2 Correlation of geotechnical parameters

For the correlation of the geotechnical parameters the Spearman rank correlation is used, because a normal distribution of the data is not necessary. Therefore, the requirements are met for the data of cohesion, m_i and friction angle. Only significant correlation with a p-value <0.05 and a r^2 of >0.5 are described and discussed (figure 79).

By taking a closer look at the correlation coefficient given by Spearman correlation, the high correlation coefficient values between porosity and nearly all other parameters, except Poisson's ratio and Vp-reduction stand out. In addition, correlations between related parameters like UCS and Young's modulus, UCS and σ_{ci} or cohesion, friction angle and σ_{ci} occur.

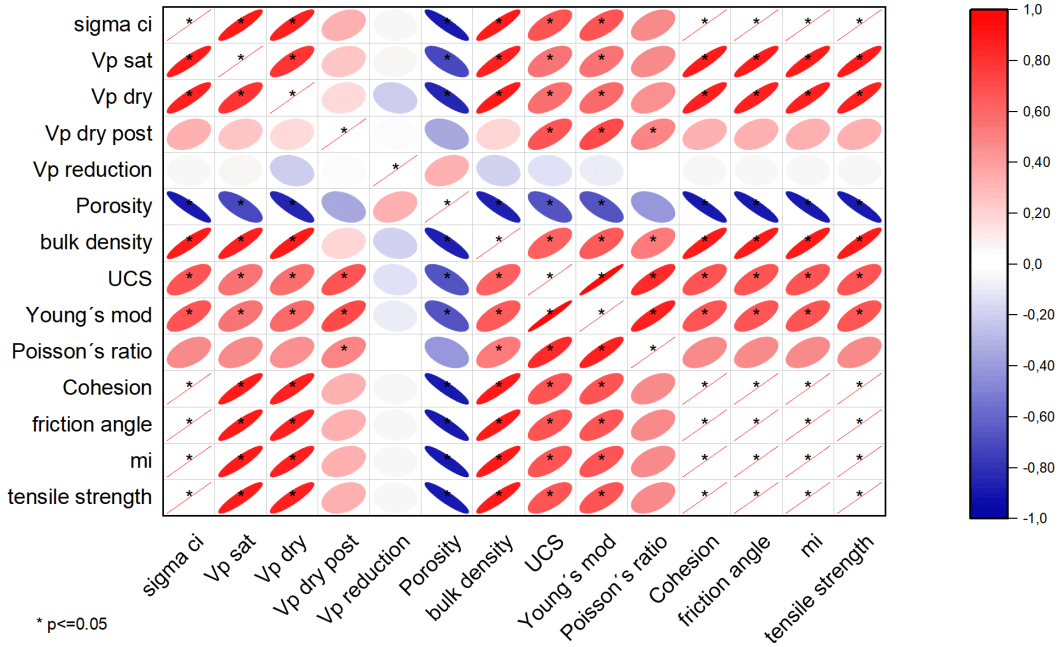

Figure 79: Correlation matrix of the geotechnical parameter

UCS, σ_{ci} and cohesion correlation with porosity

The UCS, the calculated σ_{ci} and cohesion show a trend to decrease rapidly with increasing porosity (figure 80 A & C). This trend is also described in Heap and Violay (2021) and compared to the effect known in sedimentary rocks. Similar to Heap and Violay (2021) a significant scattering of the data occurs, as for the UCS values of 59.28 MPa up to 124.1 MPa can be found at approximately 5 % porosity. This effect is even stronger in σ_{ci}. Noticeably the scattering is decreasing with increasing porosity as also described in Heap and Violay (2021). The scattering is traced back to microstructural differences as pore size and shape and alteration differences (Heap and Violay 2021). As shown in figure 80 A, the uniaxial compressive strength can be displayed as a nonlinear function of porosity. As an explanation for the stability decrease with porosity, the pore crack model of Sammis and Ashby (1986) is described in Heap and Violay (2021). Heap et al. (2016) conducted a simulated numerical measurement with pore spaces, showing fracture propagation starting from the pores and interconnecting. Also, the described function of the decreasing cohesion with increasing porosity, as demonstrated by Heap and Violay (2021) too, can be seen nicely in figure 80 B. The scattering of the UCS data at low porosities is present again, ranging at 5 % porosity from 6.3 to 20.1 GPa.

Tensile strength and porosity correlation

The tensile strength of the samples shows a decreasing trend with increasing porosity (figure 80 C). In contrast to Heap and Violay (2021) the declining function is almost linear. A high difference between median and mean values is not visible, but again scattering at low porosity occurs, at 5 % porosity the tensile strength ranges from 2.56 to 4.31 MPa. As a source of decreasing strength similar reasons as for the UCS are assumed.

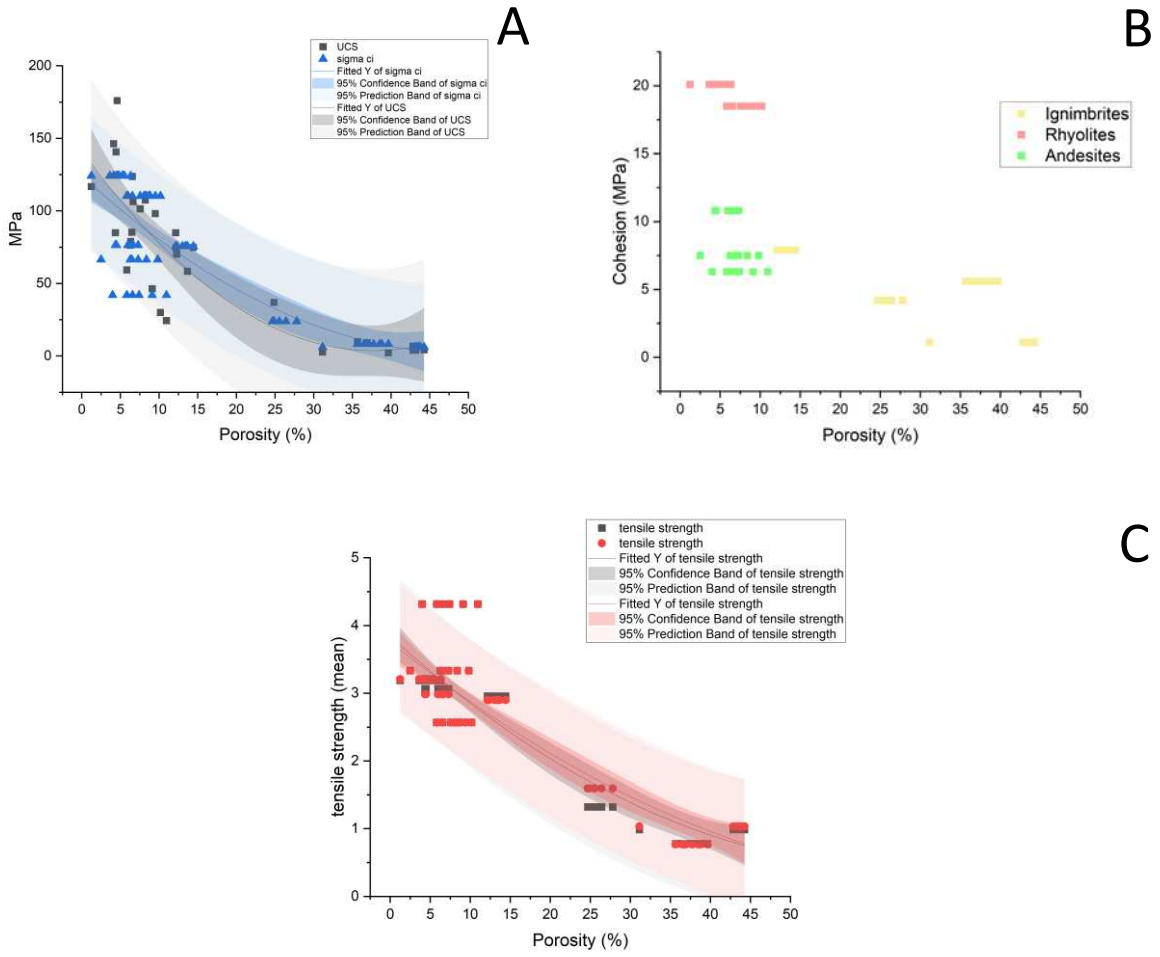

Figure 80: Correlation between UCS [A], cohesion [B] and tensile strength [C] versus porosity

P wave velocity

As described in multiple publications such as Heap et al. (2021) and Heap et al. (2016), the porosity seems to be a dominant factor in the control of nearly all geotechnical parameters. The p values show a strong negative correlation of -0.79 to -0.89 with the Vp sat, Vp dry and Vp post, UCS, Youngs modulus, bulk density, cohesion, friction angle and tensile strength.

If plotted against the porosity it stands out, that with increase of porosity a rapid decrease of p wave velocity occurs (figure 81). The decrease of velocity does not differ from saturated to dried sample, but in comparison to post failure testing the difference is noticeable. The curve

of Vp post with porosity is here almost linear in shape. Also, the correlation coefficient changes from around -0.82 to -0.79. The decrease in velocity with porosity is typical, because compressive waves are faster in water or solid rock than in gas (Xayavong et al. 2020). It is interesting, that still with a saturated sample the decrease is similar as in the dry state and in samples with very high porosity the values of the saturated versus the dried sample are as strong as at low porosities. This could be correlated to a higher content of isolated pores in the samples with lower porosity. The missing correlation of the Vp reduction to the porosity can have multiple reasons. On the one hand there is the possibility that failure occurs before major pore closure. Or on the other hand, a stronger interconnection of existing pores and formation of cracks leads to a higher connected porosity. This is supported by the oil contaminated values, which show higher p wave velocities than the water saturated samples. It has to be noted, that neither the different properties of oil and water, nor the saturation time has been taken into account in the correlation.

The p-wave velocity correlation with other parameters, like UCS, Youngs modulus, bulk density, cohesion, friction angle and tensile strength, is most likely caused by the correlation with the porosity.

Therefore, the major influence factor for nearly all measured geotechnical parameters is the porosity.

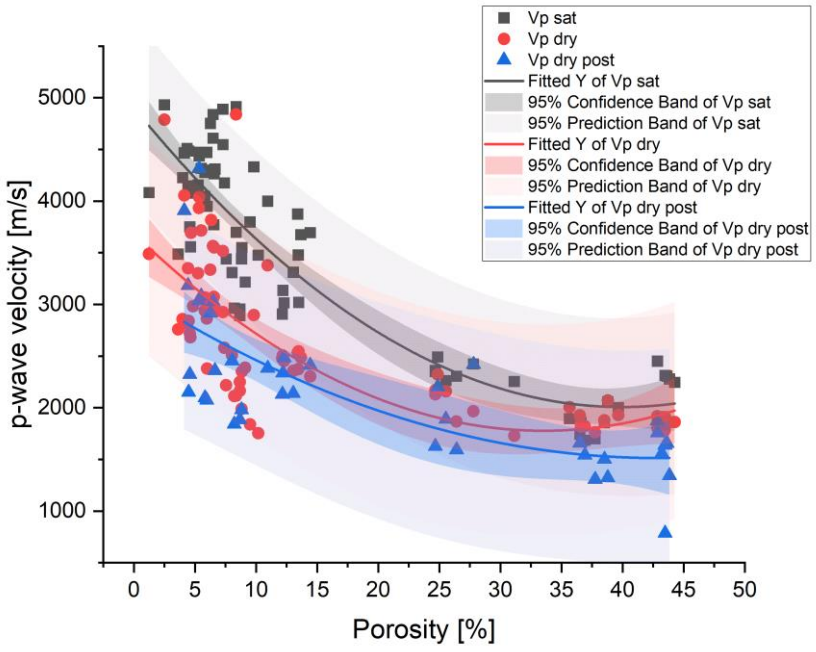

Figure 81: P-wave velocity of saturated and dry samples before and after UCS- or TCS-testing versus porosity

5.4 Correlation between geology and geotechnics

5.4.1 General

For the correlation with the geotechnical parameters, the geological parameters SiO_2, K_2O, Fe_2O_3, Na_2O in % besides the content of phenocrysts [%], maximum phenocryst size, pore size and maximal fracture size from the BIB-SEM are used. Caused by the limited number of values, a ranked correlation after Spearman is best suited. For the meaningfulness of correlation, it must be pointed out, that many of the geological data, as described in chapter 5.1 "Acknowledgment of error sources and uncertainties" represent only a very local condition and composition. Therefore, correlations, even if they show significance, cannot be seen as necessarily true correlations, rather as tendencies.

Considering all data some minor correlations between the geological properties occur. Mostly tendencies between the compressive strength parameters and the phenocryst amount are shown, occasionally also pore size and fractures. As discussed in the chapter Correlation of geotechnical parameter the porosity has a major influence on the rock strength. To reduce the porosity effect and other effects, like the ones between pyroclastic rocks and rhyolites, which are very similar in composition, the dataset is separated into the "Pyroclastics" group of M1, M2, M7 and M8 and the "Effusives" group, consisting of M3, M4, M6, M9 and M10. Through this separation the data amount for the correlation is further decreased, decreasing the statistic validity.

5.4.2 Correlations in pyroclastic rocks

Taking only the ignimbrite properties into consideration, new tendencies are revealed. Besides the still present effects of porosity, the content of phenocrysts, the iron content, pore and fracture size show correlation coefficients > 0.8. According to the Spearman correlation of the ignimbrite data, a strong negative tendency with $r^2 = 0.94$ can be found between the phenocryst content and the porosity. As described in the geotechnical parameter correlation, the porosity has a strong negative correlation with most rock mechanical parameters. Therefore, the phenocrysts show a positive relation, reaching from $r^2 = 0.65$ in the Vp post, over $r^2 = 0.742$ in the tensile strength to $r^2 = 0.90$ in the Young's modulus. Exceptions are here the Poisson's ratio, which shows no significance, as well as friction angle and m_i, where the correlation coefficient lies below 0.5. This negative correlation between porosity and phenocryst amount has also been described by Zorn et al. (2018). The investigations of lava dome and ash and block flow deposits of Mt Taranaki (NZ) showed a correlation between rock strength, porosity and phenocryst content. The suggested reason was crystallization and degassing in an undercooled magma, experiencing stiffening under higher pressures (Zorn et al. 2018). If applied to the ignimbrites, a differing phenocryst content could indicate a differing

ascent, preeruptive degassing and preeruptive cooling rate. For application of the theory to the samples of Misti, the way of deposition of ignimbrites, the amount of secondary porosity and welding can be seen as objection, because the origin and closure of the pores differs for the samples of Zorn et al. (2018). This might be the reason, why this correlation is rather weak (r^2= -0.475), if all lithologies are considered.

Beside the melt development, the data allow two different interpretations. One possible interpretation is, that an increased phenocryst content leads to an increase of rock strength. The other possible interpretation is, that the porosity is overriding this effect, leading to an increase in strength with phenocryst content, while porosity is still the controlling factor. In addition, the influence of the phenocrysts is less significant than porosity and cannot be determined by this data set.

In favor of the first statement, the strengthening of the rock with increasing phenocryst content, different approaches can be made. Chen et al. (2023) investigate the dependence of different mineral content in sedimentary rocks, like carbonates, sandstone and shales. The result did show a dependence of effect of mineral content on the rock strength. While in sandstone quartz increase the strength, the same mineral causes a decrease in carbonates and shows no effect in shales. Even if volcanic rocks differ significantly in many ways, it shows the complexity of mineral and crystal or grain content and rock strength. From a material sciences perspective, the porphyry texture of a volcanite is similar to concrete with its aggregates. As shown in Meddah and Salim (2010), the aggregate has an optimal content, differing contents lead to strength weakening. Taking these two publications into account, it could be, that under certain circumstances the phenocrysts can control and increase the rock strength, by interlocking and supporting a weaker matrix. In contrast they can cause local areas of higher stress resulting in rock failure and fracture propagation.

As in favor of the second interpretation, a minor effect or even a strength weakening by an increased phenocryst content, the following processes are possible. Zorn et al. (2018) imply a correlation of porosity and crystal content to the rock strength, represented by a triaxial strength at 3 MPa confined pressure and tensile strength. It is also mentioned that the discrimination of the individual relative influence on properties are difficult. A sample with both relatively high values of porosity and crystal content indicated a dominant failure control of porosity. Similar observations have been done by a simulation of Heap et al. (2016), leading to the conclusion that both crystal content and porosity have a negative influence on rock strength. The simulation was done with weaker phenocrysts than matrix, to represent microcracks and defects common in crystals of volcanic rocks (Heap et al. 2016). Microcracks have also been observed in this thesis Broad ion beam scanning microscope (BIB-SEM). The decrease of rock strength with increasing porosity was quantified with the factor 7.6 while

with an increase of crystal content with 1.4. Having said this, in Heap et al. (2016) the crystal composition, shape and size distribution, changing matrix conditions, pore size and shape have not been considered. Further, the displayed combined simulations of porosity and crystal fraction consider only a crystal content of up to 40% and a porosity of 25 %. Therefore, Heap et al. (2016) miss the influence of minor crystals contents at high porosity, as found in the samples of Misti.

In conclusion, it can be said that even if the data show an increase of the stability with increase of crystal content, it is more likely that the controlling factor of porosity is causing this effect (figure 82). Even if there are some factors missing in literature, the significantly stronger decrease in porosity would need a major effect from the phenocrysts, which should be also visible throughout the whole dataset, which it is not. Nevertheless, the effect of probably more stable phenocrysts in a highly porous rock, such as the ignimbrites, has not been sufficiently investigated. An apex point of optimal phenocryst content is conceivable.

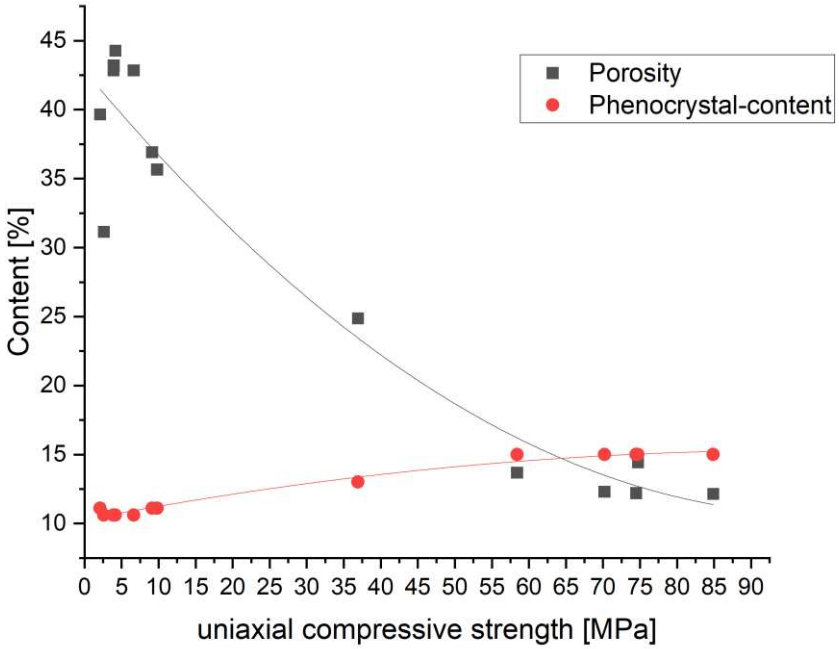

Figure 82: Phenocrystal content and porosity versus the uniaxial compressive strength

Influence of the pore size on the geotechnical parameters of Ignimbrites

A similar, but reversed correlation as for the phenocryst content occurs for the pore size (figure 83). The positive correlation between porosity and pore size has been already found by Heap et al. (2014) and Heap and Violay (2021). The influence of the pore size is difficult to determine, because the size is dependent on the point of measuring and the pore shape. In addition, the pore sizes have a high variation and to find fitting samples in nature is difficult.

Nevertheless, the pore size seems to amplify with the already described decrease of strength with increasing porosity. Heap et al. (2014) describe this effect as well and suggest that the best fitting modeled rock strength will be the one modeled with the largest pore size because the larger vesicles cause an increase of stress required to "propagate vesicle emanating microcracks" (Heap et al. 2014).

Influence of the fracture size on the geotechnical parameters of Ignimbrites

The influence of fracture size is less dominant than prior characteristics, even if significantly weaker coefficients occur, same relations as for the pore size occur. Noticeably, for the fracture size a negative correlation tendency between the p-wave velocity is visible (r^2=-0.52 to -0.69). The negative correlation to density seems logical as does the negative correlation to UCS, Youngs modulus, cohesion, friction angle, and tensile strength. In conclusion, a weakening of the rock through larger fractures is supported by the data.

A positive correlation between Fe_2O_3 from the XRF results to the porosity and a negative correlation to density was found. The amount of iron containing phases make an assignment to a certain mineral not possible. Therefore, a reasonable explanation for this relation has not been found.

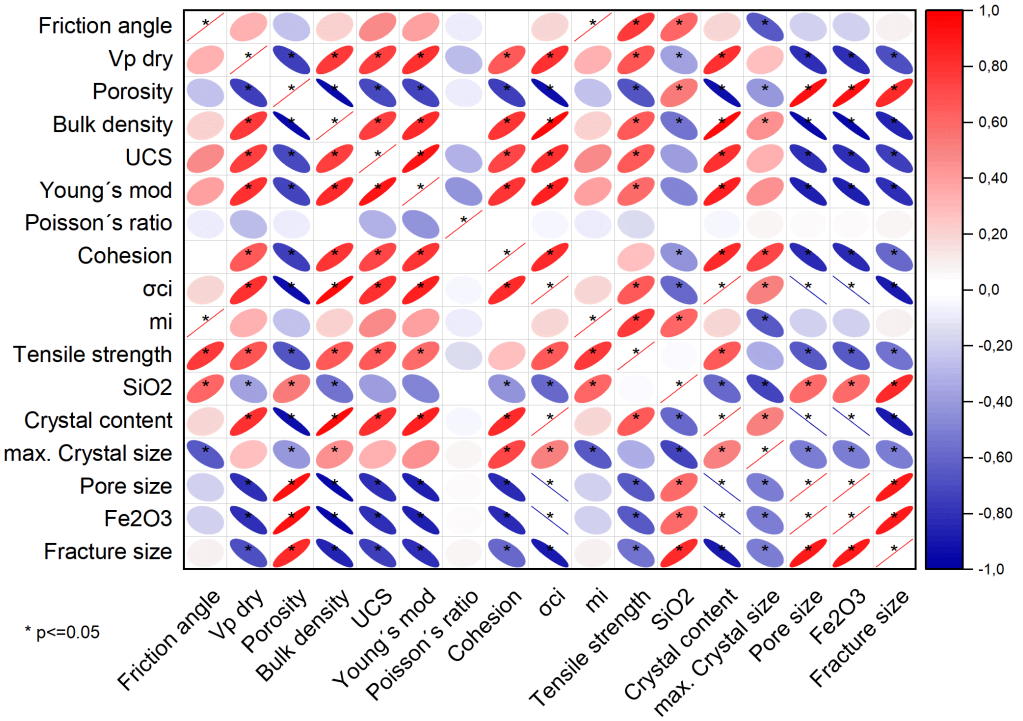

Figure 83: Correlation matrix after Spearman with the marked significance >0.05

5.4.3 Correlations in effusive rocks

The correlation of the effusive rocks, consisting of rhyolites and andesites, differs from the pyroclastic rocks. Even if the porosity is still a controlling factor, the phenocryst content shows no or weak correlation to rock strength parameters. An exception is the tensile strength. For tensile strength, a decreasing trend of tensile strength with increasing phenocryst content (r^2= -0.88) occurs, correlating with porosity, supporting the observations made by Heap et al. (2016) and Zorn et al. (2018). In those quite low porosity lithologies, the increase of weaker crystal content leads to local failure and growth of fractures propagating from those failed crystals (Heap et al. 2016). Caused by a higher crystal content in the samples also the chain and cluster formation theory of Heap et al. (2016) is possible, even if it was not observed in the samples (figure 83).

More dominant correlations can be seen between SiO_2 and K_2O content and the UCS, Young's modulus, cohesion friction angle and m_i (r^2=0.60(UCS and Young's modulus), 0.96 (friction angle)). Noticeably, no correlation with tensile strength has been found. Fe_2O_3 shows a reversed trend in comparison to the SiO_2.

The SiO_2 and K_2O content can be seen as representatives of the matrix. In the SEM both oxides were dominant in the matrix composition, especially in the rhyolites. There are multiple reasons, why this relation between rock strength and matrix occurs. First, a change of composition can influence the property of the volcanic glass. Unfortunately, no publications on this topic have been found, making it difficult to discuss this hypothesis. Nevertheless, it is known that SiO_2 is a chain building component of the melt (Markl 2014), and it is possible that this silica chains influence the stability of the volcanic glass. Second, samples M3 and M4, representing the rhyolites, show signs of devitrification. These fine SiO_2 and feldspar crystals might change the property of the matrix, even closing cooling fractures and therefore lead to an overall strength increase. This devitrification occurs far more frequent in high silica rocks like rhyolites glass (Marshall 1961). Alternatively, the SiO_2 content simply represents the amount of matrix in contrast to the phenocrysts, which can cause a decrease of strength in many volcanic rocks (Heap et al. 2016), as discussed above.

In addition, pore size has a negative ratio to tensile strength. Also, minor tendencies have been found. Pore size has only minor negative influence on cohesion, friction angle and m_i. This observation fits to the observations of Heap et al. (2014). Surprisingly no influence on UCS and tensile strength was observed (figure 84).

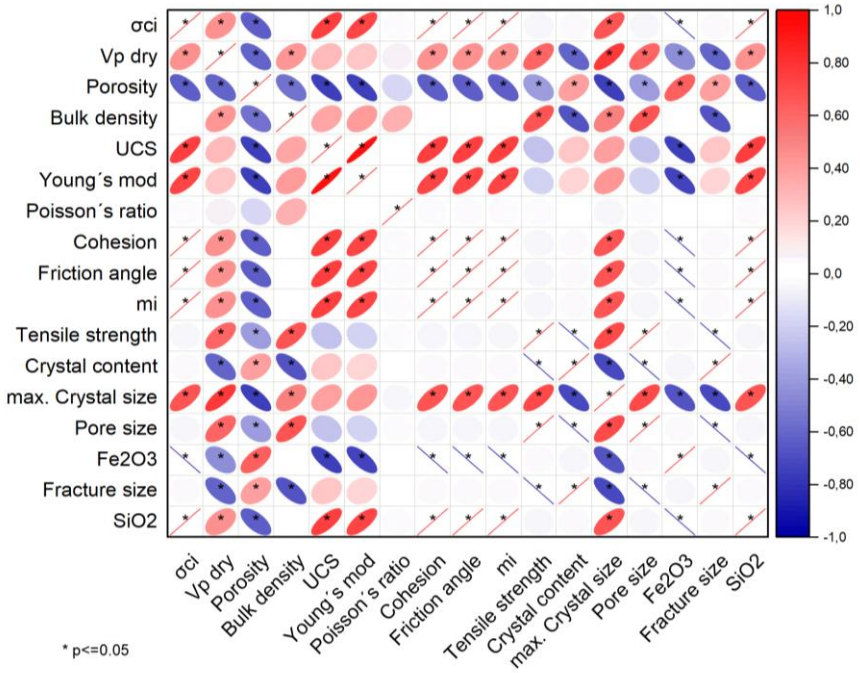

Figure 84: Correlation matrix of geotechnical and geological parameter for effusive rocks

6 Conclusions

The volcanic rocks of Misti, consisting of ignimbrites, andesites and rhyolites show variations in their composition, mineralogy and rock strength. These parameters partly correlate and allow the following geological statements about the investigated samples:

- The ignimbrites of Misti are homogeneous in composition and geochemistry. All are rhyolitic in composition, also the mineralogical composition is very similar
- The rhyolites of Misti are very similar in composition to the ignimbrites and show similar mineralogical compositions
- The andesites differ significantly from each other in geochemistry, the samples from Rio Andamayo almost reach a trachyandesitic composition. Even if the geochemistry differs, the mineralogy is similar, with differences only in total crystal content
- All samples show a high-K calc alkaline trend, typical for subduction related volcanism

The geotechnical parameters of the samples show similar results as found on other stratovolcanoes. Differences have been found for the friction angle, cohesion and mi, which show a high variability. The main statement for the general geotechnics is:

- The porosity is a dominant strength controlling factor in all samples

If separated into lava flow and pyroclastic rock samples further can be said:

- In the pyroclastic rocks the main strength controlling parameter is the porosity. Additionally, the crystal content, which shows a strong negative relation to porosity, influences the rock stability. Whether the increase in rock strength is caused by the decrease of porosity or by the increase of crystal content could not be determined.
- The lava flow samples show also another factor of influence, namely the matrix composition. An increase in SiO_2, representing the matrix, leads to an increase of strength in the samples. Due to the low variation in porosity in those samples, the effect of the matrix is considered as significant.

Due to the intercorrelation of different parameters a quantification of those factors of influence is difficult to determine. Therefore, further research is necessary.

7 List of figures

8 List of tables

9 References

Ali, Asif; Zhang, Ning; Santos, Rafael (2023): Mineral Characterization Using Scanning Electron Microscopy (SEM): A Review of the Fundamentals, Advancements, and Research Directions. In: *Applied Sciences* 13, S. 12600. DOI: 10.3390/app132312600.

Anderson, Don (1983): Chemical Composition of the Mantle. In: *Journal of Geophysical Research Atmospheres* 14, S. 41. DOI: 10.1029/JB088iS01p00B41.

ASTM (2019): D4543-19: Practices for Preparing Rock Core as Cylindrical Test Specimens and Verifying Conformance to Dimensional and Shape Tolerances. DOI: 10.1520/D4543-19

ASTM (2000): D 2845-00. Standard Test Method for Laboratory Determination of Pulse Velocities and Ultrasonic Elasitc Constants of Rock. https://doi.org/10.1520/D2845-00.

Barsanescu, Paul; Sandovici, Adrian; Serban, Alexandru (2018): Mohr-Coulomb criterion with circular failure envelope, extended to materials with strength-differential effect. In: *Materials & Design* 148, S. 49–70. DOI: 10.1016/j.matdes.2018.03.043.

Basu, Arindam; Mishra, Deepak; Roychowdhury, Kaberi (2013): Rock failure modes under uniaxial compression, Brazilian, and point load tests. In: *Bulletin of Engineering Geology and the Environment* 72. DOI: 10.1007/s10064-013-0505-4.

Bhattacharya, Sourabh; Panigrahi, Mruganka; Jayananda, Mudlappa (2014): Mineral thermobarometry and fluid inclusion studies on the Closepet Granite, Eastern Dharwar Craton, south India: Implications to emplacement and evolution of late-stage fluid. In: *Journal of Asian Earth Sciences* 91, S. 1–18. DOI: 10.1016/j.jseaes.2014.04.004.

Boschman, Lydian (2021): Andean mountain building since the Late Cretaceous: A paleoelevation reconstruction. In: *Earth-Science Reviews* 220, S. 103640. DOI: 10.1016/j.earscirev.2021.103640.

Chen, Po-Fei; Bina, Craig; Okal, Emile (2001): Variations in slab dip along the subducting Nazca Plate, as related to stress patterns and moment release of intermediate-depth seismicity and to surface volcanism. In: *Geochemistry Geophysics Geosystems - GEOCHEM GEOPHYS GEOSYST* 2. DOI: 10.1029/2001GC000153.

Chen, Zhen-Liang; Shi, Huai-Zhong; Xiong, Chao; He, Wen-Hao; Wang, Hai-Zhu; Wang, Bin et al. (2023): Effects of mineralogical composition on uniaxial compressive strengths of sedimentary rocks. In: *Petroleum Science* 20 (5), S. 3062–3073. DOI: 10.1016/j.petsci.2023.03.028.

Deer, William Alexander; Howie, Robert Andrew; Zussman, Jack (2013): An introduction to the rock-forming minerals: Mineralogical Society of Great Britain and Ireland.

Demonterova, E. I.; Ivanov, A. V.; Palessky, S. V.; Posokhov, V. F.; Karmanov, N. S.; Pel'gunova, L. A. (2023): Feldspar Megacrysts as a Source of Information on Crustal Contamination of Basaltic Melt. In: *Geochemistry International* 61 (7), S. 669–686. DOI: 10.1134/S0016702923070029.

Devine, Joseph D. (1995): Petrogenesis of the basalt-andesite-dacite association of Grenada, Lesser Antilles island arc, revisited. In: *Journal of Volcanology and Geothermal Research* 69 (1), S. 1–33. DOI: 10.1016/0377-0273(95)00024-0.

Dimitruk, Peter and Davidson, Michael W.: Microscope Alignment. Online available: https://static3.olympus-lifescience.com/data/olympusmicro/primer/techniques/polarized/images/polmicroalignmentfigure1.jpg?rev=5CF2.

Droop, G. T. R. (1987): A general equation for estimating Fe 3+ concentrations in ferromagnesian silicates and oxides from microprobe analyses, using stoichiometric criteria. In: *Mineral. mag.* 51 (361), S. 431–435. DOI: 10.1180/minmag.1987.051.361.10.

Drüppel, Kirsten; Lehmann, Christian (2009): Fire bombing of the Tell Halaf Museum in Berlin during World War II—new insights based on mineralogical observations. In: *European Journal of Mineralogy - EUROPEAN J MINERAL* 21, S. 443–456. DOI: 10.1127/0935-1221/2009/0021-1901.

Gertisser, Ralf; KELLER, J. (2003): Trace Element and Sr, Nd, Pb and O Isotope Variations in Medium-K and High-K Volcanic Rocks from Merapi Volcano, Central Java, Indonesia: Evidence for the Involvement of Subducted Sediments in Sunda Arc Magma Genesis. In: *Journal of Petrology - J PETROL* 44, S. 457–489. DOI: 10.1093/petrology/44.3.457.

Ghimire, Amrit; Noor-E-Khuda, Sarkar; Ullah, Shah Neyamat; Suntharavadivel, Thuraichamy (2022): Determination of Mohr–Coulomb failure envelope, mechanical properties and UPV of commercial cement-lime mortar. In: *Materials and Structures* 55 (4), S. 111. DOI: 10.1617/s11527-022-01959-z.

Gill, Robin (2010): Igneous rocks and processes. A practical guide. Chichester: Wiley-Blackwell.

Golovko, A.; Kaminsky, Felix (2010): The Shoshonite-Absarokite-Picrite Karashoho Pipe, Uzbekistan: An Unusual Diamond Deposit in an Atypical Tectonic Environment. In: *Economic Geology* 105, S. 825–840. DOI: 10.2113/gsecongeo.105.4.825.

Gribble, C. D.; Hall, A. J. (1985): A Practical Introduction to Optical Mineralogy. Dordrecht: Springer Netherlands.

Gribble, C. D.; Hall, A. J. (1992): Optical Mineralogy. Boston, MA: Springer US.

Grove, Timothy; Till, Christy; Krawczynski, Michael (2012): The Role of H2O in Subduction Zone Magmatism. In: *Annual Review of Earth and Planetary Sciences* 40, S. 413–439. DOI: 10.1146/annurev-earth-042711-105310.

Heap, M. J.; Xu, Tao; Chen, Chongfeng (2014): The influence of porosity and vesicle size on the brittle strength of volcanic rocks and magma. In: *Bulletin of Volcanology* 76. DOI: 10.1007/s00445-014-0856-0.

Heap, Michael J.; Violay, Marie E.S. (2021): The mechanical behaviour and failure modes of volcanic rocks: a review. In: *Bulletin of Volcanology* 83 (5), S. 33. DOI: 10.1007/s00445-021-01447-2.

Heap, Michael J.; Wadsworth, Fabian B.; Heng, Zhen; Xu, Tao; Griffiths, Luke; Aguilar Velasco, Andrea et al. (2021): The tensile strength of volcanic rocks: Experiments and models. In: *Journal of Volcanology and Geothermal Research* 418, S. 107348. DOI: 10.1016/j.jvolgeores.2021.107348.

Heap, Michael J.; Wadsworth, Fabian B.; Xu, Tao; Chen, Chong-feng; Tang, Chun'an (2016): The strength of heterogeneous volcanic rocks: A 2D approximation. In: *Journal of Volcanology and Geothermal Research* 319, S. 1–11. DOI: 10.1016/j.jvolgeores.2016.03.013.

Hoek, E. (1968): A simple triaxial cell for field and laboratory testing of rock. In Trans. Instn Min. Metall. (77), pp 22-236.

Hoek E. (2007): Practical Rock Engineering. Chapter 11: Rock Mass Properties.

Hollocher, Kurt: Petrology: Whole Rock Geochemical Discriminant Diagrams. Winchester and Floyd, 1977 Immobile trace elements and SiO2 classification for igneous rocks, especially volcanics. Geology Department, Union College. Schenectady, NY, U.S.A. online available: https://muse.union.edu/hollochk/files/2021/07/winchester_floyd_1977.xlsx, zuletzt geprüft am 29.09.2024.

Irvine, T. N.; Baragar, W. R. A. (1971): A Guide to the Chemical Classification of the Common Volcanic Rocks. In: *Can. J. Earth Sci.* 8 (5), S. 523–548. DOI: 10.1139/e71-055.

ISRM (1978): Suggested methods for determining tensile strength of rock materials. In: *International Journal of Rock Mechanics and Mining Sciences & Geomechanics Abstracts* 15 (3), S. 99–103. DOI: 10.1016/0148-9062(78)90003-7.

ISRM (1979): Suggested methods for determining water content, porosity, density, absorption and related properties and swelling and slake-durability index properties. In: *International Journal of Rock Mechanics and Mining Sciences & Geomechanics Abstracts* 16 (2), S. 143–151. DOI: 10.1016/0148-9062(79)91452-9.

ISRM (1983): Suggested methods for determining the strength of rock materials in triaxial compression: Revised version. In: *International Journal of Rock Mechanics and Mining Sciences & Geomechanics Abstracts* 20 (6), S. 285–290. DOI: 10.1016/0148-9062(83)90598-3.

Jaeger, J.; Cook, N.; Zimmerman, R. (2007): Fundamental of Rock Mechanics 4th edition. In: Blackwell publishing Ltd

Kretz, Ralph (1983): Symbols for rock-forming minerals. In: *American Mineralogist* 68 (1-2), S. 277–279.

Leake, Bernard; Woolley, Alan; Arps, Charles; Birch, William; Gilbert, Charles; Grice, Joel et al. (1997): Nomenclature of amphiboles; Report of the Subcommittee on Amphiboles of the International Mineralogical Association, Commission on New Minerals and Mineral Names. In: *American Mineralogist* 82, S. 1019–1037.

Lebti, Perrine; Jean-Claude, Thouret; Wörner, Gerhard; Fornari, Michel (2006): Neogene and Quaternary ignimbrites in the area of Arequipa, Southern Peru: Stratigraphical and petrological correlations. In: *Journal of Volcanology and Geothermal Research* 154, S. 251–275. DOI: 10.1016/j.jvolgeores.2006.02.014.

Lomize, M. G. (2008): The Andes as a peripheral orogen of the breaking-up Pangea. In: *Geotecton.* 42 (3), S. 206–224. DOI: 10.1134/S0016852108030047.

Macdonald, Ray; Bagiński, Bogusław; Belkin, Harvey E.; Stachowicz, Marcin (2019): Composition, paragenesis, and alteration of the chevkinite group of minerals. In: *American Mineralogist* 104 (3), S. 348–369. DOI: 10.2138/am-2019-6772.

Marguí, E.; Queralt, I.; Almeida, E. de (2022): X-ray fluorescence spectrometry for environmental analysis: Basic principles, instrumentation, applications and recent trends. In: *Chemosphere* 303, S. 135006. DOI: 10.1016/j.chemosphere.2022.135006.

Markl, Gregor (2015): Minerale und Gesteine. Berlin, Heidelberg: Springer Berlin Heidelberg.

Marshall, Royal R. (1961): Devitrification of Natural Glass. In: *GSA Bulletin* 72 (10), S. 1493–1520. DOI: 10.1130/0016-7606(1961)72[1493:DONG]2.0.CO;2.

McPhie L.; Doyle M.; Allen R. (1993): Volcanic Textures. A guide to the interpretation of textures in volcanic rocks: CODES Key Centre.

Meddah, Seddik; Salim, Zitouni (2010): Effect of Size and Content of Coarse Aggregate on the Compressive Strength of Concrete. In: *Construction and Building Materials* V. 24, pp. 505-512.

Moon, Vicki G. (1993): Geotechnical characteristics of ignimbrite: A soft pyroclastic rock type. In: *Engineering Geology* 35 (1), S. 33–48. DOI: 10.1016/0013-7952(93)90068-N.

Mordensky, S. P.; Villeneuve, M. C.; Kennedy, B. M.; Heap, M. J.; Gravley, D. M.; Farquharson, J. I.; Reuschlé, T. (2018): Physical and mechanical property relationships of a shallow intrusion and volcanic host rock, Pinnacle Ridge, Mt. Ruapehu, New Zealand. In: *Journal of Volcanology and Geothermal Research* 359, S. 1–20. DOI: 10.1016/j.jvolgeores.2018.05.020.

Mordensky, S. P.; Villeneuve, M. C.; Kennedy, B. M.; Struthers, J. D. (2022): Hydrothermally induced edifice destabilisation: The mechanical behaviour of rock mass surrounding a shallow intrusion in andesitic lavas, Pinnacle Ridge, Ruapehu, New Zealand. In: *Engineering Geology* 305, S. 106696. DOI: 10.1016/j.enggeo.2022.106696.

Morimoto, N. (1988): Nomenclature of Pyroxenes. In: *Mineralogy and Petrology* 39 (1), S. 55–76. DOI: 10.1007/BF01226262.

MTS Systems Corporation (Hg.) (2023): Triaxial Accessories for Rock Mechanics Testing. Replicate in situ conditions with exceptional accuracy. 100-213-762a TriaxialAccessories. *Triaxial testing solutions* 2023. USA.

Nitoi, Eugenia; Munteanu, Marian; Marincea, Stefan (2000): Magma – enclaves interaction in the subvolcanic zone of the East Carpathians.

Oyedotun, Temitope D. Timothy (2018): X-ray fluorescence (XRF) in the investigation of the composition of earth materials: a review and an overview. In: *Geology, Ecology, and Landscapes* 2 (2), S. 148–154. DOI: 10.1080/24749508.2018.1452459.

Peccerillo, Angelo; Taylor, S. R. (1976): Geochemistry of eocene calc-alkaline volcanic rocks from the Kastamonu area, Northern Turkey. In: *Contributions to Mineralogy and Petrology* 58 (1), S. 63–81. DOI: 10.1007/BF00384745.

Perras, Matthew A.; Diederichs, Mark S. (2014): A Review of the Tensile Strength of Rock: Concepts and Testing. In: *Geotech Geol Eng* 32 (2), S. 525–546. DOI: 10.1007/s10706-014-9732-0.

Pichler, H.; Schmitt-Riegraf, C. (1997): Rock-forming Minerals in Thin Section. Dordrecht: Springer Netherlands.

Prinz, Helmut; Strauß, Roland (2018): Ingenieurgeologie. Berlin, Heidelberg: Springer Berlin Heidelberg.

ÖNORM B 3124-9, 1986: Prüfung von Naturstein; mechanische Gesteinseigenschaften; Elastizitätsmodul, Arbeitslinie, Verformungsmodul und Querdehnungszahl bei einaxialer Druckbelastung.

ÖNORM EN 1926, 2007: Prüfverfahren für Naturstein - Bestimmung der einachsigen Druckfestigkeit.

Rieder, Milan; Cavazzini, Giancarlo; D'yakonov, Yurii S.; Frank-Kamenetskii, Viktor A.; Gottardi, Glauco; Guggenheim, Stephen et al. (1998): Nomenclature of the Micas. In: *Clays and clay miner.* 46 (5), S. 586–595. DOI: 10.1346/CCMN.1998.0460513.

Rivera, Marco; Martin, Herve; Le Pennec, Jean-Luc; Jean-Claude, Thouret; Gourgaud, Alain; Gerbe, Marie-Christine (2016): Petro-geochemical constraints on the source and evolution of magmas at El Misti volcano (Peru). In: *Lithos* 268. DOI: 10.1016/j.lithos.2016.11.009.

Sandri, Laura; Jean-Claude, Thouret; Constantinescu, Robert; Biass, Sebastien; Tonini, Roberto (2014): Long-term multi-hazard assessment for El Misti volcano (Peru). In: *Bulletin of Volcanology* 76. DOI: 10.1007/s00445-013-0771-9.

Schaefer, Lauren N.; Kereszturi, Gabor; Kennedy, Ben M.; Villeneuve, Marlène (2023): Characterizing lithological, weathering, and hydrothermal alteration influences on volcanic rock properties via spectroscopy and laboratory testing: a case study of Mount Ruapehu volcano, New Zealand. In: *Bulletin of Volcanology* 85 (8). DOI: 10.1007/s00445-023-01657-w.

Shi, Xiangyun; Misch, David; Vranjes-Wessely, Sanja (2023): A comprehensive assessment of image processing variability in pore structural investigations: Conventional thresholding vs. machine learning approaches. In: *Gas Science and Engineering* 115, S. 205022. DOI: 10.1016/j.jgsce.2023.205022.

Temiz, C. (2022): Scanning Electron Microscopy. In:

Thouret, Jean-Claude; Finizola, Anthony; Fornari, Michel; Legeley-Padovani, Annick; Suni, Jaime; Frechen, Manfred (2001): Geology of El Misti volcano near the city of Arequipa, Peru. In: *Geological Society of America Bulletin - GEOL SOC AMER BULL* 113, S. 1593–1610. DOI: 10.1130/0016-7606(2001)113<1593:GOEMVN>2.0.CO;2.

Tutluoglu, Levent; Öge, Ibrahim; Karpuz, Celal (2014): Relationship Between Pre-failure and Post-failure Mechanical Properties of Rock Material in Different Origin. In: *Rock Mechanics and Rock Engineering*.

Valido, J. A.; Cáceres, J. M.; Sousa, Luís M. O. (2023): Physical and mechanical properties of Ignimbrite from Arucas, Canary Islands. In: *Environmental Earth Sciences* 82 (13), S. 342. DOI: 10.1007/s12665-023-11024-9.

Villeneuve, Marlène C.; Heap, Michael J. (2021): Calculating the cohesion and internal friction angle of volcanic rocks and rock masses. In: *Volcanica* 4 (2), S. 279–293. DOI: 10.30909/vol.04.02.279293.

Vingiani, Simona; Scarciglia, Fabio; Mileti, Florindo; Donato, Paola; Terribile, Fabio (2014): Occurrence and origin of soils with andic properties in Calabria (southern Italy). In: *Geoderma* s 232–234, S. 500–516. DOI: 10.1016/j.geoderma.2014.06.001.

Weydt, Leandra M.; Ramírez-Guzmán, Ángel Andrés; Pola, Antonio; Lepillier, Baptiste; Kummerow, Juliane; Mandrone, Giuseppe et al. (2021): Petrophysical and mechanical rock property database of the Los Humeros and Acoculco geothermal fields (Mexico). In: *Earth Syst. Sci. Data* 13 (2), S. 571–598. DOI: 10.5194/essd-13-571-2021.

Wilson, Marjorie (2000): Igneous Petrogenesis. Dordrecht: Springer Netherlands.

Winchester, J. A.; Floyd, P. A. (1977): Geochemical discrimination of different magma series and their differentiation products using immobile elements. In: *Chemical Geology* 20, S. 325–343. DOI: 10.1016/0009-2541(77)90057-2.

Xayavong, Viengthong; Vu, Minh; Duong, Nguyen; Tuan, Vu (2020): Seismic Refraction Exploration for Groundwater Potential Evaluations: A Case Study of Vientiane Province, Laos. In: *VNU Journal of Science Earth and Environmental Sciences* 36, S. 90–101. DOI: 10.25073/2588-1094/vnuees.4651.

Zepp, Harald (2011): Geomorphologie. Eine Einführung. 5., durchges. Aufl. Paderborn, München, Wien, Zürich: Schöningh (utb.de Bachelor-Bibliothek, 2164).

Zorn, Edgar U.; Rowe, Michael C.; Cronin, Shane J.; Ryan, Amy G.; Kennedy, Lori A.; Russell, James K. (2018): Influence of porosity and groundmass crystallinity on dome rock strength: a case study from Mt. Taranaki, New Zealand. In: *Bulletin of Volcanology* 80 (4), S. 35. DOI: 10.1007/s00445-018-1210-8.

10 Appendix

10.1 Abbreviations mineral names

Mineral abbreviations (Kretz 1983)

Abbreviations	Full name	Abbreviations	Full name
(C)px	(Clino)pyroxene	Olg	Oligoclase
Opx	Orthopyroxene	Or	Orthoclase
Di	Diopside	Lb	Labradorite
En	Enstatite	Kfs	Kali-feldspar
Aug	Augite	Sa	Sanidine
Amp	Amphibole	Qtz	Quartz
Hs	Hastingite	Liq	SiO_2 melt
Prg	Pargasite	Sph	Spherulites
Hbl	Hornblende	Sph-rad	Radial Spherulites
Ed	Edenite	Sph-ax	Axiolitic Spherulites
Ts	Tschermakite	Mag	Magnetite
Pl	Plagioclase	Ill	Illmenite
Ads	Andesine	Zrn	Zircon
An	Anorthite	Bt	Biotite

10.2 Abbreviations methods

Abbreviations	Full name
TCS	Triaxial compressive strength
UCS	Uniaxial (unconfined) compressive strength
DTS	Direct tensile strength
SEM-EDX	Scanning electron microscope -energy dispersive X-ray spectroscopy
BIB-SEM	Broad ion beam scanning electron microscope
XRF -WDX	X-ray fluorescence -wavelength dispersive X-ray spectroscopy

10.3 SEM-Measurements

10.3.1 Feldspar- SEM measurements- per formular unit [pfu] 1/8

Sample	Na	Si	Al	Ca	Ba	K	∑Cation
	[pfu]	[pfu]	[pfu]	[pfu]	[pfu]	[pfu]	[pfu]
M1 10	0,80	2,81	1,18	0,17	0,00	0,07	5,03
M1 11	0,80	2,80	1,19	0,19	0,00	0,07	5,04
M1 12	0,79	2,81	1,18	0,17	0,00	0,07	5,02
M1 13	0,79	2,83	1,16	0,16	0,00	0,08	5,03
M1 18	0,58	2,54	1,43	0,45	0,00	0,02	5,02
M1 19	0,83	2,87	1,12	0,14	0,00	0,08	5,03

Feldspar- SEM measurements- per formular unit [pfu] 2/8

Sample	Na	Si	Al	Ca	Ba	K	∑Cation
	[pfu]	[pfu]	[pfu]	[pfu]	[pfu]	[pfu]	[pfu]
M1 21	0,38	3,15	0,84	0,02	0,00	0,45	4,85
M1 23	0,40	2,97	1,04	0,01	0,01	0,53	4,97
M1 24	0,42	2,97	1,04	0,01	0,01	0,54	4,99
M1 25	0,62	2,59	1,42	0,37	0,00	0,02	5,02
M1 34	0,73	2,73	1,26	0,26	0,00	0,05	5,03
M1 35	0,55	2,52	1,48	0,46	0,00	0,02	5,03
M1 36	0,71	2,69	1,30	0,30	0,00	0,04	5,04
M1 37	0,80	2,82	1,17	0,16	0,00	0,07	5,03
M1 8	0,79	2,79	1,20	0,19	0,00	0,06	5,04
M1 9	0,79	2,79	1,20	0,18	0,00	0,06	5,03
M1-6	0,40	2,96	1,04	0,00	0,02	0,59	5,02
M1-N- 1	0,60	2,75	1,25	0,31	0,00	0,05	4,95
M1-N- 2	0,65	2,83	1,15	0,26	0,00	0,08	4,96
M1-N- 4	0,34	3,08	0,95	0,00	0,00	0,50	4,87
M2 11	0,67	2,59	1,32	0,50	0,00	0,00	5,08
M2 12	0,49	2,51	1,52	0,46	0,00	0,00	4,97
M2 13	0,43	2,49	1,55	0,48	0,00	0,00	4,95
M2 16	0,45	2,57	1,47	0,44	0,00	0,00	4,93
M2 18	0,39	2,99	1,03	0,00	0,00	0,57	4,97
M2 19	0,78	2,77	1,20	0,24	0,00	0,07	5,05
M2 20	0,58	2,52	1,43	0,50	0,00	0,03	5,07
M2 21	0,61	2,58	1,39	0,43	0,00	0,03	5,04
M2 22	0,64	2,60	1,37	0,41	0,00	0,02	5,04
M2 23	0,64	2,62	1,35	0,39	0,00	0,03	5,04
M2 24	0,69	2,65	1,31	0,37	0,00	0,04	5,06
M2 25	0,69	2,77	1,22	0,25	0,00	0,04	4,98
M2 26	0,66	2,85	1,14	0,22	0,00	0,08	4,95
M2 27	0,39	2,98	1,03	0,00	0,00	0,61	5,01
M2 28	0,41	2,91	1,11	0,00	0,06	0,51	5,00
M2 29	0,61	2,59	1,39	0,41	0,00	0,02	5,03
M2 30	0,63	2,60	1,36	0,43	0,00	0,03	5,05
M2 33	0,41	2,47	1,54	0,56	0,00	0,00	4,97
M2 36	0,58	2,56	1,42	0,43	0,00	0,00	4,99
M2 37	0,70	2,72	1,15	0,46	0,00	0,04	5,07
M2 38	0,64	2,62	1,28	0,33	0,00	0,05	4,92
M2 47	0,20	3,52	0,49	0,00	0,00	0,23	4,45
M2 48	0,79	2,81	1,18	0,17	0,00	0,07	5,03
M2 49	0,79	2,81	1,18	0,19	0,00	0,08	5,04
M2 50	0,67	2,83	1,17	0,22	0,00	0,05	4,95

Feldspar- SEM measurements- per formular unit [pfu] 3/8

Sample	Na	Si	Al	Ca	Ba	K	∑Cation
	[pfu]	[pfu]	[pfu]	[pfu]	[pfu]	[pfu]	[pfu]
M2 51	0,75	2,75	1,22	0,27	0,00	0,07	5,05
M2 52	0,75	2,74	1,24	0,25	0,00	0,05	5,03
M2 53	0,41	2,93	1,07	0,00	0,03	0,57	5,02
M2 54	0,75	2,76	1,23	0,24	0,00	0,06	5,04
M2 55	0,33	2,95	1,07	0,00	0,03	0,58	4,97
M3 1	0,48	2,42	1,53	0,61	0,00	0,02	5,06
M3 14	0,41	2,97	1,04	0,00	0,00	0,57	5,00
M3 15	0,33	3,02	1,00	0,00	0,00	0,61	4,95
M3 2	0,48	2,42	1,56	0,57	0,00	0,01	5,05
M3 22	0,47	3,12	0,87	0,00	0,00	0,43	4,89
M3 23	0,82	2,82	1,17	0,17	0,00	0,07	5,05
M3 24	0,20	3,54	0,47	0,01	0,00	0,24	4,45
M3 25	0,51	3,25	0,74	0,05	0,00	0,14	4,70
M3 26	0,77	2,77	1,22	0,21	0,00	0,06	5,03
M3 3	0,61	2,57	1,41	0,43	0,00	0,02	5,04
M3 4	0,49	2,59	1,41	0,45	0,00	0,03	4,96
M3 5	0,56	2,51	1,44	0,54	0,00	0,02	5,07
M3 6	0,51	2,44	1,52	0,58	0,00	0,02	5,07
M3-Z- 13	0,34	3,17	0,83	0,00	0,00	0,48	4,83
M3-Z- 17	0,19	3,58	0,43	0,00	0,00	0,20	4,40
M3-Z- 2	0,61	2,88	1,11	0,24	0,00	0,07	4,90
M3-Z- 21	1,05	2,84	1,03	0,22	0,00	0,07	5,20
M3-Z- 22	0,89	2,84	1,06	0,26	0,00	0,07	5,12
M3-Z- 23	0,67	2,76	1,26	0,25	0,00	0,00	4,94
M3-Z- 24	0,57	2,56	1,41	0,47	0,00	0,00	5,02
M3-Z- 25	0,79	2,84	1,10	0,23	0,00	0,08	5,04
M3-Z- 3	0,52	3,35	0,64	0,00	0,00	0,16	4,67
M3-Z- 5	0,41	3,01	0,97	0,00	0,00	0,62	5,01
M3-Z- 7	0,75	2,81	1,18	0,19	0,00	0,08	5,01
M3-Z- 8	0,21	3,64	0,35	0,00	0,00	0,17	4,37
M3-Z- 9	0,18	3,36	0,65	0,00	0,00	0,41	4,60
M4 10	0,52	3,04	0,98	0,03	0,00	0,34	4,90
M4 13	0,41	2,97	1,04	0,01	0,00	0,56	5,00
M4 15	0,40	2,96	1,02	0,02	0,00	0,65	5,05
M4 23	0,80	2,79	1,19	0,21	0,00	0,07	5,05
M4 27	0,55	2,49	1,47	0,52	0,00	0,04	5,07
M4 29	0,35	3,28	0,70	0,02	0,00	0,36	4,72
M4 30	0,62	3,15	0,84	0,07	0,00	0,14	4,81
M4 36	0,79	2,79	1,19	0,20	0,00	0,07	5,05

Feldspar- SEM measurements- per formular unit [pfu] 4/8

Sample	Na	Si	Al	Ca	Ba	K	∑Cation
	[pfu]	[pfu]	[pfu]	[pfu]	[pfu]	[pfu]	[pfu]
M4 37	0,71	2,81	1,18	0,23	0,00	0,06	4,99
M4 38	0,59	2,56	1,40	0,46	0,00	0,03	5,04
M4 39	0,50	2,54	1,47	0,47	0,00	0,01	4,98
M4 4	0,38	3,05	0,97	0,01	0,00	0,52	4,92
M4 40	0,39	2,99	1,01	0,00	0,00	0,62	5,01
M4 41	0,80	2,82	1,15	0,18	0,00	0,09	5,04
M4 5	0,40	3,04	0,96	0,00	0,00	0,55	4,96
M4 8	0,48	3,04	0,96	0,00	0,00	0,45	4,94
M4 9	0,34	3,15	0,82	0,03	0,00	0,51	4,86
M4-2- 10	0,34	2,99	1,03	0,00	0,00	0,62	4,98
M4-2- 11	0,39	3,08	0,90	0,00	0,00	0,58	4,96
M4-2- 12	0,32	3,59	0,41	0,00	0,00	0,11	4,42
M4-2- 13	0,38	3,41	0,62	0,00	0,00	0,12	4,53
M4-2- 15	0,41	3,01	1,01	0,00	0,00	0,52	4,95
M4-2- 16	0,50	3,08	0,94	0,00	0,00	0,33	4,86
M4-2- 17	0,39	3,30	0,73	0,00	0,00	0,25	4,66
M4-2- 18	0,40	3,10	0,92	0,00	0,00	0,44	4,86
M4-2- 19	0,07	3,93	0,07	0,00	0,00	0,00	4,07
M4-2- 20	0,04	3,87	0,14	0,00	0,00	0,05	4,10
M4-2- 22	0,40	3,09	0,92	0,00	0,00	0,46	4,87
M4-2- 24	0,42	3,17	0,84	0,00	0,00	0,41	4,83
M4-2- 25	0,51	2,59	1,38	0,48	0,00	0,00	4,97
M4-2- 26	0,67	2,69	1,27	0,39	0,00	0,00	5,01
M4-2- 27	0,70	2,70	1,28	0,32	0,00	0,04	5,03
M4-2- 28	0,78	2,84	1,17	0,15	0,00	0,06	4,99
M4-2- 29	0,91	2,86	1,08	0,17	0,00	0,06	5,08
M4-2- 30	0,56	2,59	1,41	0,41	0,00	0,00	4,98
M4-2- 31	0,56	2,55	1,48	0,39	0,00	0,00	4,99
M4-2- 32	0,59	2,77	1,20	0,33	0,00	0,08	4,97
M4-2- 33	0,67	2,88	1,12	0,18	0,00	0,09	4,94
M4-2- 35	0,37	3,00	1,03	0,00	0,00	0,56	4,95
M4-2- 36	0,34	3,05	0,95	0,00	0,00	0,57	4,93
M4-2- 38	0,38	3,00	1,04	0,00	0,00	0,51	4,93
M4-2- 40	0,69	2,87	1,14	0,18	0,00	0,06	4,94
M4-2- 7	0,41	3,00	0,99	0,00	0,00	0,61	5,01
M4-2- 8	0,37	3,00	1,02	0,00	0,00	0,59	4,98
M4-2- 9	0,38	3,00	1,01	0,00	0,00	0,57	4,97
M6 15	0,28	3,24	0,69	0,00	0,00	0,35	4,56
M6 19	0,34	2,36	1,65	0,62	0,00	0,02	5,00

Feldspar- SEM measurements- per formular unit [pfu] 5/8

Sample	Na	Si	Al	Ca	Ba	K	∑Cation
	[pfu]	[pfu]	[pfu]	[pfu]	[pfu]	[pfu]	[pfu]
M6 20	0,47	2,59	1,33	0,55	0,00	0,07	5,02
M6 23	0,44	2,54	1,46	0,51	0,00	0,02	4,96
M6 24	0,45	2,88	1,06	0,28	0,00	0,21	4,88
M6 8	0,45	2,97	1,03	0,23	0,00	0,13	4,81
M6/2- 11	0,49	2,46	1,46	0,64	0,00	0,00	5,05
M6/2- 13	0,33	2,43	1,62	0,55	0,00	0,00	4,93
M6/2- 14	0,37	2,47	1,59	0,49	0,00	0,00	4,92
M6-2- 2	0,41	3,09	0,91	0,13	0,00	0,23	4,78
M6-2- 3	0,31	3,13	0,87	0,15	0,00	0,26	4,72
M6-2- 36	0,33	2,42	1,52	0,70	0,00	0,02	4,99
M6-2- 39	0,49	2,76	1,20	0,39	0,00	0,09	4,93
M6-2- 4	0,54	2,75	1,20	0,38	0,00	0,11	4,97
M6-2- 46	0,39	3,07	0,92	0,19	0,00	0,20	4,77
M6-2- 47	0,59	2,76	1,21	0,34	0,00	0,07	4,97
M6-2- 7	0,59	2,78	1,26	0,24	0,00	0,06	4,91
M7_ 15	0,48	2,45	1,49	0,61	0,00	0,00	5,04
M7_ 20	0,77	2,79	1,23	0,19	0,00	0,00	4,98
M7_ 22	0,17	3,08	0,92	0,00	0,00	0,76	4,93
M7_ 23	0,45	2,95	1,05	0,00	0,00	0,60	5,05
M7_ 24	0,76	2,76	1,25	0,20	0,00	0,07	5,03
M7_ 25	0,29	3,06	1,01	0,00	0,00	0,45	4,81
M7_ 26	0,75	2,83	1,17	0,21	0,00	0,00	4,96
M7_ 27	1,06	2,83	0,99	0,28	0,00	0,08	5,24
M7_ 28	0,79	2,75	1,23	0,24	0,00	0,06	5,06
M7_ 29	0,00	3,90	0,11	0,00	0,00	0,07	4,08
M7_ 30	0,51	3,09	0,91	0,00	0,00	0,38	4,90
M7_ 31	0,83	3,06	0,72	0,00	0,00	0,74	5,36
M7_ 36	0,38	2,98	1,01	0,00	0,00	0,67	5,04
M7_ 4	0,88	2,85	1,11	0,16	0,00	0,11	5,09
M7_ 40	0,65	2,55	1,42	0,43	0,00	0,00	5,06
M7_ 41	1,01	2,85	1,00	0,24	0,00	0,10	5,20
M7_ 46	0,80	2,76	1,22	0,22	0,00	0,07	5,07
M7_ 47	0,86	2,82	1,19	0,15	0,00	0,00	5,02
M7_ 48	0,78	2,86	1,12	0,17	0,00	0,08	5,01
M7_ 49	0,74	2,88	1,09	0,18	0,00	0,08	4,98
M7_ 5	0,64	2,93	1,06	0,18	0,00	0,08	4,90
M7_ 50	0,55	2,88	1,13	0,26	0,00	0,00	4,82
M7_ 51	0,89	2,82	1,09	0,24	0,00	0,09	5,13
M7_ 52	0,69	2,76	1,24	0,25	0,00	0,04	4,98

Feldspar- SEM measurements- per formular unit [pfu] 6/8

Sample	Na	Si	Al	Ca	Ba	K	∑Cation
	[pfu]	[pfu]	[pfu]	[pfu]	[pfu]	[pfu]	[pfu]
M7_ 53	0,55	2,61	1,40	0,39	0,00	0,00	4,96
M7_ 6	0,37	3,03	0,97	0,00	0,00	0,58	4,96
M7_ 61	0,26	3,34	0,69	0,00	0,00	0,30	4,60
M7_ 80	0,52	2,63	1,34	0,46	0,00	0,02	4,97
M7-N- 1	0,37	2,79	0,90	0,60	0,00	0,57	5,23
M7-N- 15	0,61	2,73	0,95	0,64	0,00	0,31	5,25
M7-N- 23	0,61	2,46	1,27	0,85	0,00	0,02	5,22
M7-N- 3	0,34	2,76	0,92	0,62	0,00	0,64	5,27
M7-N- 34	0,37	2,73	0,95	0,64	0,00	0,55	5,25
M7-N- 35	0,73	2,61	1,10	0,74	0,00	0,05	5,23
M7-N- 37	0,36	2,71	0,98	0,66	0,00	0,55	5,26
M7-N- 5	0,59	2,36	1,37	0,92	0,00	0,02	5,26
M7-N- 7	0,42	2,32	1,45	0,97	0,00	0,00	5,16
M8- 15	0,21	3,63	0,36	0,00	0,00	0,21	4,40
M8- 19	0,35	3,01	0,99	0,00	0,00	0,62	4,98
M8- 20	0,38	2,99	1,05	0,00	0,00	0,51	4,92
M8- 21	0,40	3,15	0,90	0,00	0,00	0,31	4,76
M8- 22	0,37	3,15	0,84	0,00	0,00	0,49	4,85
M8- 23	0,36	3,14	0,88	0,00	0,00	0,44	4,82
M8- 24	0,39	3,11	0,90	0,01	0,00	0,47	4,88
M8- 25	0,47	3,10	0,87	0,00	0,00	0,52	4,96
M8- 35	0,78	2,80	1,15	0,28	0,00	0,02	5,02
M8- 36	0,70	2,72	1,23	0,34	0,00	0,05	5,04
M8- 40	0,71	2,71	1,25	0,33	0,00	0,05	5,05
M8- 41	0,34	3,03	1,00	0,00	0,00	0,55	4,92
M8-G-2- 13	0,43	3,05	0,96	0,00	0,00	0,47	4,91
M8-G-2- 14	0,41	2,97	1,04	0,00	0,00	0,58	5,00
M8-G-2- 15	0,41	3,12	0,91	0,00	0,00	0,38	4,82
M8-G-2- 16	0,34	3,24	0,77	0,00	0,00	0,38	4,73
M8-G-2- 17	0,46	3,00	1,01	0,00	0,00	0,49	4,96
M8-G-2- 19	0,48	2,99	1,03	0,00	0,00	0,50	4,99
M8-G-2- 20	0,47	2,96	1,06	0,00	0,00	0,51	4,99
M8-G-2- 28	0,54	2,97	1,04	0,00	0,00	0,46	5,01
M8-G-2- 34	0,70	2,66	1,31	0,34	0,00	0,05	5,06
M8-G-2- 35	0,81	2,83	1,17	0,16	0,00	0,07	5,03
M8-G-2- 36	0,79	2,79	1,19	0,21	0,00	0,06	5,04
M8-G-2- 37	0,78	2,81	1,18	0,19	0,00	0,07	5,03
M8-G-2- 38	0,87	2,75	1,10	0,38	0,00	0,05	5,16
M8-G-2- 39	0,41	3,26	0,76	0,00	0,00	0,28	4,71

Feldspar- SEM measurements- per formular unit [pfu] 7/8

Sample	Na	Si	Al	Ca	Ba	K	∑Cation
	[pfu]	[pfu]	[pfu]	[pfu]	[pfu]	[pfu]	[pfu]
M9- 10	0,22	2,15	1,81	0,87	0,00	0,00	5,06
M9- 17	0,00	2,97	1,09	0,32	0,00	0,19	4,58
M9- 32	0,34	2,33	1,59	0,77	0,00	0,05	5,07
M9- 33	0,70	2,35	1,58	0,58	0,00	0,00	5,21
M9- 34	0,41	2,43	1,53	0,55	0,00	0,00	4,93
M9- 36	0,31	2,37	1,64	0,64	0,00	0,00	4,96
M9- 39	0,29	2,34	1,66	0,69	0,00	0,00	4,98
M9- 9	0,27	2,34	1,68	0,68	0,00	0,00	4,96
M9-N- 13	0,38	2,45	1,50	0,61	0,00	0,08	5,03
M9-N- 19	0,33	3,14	0,86	0,14	0,00	0,26	4,73
M9-N- 2	0,35	3,05	0,94	0,18	0,00	0,28	4,79
M9-N- 23	0,50	2,91	1,08	0,24	0,00	0,12	4,85
M9-N- 24	0,27	3,31	0,71	0,00	0,00	0,36	4,65
M9-N- 27	0,33	2,36	1,56	0,77	0,00	0,00	5,02
M9-N- 28	0,27	3,29	0,74	0,00	0,00	0,36	4,65
M9-N- 3	0,28	3,26	0,77	0,00	0,00	0,38	4,68
M9-N- 30	0,50	2,66	1,26	0,49	0,00	0,08	4,99
M9-N- 31	0,48	3,01	0,96	0,19	0,00	0,22	4,86
M9-N- 4	0,27	3,30	0,72	0,00	0,00	0,37	4,66
M10- 15	0,19	2,16	1,83	0,84	0,00	0,00	5,02
M10- 16	0,46	2,47	1,50	0,58	0,00	0,00	5,00
M10- 17	0,26	2,24	1,78	0,72	0,00	0,00	5,00
M10- 18	0,40	2,40	1,56	0,65	0,00	0,00	5,02
M10- 23	0,37	2,47	1,52	0,60	0,00	0,00	4,95
M10- 24	0,44	2,40	1,59	0,60	0,00	0,00	5,03
M10- 25	0,20	2,34	1,66	0,74	0,00	0,00	4,93
M10- 26	0,34	2,43	1,60	0,56	0,00	0,00	4,94
M10- 27	0,24	2,21	1,80	0,76	0,00	0,00	5,01
M10- 28	0,29	2,42	1,60	0,61	0,00	0,00	4,92
M10- 29	0,21	2,20	1,78	0,82	0,00	0,00	5,02
M10- 30	0,30	2,35	1,68	0,63	0,00	0,00	4,96
M10- 36	0,23	2,32	1,68	0,73	0,00	0,00	4,96
M10- 44	0,37	2,48	1,61	0,45	0,00	0,00	4,90
M10- 5	0,45	3,10	0,90	0,14	0,00	0,15	4,74
M10- 57	0,45	2,70	1,27	0,45	0,00	0,05	4,91
M10- 58	0,64	2,85	1,15	0,21	0,00	0,08	4,94
M10-N 13	0,65	2,83	1,14	0,27	0,00	0,09	4,97
M10-N 18	0,47	2,76	1,21	0,39	0,00	0,08	4,91
M10-N 19	0,55	2,68	1,30	0,40	0,00	0,04	4,96

Feldspar- SEM measurements- per formular unit [pfu] 8/8

Sample	Na	Si	Al	Ca	Ba	K	∑Cation
	[pfu]	[pfu]	[pfu]	[pfu]	[pfu]	[pfu]	[pfu]
M10-N 4	0,54	2,68	1,30	0,39	0,00	0,04	4,96
M10-N 5	0,50	3,03	0,97	0,16	0,00	0,14	4,80
M10-N 6	0,33	3,35	0,67	0,00	0,00	0,27	4,62
M10-N 9	0,30	2,40	1,55	0,72	0,00	0,00	4,97

10.3.2 Pyroxene

Pyroxene - SEM measurements- per formular unit [pfu] 1/3

sample	Na	Mg	Si	Fe	Ca	Mn	Ti	K
	[pfu]	[pfu]	[pfu]	[pfu]	[pfu]	[pfu]	[pfu]	[pfu]
M1 30	0,03	1,37	1,93	0,61	0,02	0,02	0,00	0,00
M1 31	0,04	0,23	2,16	1,02	0,12	0,00	0,00	0,03
M2 7	0,03	0,82	1,86	0,31	0,92	0,00	0,03	0,00
M2 8	0,04	0,83	1,86	0,31	0,85	0,00	0,02	0,00
M2 32	0,00	0,46	2,08	1,02	0,11	0,00	0,00	0,00
M6/2- 6	0,00	1,20	2,04	0,60	0,05	0,00	0,00	0,00
M6/2- 7	0,00	1,21	1,95	0,77	0,06	0,00	0,00	0,00
M6/2- 9	0,00	1,20	1,96	0,70	0,10	0,00	0,00	0,00
M6/2- 15	0,11	0,32	2,09	0,57	0,18	0,00	0,07	0,15
M6/2- 16	0,10	0,34	2,05	0,62	0,28	0,00	0,08	0,12
M6/2- 17	0,11	0,48	1,96	0,73	0,22	0,00	0,08	0,08
M6/2- 18	0,12	0,30	2,20	0,38	0,20	0,00	0,06	0,14
M6/2- 19	0,05	0,48	1,93	0,80	0,25	0,00	0,10	0,06
M6/2- 22	0,12	0,36	2,01	0,75	0,14	0,00	0,10	0,11
M6/2- 27	0,30	0,00	2,30	0,06	0,11	0,00	0,00	0,00
M6/2- 28	0,11	0,53	2,08	0,56	0,19	0,00	0,00	0,11
M6/2- 30	0,39	0,11	2,00	0,06	0,27	0,00	0,00	0,03
M6/2- 31	0,32	0,08	2,15	0,10	0,28	0,00	0,00	0,13
M6/2- 35	0,11	0,52	2,07	0,45	0,22	0,00	0,00	0,07
M6 1	0,00	1,28	1,97	0,64	0,05	0,00	0,00	0,00
M6 7	0,00	1,25	1,96	0,57	0,13	0,00	0,00	0,00
M6 22	0,05	0,83	1,94	0,20	0,88	0,00	0,00	0,00
M6-2- 1	0,02	0,72	1,90	0,35	0,93	0,00	0,00	0,00
M6-2- 5	0,12	0,44	2,22	0,46	0,07	0,00	0,00	0,15
M6-2- 11	0,00	1,29	1,94	0,62	0,08	0,00	0,00	0,00
M6-2- 17	0,46	0,00	1,99	0,14	0,20	0,00	0,00	0,13
M6-2- 41	0,07	0,57	2,11	0,47	0,13	0,00	0,04	0,12
M6-2- 42	0,11	0,59	2,22	0,31	0,11	0,00	0,00	0,10
M6-2- 43	0,00	0,88	2,00	0,66	0,21	0,00	0,00	0,03

Pyroxene - SEM measurements- per formular unit [pfu] 2/3

sample	Na	Mg	Si	Fe	Ca	Mn	Ti	K
	[pfu]	[pfu]	[pfu]	[pfu]	[pfu]	[pfu]	[pfu]	[pfu]
M6-2- 44	0,08	0,63	1,92	0,87	0,10	0,00	0,06	0,10
M6-2- 45	0,00	1,12	1,87	0,74	0,23	0,00	0,00	0,00
M9-N- 1	0,00	1,15	1,96	0,71	0,07	0,00	0,00	0,00
M9-N- 7	0,00	1,11	1,97	0,79	0,11	0,00	0,00	0,00
M9-N- 9	0,00	1,26	1,93	0,78	0,11	0,00	0,00	0,00
M9-N- 10	0,17	0,55	1,96	0,39	0,24	0,00	0,00	0,03
M9-N- 14	0,00	0,70	1,76	0,37	0,98	0,00	0,07	0,00
M9-N- 29	0,00	1,06	1,93	0,79	0,14	0,00	0,00	0,03
M9-N- 32	0,00	1,07	1,96	0,89	0,12	0,00	0,00	0,00
M9- 13	0,00	0,61	1,93	0,35	1,09	0,00	0,00	0,00
M9- 14	0,00	1,38	1,96	0,56	0,04	0,00	0,00	0,00
M9- 18	0,00	1,33	1,96	0,56	0,07	0,00	0,00	0,00
M9- 21	0,00	1,10	1,97	0,81	0,15	0,00	0,00	0,00
M9- 23	0,00	1,13	1,97	0,71	0,14	0,00	0,00	0,00
M9- 24	0,00	1,33	1,91	0,66	0,08	0,00	0,00	0,00
M9- 25	0,00	1,22	1,96	0,76	0,10	0,00	0,00	0,00
M9- 31	0,08	0,65	1,93	0,27	0,67	0,00	0,03	0,00
M9- 35	0,00	0,90	2,02	0,84	0,10	0,00	0,00	0,05
M9- 37	0,00	1,29	1,95	0,66	0,05	0,00	0,00	0,00
M9- 18	0,00	1,33	1,96	0,56	0,07	0,00	0,00	0,00
M9- 17	0,32	0,00	2,15	0,06	0,23	0,00	0,00	0,14
M9- 1	0,00	0,63	2,00	0,30	0,96	0,00	0,00	0,00
M9- 2	0,00	1,34	1,99	0,64	0,05	0,00	0,00	0,00
M9- 3	0,00	1,38	1,91	0,64	0,04	0,00	0,00	0,00
M9- 7	0,00	0,93	1,97	0,68	0,17	0,00	0,03	0,03
M10- 6	0,00	1,33	1,93	0,65	0,06	0,00	0,00	0,00
M10- 14	0,03	0,60	2,04	0,44	0,87	0,00	0,00	0,00
M10- 35	0,00	1,37	2,02	0,40	0,07	0,00	0,00	0,00
M10- 37	0,00	1,20	1,81	0,66	0,06	0,00	0,00	0,06
M10- 38	0,00	1,37	1,94	0,52	0,10	0,00	0,00	0,00
M10- 48	0,00	1,23	2,00	0,63	0,05	0,00	0,00	0,00
M10- 50	0,35	0,34	2,08	0,18	0,27	0,00	0,00	0,06
M10- 52	0,00	1,09	2,00	0,69	0,11	0,00	0,00	0,00
M10- 53	0,00	1,15	2,02	0,62	0,08	0,00	0,00	0,00
M10- 55	0,00	1,17	1,87	0,81	0,15	0,00	0,00	0,00
M10- 56	0,04	1,12	2,02	0,59	0,05	0,00	0,00	0,04
M10-N 1	0,11	0,60	2,06	0,56	0,15	0,00	0,00	0,05
M10-N 2	0,06	1,01	2,01	0,66	0,09	0,00	0,00	0,03
M10-N 10	0,00	1,38	1,94	0,60	0,05	0,00	0,00	0,00

Pyroxene - SEM measurements- per formular unit [pfu] 3/3

sample	Na	Mg	Si	Fe	Ca	Mn	Ti	K
	[pfu]	[pfu]	[pfu]	[pfu]	[pfu]	[pfu]	[pfu]	[pfu]
M10-N 12	0,03	0,98	1,97	0,75	0,17	0,00	0,00	0,00
M10-N 15	0,00	1,25	1,95	0,65	0,08	0,00	0,00	0,00
M10-N 17	0,00	1,17	1,98	0,66	0,10	0,00	0,00	0,00

10.3.3 Amphibole

Amphibole - SEM measurements- per formular unit [pfu] 1/2

sample	Na	Mg	Si	Fe	Al	Ca	Mn	Ti	K
	[pfu]	[pfu]	[pfu]	[pfu]	[pfu]	[pfu]	[pfu]	[pfu]	[pfu]
M1 26	0,63	3,01	6,04	2,13	1,89	2,09	0,00	0,27	0,00
M1 26	0,63	3,00	6,03	2,12	1,88	2,09	0,00	0,27	0,11
M1 17	0,81	2,83	5,56	2,25	2,12	2,21	0,00	0,35	0,13
M2 4	0,44	3,51	7,03	1,56	0,88	1,91	0,14	0,12	0,09
M2 14	0,64	2,88	6,48	1,70	1,71	1,99	0,00	0,26	0,12
M2 31	0,40	3,21	7,02	1,74	0,89	1,92	0,17	0,17	0,09
M3 27	0,38	3,37	7,07	1,69	0,79	1,96	0,16	0,13	0,08
M3 28	0,37	3,21	7,02	1,81	0,88	2,06	0,00	0,17	0,12
M3-Z- 12	0,50	3,64	7,27	1,25	0,93	1,55	0,00	0,19	0,00
M4 20	0,42	3,34	6,99	1,67	0,86	2,00	0,16	0,15	0,08
M4 21	0,45	3,61	7,08	1,51	0,84	1,83	0,13	0,12	0,07
M6 9	0,57	2,86	5,90	2,05	1,87	2,14	0,00	0,49	0,13
M6 10	0,73	2,78	6,13	1,79	1,88	2,03	0,00	0,44	0,14
M6 11	0,60	3,00	6,29	1,53	2,09	1,87	0,00	0,27	0,09
M6 12	0,50	2,66	6,24	1,73	2,00	1,96	0,00	0,43	0,13
M6 13	0,51	2,44	6,25	1,91	1,98	2,01	0,00	0,42	0,17
M6/2- 34	0,24	2,10	6,29	1,90	1,55	2,23	0,00	0,81	0,22
M8- 5	0,40	2,92	6,93	1,52	0,81	1,79	0,00	0,00	0,00
M8- 8	0,36	3,40	7,56	1,26	0,90	1,47	0,00	0,11	0,00
M8- 9	0,43	3,42	7,19	1,46	0,92	1,86	0,00	0,14	0,00
M8- 10	0,49	3,51	7,16	1,48	0,96	1,65	0,00	0,18	0,00
M8- 37	0,39	3,63	7,53	1,31	0,82	1,59	0,00	0,00	0,00
M9- 15	0,34	2,54	6,55	2,16	1,64	1,85	0,00	0,36	0,00
M9- 19	0,34	2,28	5,57	2,80	1,90	2,59	0,00	0,58	0,00
M9- 20	0,62	2,95	6,07	1,77	1,98	1,93	0,00	0,43	0,14
M9- 27	0,66	3,00	6,10	1,76	1,90	1,95	0,00	0,41	0,16
M9- 31	0,31	2,51	7,40	1,05	1,11	2,57	0,00	0,13	0,00
M10- 2	0,77	3,42	6,46	1,14	2,13	1,49	0,00	0,22	0,00
M10- 3	0,96	3,21	6,57	1,20	2,04	1,44	0,00	0,24	0,00

Amphibole - SEM measurements- per formular unit [pfu] 2/2

sample	Na	Mg	Si	Fe	Al	Ca	Mn	Ti	K
	[pfu]	[pfu]	[pfu]	[pfu]	[pfu]	[pfu]	[pfu]	[pfu]	[pfu]
M10- 8	0,69	3,04	6,34	1,44	2,09	1,70	0,00	0,33	0,00
M10- 13	0,99	0,00	6,74	0,23	4,36	2,26	0,00	0,00	0,00
M10- 20	0,80	3,30	6,43	1,10	2,28	1,43	0,00	0,25	0,00
M10- 22	0,59	2,65	6,26	1,71	1,94	2,08	0,00	0,42	0,00
M10- 32	0,77	3,30	6,49	1,15	2,19	1,38	0,00	0,25	0,00
M10- 41	0,53	2,82	6,83	1,28	1,99	1,40	0,00	0,30	0,00
M10- 42	0,60	2,74	6,06	1,88	1,82	2,20	0,00	0,47	0,18
M10- 49	0,50	2,85	6,60	1,41	1,84	1,99	0,00	0,24	0,10
M10- 54	0,83	3,21	6,31	1,38	2,25	1,53	0,00	0,23	0,00
M6-2- 9	0,56	2,83	6,29	1,66	1,86	1,91	0,00	0,44	0,14
M6-2- 10	0,68	3,18	6,27	1,59	1,89	1,79	0,00	0,34	0,12
M6-2- 12	0,62	2,86	6,09	1,83	1,92	2,06	0,00	0,39	0,17
M6-2- 13	0,66	3,13	6,13	1,58	2,11	1,73	0,00	0,38	0,11
M6-2- 14	0,53	3,07	6,57	1,20	2,18	1,63	0,00	0,22	0,00
M6-2- 15	0,73	3,26	5,72	1,73	2,05	2,17	0,00	0,44	0,18
M6-2- 18	0,67	3,18	6,32	1,30	1,96	1,97	0,00	0,28	0,16
M6-2- 20	0,64	2,97	6,23	1,62	2,07	1,86	0,00	0,33	0,00
M6-2- 21	0,61	2,82	6,16	1,62	2,13	1,85	0,00	0,42	0,14
M6-2- 22	0,65	2,75	6,40	1,02	2,57	1,69	0,00	0,25	0,10
M6-2- 23	0,58	2,92	5,93	1,78	1,99	2,23	0,00	0,42	0,18
M6-2- 24	0,59	2,81	6,13	1,73	1,99	2,17	0,00	0,34	0,12
M6-2- 25	0,67	3,13	5,92	1,57	2,09	2,13	0,00	0,39	0,14
M6-2- 35	0,72	3,34	6,12	1,33	1,97	1,92	0,00	0,40	0,11
M6-2- 37	0,65	3,20	6,17	1,56	1,89	2,04	0,00	0,31	0,13
M6-2- 38	0,63	3,08	6,40	1,55	1,94	1,75	0,00	0,26	0,13
M7-N- 33	1,08	0,56	5,36	1,91	3,37	1,33	0,00	1,37	0,26
M9-N- 6	0,33	2,42	7,42	2,03	0,94	2,04	0,00	0,00	0,21
M9-N- 15	0,32	2,21	5,84	2,54	2,06	2,31	0,00	0,50	0,00
M9-N- 16	0,68	1,98	5,96	2,03	2,98	1,43	0,00	0,42	0,00
M10-N 8	0,15	3,19	7,29	1,00	0,54	3,34	0,00	0,00	0,00
M10-N 14	0,62	3,11	6,25	1,63	1,86	1,90	0,00	0,39	0,00
M1-N- 7	0,72	2,99	6,09	2,38	1,74	1,92	0,00	0,28	0,00
M1-N- 8	0,51	2,63	6,47	1,87	2,05	1,83	0,00	0,20	0,00
M1-N- 9	0,96	2,94	6,72	1,57	1,90	1,37	0,00	0,18	0,00
M4-2- 3	0,56	3,41	7,06	1,57	0,99	1,81	0,00	0,16	0,00
M4-2- 4	0,46	3,42	7,14	1,56	0,95	1,84	0,00	0,13	0,00
M8-G-2- 8	0,47	3,56	7,23	1,49	0,92	1,63	0,00	0,12	0,00
M8-G-2- 9	0,39	3,37	7,59	1,33	0,92	1,54	0,00	0,00	0,00
M8-G-2- 10	0,46	3,44	7,10	1,67	0,80	1,99	0,00	0,14	0,00

10.3.4 Biotite

Biotite - SEM measurements- per formular unit [pfu]

Sample	Na	Mg	Si	Fe	Al	Mn	Ti	K	Cl	F
	[pfu]	[pfu]	[pfu]	[pfu]	[pfu]	[pfu]	[pfu]	[pfu]	[pfu]	[pfu]
M1 14	0,10	1,86	2,95	1,25	1,19	0,06	0,31	0,96	0,00	0,00
M1-N- 13	0,00	1,69	2,87	1,38	1,30	0,00	0,36	1,02	0,00	0,00
M1-N- 14	0,00	1,50	3,05	1,28	1,20	0,20	0,34	0,86	0,00	0,00
M1-N- 15	0,07	1,52	3,01	1,38	1,21	0,00	0,38	0,95	0,00	0,00
M1-N- 16	0,10	1,81	2,97	1,17	1,33	0,00	0,30	0,85	0,00	0,00
M1 16	0,08	1,63	2,78	1,73	1,21	0,10	0,34	0,86	0,01	0,00
M1 38	0,13	1,66	2,71	1,36	1,18	0,45	0,39	0,94	0,02	0,00
M2 45	0,00	1,69	2,73	1,90	1,20	0,16	0,30	0,76	0,00	0,00
M3 7	0,24	1,93	2,72	1,35	1,28	0,00	0,28	0,71	0,00	0,55
M3 8	0,12	1,73	3,07	1,21	1,25	0,00	0,28	0,84	0,00	0,00
M3 13	0,12	1,84	3,14	1,09	1,22	0,00	0,27	0,77	0,00	0,00
M3 16	0,15	1,56	2,55	2,24	1,15	0,00	0,31	0,75	0,00	0,53
M4 17	0,11	1,74	3,03	1,38	1,21	0,00	0,27	0,86	0,00	0,00
M4 18	0,11	1,87	2,87	1,11	1,23	0,00	0,36	0,88	0,02	0,34
M4 25	0,13	1,80	2,80	1,30	1,27	0,00	0,31	0,80	0,00	0,51
M7_ 54	0,00	1,64	2,98	1,21	1,32	0,00	0,35	0,98	0,00	0,00
M8- 32	0,09	2,02	3,06	0,89	1,14	0,00	0,20	0,75	0,00	0,74
M8- 33	0,00	1,91	2,78	1,26	1,23	0,00	0,30	0,74	0,00	0,78

10.4 Microscope panorama images

M1- reflected and transmitted light with crossed polarizers

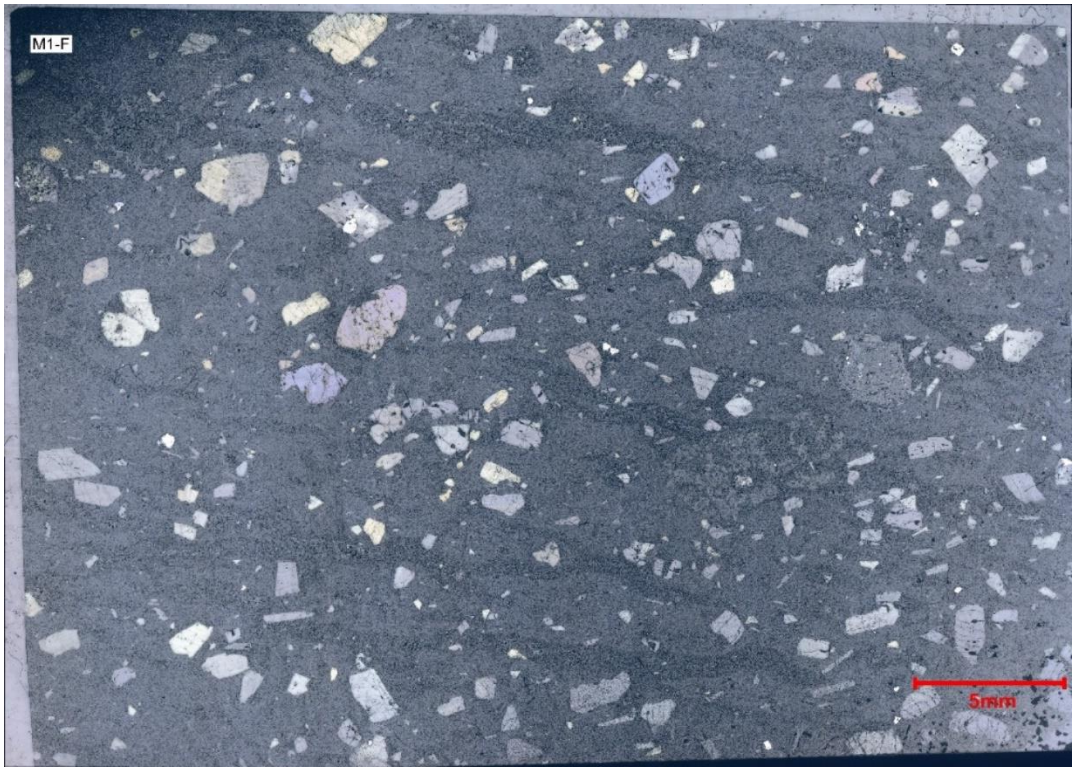

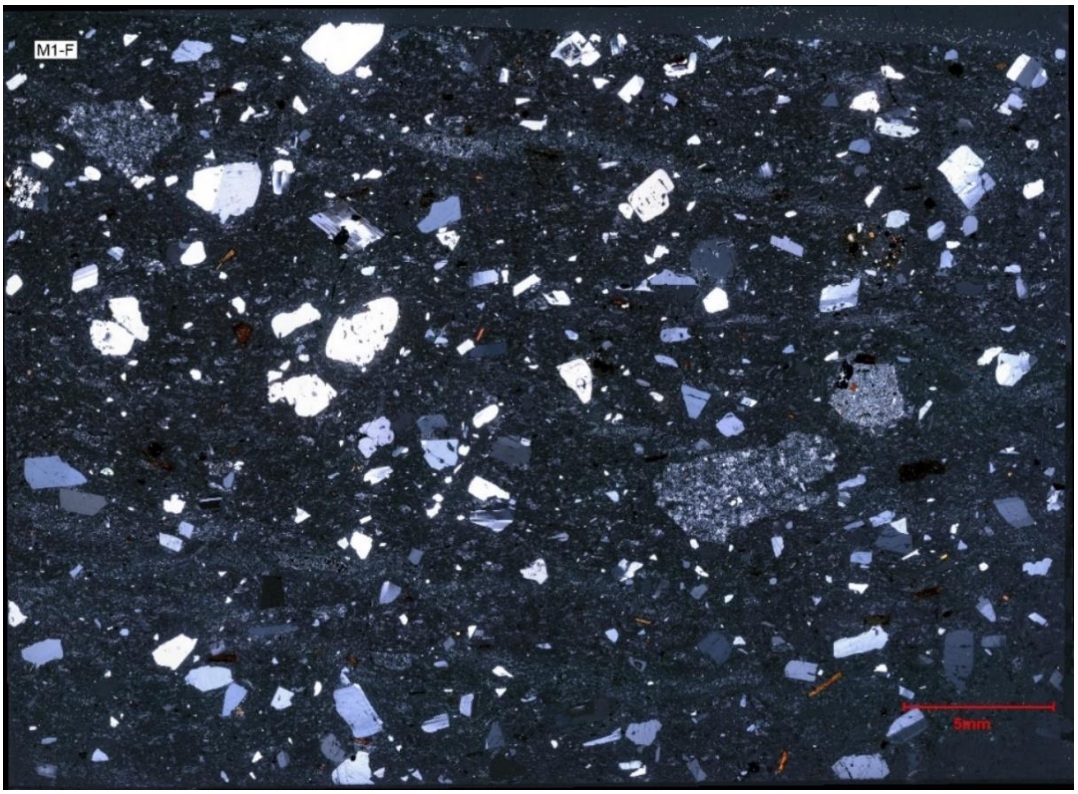

M2- reflected and transmitted light with crossed polarizers

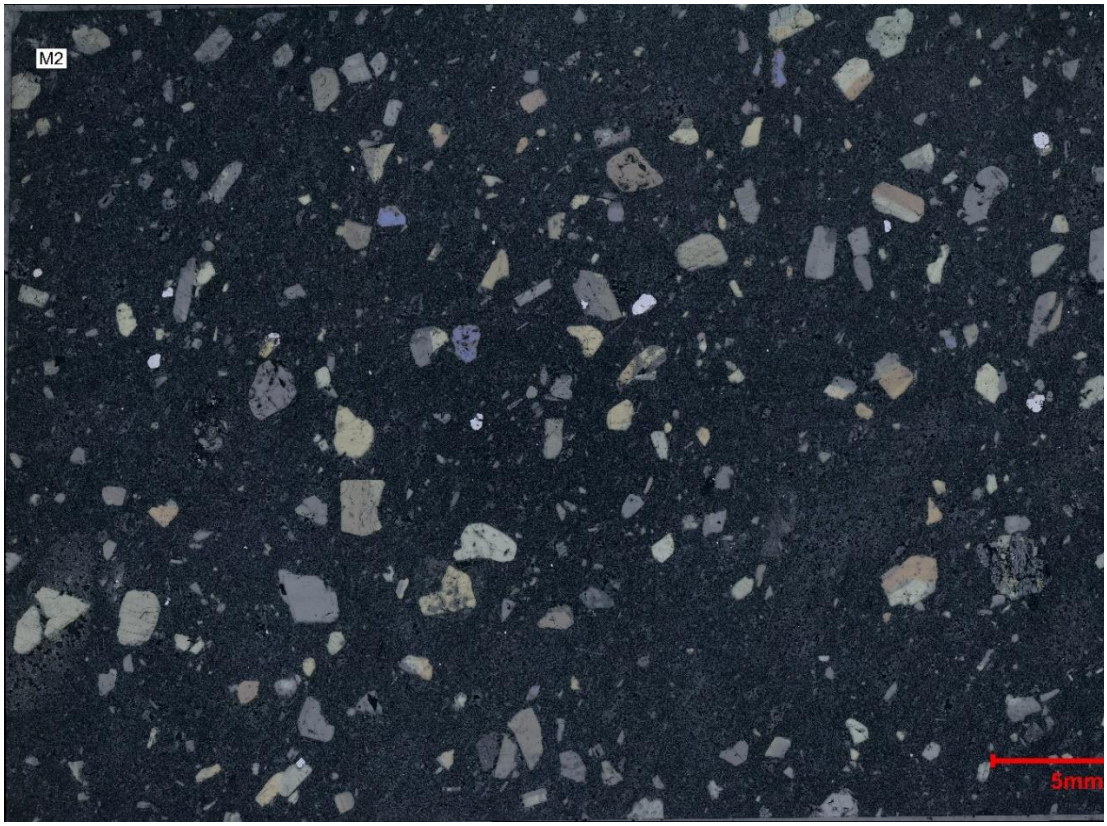

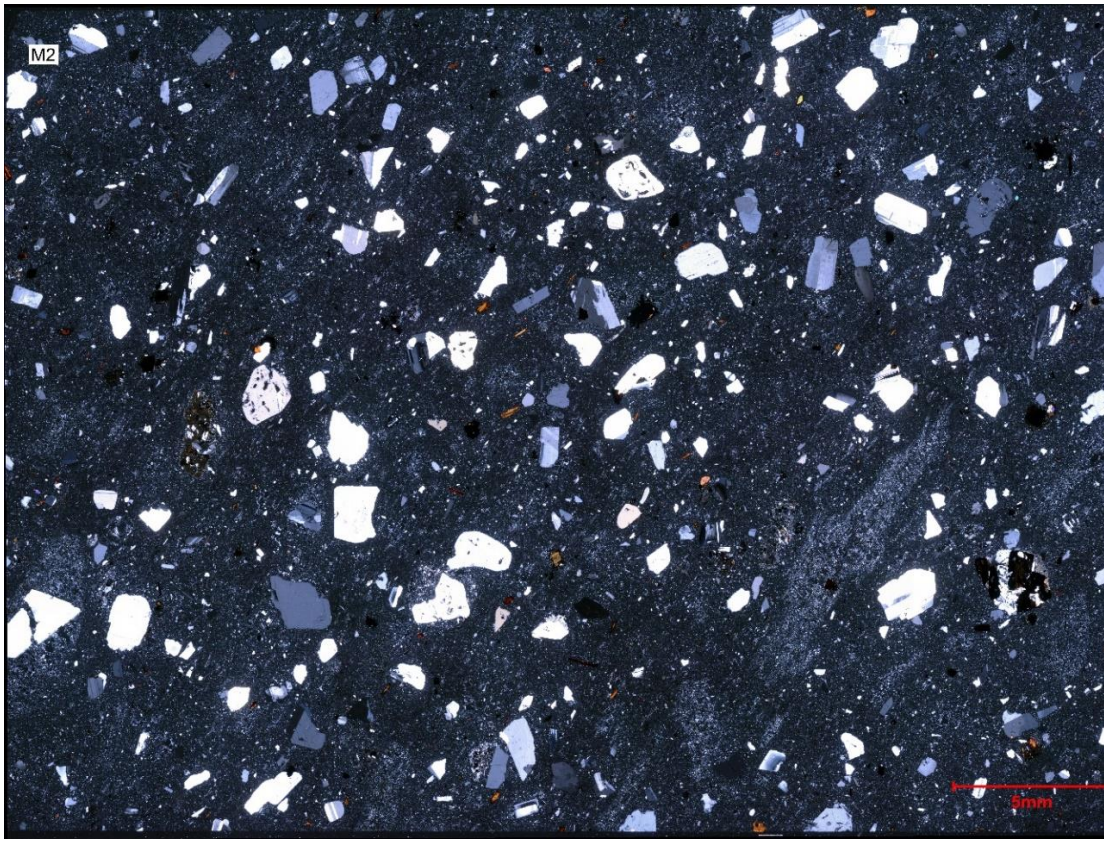

M3- reflected and transmitted light with crossed polarizers

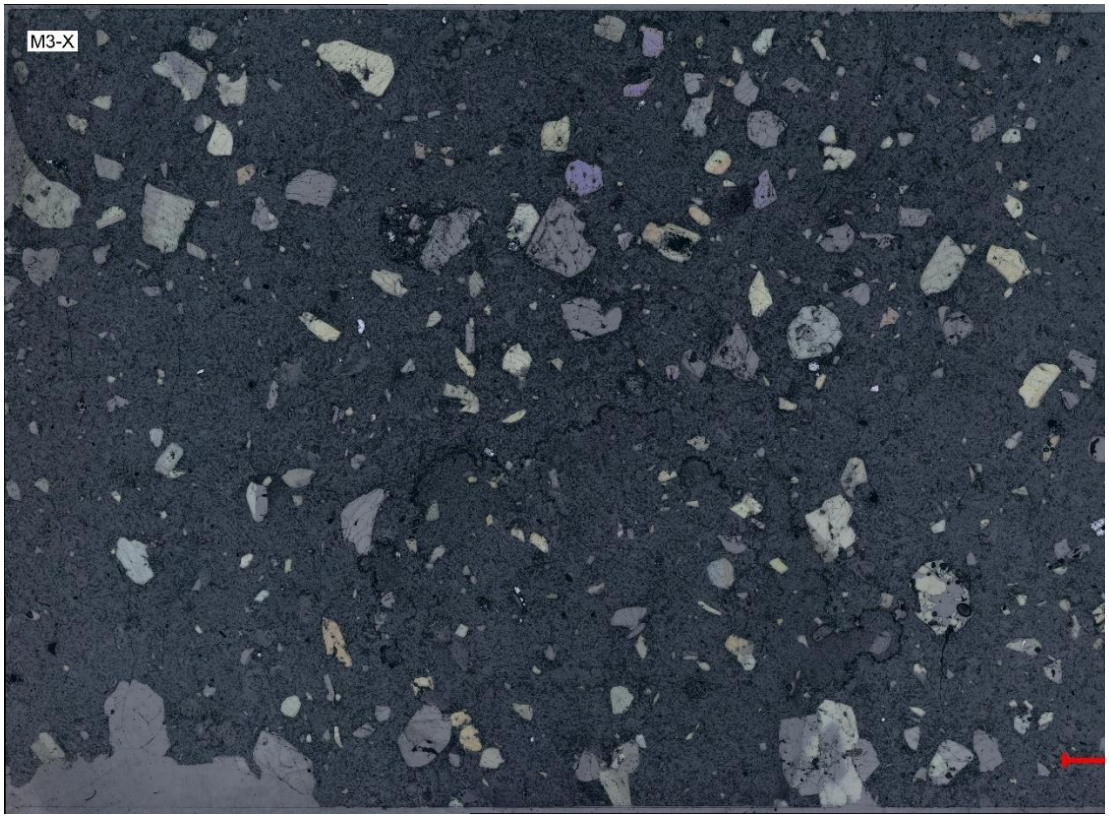

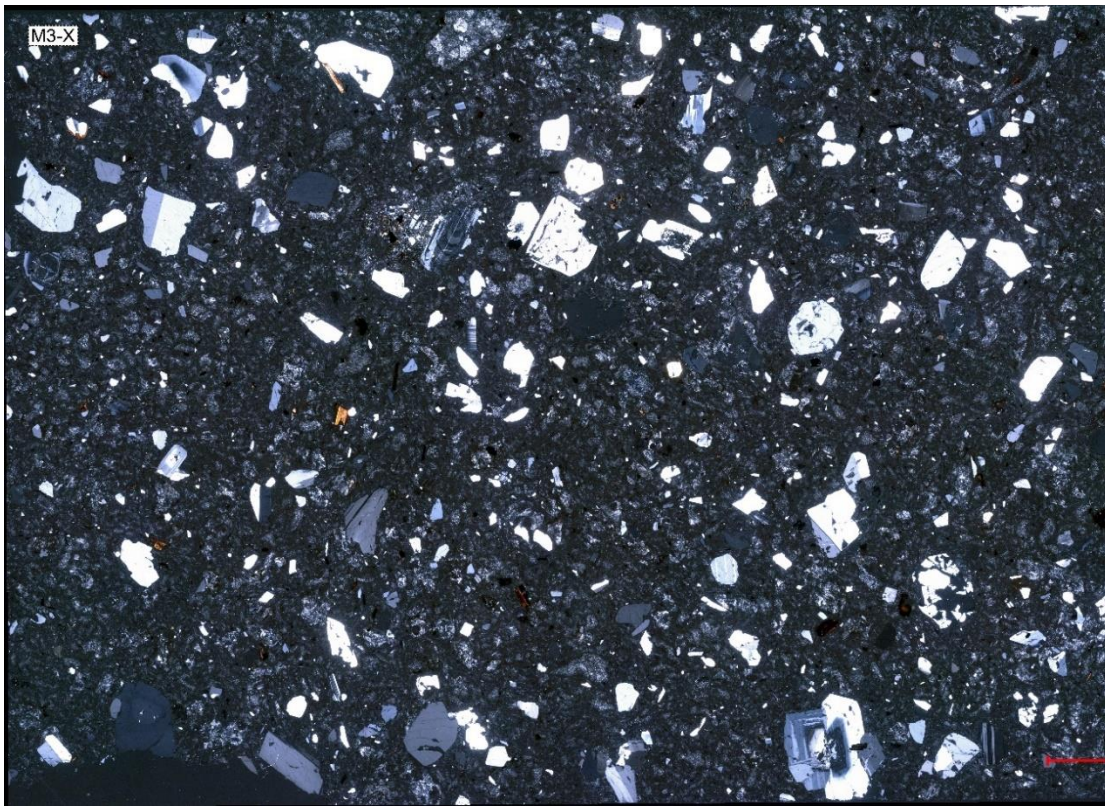

M4- reflected and transmitted light with crossed polarizers

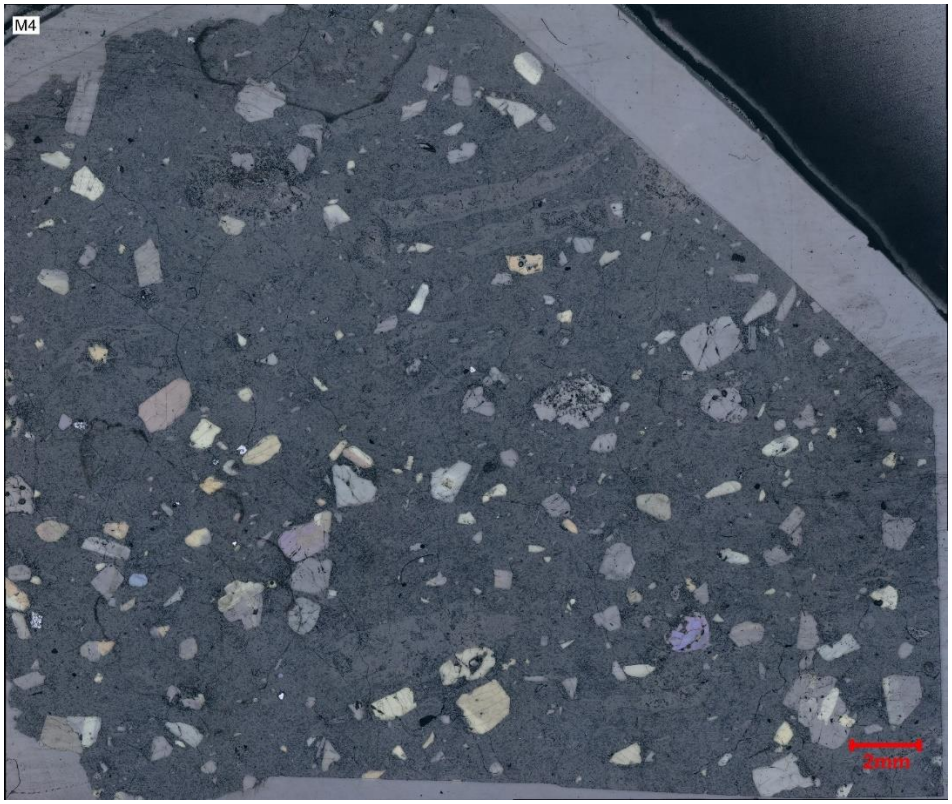

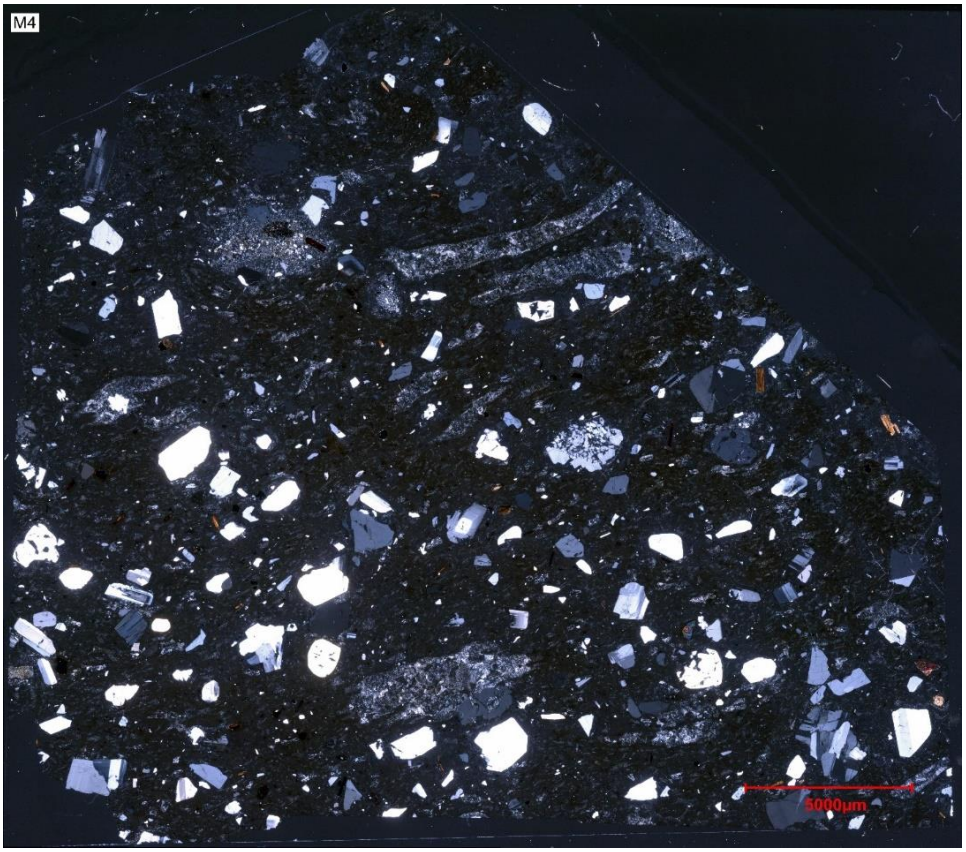

M6- reflected and transmitted light with crossed polarizers

M7- reflected and transmitted light with crossed polarizers

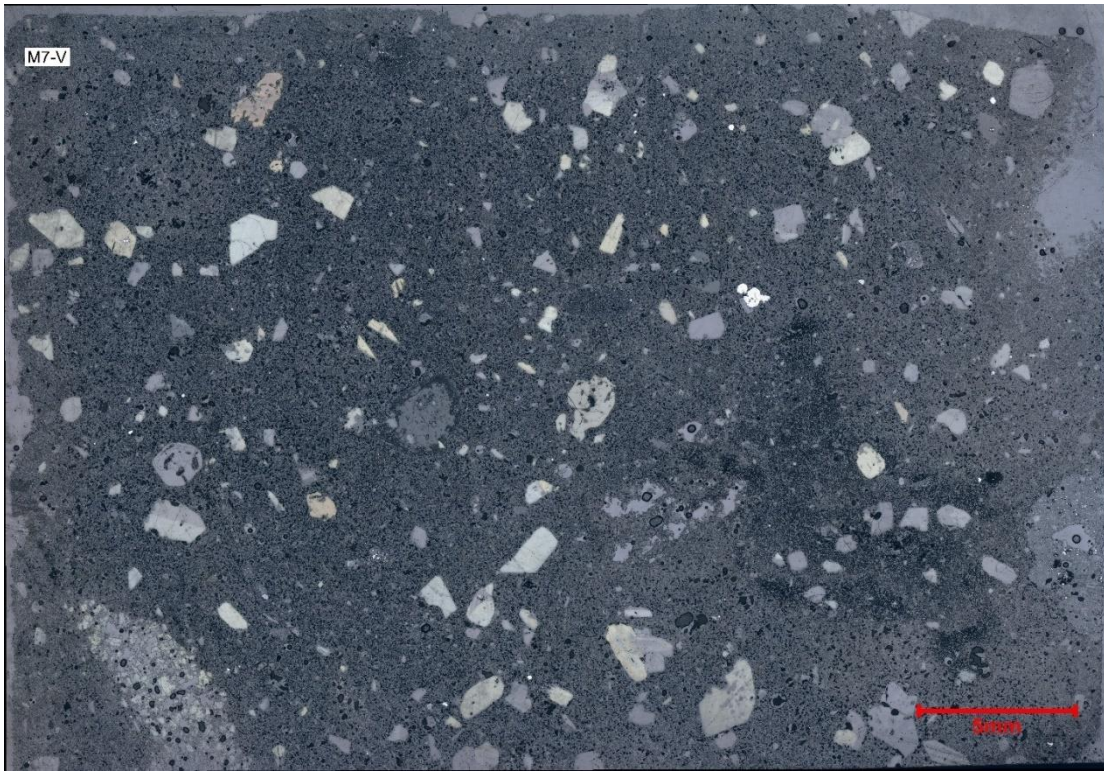

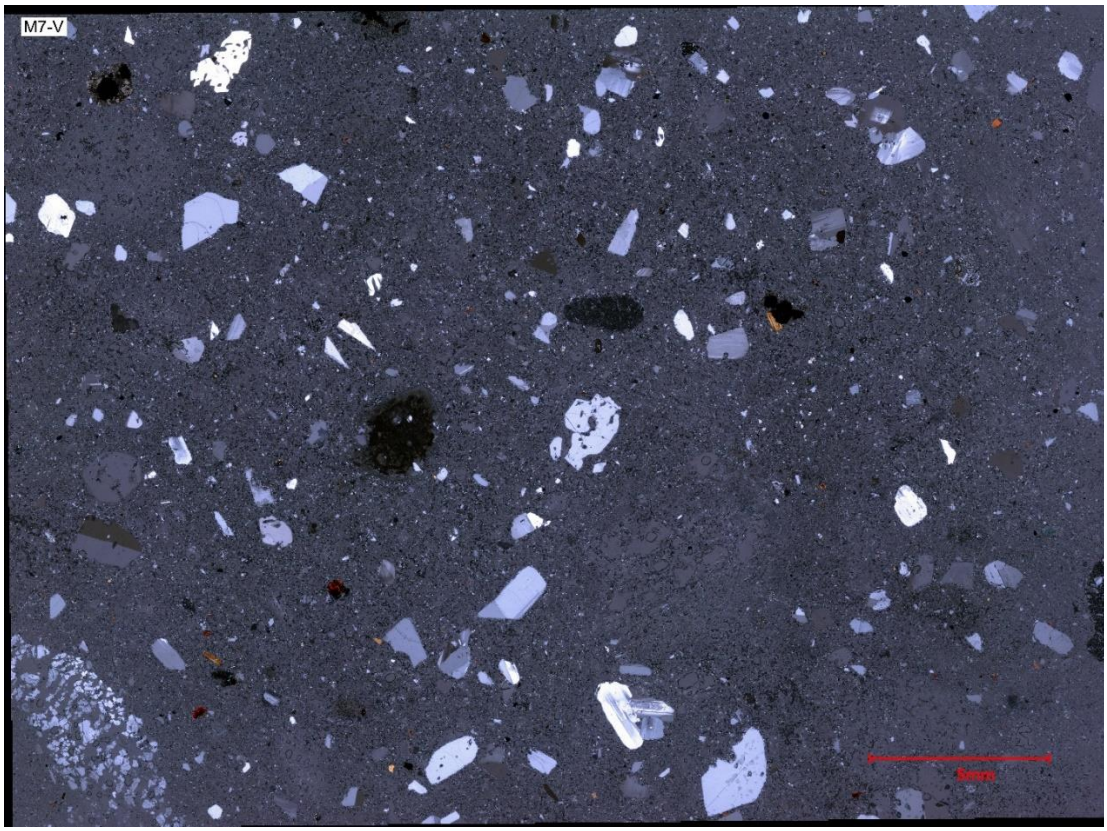

M8- reflected and transmitted light with crossed polarizers

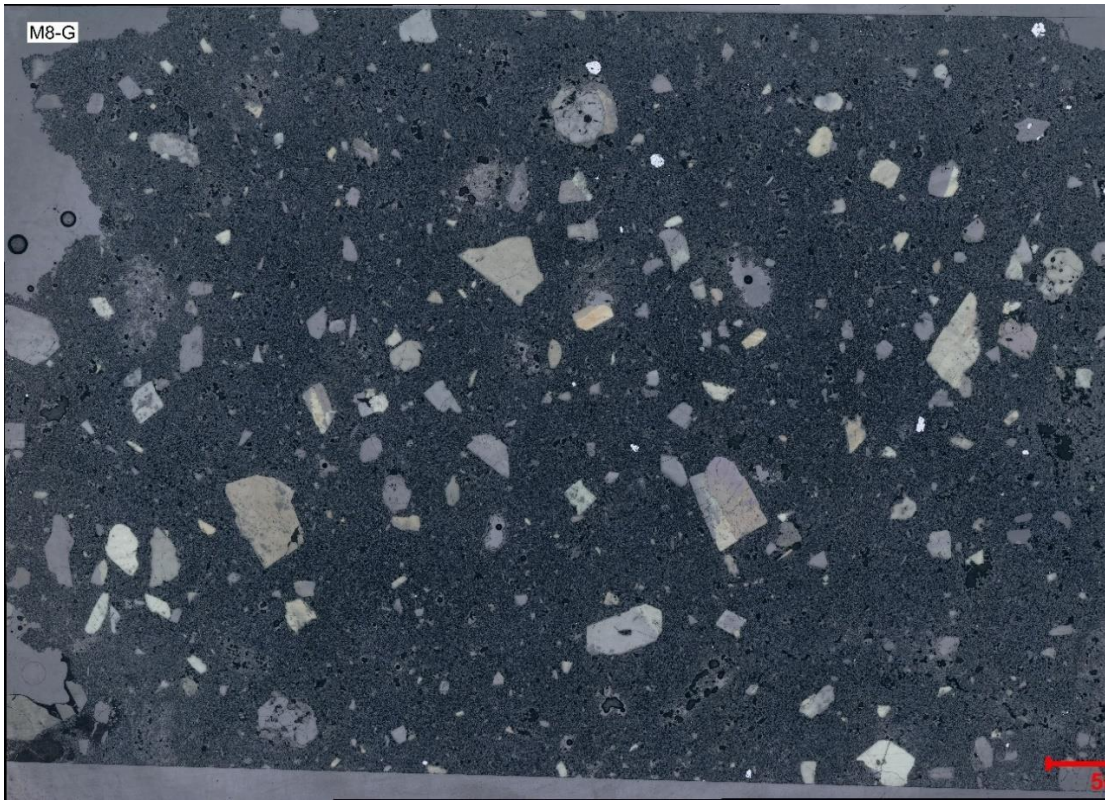

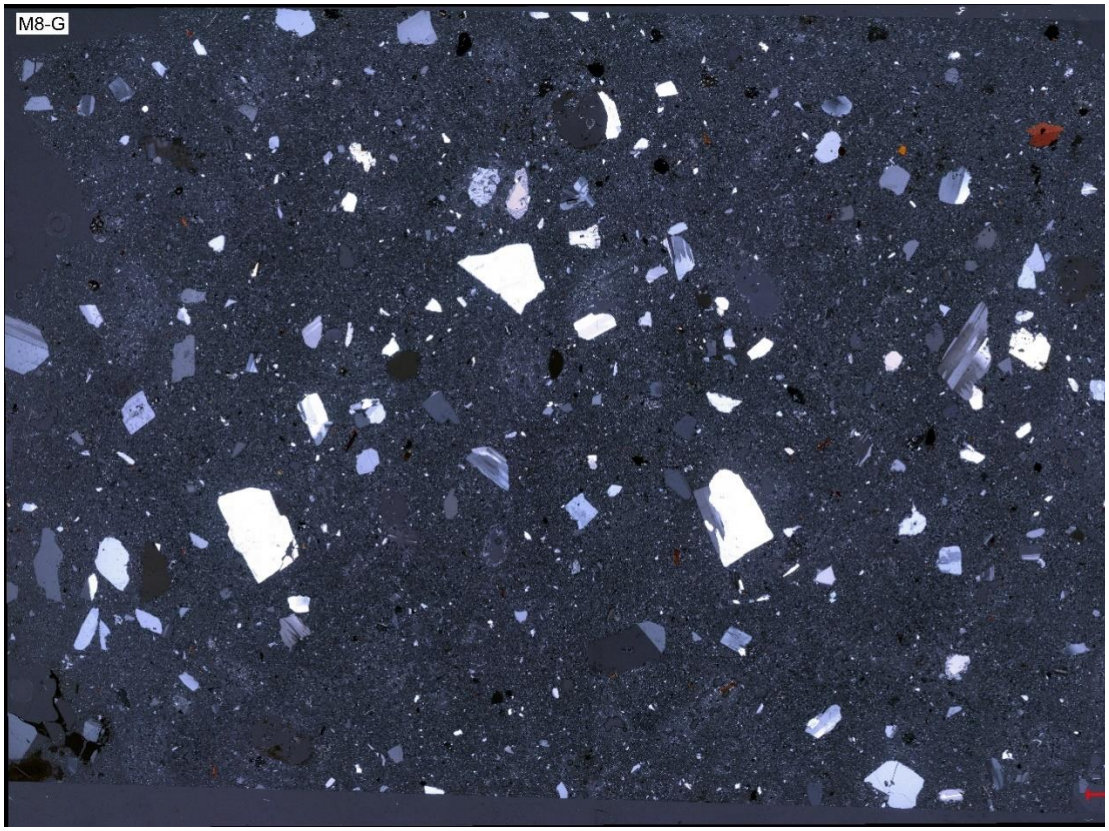

M9- reflected and transmitted light with crossed polarizers

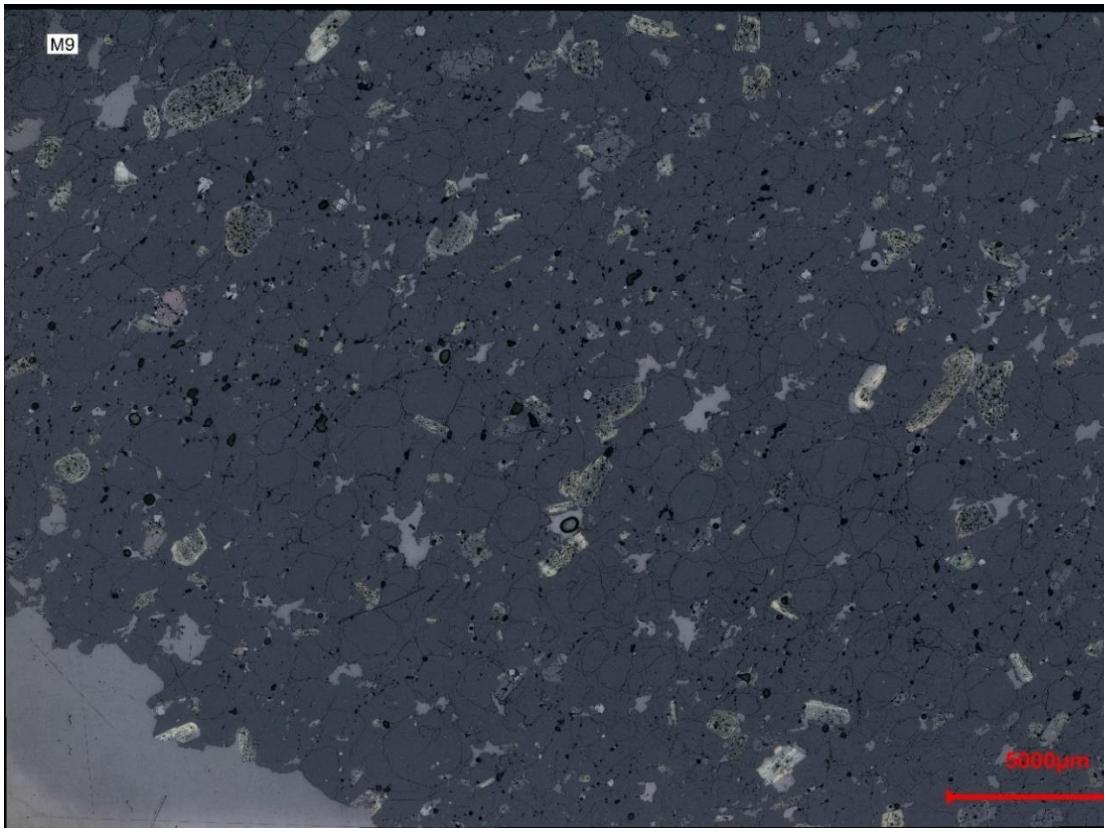

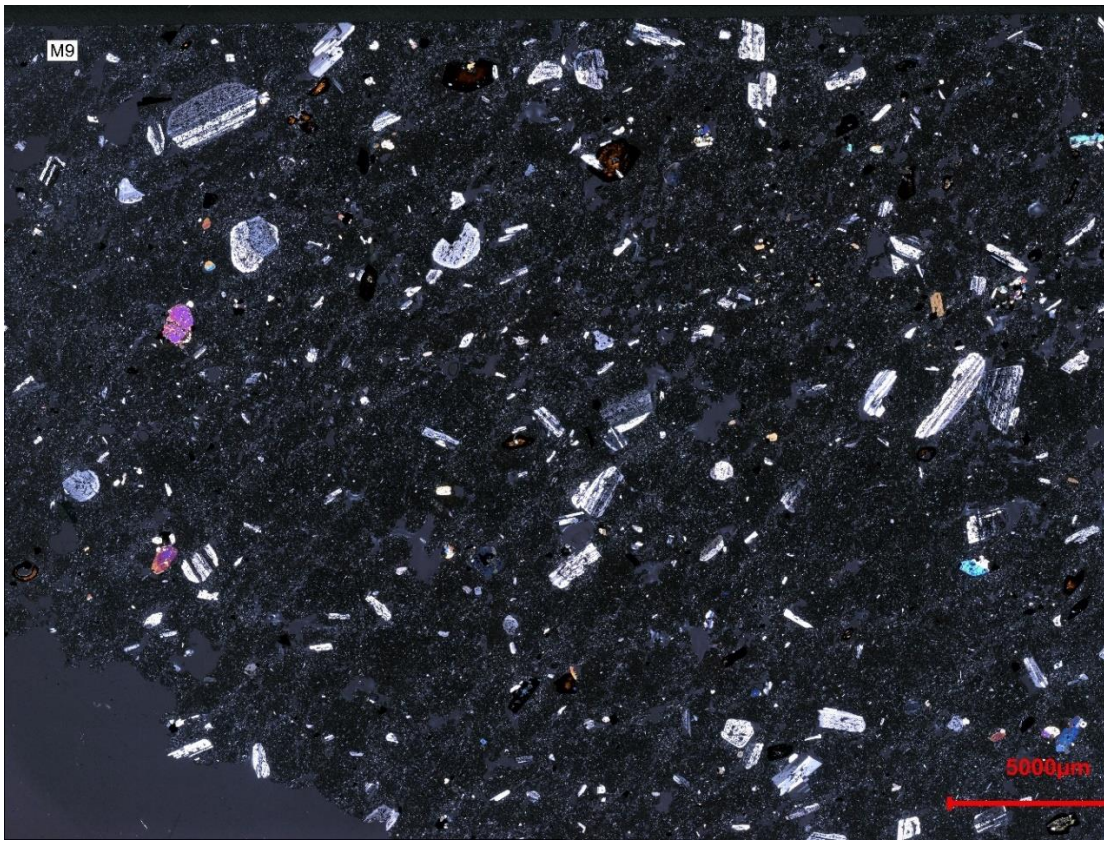

M10- reflected and transmitted light with parallel polarizers

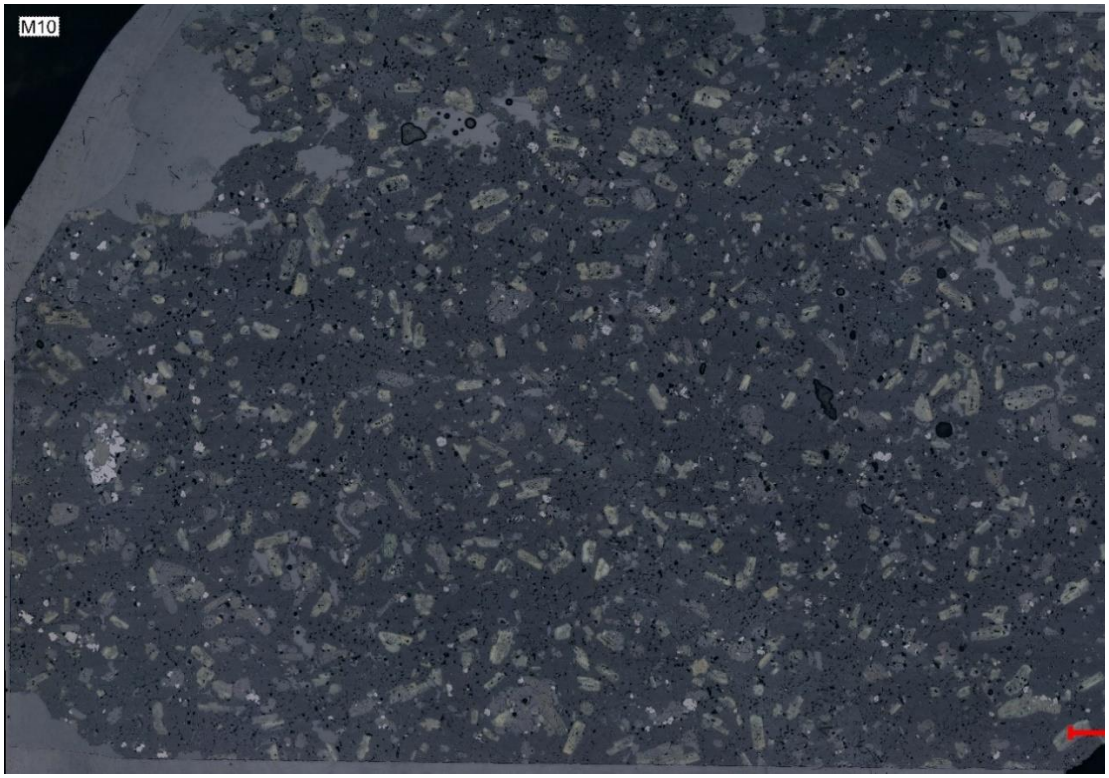

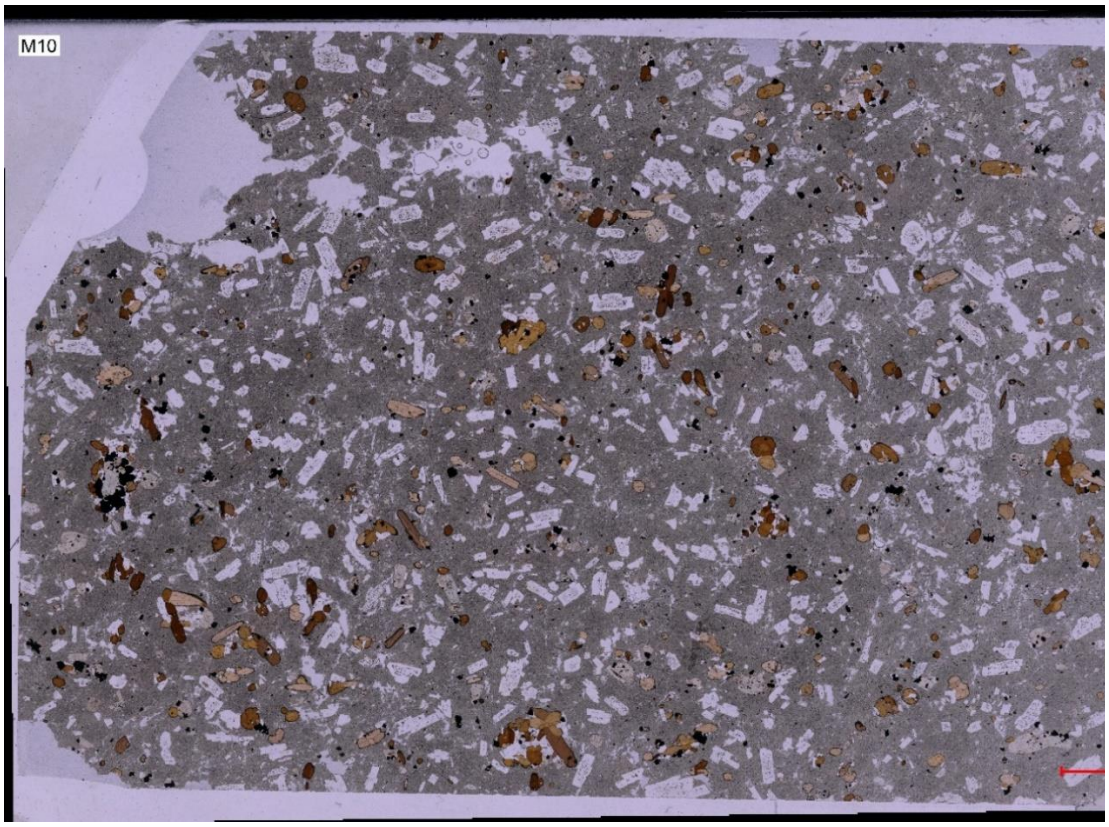

10.5 Geotechnical parameter measurements

10.5.1 Porosity and density

Porosity and density measurements 1/2

Sample	Msub	Msat	Mdry	New Mdry	Porosity	bulk density
	g	g	g	g	%	g/cm3
M1-A	258,48	459,27	434,88	-	12,15	2,16
M1-B	254,23	453,18	426,33	420,8	13,50	2,14
M1-C	258,8	458,22	433,9	-	12,20	2,17
M1-D	253,89	450,94	426,7	412,16	12,30	2,16
M1-E	266,15	470,04	440,61	-	14,43	2,16
M1-H	265,35	466,2	439,26	-	13,41	2,18
M1-G	264,71	466,62	440,27	-	13,05	2,16
M1-V	269,31	475,7	447,92	-	13,46	2,16
M1-W	288,92	510,45	480,15	-	13,68	2,17
M2-A	218,51	413,96	365,74	-	24,67	1,86
M2-A1	220,77	417,65	368,69	-	24,87	1,87
M2-B	209,14	403,08	349,17	-	27,80	1,79
M2-C	212,68	407,29	355,9	-	26,41	1,82
M2-D	220,14	418,16	369,29	-	24,68	1,85
M2-E	215,4	411,56	361,46	-	25,54	1,82
M3-A	267,06	456,87	448,44	-	4,44	2,35
M3-B	281,88	486,07	477,64	-	4,13	2,33
M3-C	269,69	463,63	456,61	-	3,62	2,34
M3-D	286,09	489,36	479,52	467,08	4,84	2,35
M3-E	283,62	487,25	477,81	462,18	4,64	2,34
M3-G	266,12	456,53	447,8	-	4,58	2,35
M3-H	273,35	470,37	459,87	-	5,33	2,32
M3-I	281,01	482,92	472,12	-	5,35	2,36
M3-J	277,63	477,1	466,09	-	5,52	2,30
M3-S	279,99	481,30	468,57	-	6,32	2,32
M3-T	281,05	484,29	474,75	-	4,69	2,33
M3-U	286,68	483,02	480,58	-	1,24	2,30
M3-V	274,04	469,55	459,29	-	5,25	2,32
M4-D	268,14	465,36	448,26	-	8,67	2,26
M4-A1	277,06	479,50	462,56	-	8,37	2,28
M4-T	283,09	490,77	471,03	-	9,51	2,26
M4-U	287,63	478,21	461,42	-	8,81	2,27
M4-A2	-	-	457,8	-		2,32
M4-B1	270,39	462,02	450,87	-	5,82	2,34
M4-C1	275,62	471,96	459,12	-	6,54	2,33
M4-E1	276,96	473,02	461,28	-	5,99	2,33
M4-A	275	476,78	460,19	-	8,22	2,27
M4-B	269,43	468,09	452,11	-	8,04	2,25
M4-C	267,1	464,54	447,42	-	8,67	2,26

Porosity and density measurements 2/2

Sample	Msub	Msat	Mdry	New Mdry	Porosity	bulk density
	g	g	g	g	%	g/cm3
M4-V	278,30	481,60	466,24	-	7,56	2,29
M4-W	267,37	465,70	445,52	-	10,17	2,24
M4-Z	287,63	498,21	479,60	-	8,84	2,26
M6-A	286,26	481,34	466,88	-	7,41	2,39
M6-B	301,07	503,68	491,87	-	5,83	2,41
M6-C	303,13	501,95	494	-	4,00	2,47
M6-D	296,74	497,94	484,72	-	6,57	2,38
M6-E	268,34	458,59	437,75	-	10,95	2,26
M6-F	246,35	414,77	399,41	-	9,12	3,15
M7-A	174,57	381,21	292,68	275,66	42,84	1,39
M7-B	157,07	341,59	261,88	-	43,20	1,38
M7-C	172,15	374,71	287,17	264,77	43,22	1,39
M7-D	170,09	361,65	279,55	-	42,86	1,42
M7-E	155,01	337,53	258,2	-	43,46	1,35
M7-F	167,25	358,89	275,27	-	43,63	1,42
M7-G	169,66	364,56	279,12	-	43,84	1,41
M7-H	170,24	367,19	279,99	-	44,28	1,40
M7-I	167,45	358,32	275,32	-	43,49	1,42
M7-A1	164,41	354,61	295,38	-	31,14	1,52
M8-A	177,17	370,2	295,84	-	38,52	1,52
M8-B	170,31	359,3	284,36	-	39,65	1,46
M8-C	175,82	363,67	294,92	-	36,60	1,55
M8-D	175,24	367,45	292,89	-	38,79	1,51
M8-E	188,08	390,09	315,53	-	36,91	1,53
M8-F	190,69	396,93	321,64	-	36,51	1,53
M8-G	186,6	386,15	314,99	-	35,66	1,57
M8-H	184,45	385,05	309,31	-	37,76	1,50
M9-01	255,39	456,18	439,37	-	8,37	2,18
M9-02	258,84	454,58	449,68	-	2,50	2,28
M9-A	287,14	481,56	468,95	-	6,48	2,41
M9-B	286,63	480,52	468,37	-	6,27	2,39
M9-C	279,15	469,4	455,55	-	7,28	2,38
M9-D	284,05	481,65	462,24	-	9,82	2,31
M10-A	292,13	485,5	472,67	-	6,63	2,43
M10-B	305,06	502,84	493,98	486,87	4,48	2,48
M10-C	300,25	497,05	485,3	-	5,97	2,45
M10-D	305,53	502,79	494,21	488,32	4,35	2,49
M10-E	319,32	526,08	510,99	-	7,30	2,47
M10-F	316,35	519,92	506,73	-	6,48	2,48

10.5.2 Tensile strength

Sample	Braz	Braz	DTS	Average DTS	mean DTS	standard deviation
	kN	MPa	MPa	MPa	MPa	
M1-F	6,79	3,09	2,56	2,96	2,90	0,376505423
M1-X	11,27	4,17	3,46			
M1-Y	8,89	3,17	2,63			
M1-Z	7,68	3,82	3,17			
M2-X	3,8	1,92	1,59	1,32	1,59	0,473135681
M2-Y	4,26	2,06	1,71			
M2-Z	1,5	0,79	0,65			
M3-W	6,18	3,23	2,68	3,19	3,21	0,34404233
M3-X	7,79	3,85	3,20			
M3-Y	7,88	3,88	3,22			
M3-Z	8,97	4,40	3,66			
M4-X	5,46	2,51	2,08	2,57	2,57	0,488308493
M4-Y	7,31	3,68	3,06			
M6-Z	12,45	5,20	4,31	-	-	-
M7-W	2,82	1,48	1,23	0,98	1,03	0,212086983
M7-X	2,21	1,22	1,01			
M7-Y	1,38	0,78	0,64			
M7-Z	2,39	1,28	1,06			
M8-G	2,07	0,98	0,81	0,78	0,77	0,064336824
M8-H	1,73	0,86	0,71			
M8-Y	2,1	1,04	0,86			
M8-Z	1,61	0,87	0,72			
M9-Z	8,89	4,01	3,33	-	-	-
M10-B	5,72	3,13	2,60	3,07	2,98	0,393528945
M10-U	6,5	3,26	2,70			
M10-V	7,07	3,59	2,98			
M10-Y	8,08	4,21	3,49			
M10-Z	8,08	4,28	3,55			

10.5.3 Triaxial strength

Triaxial testing – 1/2

Sample	P-confining	σ_1-max	Sample	Cohesion	friction angle	σ_{ci}	mi	r^2
Spalte1	MPa	MPa	-	MPa	°	MPa	-	-
M10-A	10	170,53	M10	10,8	52,3	76,3	37,6	0,99
M10-B	5	188,3						
M10-C	40	390,58						
M10-E	20	162,45						
M10-F	30	175,11						
M1-B	40	219,34	M1	7,9	55,1	75,6	26,4	1
M1-G	20	232,99						
M1-H	30	236,25						
M1-V	10	172,03						
M2-A	10	86,51	M2	4,2	36,6	23,9	8,5	0,9
M2-B	5	32,97						
M2-C	20	86,46						
M2-D	15	55,48						
M2-E	15	79,18						
M3-D	50	450,00	M3	20,1	60,4	124,1	60,2	0,97
M3-E	20	441						
M3-H	5	245,39						
M3-I	10	285,08						
M3-J	15	359,66						
M4-A1	15	267,35	M4	18,5	56,1	110,2	37	0,97
M4-B	20	258,21						
M4-B1	40	223,83						
M4-C	10	245,73						
M4-D	5	192,15						
M4-E1	30	367,6						
M4-K	21	341,55						
M4-U	50	156,79						
M4-Z	30	267,35						
M6-A	35	222	M6	6,3	50,7	42	29	0,92
M6-C	5	212						
M6-D	30	289						
M6-K	5	64,39						
M6-W	10	118,09						
M6-X	5	36,52						
M6-Y	20	190,65						
M7-C	1,5	10,2	M7	1,1	43,4	6,1	8,8	0,91
M7-E	0,5	7,37						
M7-F	1	10,88						
M7-G	2,5	13,73						
M7-I	1,5	12,79						

Triaxial testing – 1/2

Sample	P-confining	σ_1-max	Sample	Cohesion	friction angle	σ_{ci}	mi	r^2
Spalte1	MPa	MPa	-	MPa	°	MPa	-	-
M8-A	1	14,54	M8	5,6	35,8	8,2	5,6	0,88
M8-C	3	20,4						
M8-D	5	22,03						
M8-E	2,5	12,15						
M8-F	2	16,58						
M8-H	2,5	14,35						
M8-S	4	17,59						
M9/10	20	260,56	M9	7,5	55,8	66,4	35,3	0,9
M9-C	10	135,76						
M9-D	20	98,41						

10.5.4 P-wave velocity

P-wave velocity measurements 1/2

Sample	P travel time sat	P travel time dry	P travel time post failure	Vp sat	Vp dry	Vp dry post	Vp reduction
	micro sec	micro sec	micro sec	m/s	m/s18	m-s	%
M1-A	34,88	40,88	47,55	2905,96	2479,45	2131,65	-14,03
M1-B	33,25	39,44	29,50	3019,25	2545,39	3403,05	33,69
M1-C	32,13	40,25	43,10	3135,70	2503,11	2337,59	-6,61
M1-D	33,06	40,63	40,13	3014,82	2453,11	2483,68	1,25
M1-E	27,9	44,74	42,75	3693,55	2303,31	2410,53	4,65
M1-H	26,18	40	29,9	3873,82	2535,42	3391,86	33,78
M1-G	30,7	43,13	47,5	3310,10	2356,13	2139,37	-9,20
M1-V	29,95	43,88	32,55	3478,24	2374,05	3200,41	34,81
M1-W	30,36	44,86	-	3674,90	2487,07	-	-
M2-A	42,31	46,06	61,40	2360,04	2167,90	1626,28	-24,98
M2-A1	39,75	42,63	44,95	2491,32	2323,01	2203,11	-5,16
M2-B	40,69	50,19	55,7	2422,87	1964,27	1769,96	-9,89
M2-C	43,25	53,37	62,5	2304,05	1867,15	1594,40	-14,61
M2-D	42,8	47,25	31,9	2351,64	2130,16	3155,17	48,12
M2-E	44,4	46,55	53,12	2262,61	2158,11	1891,19	-12,37
M3-A	23,44	28,88	30,38	4126,71	3349,38	3184,00	-4,94
M3-B	23,01	25,35	26,30	4465,88	4053,65	3907,22	-3,61
M3-C	28,07	35,5	-	3486,40	2756,71	-	-
M3-D	25,38	34,69	-	4076,70	2982,61	-	-
M3-E	28,88	38,31	32,63	3556,21	2680,85	3147,51	17,41
M3-G	25,63	35,38	41,38	3750,68	2717,07	2323,10	-14,50
M3-H	22,2	25,24	23	4472,07	3933,44	4316,52	9,74
M3-I	22,65	24,9	33,1	4437,09	4036,14	3036,25	-24,77
M3-J	23,55	27,38	33	4317,48	3713,54	3081,11	-17,03
M3-S	23,55	26,52	-	4298,94	3817,50	-	-
M3-T	24,70	27,75	-	4146,96	3691,17	-	-
M3-U	25,65	30	-	4081,35	3489,56	-	-
M3-V	23,95	30,13	-	4154,35	3302,25	-	-
M4-D	33,75	46,12	52,95	2955,26	2162,62	1883,66	-12,90
M4-A1	27,60	48,23	24,45	3697,22	2115,76	4173,55	97,26
M4-T	27,55	56,9	-	3797,58	1838,72	-	-
M4-U	29,65	51,34	51,5	3441,48	1987,53	1981,36	-0,31
M4-B1	24,07	33,12	21,25	4045,01	2939,71	4581,80	55,86
M4-C1	26,45	32,46	-	3770,38	3072,29		
M4-E1	25,21	41,84	27,2	3949,36	2379,62	3660,42	53,82
M4-A	34,31	48,12	55,15	2962,21	2112,08	1842,85	-12,75
M4-B	30,25	39,87	40,76	3307,33	2509,32	2454,53	-2,18
M4-C	34,38	44,19	-	2891,41	2249,53	-	-

P-wave velocity measurements 2/2

Sample	P travel time sat	P travel time dry	P travel time post failure	Vp sat	Vp dry	Vp dry post	Vp reduction
	micro sec	micro sec	micro sec	m/s	m/s18	m-s	%
M4-V	29,75	46,13	-	3439,78	2218,37	-	-
M4-W	28,75	56,99	-	3476,06	1753,58	-	-
M4-Z	29,95	45,25	30,15	3549,92	2349,61	3526,37	50,08
M6-A	23,51	38,05	-	4175,95	2580,20	-	-
M6-B	23,75	33,15	48,45	4279,16	3065,76	2097,63	-31,58
M6-C	23,69	35,06	-	4226,82	2856,06	-	
M6-D	24,06	28,88	-	4262,95	3551,48	-	
M6-E	24,13	28,56	40,50	3997,93	3377,80	2381,98	-29,48
M6-F	19,85	26,75	-	3216,12	2386,54	-	-
M7-A	56,9	55,7	57,00	1876,80	1917,24	1873,51	-2,28
M7-B	49,8	49,95	-	1913,12	1907,37	-	-
M7-C	56,56	60,81	69,36	1912,66	1778,98	1559,69	-12,33
M7-D	40,4	54,99	56,38	2450,74	1800,51	1756,12	-2,47
M7-E	53,44	55,19	60	1840,44	1782,09	1639,22	-8,02
M7-F	42,58	52,99	59,36	2306,48	1853,37	1654,48	-10,73
M7-G	43,86	53,75	74,35	2277,85	1858,73	1343,73	-27,71
M7-H	45,35	54,75	-	2245,06	1859,60	-	-
M7-I	42,35	51,38	124,7	2312,87	1906,38	785,49	-58,80
M7-A1	43,50	56,75	-	2252,87	1726,87	-	-
M8-A	53,2	52,5	65,64	1853,70	1878,41	1502,39	-20,02
M8-B	49,3	51,15	-	2002,10	1929,68	-	-
M8-C	52,15	53,25	27,8	1857,85	1819,47	3485,13	91,55
M8-D	47,8	47,5	74,25	2056,21	2069,19	1323,73	-36,03
M8-E	61,75	57,1	67,44	1684,80	1822,01	1542,66	-15,33
M8-F	60,75	54,9	63,76	1741,18	1926,72	1658,98	-13,90
M8-G	53,8	50,8	-	1894,61	2006,50	-	-
M8-H	61,6	59,4	80,02	1699,73	1762,68	1308,46	-25,77
M9-01	20,38	20,69	-	4912,66	4839,05	-	-
M9-02	20,2	20,8	-	4930,53	4788,30	-	-
M9-A	20,31	27,56	32,45	4838,01	3565,31	3028,04	-15,07
M9-B	20,75	29,56	33,80	4751,65	3335,48	2917,06	-12,54
M9-C	19,75	27,45	-	4888,10	3516,94	-	-
M9-D	23,25	34,75	-	4331,33	2897,94	-	-
M10-A	22,81	33,5	41,65	4310,24	2934,83	2360,54	-19,57
M10-B	22,44	35,44	46,8	4483,21	2838,69	2149,64	-24,27
M10-C	22,5	35,13	48,49	4470,67	2863,36	2074,45	-27,55
M10-D	22,31	35,69	-	4508,14	2818,06	-	-
M10-E	23,25	36,15	-	4546,09	2923,84	-	-
M10-F	22,4	33,79	-	4608,48	3055,05	-	-